FITNESS-FOR-SERVICE CRITERIA FOR PIPELINE GIRTH WELD QUALITY

Final Report

to: Materials Transportation Bureau
U.S. Department of Transportation
400 7th Street SW
Washington, DC 20590

Welding Research Council
United Engineering Center
345 E. 47th Street
New York, NY 10017

from: Fracture and Deformation Division
National Bureau of Standards
Boulder, Colorado 80303

November 1, 1983

CONTENTS

FITNESS-FOR-SERVICE CRITERIA FOR PIPELINE GIRTH-WELD QUALITY

R. P. Reed, M. B. Kasen, H. I. McHenry, C. M. Fortunko, and D. T. Read

ABSTRACT

Criteria have been developed for applying fitness-for-service analyses to flaws in the girth welds of the Alaska Natural Gas Transmission System pipeline. A critical crack-opening-displacement elastic-plastic fracture mechanics model was developed and experimentally verified. Procedures for constructing flaw acceptence criteria curves based on this model are provided. A significantly improved ultrasonic method for detecting and dimensioning significant weld flaws was developed and demonstrated on pipeline sections. The probability of crack initiation from blunt flaws was shown to be very low under severe low-cycle fatigue. Suggestions are offered for technical implementation of field inspection procedures and for practical implementation of the flaw acceptence criteria.

EXECUTIVE SUMMARY

The utility of fitness-for-service criteria for judging the need to repair pipeline girth welds containing flaws exceeding that permitted under prevailing workmanship standards was demonstrated during construction of the Trans-Alaska Pipeline System (TAPS). Here, fracture mechanics principles provided a quantitative technical basis for decision making, eliminating the need for unnecessary repair of many welds while maintaining assurance of the structural integrity of the pipeline.

The National Bureau of Standards (NBS) provided the Department of Transportation (DOT) with the technical information for implementing the TAPS fitness-for-service approach. The DOT recognized that the general use of fitness-for-service criteria in general pipeline construction would be beneficial. In 1978 NBS was requested to initiate a research program leading to this objective. However, soon after the work began, the DOT requested that the NBS program concentrate on developing criteria that could be implemented during construction of the proposed Alaska Natural Gas Transportation System (ANGTS), which was then in the planning stage. It was the intention, then, to redirect the program to generalization of the ANGTS research and, indeed, a portion of the research was redirected in 1981. However, the present report emphasizes the specifics of the ANGTS line rather than the case of pipelines in general.

Fracture mechanics analysis was used in this research. Fracture mechanics permits mechanical understanding of the relationship between the maximum stress and strain imposed on a pipeline during its lifetime, the pipeline and weldment properties, and flaws of different sizes and configurations. This understanding required development and verification of a model relating these

parameters to weldment performance. Although the basic principles of fracture mechanics are well understood and widely implemented in the aerospace industry, their application to pipeline fabrication was complicated by the relatively high ductility of the materials used in their construction. It was necessary to understand crack initiation and propagation in the elastic-plastic range instead of linear-elastic failure typical for materials and structures displaying lower ductility.

It was assumed that a pipeline would be subjected to predictable stresses, that it would be constructed from API line-pipe steel having known minimum properties, and that the pipe would be welded by a process producing predictable minimum weldment strength and toughness. This design and materials information was then fed into the theoretical model to develop a series of curves relating the combination of maximum flaw length and through-wall depth permissible for the maximum applied load (allowable flaw-size curves). Practical use of such curves presupposes the ability to detect and measure girth-weld flaws, and methods to accomplish this had to be developed.

Research was directed into three areas:

1. Refinement and experimental verification of the fracture mechanics model linking flaw size (length and through-wall depth) to pipeline stresses and weldment strength and toughness. Analytical predictions were compared with experimental results obtained on surface-cracked tensile panels and large-diameter pipe tests. The critical crack-opening-displacement (COD) model (used in the TAPS evaluation) was modified to optimize agreement between analysis and experiment. Modifications included: superposition of the elastic and post-ligament-yield solutions for crack-tip-opening displacement, use of a strip-yield plastic-zone correction on both crack length and crack

depth, and use of a curvature correction for pipes. In summary, a fracture analysis model that relates allowable flaw sizes to the applied stress level and the weldment strength and toughness was developed, verified experimentally, and used to calculate allowable flaw sizes for proposed operating conditions of the ANGTS pipeline.

Procedures for the use of elastic-plastic fracture mechanics for the derivation of allowable flaw-size curves are in the early stages of development. Further work is recommended to increase confidence in the analytical results.

2. Development of a practical method of determining the through-wall flaw dimension. The TAPS experience showed that estimation of dimensions from conventional radiographs was so inaccurate that very large safety factors were required. This resulted in fitness-for-service criteria that were far more restrictive than necessary. Initially, efforts were made to refine the densitometry method of assessing flaw through-wall dimensions. Although some improvement was realized, it became evident that this approach was intrinsically deficient in its ability to measure sharp flaws, such as lack of fusion or cracks, which are the most significant in a fitness-for-service analysis. A more promising approach was provided by ultrasonic methods, which are intrinsically sensitive to sharp flaws. Although ultrasonic inspection systems based on high-frequency piezoelectric transducers have long been used for flaw detection in welds, incorporation of even the most advanced automation and signal processing has thus far failed to produce systems capable of providing the required flaw measuring capability. Therefore, we tried a new approach -- the development of an ultrasonic inspection system optimized for pipeline use based on electromagnetic transducers (EMATs), which transmit and receive low-frequency shear/horizontal (SH) waves. Unlike conventional systems, this approach provides a signal amplitude that increases

monotonically with through-wall flaw depth. The system can be gated to ignore flaws of noncritical dimensions and to trigger an alarm automatically when flaws of significant size are present. Coupling agents are not required between the transducer and pipe, and reliability is not affected by geometric factors such as the weld reinforcement. Its accuracy is comparatively insensitive to operator skill, and a permanent record is produced. The theory underlying flaw detection and sizing by this new method has been developed and validated by the inspection of welds containing a variety of artificial and real flaws at different depths and orientations. The necessary transducer arrays and associated signal processing equipment have been developed. Field trials and assessment of reliability are needed to confirm the usefulness of this system as an adjunct to the fitness-for-service approach to girth-weld quality assessment.

3. A convincing demonstration of the probably innocuous nature of blunt flaws, such as porosity, slag, and arc burns. We found that blunt flaws (porosity, slag) and arc burns do not decrease weldment strength and fatigue life. Subjecting pipeline welds containing large quantities of such flaws to severe low-cycle fatigue at -2°C (+28°F) had little effect on crack initiation. However, should it be desired to include blunt flaws in a fracture mechanics analysis, metallographic studies of welds containing porosity and slag showed that their depth is limited to the depth of one weld pass, eliminating the necessity for through-wall dimensioning. In metallographic studies during the TAPS program, arc-burn width was related to arc-burn depth, thus providing an easy size characterization procedure for such flaws.

On the basis of these results, three technical options are suggested for implementing field inspection oriented toward fitness for service. 1) The use of ultrasonic methods for primary inspection combined with traditional radiography for assessing workmanship and for materials and procedure control

appears to be feasible and is the most technically desirable. 2) Conventional radiography could be used as the primary inspection method, using a simplified ultrasonic system for measuring flaws. We believe that the EMAT system developed in this work appears to be the most promising inspection method for either of these two options; however, other systems of equivalent performance could be used should they become available. 3) In the event that ultrasonic inspection systems of demonstrated performance are not available at the time of construction of a given pipeline, radiography must be relied on exclusively. In this case, fitness-for-service criteria can still be used to assess blunt flaws. The demonstrated inherent limitations on the height of such flaws would greatly simplify this effort by eliminating the need for complex flaw-measuring procedures. Even under this least desirable option, a substantial reduction in remedial welding can be expected since the majority of detectable flaws would be of blunt configuration.

We suggest two ways in which the overall fitness-for-service approach might be implemented in pipeline construction: A generalized approach could prequalify designated sections of the line by establishing maximum allowable flaw sizes based on limits placed on weld-metal toughness, operating stresses, and other relevant variables. A specific-site approach might be used wherein the particular conditions existing for a given weldment are used to calculate safe flaw sizes.

We expect this report to contribute to a rational, technically defensible approach to assessing girth-weld quality, which will provide the fabricator with the maximum flexibility to accommodate his particular needs while maintaining pipeline safety. Additional research has been recommended to assist in generalization of the program's results.

Specific support for this work was provided by the Materials Transportation Bureau, DOT, and by the Welding Research Council. The Northwest Pipeline Company provided materials and consultation. Consultation was also provided by Nova, an Alberta corporation.

NOTATION

Roman Letter Symbols

a	flaw depth
a_o , a_1	relative amplitude of plate wave
a_m, b_m	relative transduction efficiencies of a plate wave by transmitter and receiver EMATs, respectively
a/t	normalized crack depth
a_{11}, a_{12} a_{22}	edge crack compliance constants
A_n	normalization constant for n^{th} SH plate mode
A_1	gross-section area in the plane of the crack
A_2	net-section area in the plane of the crack
c	contour surrounding crack tip at a point along crack front
C_{00}, C_{20}, C_{02}	coefficients in Kobayashi's solution for CMOD of an elastic surface crack
D_f	blunt flaw through-wall dimension
E	Young's modulus
f	wave frequency
f_c	cutoff frequency of SH plate waves
f_w	finite width correction of Newman
F	force per unit length
F_b	boundary correction factor for computing stress-intensity factor of surface cracks
F_c	closing force on the ligament of a surface crack
g_b, g_t	constant for computing stress-intensity factor of an edge crack

G	shear modulus
h_c	distance of clip gage from specimen surface
H	weld-pass thickness
J	J-integral
K	stress intensity factor
ℓ_{eff}	effective crack length (includes plastic-zone correction, r_y)
ℓ	flaw length
ℓ_p	length of crack measured to ends of the plastic zone
L	gage length
L_{tr}	EMAT-to-EMAT spacing
L_f	blunt flaw length
L_2	width of weld in a fracture specimen
m	bending stress
M	moment per unit length
M_c	collapse moment of a pipe
$\hat{n}$	inward-directed unit-normal to the crack face
N_c	number of fatigue cycles
p	applied jack pressure
P	applied load
P_1, P_2	power level delivered to EMAT
p_t	resultant tensile stress
Q	square of elliptic integral of second kind
r_y	radius of plastic zone and plastic-zone correction to crack length
r_{yd}	plastic zone correction to crack depth

R	pipe radius
R_s	scattered signal amplitude ratio
R_{ell}	scattered amplitude ratio for an elliptical flaw
S_F	surface surrounding a flaw
t	specimen or plate thickness
T_w	mean thickness of weld reinforcement
$\overleftrightarrow{T}$	dynamic stress tensor
T_{xz}, T_{xy}	dynamic stress field components associated with SH waves propagating along z
u	displacement vector
v_g	group velocity
v_p	phase velocity
v_s	bulk SH-wave velocity
v_x	particle velocity
V_p	plastic component of clip-gage-opening displacement
w	strain energy density
w_o	half-width of the ultrasonic beam near the transmitter EMAT
W	specimen width
W_w	mean width of weld reinforcement
W_f	blunt flaw width
x_1	direction normal to crack front
x,y,z	orthogonal coordinates
Y	stress intensity coefficient at a/W
z	distance between flaw and EMAT

Greek Letter Symbols

α, β, θ	angles or angular displacements
β_n	wave propagation constant
Γ	reflection coefficient of EMAT ultrasonic signals
δ	CMOD
δ_c	CTOD
Δ'	remote displacement in a center-cracked panel
Δ_c	edge crack compliance
Δ_o	1/2 CMOD
Δu	mode III displacement jump across the face of a crack
ε_L	gage-length strain
$\Delta\varepsilon_t$	total strain range in low-cycle fatigue
ε_{NSY}	strain at net-section yield
ε_y	yield strain
ε_{yy}	component of strain
θ_c	edge crack rotational compliance
θ_n	angle of elliptical flaw with plate surface normal
λ	wavelength
ν	Poisson's ratio
ρ	extent of Dugdale plastic zone
σ	stress
$\tilde{\sigma}$	flow stress
σ_c	closing stress
σ_{LY}	applied stress at which ligament yield of a surface crack occurs
σ_{NSY}	net-section yield stress

σ_o	average tensile stress
σ_u	ultimate tensile strength
σ_{xy} σ_{yz}	shear stresses
σ_y	yield stress
τ	time
$\emptyset$	angular position along crack front
ϕ	elliptic integral of the second kind
ω	angular frequency

Acronyms and Similar Abbreviations

ANGTS	Alaska Natural Gas Transportation System
API	American Petroleum Institute
AWS	American Welding Society
BWI	British Welding Institute
CE	carbon equivalent
CMOD	crack-mouth opening displacement
$CMOD_{LY}$	crack-mouth opening displacement in the post-ligament-yield range
$CMOD_{NSY}$	crack-mouth opening displacement at net-section yield strength
COD	crack opening displacement
CTOD	crack-tip opening displacment
$CTOD_E$	elastic component of CTOD
$CTOD_{LY}$	ligament yielding component of CTOD;
$CTOD_{RS}$	residual stress component of CTOD
DOT	U.S. Department of Transportation
ECA	engineering critical assessment

EDM	electrical-discharge machined
EMAT	electromagnetic-acoustic transducer
GMA	gas-metal arc
GSY	gross-section yielding
GTAW	tungsten-inert gas
HAZ	weldment heat-affected zone
HRA	hardness, Rockwell A scale
HRB	hardness, Rockwell B scale
HRC	hardness, Rockwell C scale
LVDT	linear variable differential transducer
NBS	National Bureau of Standards
NDE	nondestructive evaluation
NSY	net-section yielding
PPM	periodic permanent magnet
RT	radiographic inspection
SH	shear-horizontal ultrasonic waves
SMA	shielded metal arc
SMYS	specified minimum yield strength
TAPS	Trans-Alaska Pipeline System
UT	ultrasonic inspection
WM	weld metal

1. INTRODUCTION

Extensive repair to girth welds on the Trans-Alaska Pipeline System (TAPS) resulted from the discovery that a large number of completed and buried welds failed to meet the Department of Transportation (DOT) standards[1] related to girth welds of liquid pipelines, which incorporate the workmanship criteria of the 15th edition of API Standard 1104.[2] This remedial welding was expensive because pipe sections buried under permafrost and rivers at remote locations had to be excavated or looped.

At that time it was recognized that many of the flaws outside workmanship standards were unlikely to endanger the safety of the line and that repairs might do more damage to the integrity of the line and to the environment than if the flaws were left unrepaired. Unfortunately, there was no established technical basis for such a decision. Repairs were therefore begun.

At the same time, fracture mechanics studies were begun to establish a technical foundation for assessing flaw significance on a fitness-for-service basis as an alternative to workmanship criteria. The results of this work[3,4] brought about federal acceptance of this approach. Consequently, the amount of TAPS repair welding was reduced and a substantial amount was saved in unnecessary repair.[5] The DOT concluded in 1976 that "fracture mechanics analysis is acceptable as a basis for granting exemptions from existing standards in appropriate circumstances, if such analysis produces a convincing and conservative estimate of structural integrity."[6]

It was anticipated that the need for long-distance transport of oil and gas would lead to additional use of fitness-for-service analysis in pipeline

construction. The proposed Alaska Natural Gas Transportation System (ANGTS) was to operate at lower temperatures than the TAPS line and would be entirely buried, placing additional demands on system performance. Furthermore, since adoption of the API 1104 workmanship standards upon which the DOT standards are based, pipeline wall thickness and diameter have increased significantly, increasing the complexity and cost of weld repair. It was evident that much additional work was required before the fitness-for-service concept could be efficiently used to facilitate construction of a safe pipeline at minimum cost.

Research at NBS was initiated in 1978 to address the generic problems associated with possible amendment of the DOT liquid and gas pipeline federal regulations to include a fitness-for-service alternative. This included research on fracture mechanics, radiography, blunt flaws, and corrosion of pipelines. In 1979, the apparent imminent start of construction of the ANGTS gas pipeline led the DOT to request that the NBS program redirect its focus onto the operating conditions and materials anticipated for that line. This report, therefore, concentrates primarily on developing fitness-for-service criteria for the ANGTS line.

At the time of the TAPS experience, two fracture mechanics models were proposed[3,4] to assess the conservatism of the Draft British Standards methodology[7] (later published officially by the British Standards Institution[8]), which was used in the Alyeska waiver request to DOT. One was based on elastic-plastic fracture mechanics principles [critical crack-tip-opening displacement (CTOD) model]; the other considered only plastic instability of the uncracked ligament. Both of these newer models proved less conservative than the Draft British Standards.

In this study we have focused on the extension of the critical COD model. Modifications relating to crack-tip physics and mechanics were developed and measurements were performed, leading to an experimentally verified elastic-plastic fracture mechanics model. Consideration of crack growth from fatigue stresses, included in the TAPS assessment, has not been addressed here. Except near pump statons, cyclic stresses in the ANGTS line were not considered significant. Enhanced crack growth from environmental interactions, such as stress corrosion, also was not considered in the ANGTS case, because this origin was not considered likely.

There are serious deficiencies in the use of radiography as an inspection tool in a fitness-for-service analysis. The important flaw dimension affecting fracture is the through-wall depth of elongated, sharp flaws. But radiography provides direct information only on the projected dimensions of the flaw normal to the plane of the weldment. It is theoretically possible to relate the change in radiographic density caused by a flaw to the depth of the flaw; this approach was used in the TAPS analysis.[3,4] However, it became evident that the combination of uncertainties in the conditions under which field radiographs are taken and processed, human bias, and the technical subjectivity of such determinations led to excessive conservatism in estimating flaw dimensions.

The majority of the repairs remove flaws of a blunt configuration--porosity, slag, and arc burns. This reflects, at least partly, the sensitivity of radiography to such flaws and its relative insensitivity to sharp flaws, such as lack of fusion or incomplete penetration. Yet, from a fitness-for-service approach, sharp flaws are more significant, since they produce the highest stress intensities and, consequently, have the highest probability of initiating fracture. A better inspection system for detecting and dimensioning flaws in girth welds was required, preferably one having optimal sensitivity to sharp flaws.

The significance of blunt flaws in crack initiation was questioned. Results of a number of studies had suggested that the presence of such weld flaws is irrelevant to the performance of structures joined with tough weld metal, but the credibility and the boundary conditions of this assumption had not been examined for pipeline girth welds.

It was likely, we thought, that the through-wall depth of blunt flaws would intrinsically be restricted to the depth of one weld pass, allowing that dimension to serve as a maximum in a fracture mechanics analysis. Although such a limitation is frequently assumed, a thorough search of the literature did not reveal the required documentation. A study was therefore conducted on inherent dimensional limitations of blunt flaws with the purpose of confirming or refuting this assumption.

It is instructive to compare the results of this study with those of other pipeline fitness-for-service approaches that have been suggested:

1. The British Standard specifically related to pipeline welding, "Specifications for Field Welding of Carbon Steel Pipelines,"[9] is currently under review. One proposal incorporating fracture mechanics analysis has been recently discussed by Carne and Harrison.[10] They proposed a three-tier approach. Tier one corresponds to workmanship standards similar to those now in existence, but incorporating minimum toughness requirements. Tier two consists of very conservative generalized fracture mechanics analysis, intended to be applied by field engineers not necessarily specialized in fracture mechanics. Tier three is applied by a specialist to a specific site and labeled engineering critical assessment (ECA). Inspection methodology was not discussed in this approach.

2. Glover and Coote[11] pointed out that the British Standards Institution fracture mechanics guidelines are also being used for ECA of segments of the new large-diameter gas pipelines in Canada. Their assessment

showed that radiographic inspection could not properly and consistently detect sharp flaws. They found that planar flaws not detected by radiography were consistently detected by high-frequency ultrasonic techniques, but that sizing was unreliable. They suggested that both radiography and ultrasonics methods be used, assuming that flaw depths are restricted to the thickness of one weld pass. The British Standards Institution Guidelines is therefore applied on the basis of flaw length and knowledge of the applied axial strain and weldment toughness. Note that this approach is limited to girth welds made by an automatic process.

3. The Japan Welding Engineering Society has recently published their first report, "Method of Assessment for Defects in Fusion-Welded Joints With Respect to Brittle Fracture."[12] This report outlines procedures for using a fitness-for-service analysis in specific cases for establishment of allowable sharp flaw sizes in terms of local weldment strain and COD weld toughness. Inspection methodology is not addressed.

4. A major revision of the American Petroleum Institute 1104 Standard for Welding Pipelines and Related Facilities (issued in May, 1983) was discussed by Von Rosenberg and Royer.[13] This generalized fitness-for-service approach requires calculation of maximum axial design stress and strain and minimum weldment toughness in terms of COD values of either 0.13 mm (0.005 in) or 0.25 mm (0.010 in). Fatigue crack growth is also considered. Inspection techniques are left to the individual companies. This revision appears as Appendix A, 16th Edition, API 1104 Standards.[2] However, at the time of this report, the 16th Edition has not been incorporated into the Federal gas and liquid pipeline safety standards.

These programs demonstrate international recognition of the need to supplement welding workmanship standards with fitness-for-service criteria for pipelines. Reduced pipeline construction time and costs through the elimination of unnecessary repairs are expected to accrue from this attention.

In summary, our research has focused on the development of a comprehensive model to calculate allowable flaw sizes and laboratory experiments to assess the validity of such models, the assessment of the significance of blunt flaws in girth weld structural integrity, the measurement of inherent blunt flaw size limitations, and the inspection methods for sharp flaws.

Our report first discusses the development and experimental verification of an elastic-plastic fracture mechanics model applicable to sharp flaws. We then address development of a new inspection technique that is optimized for the fitness-for-service approach. Research related to the significance of blunt flaws is then presented.

Finally, we recognize that nondestructive inspection has two roles in pipeline construction. One relates to quality control--the monitoring of welder and equipment performance and the quality of consumables used in the fabrication. The other is acceptance or rejection of a weld on the basis of fitness for service. Although this report concentrates on the latter role, both roles must be considered in devising an effective inspection system. Possible inspection options for achieving these goals and for implementation of the fitness-for-service approach are therefore addressed in this report.

More detailed information on selected subjects addressed in this report is given in Appendixes A and B and the final report to the U.S. DOT.[14]

2. DEVELOPMENT OF ALLOWABLE FLAW-SIZE CURVES

H. I. McHenry, Y. W. Cheng, R. deWit, R. B. King, and D. T. Read

2.1 Introduction

Allowable flaw sizes for pipeline girth welds are set forth in Section 6 of API 1104[2] on the basis of workmanship considerations; that is, flaw-size limits are based on quality levels that can reasonably be expected from a qualified welder using satisfactory materials, equipment, and procedures. In 1976, the U.S. Department of Transportation permitted the use of alternative weld quality standards to evaluate certain girth welds in the Trans-Alaska Pipeline System (TAPS). The alternative standards were in the form of allowable flaw-size curves derived on the basis of a fracture mechanics analysis.

An allowable flaw-size curve is a plot of allowable flaw depth, a, as a function of flaw length, ℓ, for a planar (crack-like) flaw as shown schematically in Fig. 1. Dimension a refers to the through-wall dimension of the flaw projected in the plane of the weld. A point on the curve represents the maximum flaw size (ℓ vs. a) that can be tolerated without impairing the service performance of the pipeline under worst-case operating conditions. Flaw sizes that fall below the curve are acceptable because they will not impair performance, and flaw sizes that lie above the curve must be repaired because they are potentially detrimental.

The purpose of this part of the program was to develop allowable flaw-size curves suitable for use in evaluating ANGTS pipeline girth welds. The specific objectives of the investigation were: 1) to develop a fracture mechanics analysis model to relate allowable flaw size to applied stress and

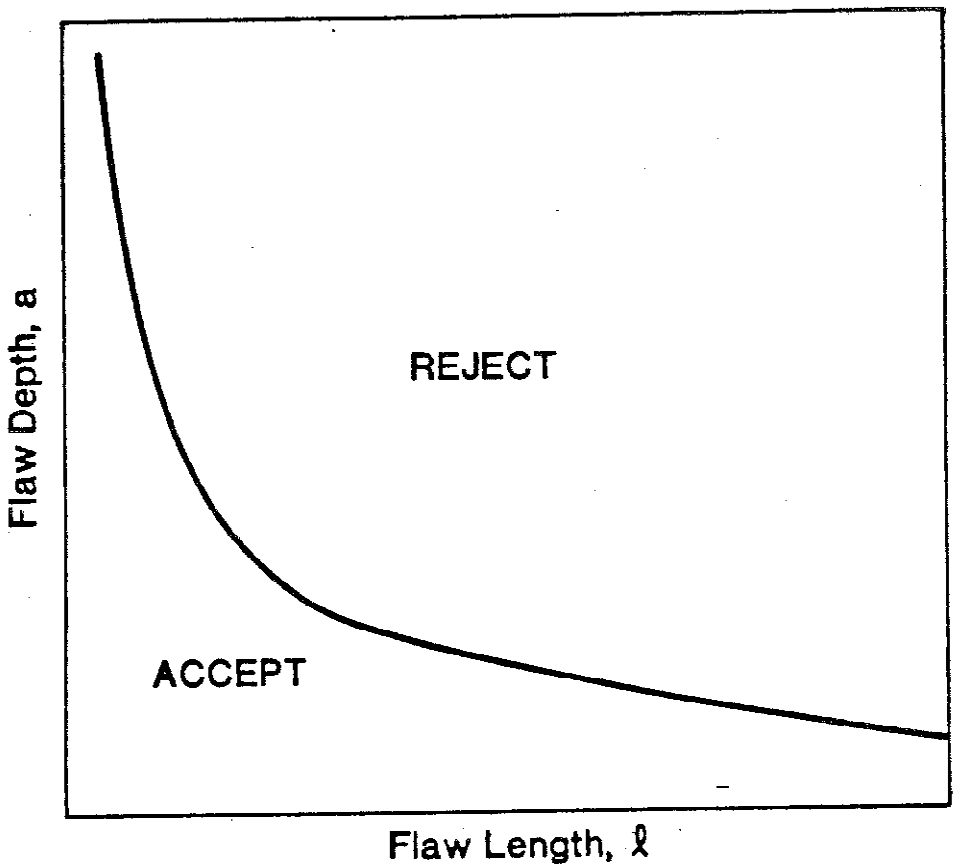

Fig. 1 - Schematic of allowable flaw-size curve.

weld toughness, 2) to verify the analytical model experimentally, and 3) to use the model to calculate allowable flaw-size curves for representative operating conditions and weld properties.

The achievement of the first two objectives required extensive research in analytical and experimental fracture mechanics. These results are summarized herein. Many of the results have been published previously, and these publications are cited where appropriate in this report. The achievement of the third objective is based on the results of the fracture mechanics studies. The allowable flaw-size curves for representative operating conditions and weld procedures are presented in Section 2.5, Allowable Flaw-Size Curves, along with the procedures used to calculate them. Section 2.5 is self-contained, and thus, readers primarily interested in the resulting curves can skip the preceding sections.

Fatigue and corrosion contributions to crack growth were not considered significant in the case of the ANGTS pipeline and are not included in this analysis. Preliminary corrosion research was conducted early in the program for generalized pipeline analysis,[14] and fatigue was included in the TAPS analysis.[3,4]

2.2 Fracture Mechanics

The principles of fracture mechanics provide the technical basis for the development of allowable flaw-size curves. Fracture mechanics is the study of the influence of loading, crack size, structural geometry, and material properties on the fracture resistance of structures containing cracks. There are two main ideas in fracture mechanics: First, fracture occurs when the driving force for fracture, a function of stress and flaw size, exceeds the resistance of the material to fracture, referred to as the fracture toughness. Second, fracture toughness is a geometry-independent material property; that

is, a simple laboratory specimen and a large structure both fracture at the same critical value of driving force. The second idea is only directly applicable to linear elastic (brittle) fracture and to certain cases of fully plastic (ductile) fracture; however, it is a conservative assumption for elastic-plastic fracture if the notch constraint in the test specimen exceeds the notch constraint in the structure. Such is the case for pipeline girth welds when full-thickness single-edge-notch-bend specimens are used to measure fracture toughness.

Several fracture criteria are used to characterize the driving force for fracture and the fracture toughness. These include the stress intensity factor, K, the J-integral, J, and the crack-tip-opening displacement, CTOD. Since K is a linear elastic parameter, it was not suitable as a fracture criterion for ANGTS pipeline girthwelds, which must operate safely at stress levels near the yield strength. However, K calculations were useful for determining the elastic component of J and CTOD, and thus, K calculations for surface flaws are discussed in this section. The main emphasis in this section is on the analytical work related to the development and experimental verification of elastic-plastic fracture mechanics models based on the CTOD concept.

2.2.1 Linear Elastic Fracture Mechanics

The stress intensity factor, K, for surface cracks has been the subject of numerous studies. Recently, the fracture committee of the Society for Experimental Stress Analysis compared several elastic numerical solutions for a surface flaw in a plate under remote tension and bending.[15] The results of Newman and Raju[16] compared favorably with the "best-estimate" results of the committee. The results of Newman and Raju are expressed in terms of numerical

equations that facilitate computation, and thus, their K solution has been used in the present study. The K solution for semielliptical cracks in simple tension is:

$$K = \sigma(\pi a/Q)^{\frac{1}{2}}F_b \tag{1}$$

for $a/\ell \leq 0.5$, $a/t < 1.0$, $\ell/W < 0.5$, and $0 \leq \phi \leq \pi$;

where σ = stress

Q = is the square of the complete elliptic integral of the second kind

F_b = boundary correction factor, given below

a = crack depth

ℓ = crack length

t = specimen thickness

W = specimen width

ϕ = angular position along crack front

The geometric variables (a, ℓ, t, and ϕ) are illustrated in Fig. 2. In this study, the K at maximum crack depth ($\phi = 90°$) was of interest.

The numerical expression for Q developed by Rawe and used in Ref. 17 is:

$$Q = 1 + 1.464(2a/\ell)^{1.65} \tag{2}$$

The boundary correction factor for tension is:

$$F_b = [b_1 + b_2(a/t)^2 + b_3(a/t)^4]f_w \tag{3}$$

where

$$b_1 = 1.13 - 0.09\ (2a/\ell) \tag{4}$$

$$b_2 = -0.54 + 0.89\ (0.2 + 2a/\ell) \tag{5}$$

$$b_3 = 0.5 - 1.0/(0.65 + 2a/\ell) + 14(1.0 - 2a/\ell)^{24} \tag{6}$$

The finite width correction, f_w, of Newman[18] is used:

$$f_w = [\sec\ (\pi\ell/2W)(a/t)^{\frac{1}{2}}]^{\frac{1}{2}} \tag{7}$$

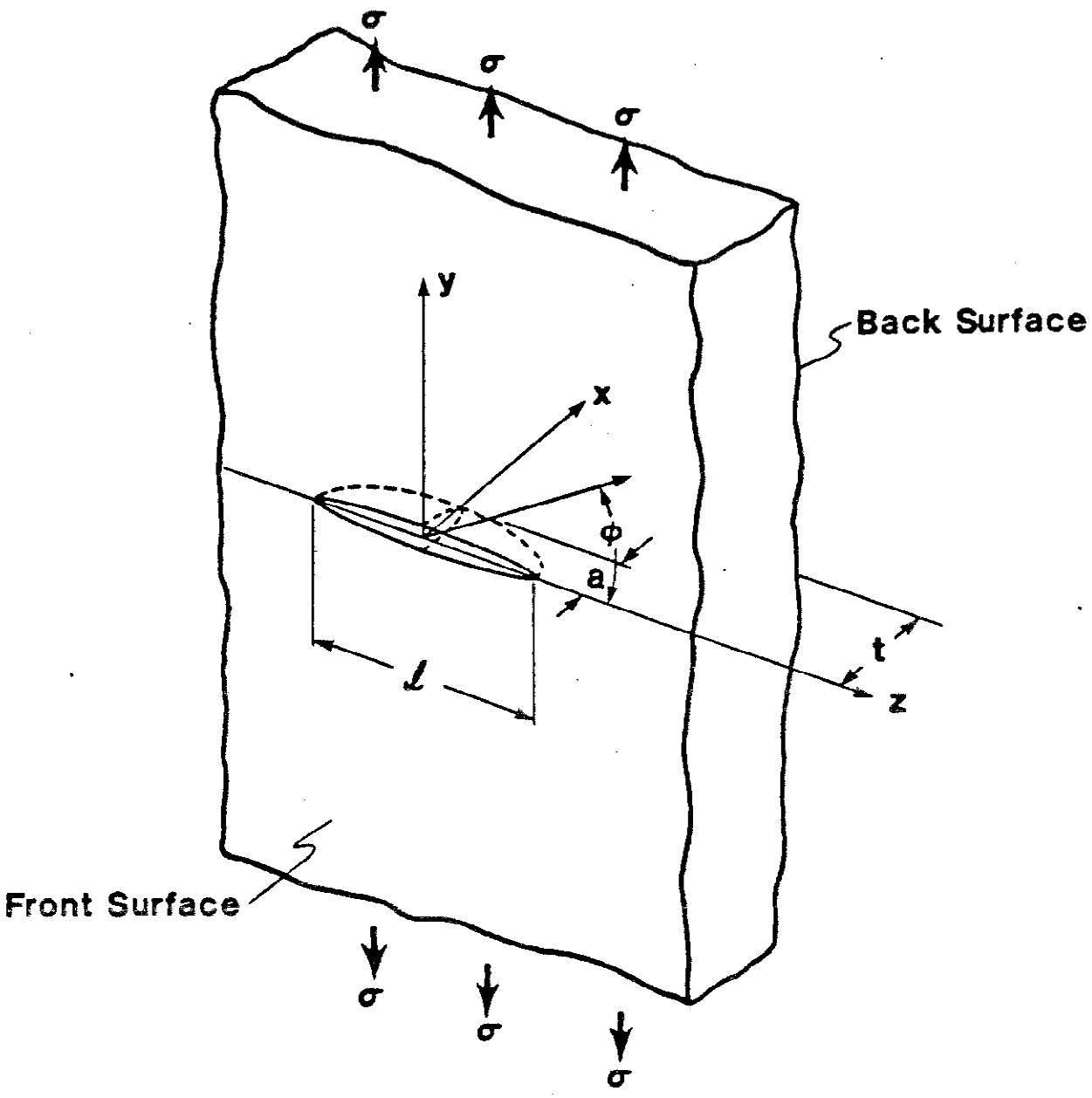

Fig. 2 - Geometry of surface flaw.

Applicability of the linear elastic analysis has been extended to conditions approaching net-section yielding by correcting for the zone of plasticity that exists at the crack tip. The idea is that the plastic material at the crack tip strains without carrying the incremental load; therefore, in the elastic sense, the crack behaves as if it were slightly longer. The Irwin[19] correction is made by adding the radius of the plastic zone, r_y, to the apparent crack length, where:

$$r_y = (K/\sigma_y)^2/2\pi \tag{8}$$

and σ_y is the yield strength

Alternatively, the plastic zone has been modeled by Dugdale[20] as a thin strip of plastic material extending from the crack tip in the plane of the crack. The extent of the Dugdale plastic zone, ρ, is given by

$$a/(a + \rho) = \cos(\pi\sigma/2\sigma_y) \tag{9}$$

If the higher order terms of the series expansion of the cosine function are neglected, Eq. 9 reduces to

$$\rho = \pi(K/\sigma_y)^2/8 \tag{10}$$

The plastic-zone correction, r_y, is taken in this report to be equal to $\rho/2$ and is approximately 23% greater than the Irwin correction.

As plasticity develops, the crack tip blunts. The extent of this blunting is the CTOD. The CTOD is calculated for the small-scale yielding case as follows:

$$\text{CTOD} = K^2(1 - \nu^2)/E\bar{\sigma} \tag{11}$$

where E = Young's modulus

ν = Poisson's ratio

$\bar{\sigma}$ = flow stress = $\frac{1}{2}(\sigma_y + \sigma_u)$

σ_u = ultimate tensile strength

K = K (stress intensity factor) from Eq. 1

2.2.2 Modified Critical-COD Model

The CODs of a surface flaw in a flat tensile panel that occur after the uncracked ligament has yielded were originally modeled by Irwin[21] by assuming the surface flaw behaves as a through-thickness crack of the same length. The opening of the equivalent through-thickness crack is reduced by closure forces equal to the product of the flow stress times the area of the uncracked ligament.

In the TAPS evaluation, a model developed from Irwin's original concept, referred to as the critical-COD model, was used to calculate allowable flaw-size curves.[4] However, there were no experimental data to evaluate the model. In this investigation, the analytical predictions were compared with experimental results, and the critical-COD model were modified to optimize agreement between analysis and experiment. Modifications include: superposition of the elastic and post-ligament-yield solutions for CTOD, use of a strip-yield plastic-zone correction on both crack length and crack depth, use of a finite-width correction for flat plates, and use of a curvature correction for pipes.

The critical-COD model treats the surface crack in a plate as a through-thickness center crack after the ligament has yielded. The COD at the middle of the center crack of length, ℓ, in an infinite plate under a remote stress, σ, is given by

$$COD = 2\ell\sigma/E \tag{12}$$

For a surface crack, the COD of Eq. 12 is reduced by the remaining ligament. The effect of ligament depth can be estimated by considering a closing force distributed over the crack-face area. Assuming the ligament is yielded, the total closing force, F_c, is

$$F_c = \ell(t - a)\bar{\sigma} \tag{13}$$

where $\bar{\sigma}$ is flow stress and is estimated as the average of the yield strength and the ultimate tensile strength, t is the plate thickness, and a is the crack depth. Distributing this closing force over the area ℓt gives a closing stress, σ_c, on the equivalent through-thickness crack of

$$\sigma_c = (1 - a/t)\bar{\sigma} \tag{14}$$

This closing force opposes the remote stress, σ, and the resultant opening of the surface crack is then

$$COD = 2\ell(\sigma - \sigma_c)/E \tag{15}$$

To account for the crack opening due to the crack-tip plasticity, the effective crack length, which includes the plastic-zone size correction, r_y, is used in place of ℓ. The resulting expression when Eq. 14 is substituted into Eq. 15 becomes

$$COD = [\sigma - (1 - a/t)\bar{\sigma}]2(\ell + 2r_y)/E \tag{16}$$

where r_y is a plastic-zone size correction with a finite width correction and is evaluated[22] as

$$\sin(\pi\ell/2W)/\sin(\pi\ell_p/2W) = \cos[(\pi/2)(\sigma'/\bar{\sigma}')] \tag{17}$$

where ℓ_p is the length of the crack measured to the ends of the plastic zone, defined as $\ell + 4\,r_y$, $\sigma'/\bar{\sigma}' = 1 - t/a(1 - \sigma/\bar{\sigma})$, and W is the plate width.

Using CTOD as the fracture criterion, the relationship among CTOD, σ, and flaw size is

$$CTOD = CTOD(elastic) + COD \tag{18}$$

where CTOD(elastic) is given in Eq. 11 and COD is given in Eq. 16. The value of COD is zero when σ is less than ligament yield stress, given by $(1 - a/t)\bar{\sigma}$.

Comparison of analytical predictions of the critical-COD model with experimental results discussed in Section 2.3, was done in terms of crack-mouth-opening displacement (CMOD); i.e., the COD at x = 0 in Fig. 2) where:

$$CMOD = CMOD(elastic) + COD \tag{19}$$

where COD is given in Eq. 16 and CMOD(elastic) is evaluated using the elasticity solution of Kobayashi[23] for cracks with aspect ratios (ℓ/a) less than 10:

$$CMOD = \frac{-8(1 - \nu)}{Ga\ell} C_{00} + \frac{4}{3a^2} C_{20} + \frac{16}{3\ell^2} C_{02} \qquad (20)$$

where G = shear modulus and the coefficients C_{00}, C_{20}, and C_{02} are governed by the geometry and loading conditions. The values for C_{00}, C_{20}, and C_{02} are taken from Kobayashi.[24] Solutions to Eq. 20 are shown in Fig. 3.

For long cracks ($\ell/a > 10$), the Kobayashi solution is not applicable and the elastic CMOD is calculated using King's[22] simplified line-spring model (discussed in Section 2.2.3).

2.2.3 Derivation of Yielded-Ligament Model from Line-Spring Model

The line-spring model was developed by Rice and Levy[25] for elastic surface cracks. Extension of the model to elastic-plastic surface cracks was speculated upon by Rice[25] and carried out by Parks.[27] For the purposes of this program, the line-spring model provided an analytical framework for extending the critical-COD model to the case of surface cracks in pipes rather than flat plates.

The use of the line-spring model was suggested after the validity of the critical-COD model was confirmed for the case of surface cracks in tensile panels (see Section 2.3.2). Thus, the same physical assumptions used in the critical-COD model were introduced into the line-spring model, and the two models predict the same results for the flat-plate case. However, the line-spring model made it possible to account for a number of complexities that exist for the case of long surface flaws in pipes, specifically, the elastic displacements of long cracks, the curvature effect, and plasticity development. On the other hand, these same physical assumptions resulted in considerable

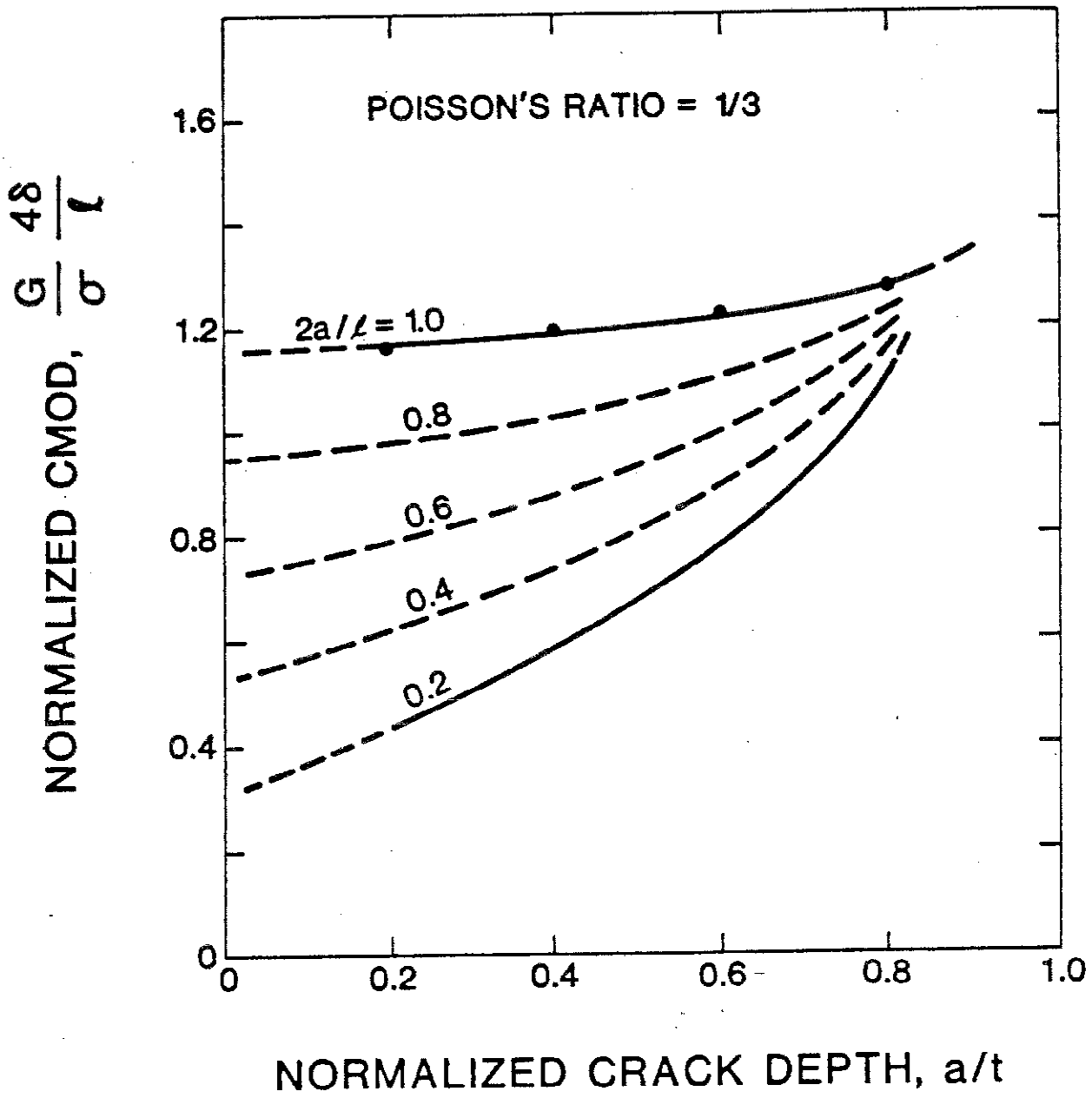

Fig. 3 - Theoretical solution for CMOD in a surface-flawed tension plate. G = shear modulus, δ = CMOD, ℓ = crack length, a = crack depth, and t = plate thickness.

simplification of the line-spring model. The derivation of the model for the case of flat plates is discussed in this section and the extension of the line-spring model to the case of surface cracks in pipes is discussed in the following section, 2.2.4.

In the line-spring model, the surface crack is treated as being equivalent to a through-crack of the same length as the surface crack. However, owing to the presence of the uncracked ligament, certain closing forces and bending moments act on the faces of the equivalent through-crack. The bending moments are caused by the eccentricity of the ligament with respect to the centerline of the plate thickness. These forces and moments can be related to the deformation of the ligament through compliance expressions. The place of the ligament can thus be thought of as being taken by "springs" connected from one face of the through-crack to the other. The compliance of these springs at a point along the crack is assumed to be equal to that of an edge crack in plane strain of the same depth as the surface crack at that point and in a plate of the same thickness. This is motivated by considering the limiting cases. If the crack were very long, it would begin to behave like an edge crack in a thick plate (thus deforming in plane strain) with all the applied load being carried by the uncracked ligament behind the crack. The other limit is that of a very deep crack, in which the ligament becomes increasingly thinner and eventually disappears entirely. In this case, the crack becomes a through-crack, and all the load is carried by the material on the sides of the crack. The actual situation is between these two extremes, and to analyze it approximately, we assume it is a mixture of the two limiting cases, so that the load is carried partially by the "edge crack" and partially by the "through-crack," as shown in Fig. 4. To determine the unknown force, $F(x)$, and moment, $M(x)$, that

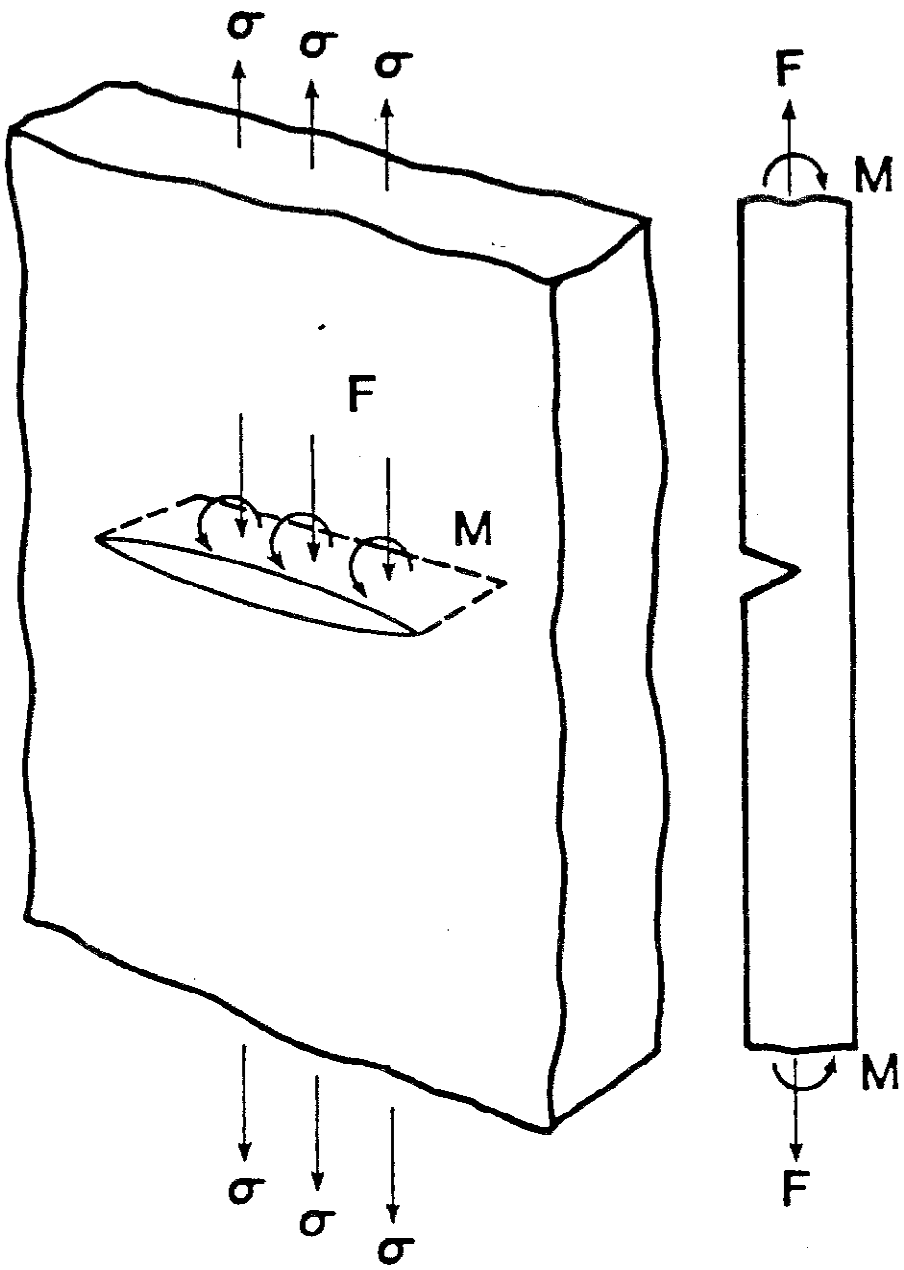

Fig. 4 - Line-spring model.

act on the edge crack at a point x along the crack and by equilibrium also act on the through-crack faces, displacement compatibility is enforced; that is, since the "through-crack" and the "edge crack" coexist in the same plate, they must exhibit the same opening displacement of the crack and the same rotation of the crack faces. Once the force and moment are known, we can compute any parameter of interest, such as J or COD, by focusing our attention on the edge crack.

To apply the line-spring model, expressions relating displacements and rotations to forces and moments must be set up. It is convenient to introduce the average tensile stress,

$$\sigma_o = F/t \tag{21}$$

and the bending stress,

$$m = 6M/t^2 \tag{22}$$

where t is the plate thickness, and F and M are the force per unit length and moment per unit length, respectively, on the edge crack. In terms of σ_o and m, the compliance expressions for the edge crack are

$$\Delta_c = \frac{2(1 - \nu)t}{E} (a_{11}\sigma_o + a_{12}m) \tag{23}$$

$$\Theta_c = \frac{12(1 - \nu^2)}{E} (a_{12}\sigma_o + a_{22}m) \tag{24}$$

where the compliance constants a_{11}, a_{12}, and a_{22} are found by considering the edge crack loaded with σ_o, m and with Δ_c and Θ_c defined as the additional displacement and rotation of the ends caused by the presence of the crack. The procedure of Rice and Levy[25] was used to calculate the compliance constants (a_{ij}), and the results for the a_{ij} as functions of crack depth are shown in Fig. 5.

The mathematical complexities in the line-spring model arise in deriving the expressions relating displacement and rotation to σ_o and m in the through-crack, because the force and moment at any position along the crack front

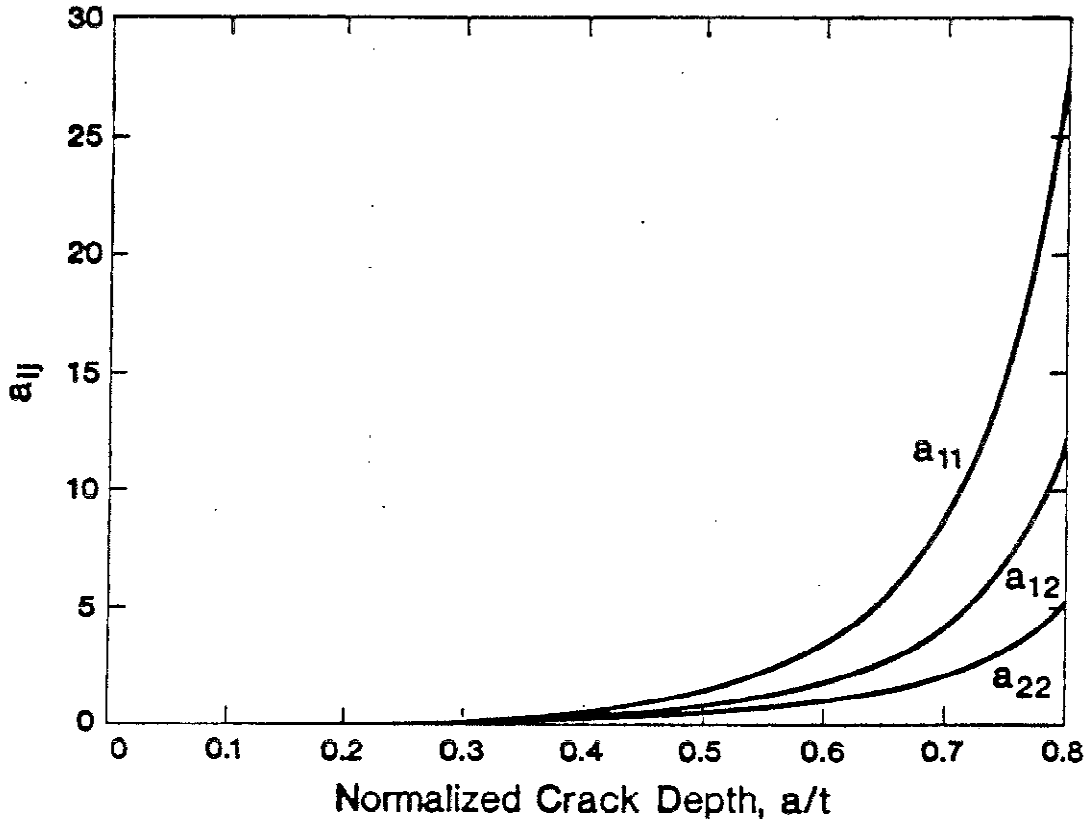

Fig. 5 - Compliance coefficients a_{11}, a_{12}, and a_{22} as a function of crack depth.

affect the displacement and rotation at any other point. Enforcing displacement compatibility results in a pair of coupled integral equations that must be solved numerically,[25,27] or the line spring may be inserted into a suitably modified finite-element program.[28,29] Extension of the model into the elastic-plastic region has been carried out by inverting Eqs. 23 and 24 and rewriting the result in an incremental form, thus relating $d\sigma_o$ and dm to $d\Delta_c$ and $d\theta_c$ through a stiffness matrix. At sections in which yielding has occurred, the "tangent stiffness" is used. This procedure was proposed by Rice[26] and successfully carried out by Parks and Lockett.[27,28,30] A further complication is the spread of plasticity from the sides of the crack. Rice[26] speculated on the possibility of handling this by using a strip-yield approach, but this has not been applied previously. If the line-spring is inserted into a finite element code, plasticity at the sides of the crack can readily be accounted for by the code.

The following simplifications reduce the model to a purely analytical one:

1. The surface crack is treated as existing in an infinite flat plate loaded in remote tension.

2. The actual crack front is replaced by a crack of constant depth, and displacement compatibility between ligament spring and through-crack is enforced only at the center of the crack. This reduces the coupled integral equations to a pair of linear algebraic equations, a simplification proposed in a slightly different form by Rice and Levy.[25] The constant crack depth used in deriving the model presented here was the maximum depth of the actual crack, so that the correct depth in the actual crack at the point of most interest is matched by the model.

3. The spring is elastic perfectly plastic; that is, it remains linear elastic until the force and moment in the spring reach a yield criterion.

4. Spread of plasticity from the sides of the through-crack is approximately accounted for by using an effective crack length of $\ell + 2r_y$, where ℓ is the crack length and the plastic-zone size correction, r_y, is obtained from a strip-yield analysis of a finite-width plate, the only manner in which finite width enters the model.

A simplified model results. The compliance of the ligament spring is still given by Eqs. 23 and 24. For an infinite plate loaded in tension by σ, with the average tensile stress, σ_o, and bending stress, m, acting on the crack faces, the displacement and rotation at the center of the crack are

$$\Delta_c = 2\ell/E\ (\sigma - \sigma_o) \tag{25}$$

$$\theta_c = \frac{-4(1 + \nu)\ell}{(3 + \nu)Et}\ m \tag{26}$$

Equation 26 is derived by integrating the solution for a point-moment applied on the crack faces.[25]

Forcing equality between Δ_c in Eqs. 23 and 25 and θ_c in Eqs. 24 and 26 results in

$$[a_{11} + \ell/t(1 - \nu^2)]\sigma_o + a_{12}m = [\ell/t(1 - \nu^2)]\sigma \tag{27}$$

$$a_{12}\,\sigma_o + [a_{22} + \frac{\ell/t}{3(1 - \nu)(3 + \nu)}]\ m = 0 \tag{28}$$

$$\sigma = \alpha\sigma \tag{29}$$

$$m = -\beta\sigma \tag{30}$$

$$\alpha = \{\ell/[t(1 - \nu^2)]\}(a_{22} + \frac{\ell/t}{3(1 - \nu)(3 + \nu)})/S \tag{31}$$

$$\beta = \{\ell/[t(1 - \nu^2)]\}\ a_{12}/S \tag{32}$$

$$\text{where } S = \{a_{11} + \ell/[t(1 - \nu^2)]\}\ [a_{22} + \frac{\ell/t}{3(1 - \nu)(3 + \nu)}] - a_{12}^2 \tag{33}$$

The spring remains elastic until satisfaction of a yield criterion is achieved in the edge crack. Various yield criteria were tried, including an upper bound slip-line solution presented by Rice,[26] a lower bound static equilibrium condition that assumes yield occurs when a plastic hinge develops in the ligament, and a simple average stress condition. The average stress condition was chosen for simplicity and because its results agreed with the experimental data presented in Refs. 31 and 32 as well as any of the yield criteria tried. Yield is assumed to occur when the average tensile stress in the ligament, σ_o, reaches a closure stress, σ_c, shown in Eq. 14, resulting in

$$\sigma_o = \frac{t - a}{t} \bar{\sigma} \tag{34}$$

From Eqs. 29 and 34 the value of applied stress at which ligament yield occurs, σ_{LY}, is determined:

$$\sigma_{LY} = \frac{1}{\alpha} \frac{t - a}{t} \bar{\sigma} \tag{35}$$

Subsequently, σ_o remains constant, given by Eq. 34, and m remains constant, given by Eq. 30 with $\sigma = \sigma_{LY}$.

Equations 25 and 26 are still used for determining Δ_c and θ_c, but after ligament yield, plasticity at the sides of the crack becomes important and the crack length, ℓ, is replaced by the "effective" length, $\ell + 2r_y$. The expression for r_y is

$$r_y = (\ell_p - \ell)/4 \tag{36}$$

and ℓ_p is evaluated from:

$$\sin(\pi\ell_p/2W) = \sin(\pi\ell/2W)/[\cos\tfrac{\pi}{2}(\tfrac{t}{a}\tfrac{\sigma}{\bar{\sigma}} - \tfrac{t}{a} + 1)] \tag{37}$$

The plate will continue to carry additional load until the strip yield reaches the edge of the plate, which occurs when the applied stress reaches the net section yield stress

$$\sigma_{NSY} = \bar{\sigma}[1 - \ell a/(Wt)] \tag{38}$$

This results directly from equilibrium or from setting $\ell_p = W$ in Eq. 37.

Equations 37 and 38 are valid for finite-width flat plates. If this model is applied to other situations, such as cracks in pipes, use of these equations would not be appropriate, and the strip-yield solution for an infinite plate might be more suitable, for which

$$\ell_p = \ell / \cos\left[\frac{\pi}{2}\left(\frac{t}{a}\frac{\sigma}{\bar{\sigma}} - \frac{t}{a} + 1\right)\right] \tag{39}$$

and the net-section yield stress becomes simply $\bar{\sigma}$.

The values of σ_o and m are now known for the entire range of applied stress. From these, both COD and the J-integral at the root of the crack can be computed. To calculate COD, it must be noted that Δ_c in Eq. 25 is the displacement at the centerline of the plate thickness. The CTOD is used as a fracture parameter, whereas the CMOD is more easily measured and is used for experimental verification of model predictions. From the geometry shown in Fig. 6,

$$\text{CTOD} = \Delta_c + \Theta_c(t - 2a) \tag{40}$$

$$\text{CMOD} = \Delta_c + \Theta_c t \tag{41}$$

An alternative method for calculating CTOD prior to ligament yield is to use the relation between CTOD and K (Eq. 11). The stress intensity factor, K, is calculated using the line-spring model, as discussed below. This method was preferable because accuracy of estimates of K using the line-spring model can be checked using published elastic numerical results.[16] After ligament yield the incremental value of CTOD was calculated using Eq. 40. This is justified because the assumption of crack faces opening as parallel lines is accurate after ligament yield, as has been confirmed experimentally using replication studies.[32] The result is

$$\text{CMOD} = (2\ell\sigma/E)\,[1 + 2(1 + \nu)\beta/(3 + \nu) - \alpha] \tag{42}$$

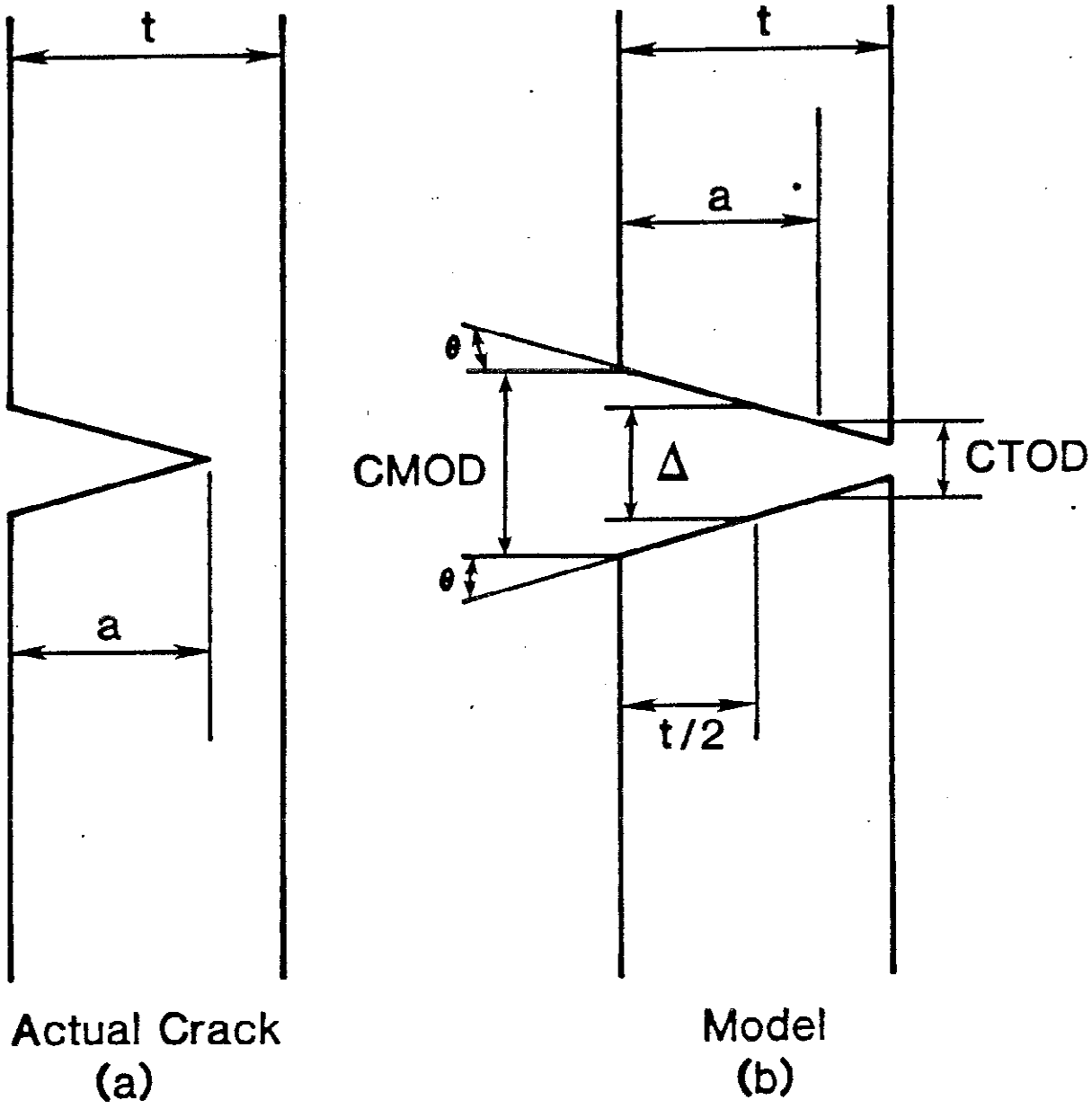

Fig. 6 - Calculation of CMOD and CTOD.

for $\sigma \leq \sigma_{LY}$

$$CMOD = [2(\ell + 2r_y)/E]\left(\sigma + \bar{\sigma}(t - a/t)\{[2(1 + \nu)\beta]/(3 + \nu)\alpha - 1\}\right) \quad (43)$$

for $\sigma_{LY} < \sigma < \sigma_{NSY}$

$$CTOD = K^2(1 - \nu^2)/E\bar{\sigma} \equiv CTOD_E \quad (44)$$

for $\sigma \leq \sigma_{LY}$

$$CTOD = CTOD_E + [2(\ell + 2r_y)/E]\,[\sigma(1 - a/t)\,\bar{\sigma}] \quad (45)$$

for $\sigma_{LY} < \sigma < \sigma_{NSY}$

Both CMOD and CTOD increase without bound at σ_{NSY}.

The model presented is for flat plates in tension. To apply it to actual structures, the value of the nominal membrane stress component normal to the crack in the vicinity of the crack (i.e., the stress that would exist in that region if the crack were not present) is calculated and used as the applied tension, σ. The redistribution of stresses caused by the crack is thus ignored.

The model that has been described in this subsection is the yielded-ligament model for flat plates. Further development of this model is discussed below.

2.2.4 Crack-Opening Displacements in Pipe

The driving force for fracture in pipes differs from that in flat tensile panels in two ways: First, shells have greater stiffness than flat plates. Thus, the rotation of the crack faces, and the resulting CMOD, is less in pipe than in plates, particularity for long cracks. Second, the axial stresses in pipes are caused by bending or by bending plus tension, whereas the flat plates were tested in tension. The bending stresses result in a stress gradient along the circumference. Therefore, as the plastic zone develops at the ends of a crack (located in the region of maximum tension), plasticity spreads into a decaying stress field. Thus, the stress for plastic collapse

is greater for pipes in bending than for plates in tension. These factors were accounted for in the analyses of the large-diameter pipe tests, (Section 2.4) and in the calculation of allowable flaw-size curves (Section 2.5).

The higher stiffness of shells relative to flat plates against rotation is approximately accounted for in the simplified line-spring model. The line-spring model treats a surface crack as being equivalent to a through-crack with closing forces and out-of-plane bending moments acting on its faces. The magnitude of these forces and moments is determined by enforcing compatibility of displacement and rotation between the through-crack faces and the ligament. The compliance of the ligament is determined by considering an edge crack of the same depth as the surface crack. The modification to the line-spring model, introduced to model long surface cracks in pipes more accurately, was to account for the effect of curvature on the relation between moment and rotation in a pipe. This relation enters the line-spring model when the compatibility calculation is made. For a flat plate, the relation between moment on the crack faces and out-of-plane rotation is

$$\theta = -24(1 + \nu)\ell M/[Et^3(3 + \nu)] \qquad (46)$$

The compliance is seen to become very large, approaching infinity in the limit for long crack lengths. However, a circumferentially cracked pipe has significant rotational stiffness, even if the crack extends completely around the circumference. For long cracks, the effects of the crack ends on rotation at the crack center may be neglected, and the moment-rotation relation may be obtained by considering the axisymmetric problem of a cylindrical shell subjected to moments distributed around its end. The relation between moment and rotation is, then

$$\theta_c = -(2R)^{1/2}[12(1 - \nu^2)]^{3/4} M/(Et^{5/2}) \qquad (47a)$$

The line spring calculations have been done in terms of bending stress m rather than moment M. These quantities are related according to Eq. 22.

$$m = 6M/t^2 \tag{22}$$

Writing Eq. 47a in terms of bending stress, m, we have

$$\theta_c = -\{(2R)^{\frac{1}{2}} [12(1-\nu^2)]^{3/4} / (6Et^{\frac{1}{2}})\}m \tag{47b}$$

Equation 47 is derived using axisymmetric shell theory. The relation between M and θ_c enters the line-spring model in the compliance calculation by replacing Eq. 26 with Eq.47b and then obtaining curvature-corrected results for Eqs. 27 through 33.

In tensile panels, plastic collapse occurs when the net-section stress exceeds the flow stress. The collapse mechanism consists of localized deformation along 45° slip lines emanating from the crack tips to the edges of the specimen. However, in a pipe subjected to bending or combined tension and bending, the collapse mechanism differs from that in a tensile panel. A lower bound estimate for the collapse load is obtained by assuming a plastic hinge develops at the cracked section, as shown in Fig. 7. Force balance at the plastic hinge determines the neutral axis location:

$$\theta_2 = (\tfrac{1}{2})[P_t/(2\sigma tR)] + (a/t)(\theta_1 + \pi) \tag{48}$$

where the angles θ_1 and θ_2 are defined in Fig. 7, P_t is the resultant of all applied loads, and R is the pipe radius. Moment balance results in

$$M = (2\bar{\sigma}R^2t)(2\sin\theta_2) - (a/t)\sin\theta_1 \tag{49}$$

where M is the applied moment. For a given crack size, Eqs. 46 and 47 will give an interaction curve of values of P_t and M corresponding to plastic collapse.

The special case $P_t = 0$ is of interest in the present study. For this case, the collapse moment is given by

$$M_c = 2\bar{\sigma}R^2t\{2\cos[(a/t)\theta_1] - (a/t)\sin\theta_1\} \tag{50}$$

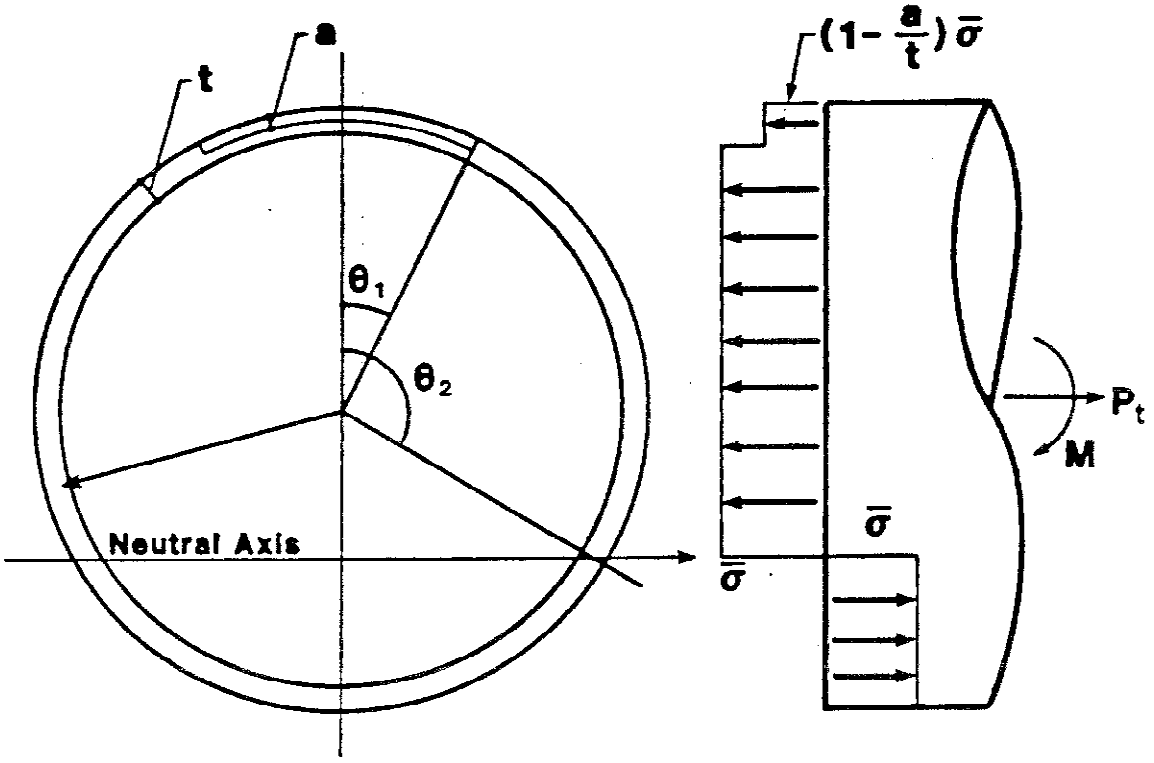

Fig. 7 - Schematic stress distribution of a pipe containing a circumferential crack under bending.

which reduces to

$$M_c = 2\bar{\sigma}R^2t[2 - (a/t)\theta_1] \tag{51}$$

for small crack lengths. The moment at which flow first occurs in an uncracked pipe is given by

$$M = \pi R^2 t\bar{\sigma} \tag{52}$$

Comparing Eqs. 52 and 51, for small crack lengths the collapse moment is approximately 27% higher than the moment corresponding to incipient yield. Thus, the pipe is capable of carrying significantly higher moments before the CMOD increases without bound than is predicted by the critical-COD model.

A modification to the critical-COD model has been derived that addresses this objection. The fully elastic contribution to CMOD is calculated as described above. The additional contribution to CMOD in the post-ligament-yield range, $CMOD_{LY}$, is computed using a new expression. The expression for $CMOD_{LY}$ is deriving using an approach similar to that used by Heald, Spink, and Worthinton[33] in deriving strip-yield solutions for the COD of finite-width tensile panels. deWit and Smith[34] followed this approach in deriving a model for a finite-width tensile panel containing a surface crack that gives analytical results for $CMOD_{LY}$ comparable to those obtained using the yielded-ligament model.

First the strip-yield expression for CMOD of a center crack in an infinite plate under tension is considered:

$$CMOD = 2\bar{\sigma}\ell/(\pi E)\cdot\ln\left\{1 + \sin(\pi\sigma/2\bar{\sigma})\right]/[1 - \sin(\pi\sigma/2\bar{\sigma})]\right\} \tag{53}$$

Equation 53 can be thought of as an expression that increases without bound as σ approaches $\bar{\sigma}$, correctly reduces to the linear elasticity expression for CMOD at small stress levels, and interpolates in between these limits using the function in braces. The desired expression for $CMOD_{LY}$ should have similar features with the following exceptions:

1. The expression for $CMOD_{LY}$ should increase without bound as the plastic collapse moment is approached. When axial load is present, proportional loading must be assumed.

2. At small moment levels, the expression for $CMOD_{LY}$ should reduce to the expression for $CMOD_{LY}$ that results when plasticity at the sides of the crack is negligible.

An expression which meets the above criteria is

$$CMOD_{LY} = [2\ell\bar{\sigma}/(\pi^2 E)][4 - a\ell/(tR) - \pi(1 - a/t)]\cdot\ln[(1 + \sin\gamma)/(1 - \sin\gamma)] \quad (54)$$

where $\gamma = (\pi/2)(M - A_o)/(M_c - A_o)$, $A_o = \pi R^2 t(1 - a/t)\bar{\sigma}$, and M_c is evaluated using Eq. 51. The model described here is called the pipe yielded-ligament model. Using Eq. 54, $CMOD_{LY}$ is seen to increase without bound as the collapse moment is approached. For small moments, the pipe is elastic, the nominal membrane stress is

$$\sigma = M/\pi R^2 t \quad (55)$$

and Eq. 54 reduces to Eq. 53. The logarithmic function interpolates between the two extremes.

2.3 Model Evaluation Tests for Surface Cracks in Tension

The critical-COD and flat plate yielded-ligament models provide an analytical relationship among the COD, applied stress, flaw size, material properties, and specimen (or structural) geometry. Both models can be expressed in terms of the CMOD or CTOD. The experimental program was based on the assumption that verification of the model in terms of CMOD is sufficient to verify the models in terms of CTOD. This assumption is required because CMOD can be readily measured, whereas CTOD cannot.

In this section, the experimental evaluation of the critical-COD and flat plate yielded-ligament models is discussed for the case of surface cracks

in tension. The CMODs of surface cracks are measured as functions of stress and strain in tensile panels of API 5LX-70 steel plates and welded pipe segments. The experimental results are compared with analytical predictions.

2.3.1 Experimental Procedures

The test materials were API 5LX-70 pipeline steel in the form of 15.9-mm (0.625-in) thick plate and pipe segments with transverse girth welds. The pipe segments were taken from 1220-mm (48-in) diameter, 15.9-mm (0.625-in) thick API 5LX-70 pipe welded using representative field practices. Metallography and properties of the base plate and welds are described in Appendix B. Chemical composition is given in Table 1, along with compositions of materials considered elsewhere in this report.

Three series of specimens with different surface crack lengths and depths were tested: one series each for the base metal, the manual welds, and the automatic welds. The test matrix is shown in Table 2. The base-metal test specimens were tensile panels (Fig. 8) that were notched in three different ways: 1) a saw cut of 0.4-mm (0.016-in) width, 2) a saw cut followed by fatigue sharpening, or 3) an electrical-discharge-machined (EDM) notch of 0.4-mm (0.016-in) width. The weld-metal test specimens were tensile panels taken from the 1220-mm (48-in) diameter pipe with the weld transverse to the tensile axis. The pipe curvature was retained in the specimens and the weld reinforcement was removed to obtain a uniform cross section. The surface notches, all prepared by EDM, were located on the concave side of the pipe at the root of the V-shaped weld.

Each of the specimens in Table 2 was loaded in tension at room temperature, and the CMOD was measured as a function of nominal stress, σ, and gage-length strain, ε_L. In the base-metal specimens, the ε_L was taken as the average strain over a gage length of 305 mm (12 in), except for the 381-mm (15-inch)

Table 1 - Chemical Analyses in Weight Percent

	C	Si	Mn	P	S	Al	Cu	Cr	Ni	Mo	V	Nb	N
Base metal (API 5LX-65)	0.08	0.3	1.45	0.015	0.003	0.039	0.08	0.09	0.03	0.10	0.07	0.036	0.009
Base metal (API 5LX-70)	0.076	0.2	1.3				0.12	0.14	0.13	0.33	<0.05		
Manual weld	0.12	0.17	0.67	0.005	0.010			0.13	1.6	0.031			
Automatic weld	0.11	0.43	1.3	0.011	0.005			0.073	0.92	0.053			

Table 2 — Test Matrix for the Experimental Evaluation of the Critical COD Model and Flat-Plate Yielded-Ligament Model

Specimen Number	Specimen Width, W,		Crack Depth, a,		Crack Length, ℓ,	
	mm	in	mm	in	mm	in
P1 *	102	4.0	6.65	0.262	40.9	1.61
P2	102	4.0	9.07	0.357	43.5	1.71
P3	102	4.0	5.64§	0.222	31.2	1.23
P4	102	4.0	6.88§	0.271	48.3	1.90
P5	76	3.0	10.54§	0.415	31.2	1.23
P6	76	3.0	4.57	0.180	13.5	0.53
P7	76	3.0	3.56	0.140	31.8	1.25
P8	76	3.0	5.08	0.200	14.7	0.58
P9	381	15.0	3.81	0.150	114.3	4.50
A1†	76	3.0	8.13	0.320	29.7	1.17
A2	102	4.0	5.72	0.225	47.5	1.87
A3	76	3.0	2.49	0.098	17.3	0.68
A4	76	3.0	4.57	0.180	11.8	0.46
M1‡	76	3.0	8.13	0.320	29.2	1.15
M2	102	4.0	5.84	0.230	47.5	1.87
M3	76	3.0	4.32	0.170	11.8	0.46
M4	76	3.0	2.16	0.085	15.0	0.59

* P: base metal
† A: automatic weld
‡ M: manual weld
§ specimen also used to evaluate the J-integral model

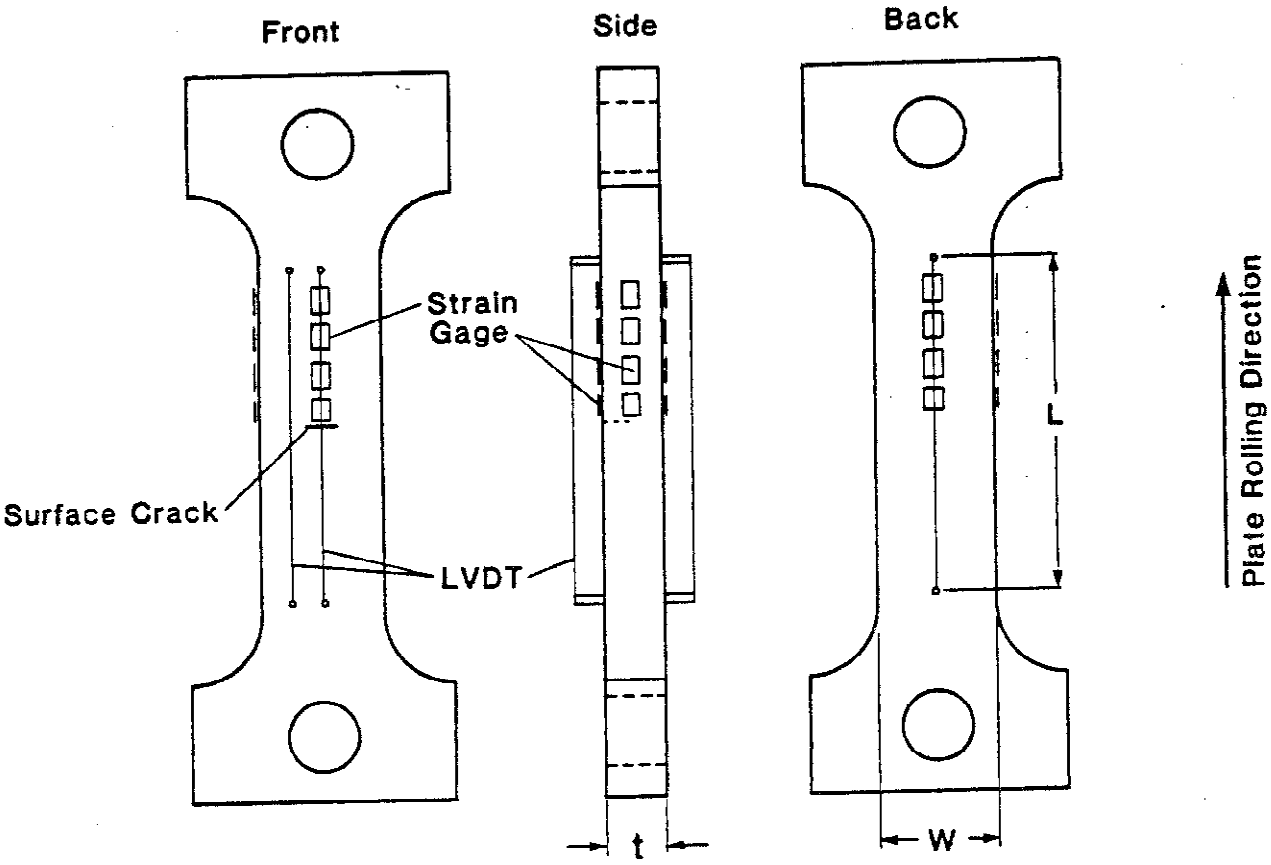

Fig. 8 - Test specimen configuration.

wide specimen that had a gage length of 610 mm (24 inch). The specimens were pulled in tension under displacement control with a closed-loop servo-controlled hydraulic testing machine. The values of CMOD were measured with a clip-on displacement gage mounted directly onto the crack mouth with the clip-on teeth about 0.13 mm (0.005 in) into the crack. The ε_L was obtained from displacements measured over the chosen gage length with linear-variable-differential transducers (LVDTs). All signals from electrical resistance strain gages, LVDTs, the clip-on gage, and the load cell were acquired and stored by a multichannel minicomputer for on-line and post-test analysis. For observation of the deformation patterns near the cracks, the specimens were coated with photoelastic material and instrumented with electrical-resistance strain gages.

The CODs in specimen P5 were measured by a replication technique. The specimen was loaded under displacement control to a CMOD of 0.2 mm (0.008 in). A liquid, silicone base, precision-impression material was mixed with a hardener and inserted into the crack. The replica material was allowed to harden at constant CMOD for about 15 min. Subsequently, loading was continued until a CMOD of 0.5 mm (0.02 in) was reached. The replica was removed and the replication procedure was repeated. The procedure was repeated at CMOD values of 0.9, 1.2, and 1.8 mm (0.035, 0.047, and 0.071 in). Each of the replicas was cut along the minor axis of the semielliptical crack and mounted in phenyl salicylate. The CODs were measured at several distances (x values) from the crack mouth with a metallographic microscope. The precision of measurement was within ±0.03 mm (±0.001 in) under 100X magnification.

2.3.2 Results and Discussion

For the test matrix shown in Table 2, CMOD has been measured as a function of applied stress, σ, and of gage-length strain, ε_L. The experimental results

of CMOD vs. σ are compared with the analytical predictions of the analytical models discussed previously.

$$\text{CMOD} = \text{CMOD(elastic)}, \quad \text{for } \sigma < [1 - (a/t)]\bar{\sigma} \tag{56a}$$

$$\text{CMOD} = [2(\ell + 2r_y)/E]\,[\sigma - (1 - a/t)\bar{\sigma}] + \text{CMOD} \tag{56b}$$

for $\sigma \geq [1 - (a/t)]\bar{\sigma}$

Equations 56 state the critical-COD model applied to prediction of crack-mouth-opening displacement. For short cracks, the critical-COD and flat-plate yielded-ligament models agree. They agree for all cracks after full-ligament yielding.

Equation 56a is evaluated using the elasticity solution of Kobayashi,[24] (Eq. 20) for cracks with aspect ratios (a/ℓ) greater than 0.1. For long cracks ($a/\ell < 0.1$), the Kobayashi solution is not applicable, and the elastic CMOD is calculated using King's[22] simplified version of the line-spring model (see Section 2.2.3). Also, for long cracks, the plastic zone development through the thickness before full ligament yielding becomes more important, and it is accounted for by adding a plastic-zone correction, r_{yd}, to the crack depth. The Dugdale plastic zone in a center-cracked finite-width panel is used. In using this solution for an edge crack in the line-spring model, bending is neglected; the underestimation of r_{yd} is considered negligible for present purposes. The addition of the through-thickness plastic zone correction to the flat plate yielded-ligament model produces a model called the flat plate yielded-ligament model with through-thickness plasticity correction.

Equation 56b is used from the onset of ligament yielding, $\sigma \geq [1 - (a - t)]\bar{\sigma}$, until net-section yielding occurs. After net-section yielding, CMOD increases without bound at a constant applied stress and is shown as a vertical line in the CMOD-vs.-σ curve, at $\sigma = \bar{\sigma}\,(1 - a\ell/tW)$. The

important quantity in the application of fracture mechanics is CTOD and not CMOD, because CTOD is recognized as being related to crack initiation. With moderate length and deep surface cracks, it is assumed that the rotation of the crack faces owing to out-of-plane bending is negligible after the ligament has yielded and the increments of CTOD at the leading edge and CMOD are equal. Measurements of the crack profile are shown in Fig. 9. At low values of COD, the replicating material did not penetrate all the way to the crack tip. Thus, there are more data points at the higher values of COD than at the lower end. As shown in Fig. 9, the assumption of negligible rotation of the crack faces owing to out-of-plane bending after ligament yielding is reasonable.

Base-Metal Results. As shown in Table 2, nine base-metal tests were conducted. The results, summarized in Figs. 10 and 11, show good agreement between experiment and analysis. Note that the shape of the CMOD-vs-σ curve for the long (ℓ = 114.3 mm, 4.500 in) crack test differs from that of the shorter crack tests; nonlinearity due to crack-tip plasticity occurs at a lower stress, and there is a more gradual transition to net-section yielding. Addition of the Dugdale plastic-zone correction to the crack depth accounts for this behavior. Thus, the analysis appears to be valid for a broad range of crack sizes.

The chronological events associated with the CMOD-vs-σ curves can be described as follows: Initial loading produces elastic specimen extension and the relationship between CMOD and stress is linear. As the stress increases, the plastic-zone size ahead of the crack tip enlarges. Eventually, the plasticity spreads to the back face of the specimen; this is termed ligament yielding. After ligament yielding, the plasticity contributing to the CTOD tends to occur in slip bands emanating from the crack tip at angles of $\pm 45°$ from the plane of the crack, and the nonlinearity of CMOD-vs-σ curves becomes

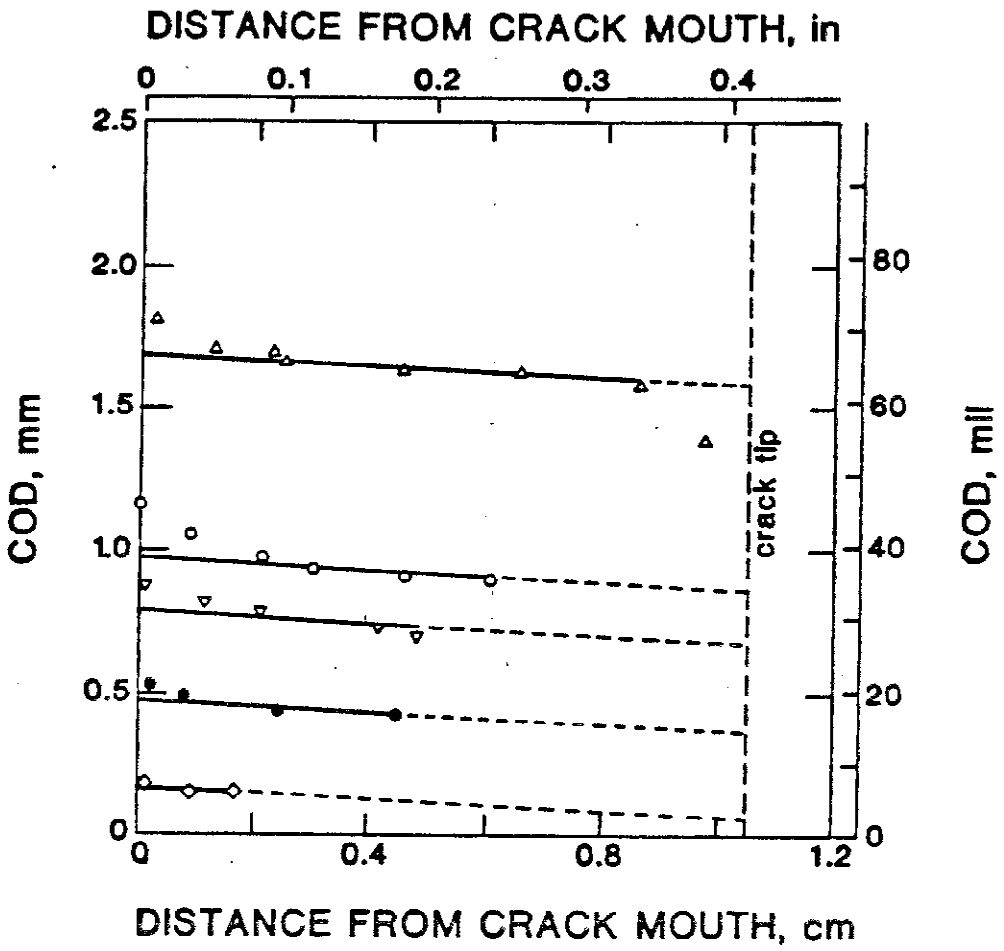

Fig. 9 - COD as a function of location along the crack face after ligament yielding. Measured with replication technique. Crack depth = 10.5 mm (0.413 in); crack length = 31.2 mm (1.23 in).

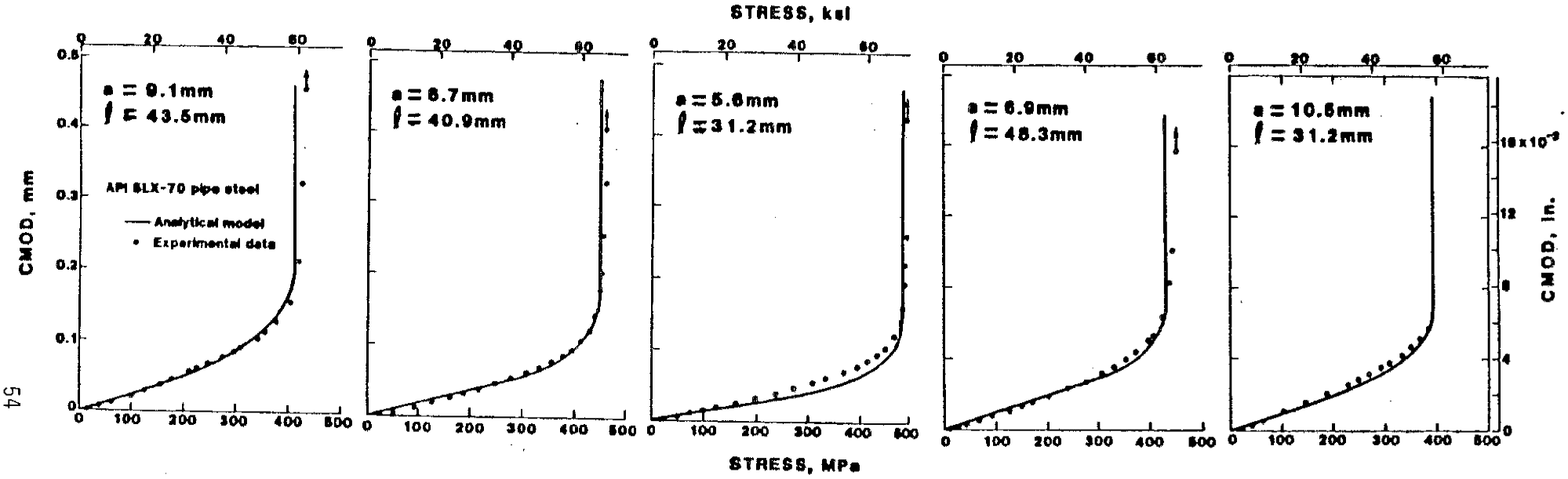

Fig. 10 - CMOD vs. nominal stress for base-metal specimens. Symbols are experimental data, and solid lines are analytical predictions based on the modified critical-COD model. To obtain a and ℓ in inches, multiply by 0.0394.

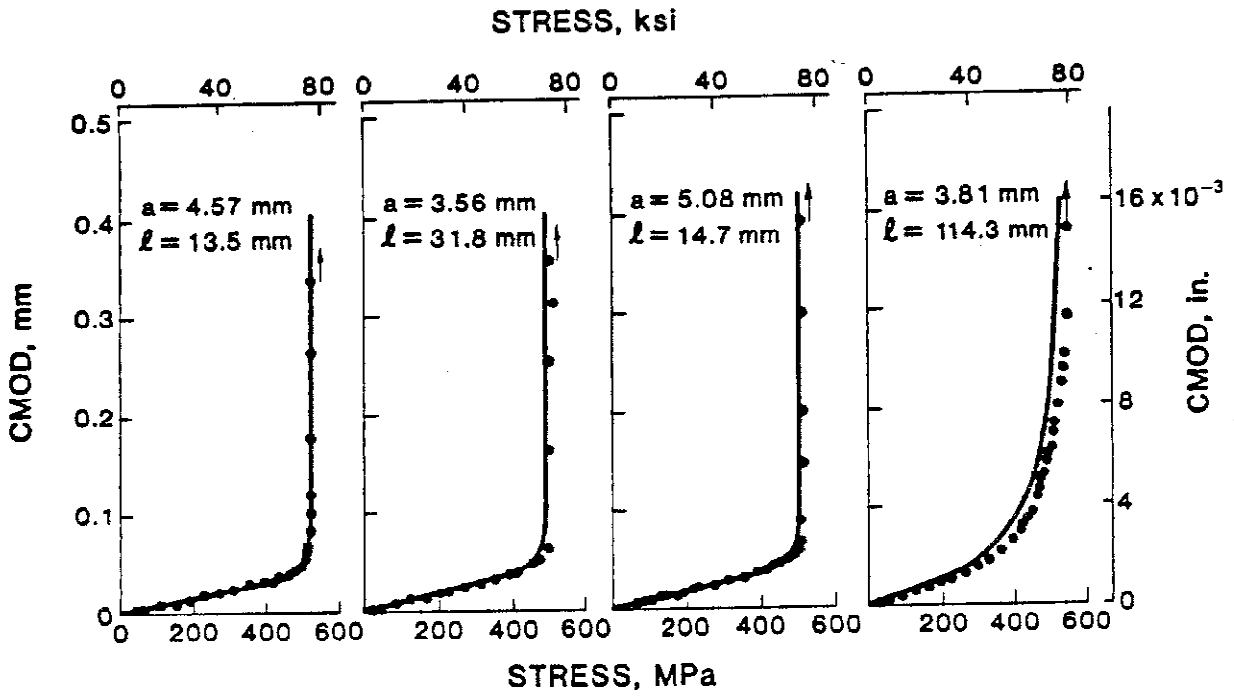

Fig. 11 - CMOD vs. nominal stress for base-metal specimens. Symbols are experimental data and solid lines are analytical predictions based on the modified critical-COD model. To obtain a and ℓ in inches, multiply by 0.0394.

noticeable. Initially, the slip bands are between the crack tip and the back face. Finally, the net section yields along ±45° slip bands between the crack and the specimen edges, and the CMOD increases asymptotically to the net-section yielding stress. These phenomena were revealed by the brittle lacquer on the front and back surfaces of the specimen. On the front surface (Fig. 12) values of strain 3.8 mm (0.15 in) above the center of the crack were more than two orders of magnitude lower than those of remote strain. The strain increased with distance from the crack plane and eventually reached the values of remote strain.

On the back surface of the specimen, the deformation phenomena were examined with brittle lacquer and electrical-resistance strain gages. As the stresses increased, the highest strains were observed at regions about ±45° from the plane of the crack emanating from the leading edge of the crack. The ligament-yielding stress estimated from $\sigma = (1 - a/t)\bar{\sigma}$ agreed well with readings from strain gages at the highest strain regions. After ligament yielding, the deformation pattern on the back of the specimen was an ellipse that surrounded the position of the crack until net-section yielding was approached. Then the pattern developed slip lines to the edge of the specimen. The strains at the region right behind the crack remained relatively low compared with the remote strains. This low-strain region could be seen necking down after extensive net-section yielding, and then the crack grew to the back surface. The strain patterns revealed by the brittle lacquer are shown in Fig. 13.

The results in terms of CMOD vs. ε_L are shown in Figs. 14 and 15. Two distinct behaviors are observed. Seven of the specimens exhibited a nearly bilinear relationship between CMOD and ε_L, with the slope sharply increasing at strain levels slightly below the yield strain, as shown in Fig. 14. The

Fig. 12 - Strain patterns revealed by brittle lacquer on the front. Note: LVDT ran across the center of the specimen, and the crack seen was only half of the surface crack.
(a) At low stress, no noticeable plastic deformation ahead of the crack tip was observed.

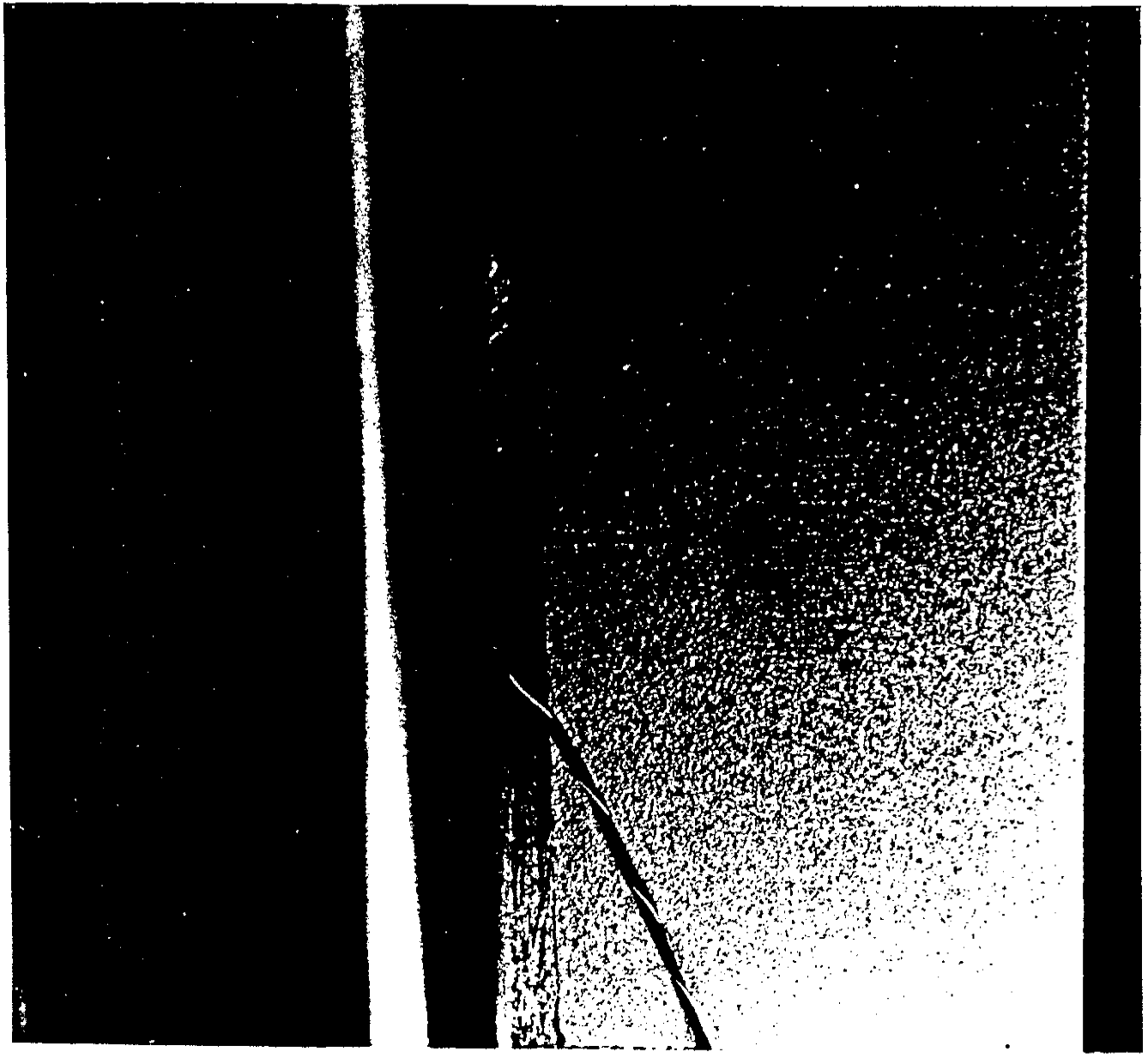

Fig. 12(b) - At intermediate stress level, plastic zone size enlarged and

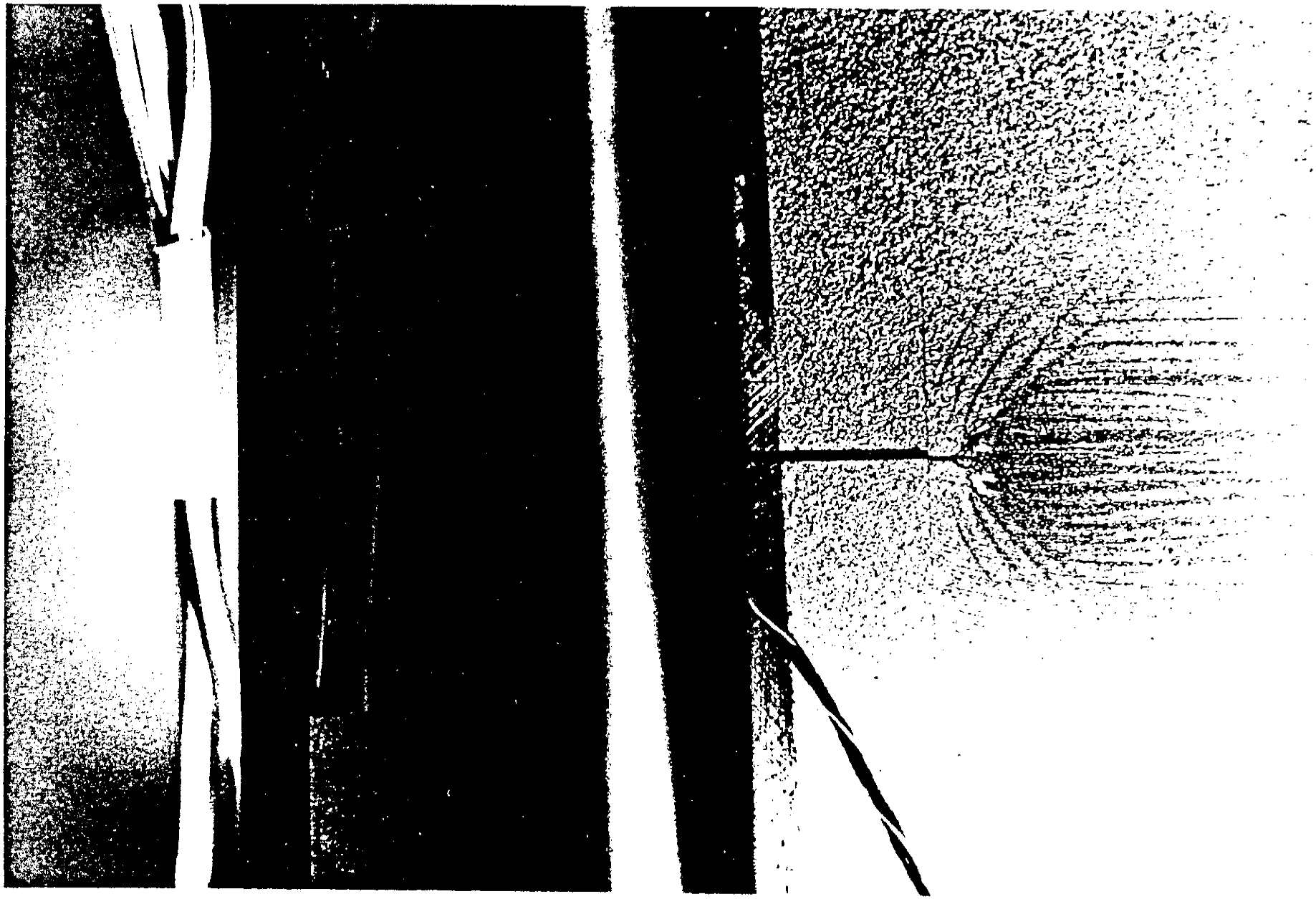

Fig. 12(c) - net section yielded.

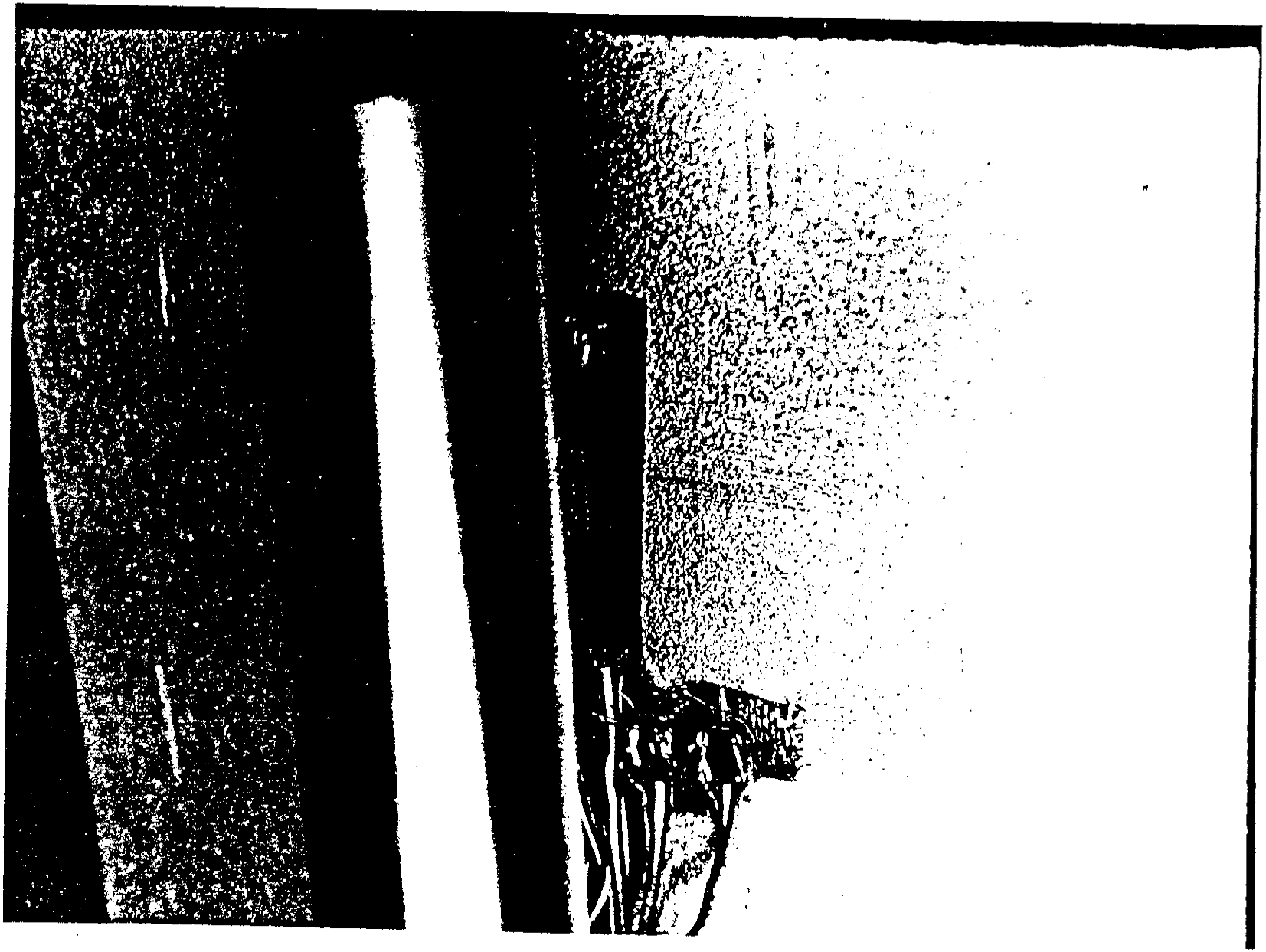

Fig. 13 - Strain patterns revealed by brittle lacquer on the back surface.
(a) The stress level was at about ligament yielding.

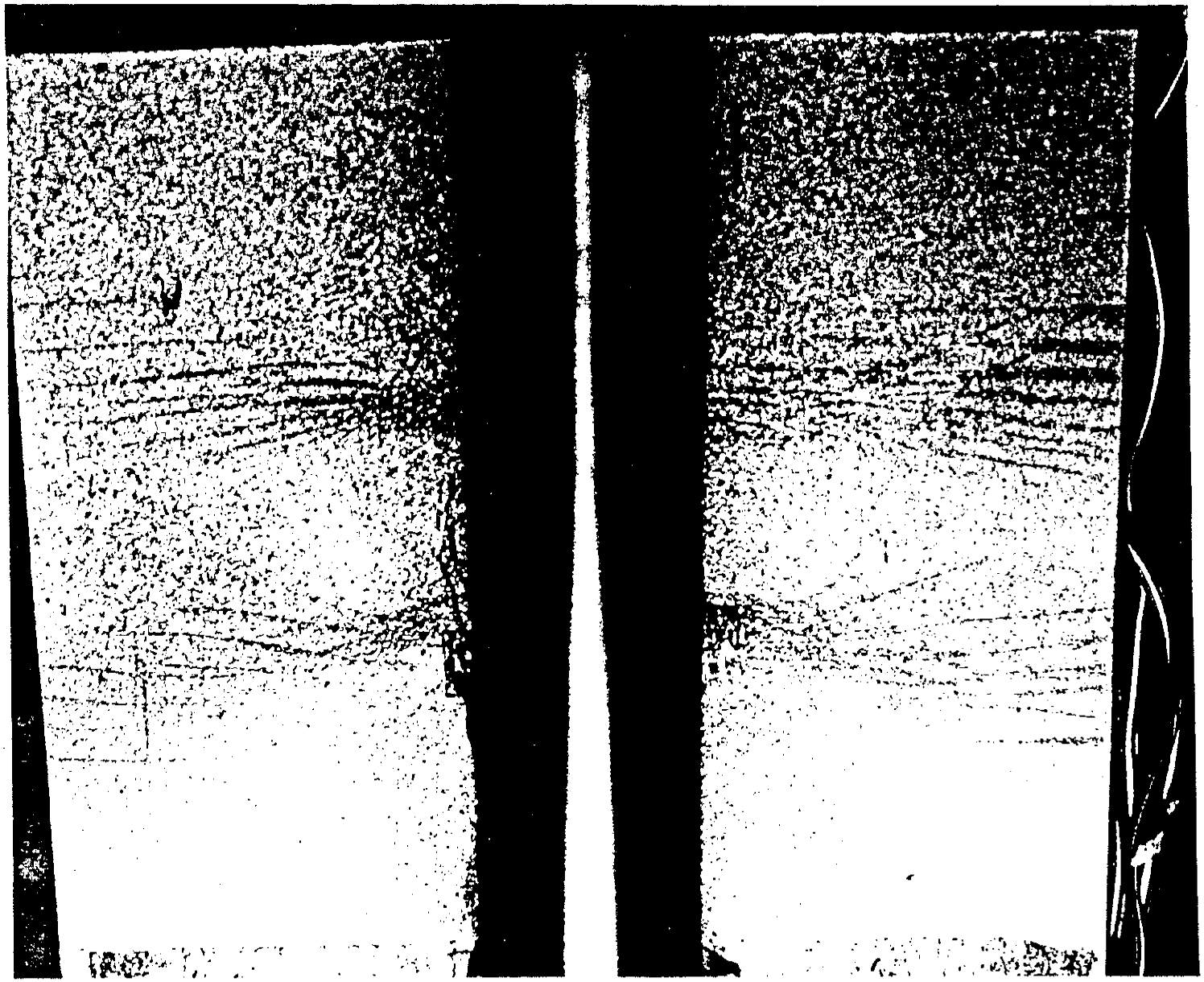

Fig. 13(b) - After net-section yielding.

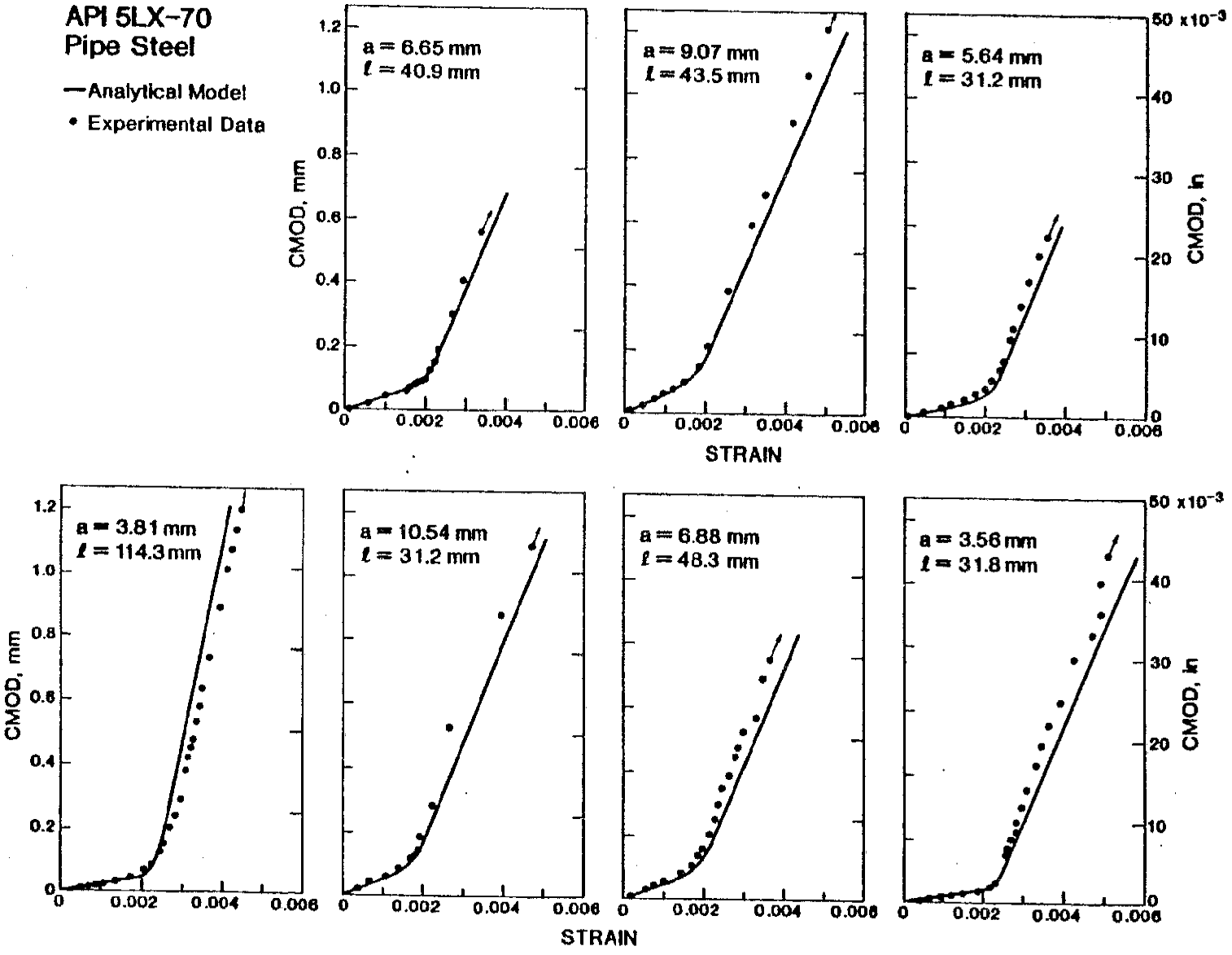

Fig. 14 - CMOD vs. gage-length strain for base-metal specimens that exhibited net-section-yielding behavior. To obtain a and ℓ in inches, multiply by 0.0394.

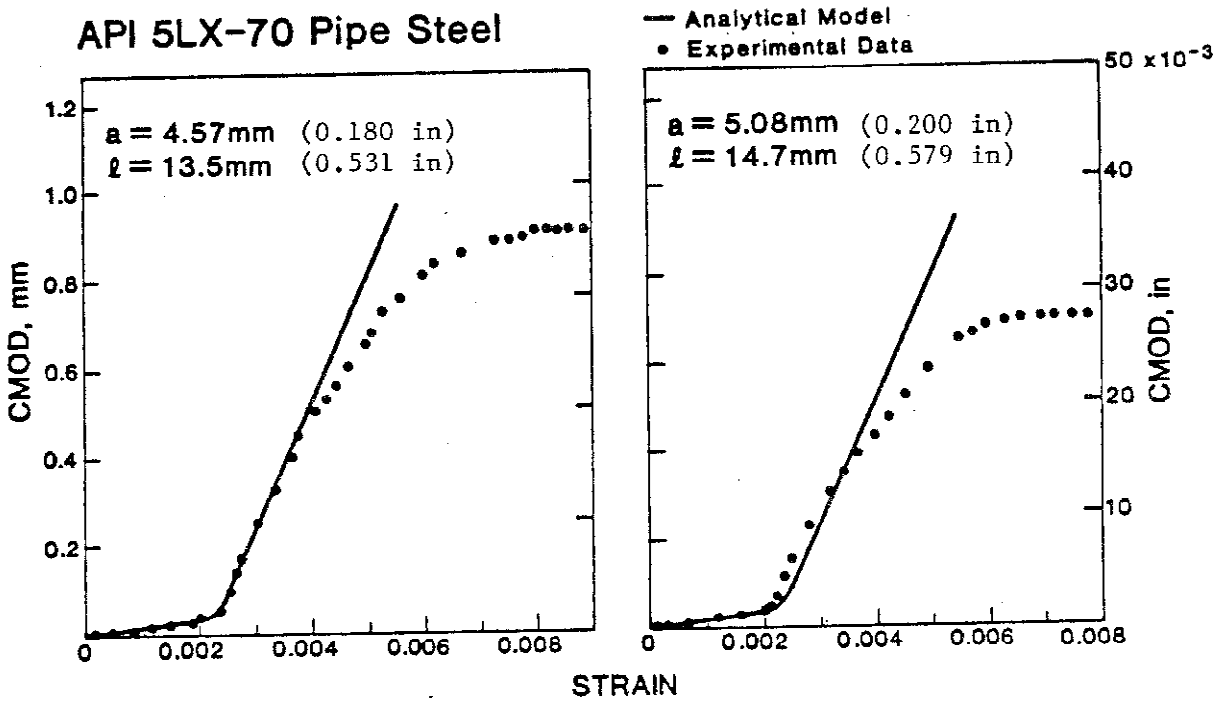

Fig. 15 - CMOD vs. gage-length strain for base-metal specimens that exhibited net-section yielding followed by gross-section yielding. (a) Specimen P6, (b) Specimen P8.

bilinear behavior results when the strains that exceed yield only occur in the net section, that is, net-section yielding. Photoelastic observations and strain gage measurements indicate that, for net-section yielding, yielding is confined to slip bands, which extend at approximately 45° angles from the crack tip to the specimen edges. As shown in Fig. 15, specimens with smaller cracks exhibited similar behavior at low strains, but at high strains the CMOD reached a plateau value, increasing only slightly with strain. The plateau develops when strain hardening elevates the flow strength in the slip bands and strains above yield occur in the gross section, that is, gross-section yielding. Once gross-section yielding occurs, the remote displacements are absorbed along the entire test section and CMOD increases slowly with ε_L.

The bilinear relationship between CMOD and ε_L can be modeled at stress levels below net-section yielding using Eq. 56, providing that the appropriate relationship between ε_L and σ has been established. At strains above net-section yielding, the slopes of the CMOD-vs.-ε_L curves are equal to the gage length; this occurs because all of the remote displacement is transmitted to the crack tip through the slip bands. Thus, after net-section yielding,

$$CMOD = CMOD_{NSY} + L(\varepsilon_L - \varepsilon_{NSY}) \tag{57}$$

where L is the gage length and the subscript NSY refers to the value of the quantity at the onset of net-section yielding.

A relationship between ε_L and σ is necessary to model CMOD vs. ε_L at stresses below net-section yielding and to compute $CMOD_{NSY}$ and ε_{NSY} for Eq. 57. The ε_L is the sum of the elastic strain, σ/E, plus the increment of ε_L due to the presence of the crack. The remote displacement, Δ', in a center-cracked panel is given by

$$\Delta' = (2\sigma\ell/E)[V(\ell/W)] \tag{58}$$

where $V(\ell/W)$ is given by Tada, Paris, and Irwin.[35] For a surface crack, Irwin's equivalent through-thickness crack concept[19] can be used to modify Eq. 58; that is, σ is reduced by the closing stress, σ_c, caused by the uncracked ligament,

$$\sigma_c = \bar{\sigma}(1 - a/t) \tag{59}$$

To account for the crack-tip plasticity, the effective crack length, ℓ_{eff}, which includes the plastic-zone size correction, r_y, is used in place of ℓ. The resultant expression becomes

$$\varepsilon_L = \sigma/E + [2(\sigma - \sigma_c)/E][\ell_{eff}/L][V(\ell_{eff}/W)] \tag{60}$$

Given Eqs. 56a, 56b, and 60, it is possible to calculate CMOD vs. ε_L for the net-section yielding case. For stresses below and equal to net-section-yield stress, Eq. 56 is used to calculate CMOD and σ is converted to ε_L using Eq. 60. For stresses above net-section-yield stress, Eq. 57 is used. Comparison of the experimental and analytical results of CMOD vs. ε_L shown in Figs. 14 and 15 indicates good agreement.

For specimens in Fig. 15, net-section yielding is followed by gross-section yielding at high strains. The transition from net-section yielding to gross-section yielding, and CMOD vs. ε_L for gross-section yielding have not been modeled. In the present study, the transition occurred at a ratio of crack area to cross-sectional area of 5%. The area ratio at which the transition occurs should be higher for materials with more strain hardening.

Weld Metal Results As shown in Table 2, four automatic-weld specimens and four manual-weld specimens were tested. As shown in Table 3, the yield and ultimate strengths of the welds were significantly different for both types of weld and for the base metal. These differences were far less in transverse-weld tensile tests on 76-mm (3.0-in) wide, full-thickness tensile panels with a 305-mm (12.0-in) gage length. The stress-strain curves obtained

Table 3 — Summary of Weld-Metal Tensile Properties

Weld Type	Test Temperature, °C	°F	Ultimate Tensile Strength, MPa	psi x 10^3	Yield Strength, 0.2% Offset, MPa	psi x 10^3	Percent Elongation in 25 mm (1.0 in)	Reduction in Area, %
Automatic	+24	+75	549	79.6	491	71.2	26	69
Automatic	+24	+75	820	119	735	107	15 *	31*
Automatic	+24	+75	800	116	715	104	21	66
	Average		810	117	725	105	21	66
Manual	+24	+75	560	81.2	470 †	68.2	28	68
Manual	+24	+75	550	79.8	460 †	66.7	29	64
	Average		555	80.5	465	67.4	28.5	66
Automatic	-101	-150	955	139	820	119	‡	61
Automatic	-101	-150	910	132	790	114	27	63
	Average		930	135	805	117	27	62
Manual	-101	-150	665	96.4	580 †	84.1	30	65
Manual	-101	-150	675	97.9	560 †	81.2	21*	30*
	Average		670	97.2	570	82.7	30	65

*Slant fracture; other specimens exhibited cup-cone fracture.

†Yield point observed; other specimens did not exhibit a yield point.

‡ Gage marks not visible on specimen after test.

using strain gages mounted in the center of the weld at midthickness on both edges are shown in Fig. 16. For the CMOD-vs.-σ model, only the flow stress values are important: 596 MPa (86.5 x 10^3 psi) for the automatic weld and 557 MPa (80.8 x 10^3 psi) for the manual weld. However, for CMOD-vs.-ε modeling using the two-tensile-bar model (discussed below), the shape of the stress-strain curve is also important.

The experimental results of CMOD vs. σ for the automatic and manual welds are compared with the analytical predictions in Figs. 17 and 18. The general behavior trends observed in the experiment are reasonably modeled; however, the agreement between experiment and analysis is not as good as it was for the base-metal tests. The correlations are best at low stresses, but the CMOD is underestimated (specimens A2 and M4 are exceptions) for stresses between the stress required for ligament yielding and the stress required for net-section yielding. At still higher stresses, CMOD is overestimated. To model the observed behavior with Eq. 56b, it would be necessary to use a variable flow stress. This option is physically sensible, because the stress-strain curves for the welds exhibit more work hardening than the base-metal curves. The quality of the correlations is also influenced by an increase in experimental uncertainty for testing the welded specimens over that encountered in base-metal tests. The principal sources of error are: 1) bending caused by distortion, misalignment, and the curved test section, 2) the presence of residual stresses in the welded specimen, and 3) thickness variations caused by hand grinding the crown and root of the weld.

The experimental results of CMOD vs. ε_L for the automatic and manual welds are shown in Figs. 19 and 20. The two characteristic trends observed in the base-metal tests, a bilinear curve for net-section yielding and a plateau when gross-section yielding occurs, are not apparent in the weld-metal

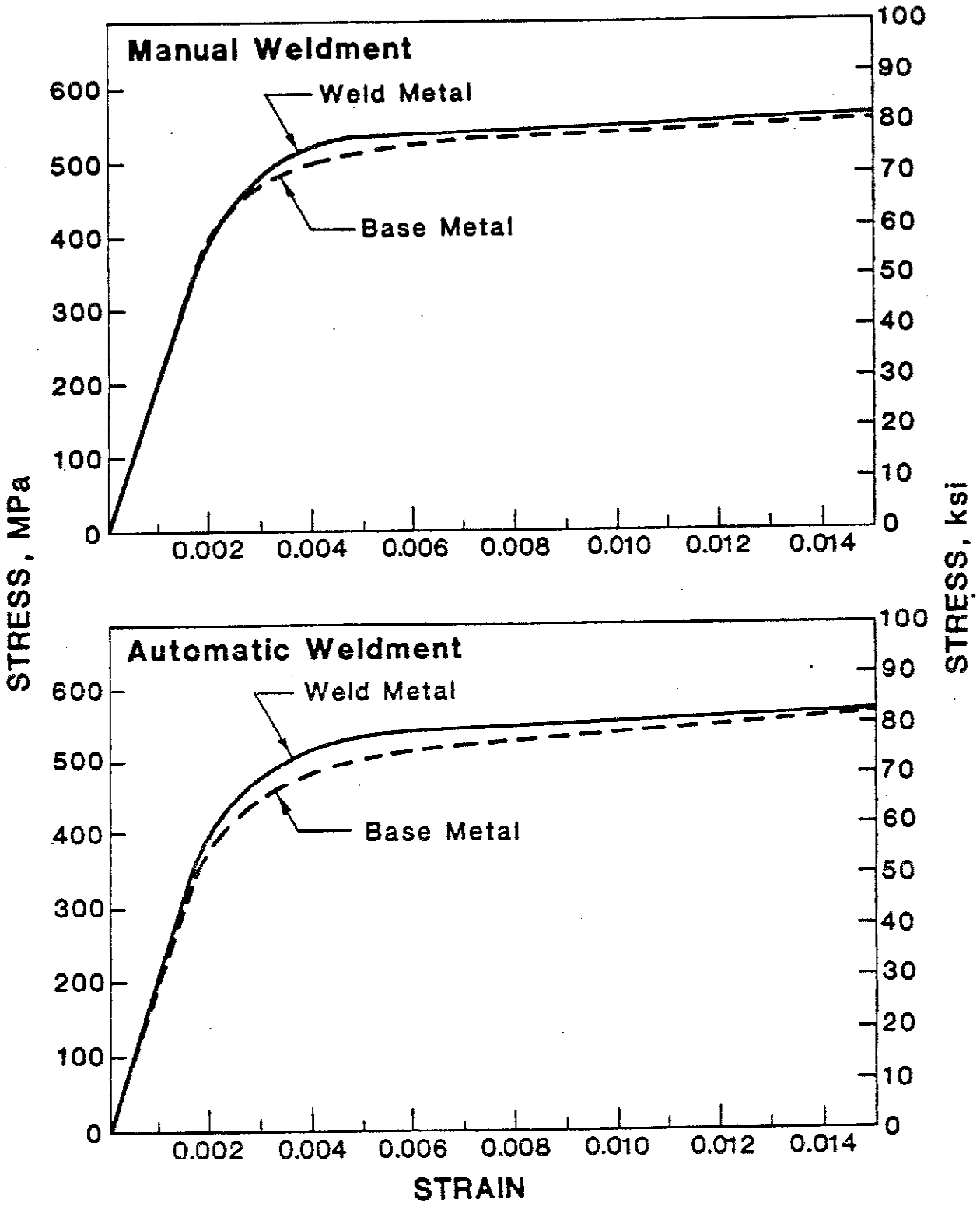

Fig. 16 - Stress-strain curves of automatic and manual weldments, as determined in transverse-weld tensile tests.

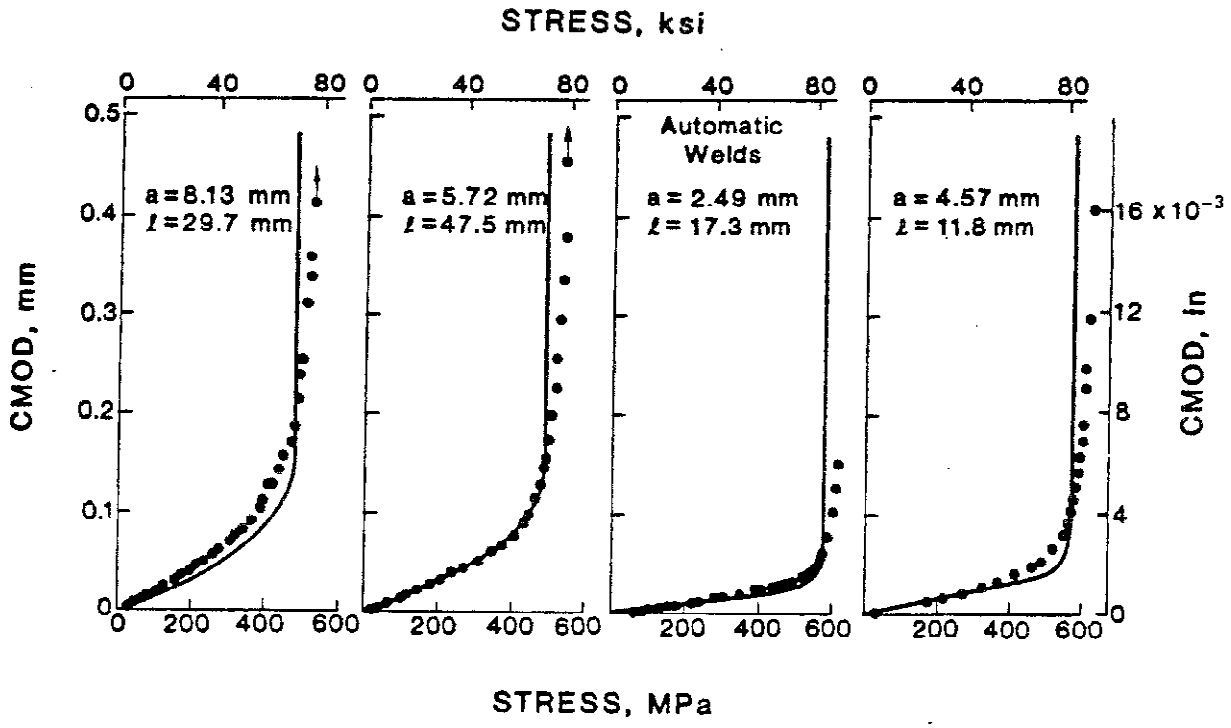

Fig. 17 - CMOD vs. nominal stress for automatic-weld specimens. Symbols are experimental data and solid lines are analytical predictions based on the modified critical-COD model. To obtain a and ℓ in inches, multiply by 0.0394.

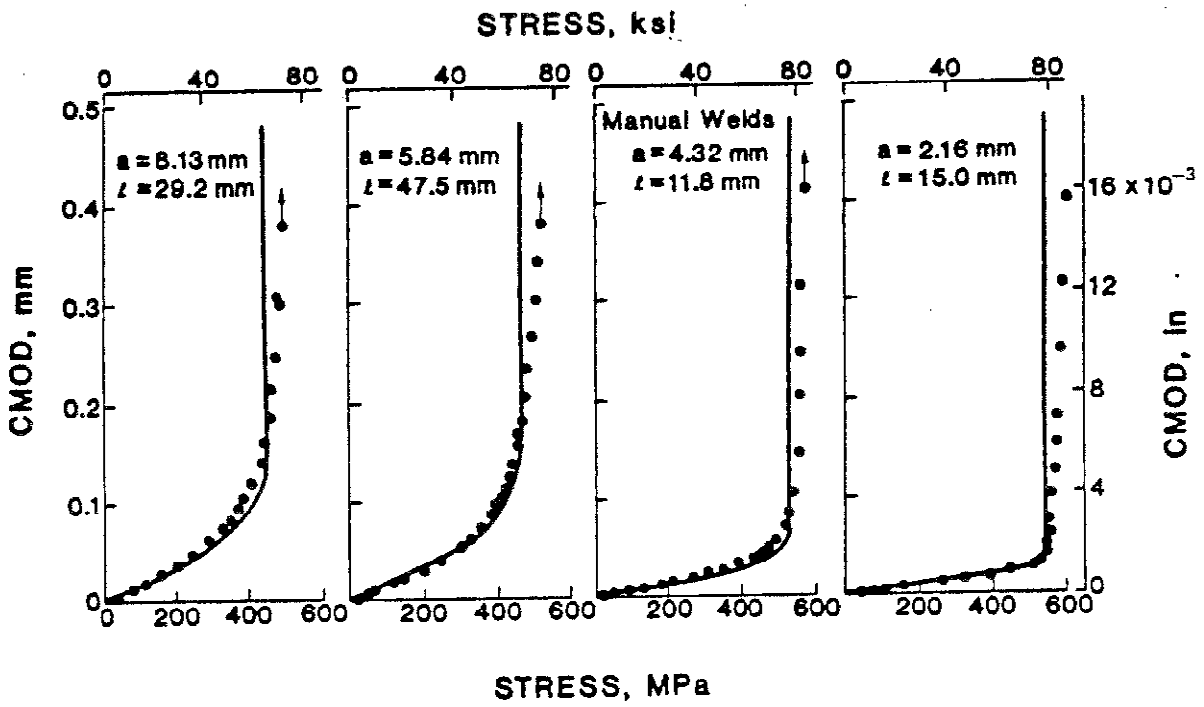

Fig. 18 - CMOD vs. nominal stress for manual-weld specimens. Symbols are experimental data, and solid lines are analytical prediction based on the modified critical-COD model. To obtain a and ℓ in inches, multiply by 0.0394.

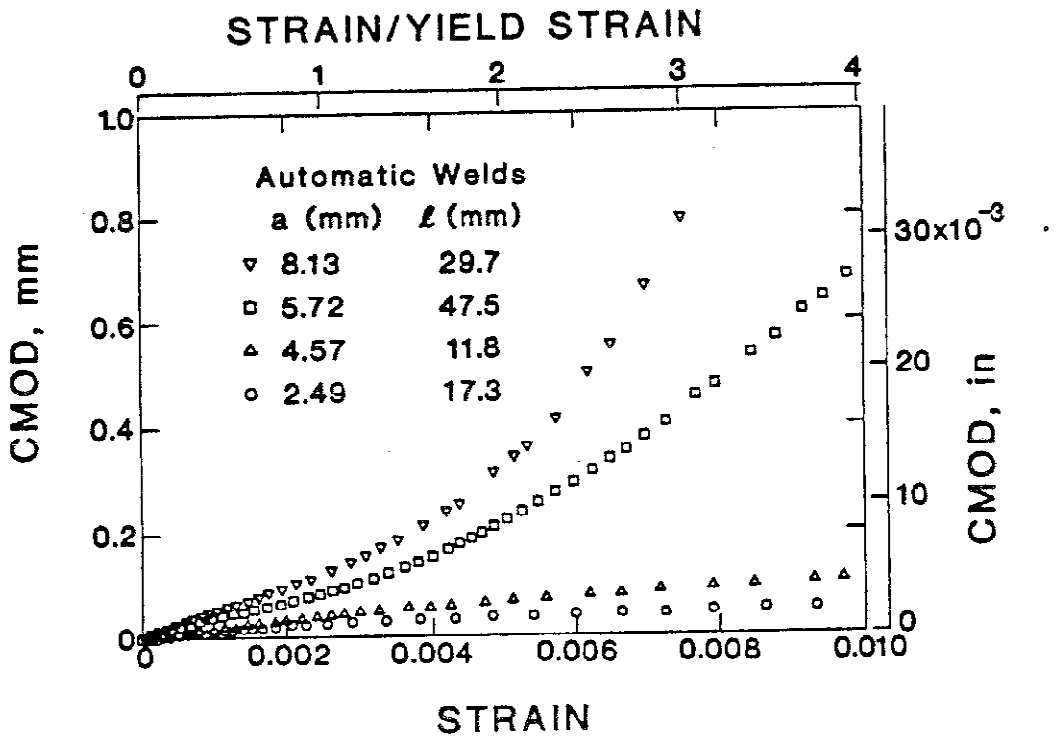

Fig. 19 - CMOD vs. gage-length strain for automatic-weld specimens. To obtain a and ℓ in inches, multiply by 0.0394.

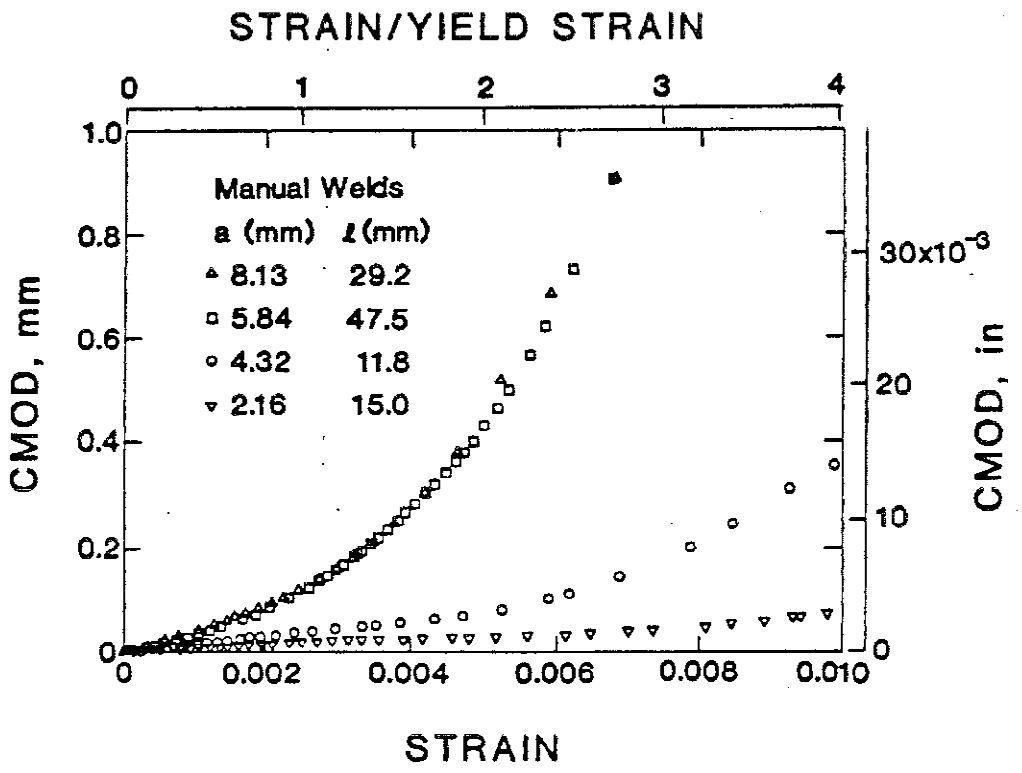

Fig. 20 - CMOD vs. gage-length strain for manual-weld specimens.

To obtain a and ℓ in inches, multiply by 0.0394.

results; however, the net-section yielding and gross-section yielding designations are still appropriate. The CMOD-vs.-ε_L curves for net-section yielding behavior in welded specimens are more parabolic than bilinear; the four specimens with the largest cracks (A1, A2, M1, M2) exhibited net-section yielding. The CMOD-vs.-ε_L curves for gross-section yielding behavior in welded specimens show a very small increase in CMOD with ε_L; the four specimens with the smallest cracks (A3, A4, M3, M4) exhibited gross-section yielding.

The differences in the CMOD-vs.-ε_L curves for the base metal and the welds can be explained by consideration of the higher yield strength and increased work-hardening rates in the weld. For small cracks, the base metal starts yielding while the weld is still elastic. Subsequent increases in stress applied to the weld depend on the work hardening in the base metal. Simply, the base metal stretches and the weld does not, and consequently CMOD increases slowly with strain. For the larger cracks (specimens A1, A2, M1, M2), 16% to 20% of the cross-sectional area of the weld is cracked. Consequently, the crack plane yields first and net-section yielding can occur. Even at the 20% crack-to-cross-sectional-area ratio, the weld work-hardens sufficiently to cause yielding in the base metal.

For the net-section yielding case, the apportionment of strain in the base metal and the weld can be modeled with the two-tensile-bar analogy shown in Fig. 21.

For a given value of remote imposed displacement, $\Delta' = \varepsilon_L L$, at the ends of two tensile bars in series, the compatibility condition is

$$\varepsilon_1 L_1 + \varepsilon_2 L_2 = \varepsilon_L L \tag{61}$$

where L is the gage length, L_2 is the width of the weld, and $L_1 = L - L_2$ (see Fig. 21). The force equilibrium is

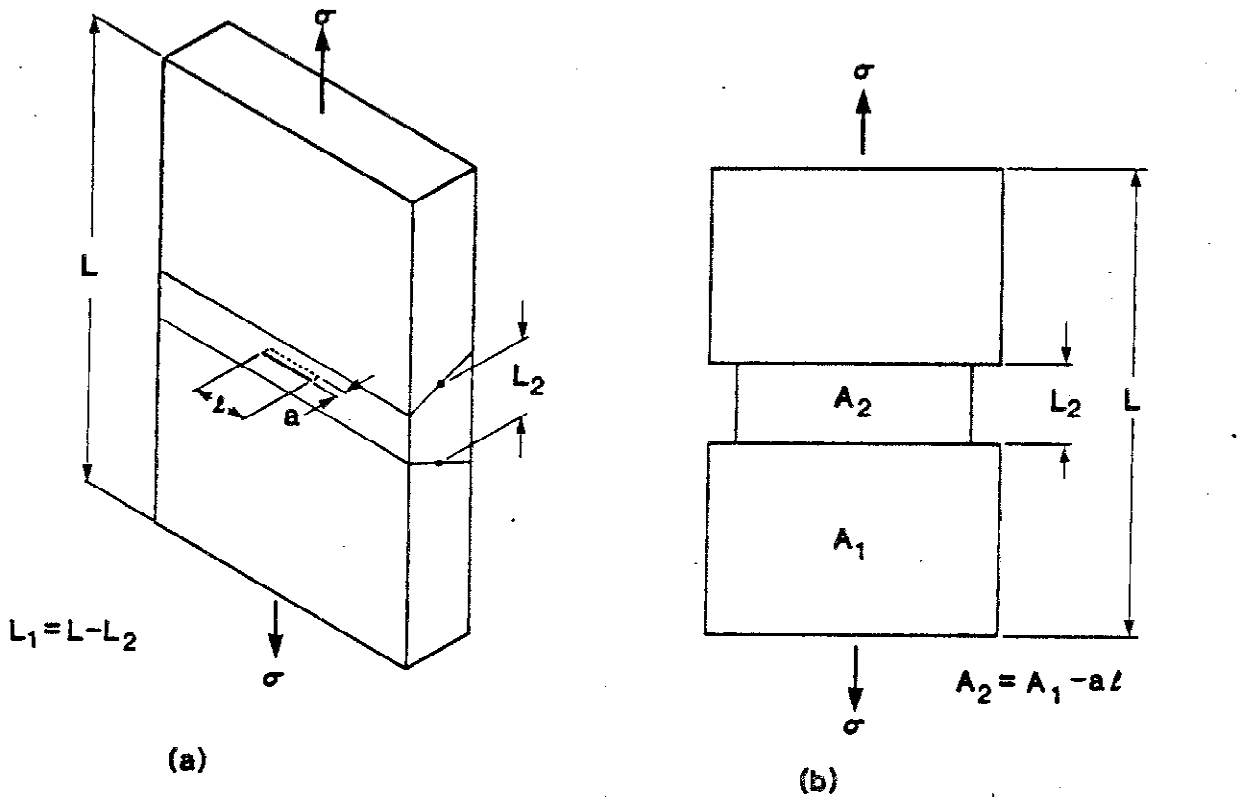

Fig. 21 - Two-tensile-bar model schematics: (a) specimen and (b) analogy.

$$[\sigma_1(\varepsilon_1)] \cdot A_1 = [\sigma_2(\varepsilon_2)] \cdot A_2 \qquad (62)$$

where $\sigma_1(\varepsilon_1)$ and $\sigma_2(\varepsilon_2)$ are the stress-strain curves for materials 1 and 2, and A_1 is the gross-section area and A_2 is the net-section area in the plane of the crack (see Fig. 21). Since the stress-strain curves are nonlinear, Eqs. 61 and 62 are solved numerically for ε_1 and ε_2. Assuming all the strain in the weld, ε_2, goes into the crack, then CMOD = $\varepsilon_2 L_2$.

A comparison of the measured CMOD-vs.-ε_L data with the values calculated using the two-tensile-bar analogy is shown in Fig. 22. The results indicate that strain partitioning due to the difference in the stress-strain curves of the base metal and the weld is a usable physical model of weldment behavior.

2.3.3 Summary and Conclusions

Crack-mouth-opening displacements (CMODs) of surface cracks have been measured as functions of stress and strain in tensile panels of API 5LX-70 steel plates and welded pipe segments. The conclusions drawn from the investigation are:

1. For CMOD vs. stress, the flat plate yielded-ligament model with through-thickness plasticity correction agrees well with the experimental results for the base metal and the welds.

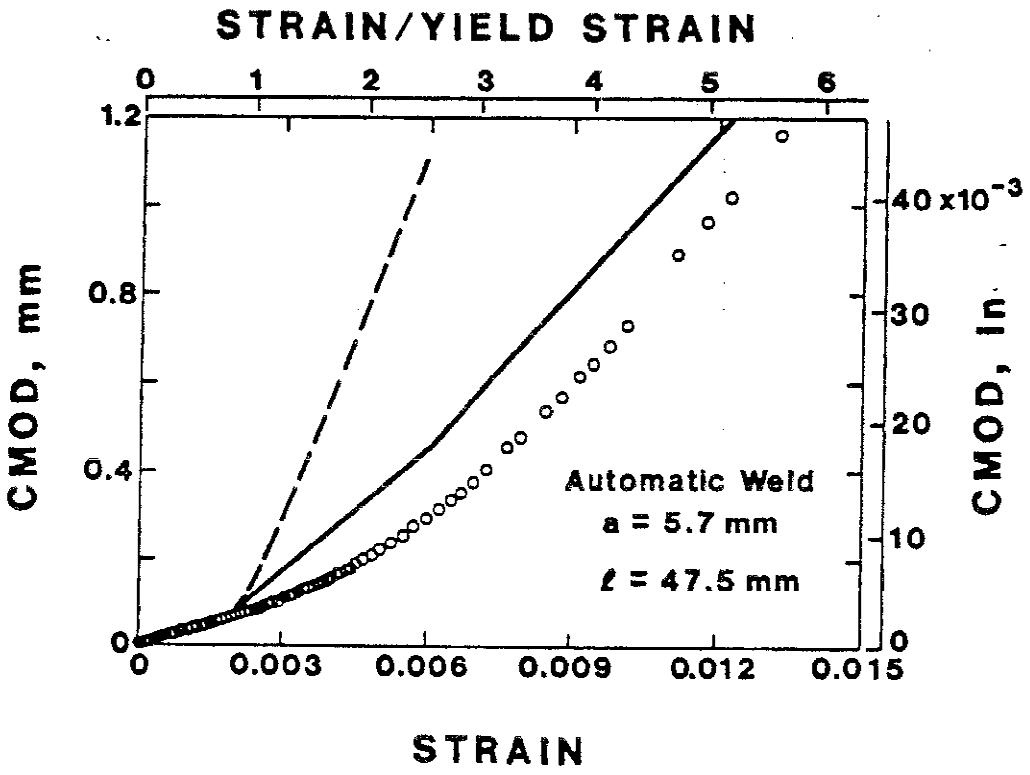

Fig. 22 - CMOD vs. gage-length strain for an automatic weld-metal specimen exhibiting net-section yielding. Symbols are experimental data; solid lines are prediction from two-tensile-bar model; dashed lines are predictions from simple net-section-yielding models.

2. For strains above net-section yielding, the relationship between CMOD and strain is complex, depending upon the specimen type (plate or weld) and crack size.

a. For large cracks in base metal, all of the remote displacement goes into the crack tip through the slip bands extending from the crack tip to the plate edges at 45°, that is, net-section yielding. This behavior was modeled and predictions from the model agree well with the experiment.

b. For cracks with crack area less than 5% of the cross-sectional area, net-section yielding is followed by gross-section yielding in which the remote displacement is distributed evenly along the length of the specimen.

c. For large cracks in steel welds, net-section yielding is observed. The observed CMOD is lower than predicted by the model because the yield strength of the weld is higher than that of the base metal. A model, based on strain partitioning, accounts for the observed behavior and provides better predictions.

d. For small cracks in steel welds, gross-section yielding is observed throughout the strain range studied.

2.4 Model Verification Tests on Large-Diameter Pipes

An extensive series of full-scale experiments on pipes were conducted by the Welding Institute of Canada.[36] The pipe was API 5LX-70 steel, 914 mm (36 in) in diameter and 11.5-mm (0.45-in) thick. Pipes containing surface cracks were tested to failure. The surface cracks varied in length from 58 mm (2.3 in) to 300 mm (11.8 in) and in depth from 3 mm (0.12 in) to 10.2 mm (0.40 in). The tests included in this report are summarized in Table 4. The tests were conducted at temperatures ranging from -90°C (-130°F) to 20°C (68°F). Twelve-meter- (39-ft) long pipe sections were loaded in bending by 20 hydraulic

Table 4 — Test Matrix for Large-Scale Tests Conducted at the Welding Institute of Canada

Test Number*	Crack Length, mm	Crack Length, in	Crack Depth, mm	Crack Depth, in	Wall Thickness, mm	Wall Thickness, in	Temperature °C	Temperature °F
2B	60.4	2.38	5.6	0.22	11.3	0.445	20	68
4	63.5	2.50	5.9	0.23	11.2	0.441	20	68
6	68.6	2.70	7.8	0.31	11.1	0.437	-90	-130
7	61.0	2.40	5.4	0.21	11.5	0.453	-90	-130
8	76.4	3.01	10.1	0.40	12.0	0.472	-90	-130
9	81.7	3.22	8.8	0.35	11.6	0.457	-50	-58
11	79.0	3.11	9.3	0.37	11.3	0.445	-50	-58
13	59.6	2.35	6.2	0.24	10.8	0.425	-50	-58
14	64.8	2.55	5.5	0.22	11.0	0.433	-5	23
15	60.4	2.38	5.5	0.22	11.2	0.441	-5	23
18	300.0	11.8	3.0	0.12	11.1	0.437	20	68
19	300.0	11.8	3.0	0.12	11.1	0.437	20	68

* Welding Institute of Canada identification numbers.

jacks at 610-mm (24-in) spacing. A clip-on gage was used to measure CMOD, and the jack pressure was recorded. Strain gages were placed at various locations to determine the strain distribution in the pipes. In the low-temperature tests, the temperature distribution was measured with thermocouples. The surface cracks were located in the girth weld or in the base metal. Manual arc welding was used. The flow strength of the welds was approximately 590 MPa (86×10^3 psi), which slightly undermatched the base metal.

On the basis of beam theory, the maximum membrane stress induced at the cracked section was calculated to be

$$\sigma = 30.6p \tag{63}$$

where p is the applied jack pressure. The bending moment at the crack section was

$$M \text{ (in N·m)} = 9.96 \times 10^6 p \quad \text{or} \quad M \text{ (in lbf·in)} = 8.82 \times 10^7 p \tag{64}$$

Equations 63 and 64 were used in this study to permit analytical computation of CMOD as a function of jack pressure.

2.4.1 Results and Discussion

Experimental results for CMOD at various temperatures as a function of jack pressure are shown in Figs. 23 through 27. The tests on plain pipe are plotted in Fig. 23. The remainder of the tests were on pipe sections containing girth welds. The tests in Fig. 27 involved relatively long surface cracks. The general form of the results is the same for each test: a linear relation between CMOD and p prevailed at low pressures, followed by a nonlinear region as yielding occurred in the vicinity of the crack, and finally a vertical asymptote as the pressure causeng collapse at the cracked section was approached.

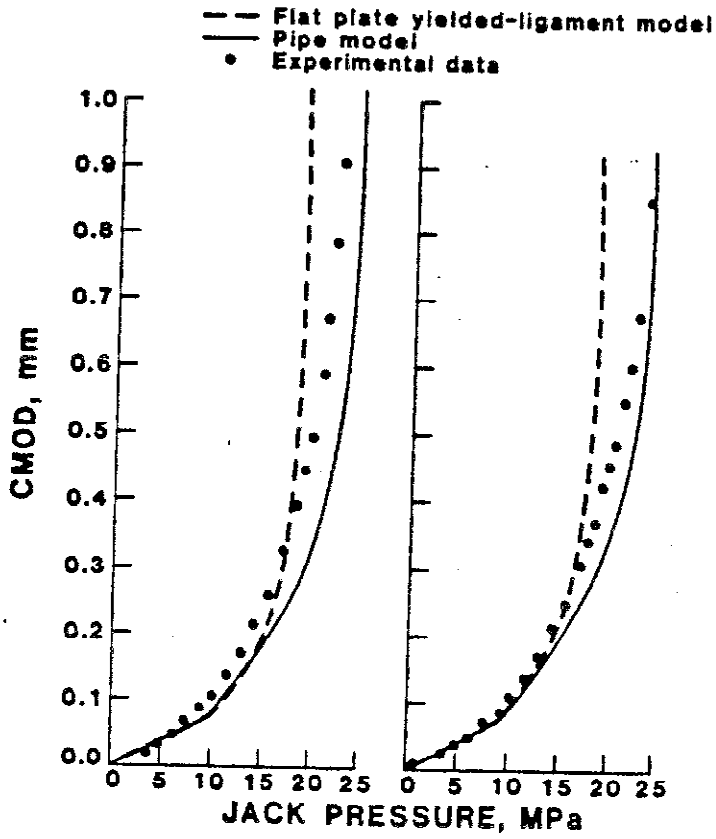

Fig. 23 - Comparison of model predictions and experimental results for CMOD vs. jack pressure. Tests were conducted at 20°C (68°F). MPa/6.894 = psi x 10^3; mm x 0.0394 = in.

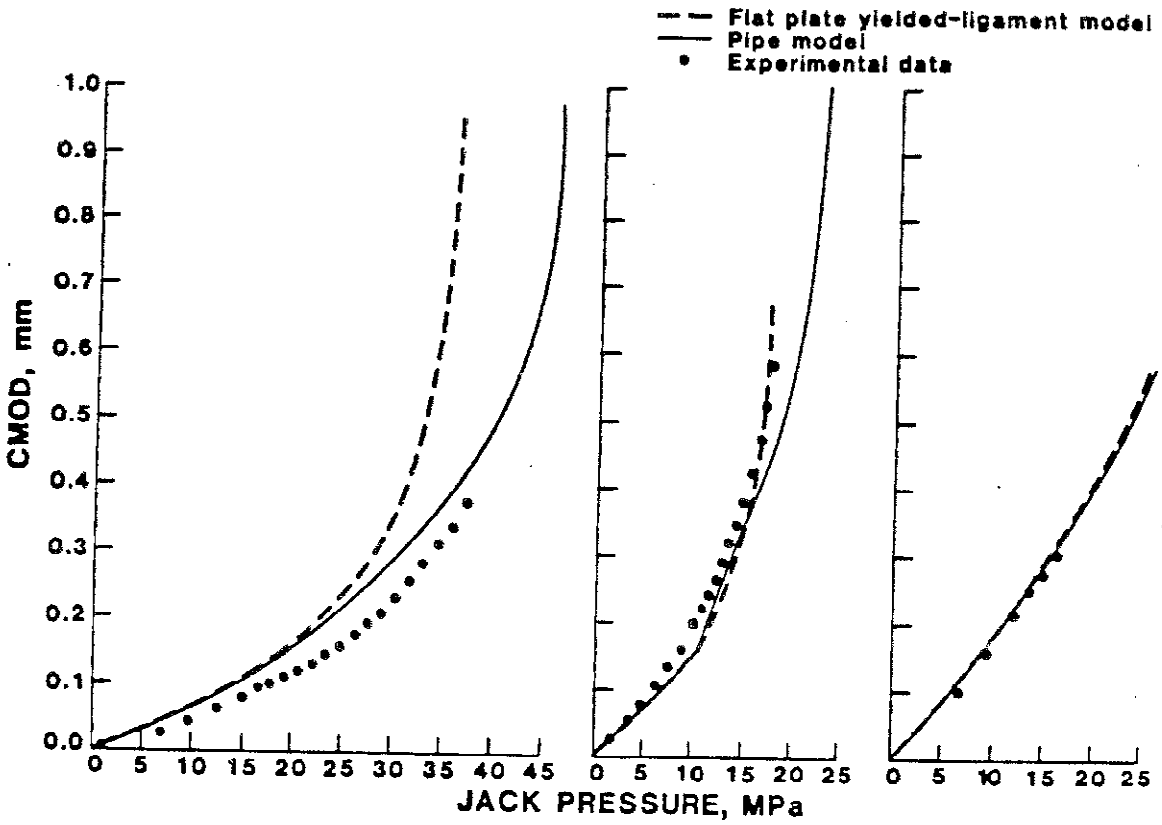

Fig. 24 - Comparison of model predictions and experimental results for CMOD vs. jack pressure. Tests were conducted at -90°C (-130° F). MPa/6.894 = psi x 10^3; mm x 0.0394 = in.

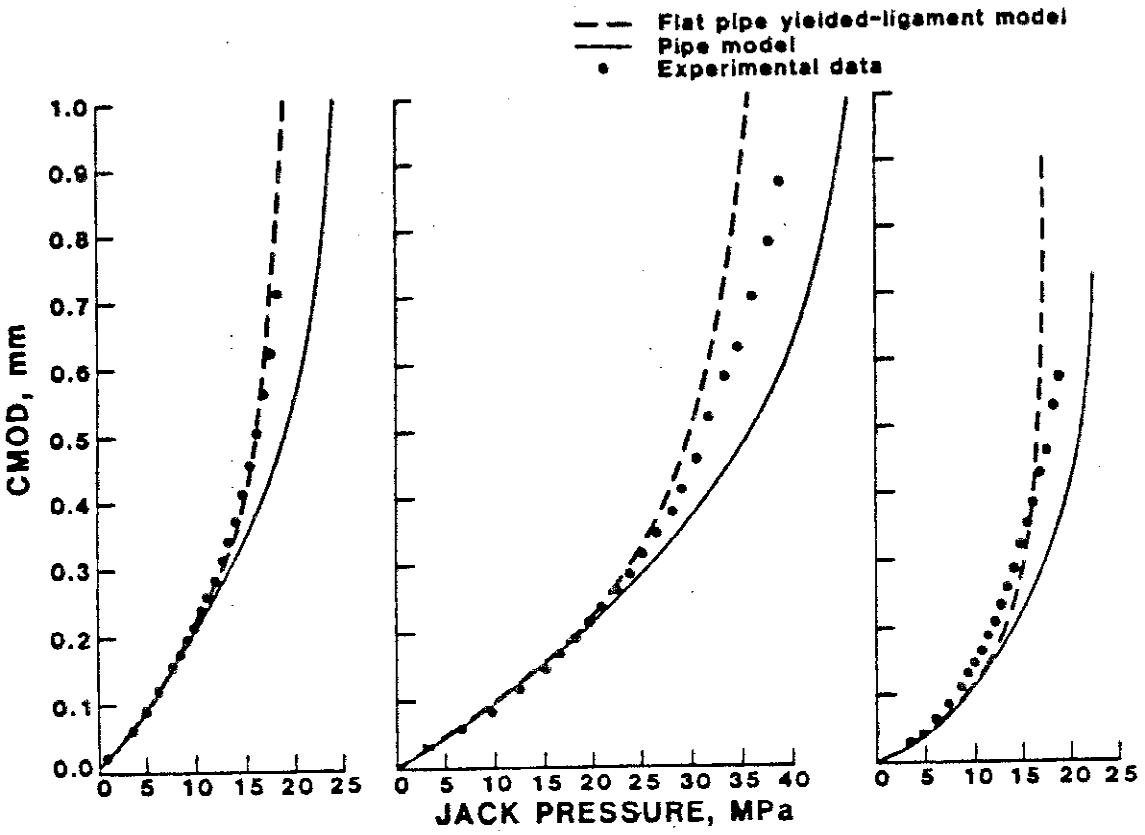

Fig. 25 - Comparison of model predictions and experimental results for CMOD vs. jack pressure. Tests were conducted at -50°C (-58°F). MPa/6.894 = psi x 10^3; mm x 0.0394 = in.

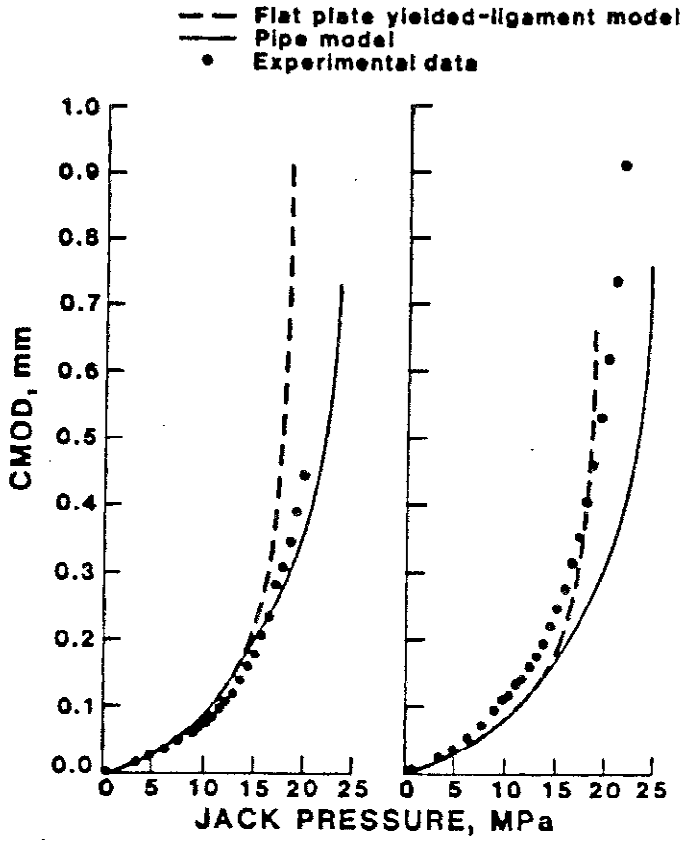

Fig. 26 - Comparison of model predictions and experimental results for CMOD vs. jack pressure. Tests were conducted at -5°C (+23°F). MPa/6.894 = psi x 10^3; mm x 0.0394 = in.

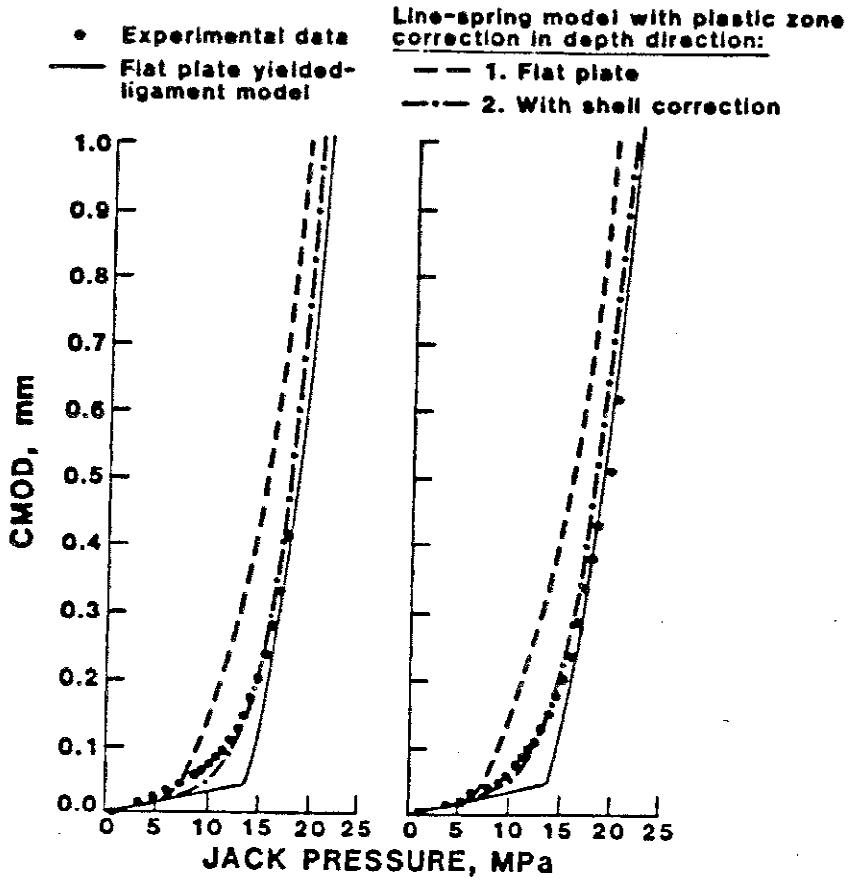

Fig. 27 - Comparison of model predictions and experimental results for CMOD vs. jack pressure. Tests were conducted at 20°C (68°F). MPa/6.894 - psi x 10^3; mm x 0.0394 = in.

Analytical predictions of CMOD as a function of jack pressure are compared with the experimental results described above. In the discussion, the original version of the yielded-ligament model (Section 2.2.3) will be referred to as the flat-plate yielded-ligament model. The modified version, which accounts for the plastic collapse mechanism of the pipe (Section 2.2.4), will be referred to as the pipe yielded-ligament model.

Typically the flat-plate yielded-ligament model agrees fairly well with observed values of CMOD until higher jack pressures, at which the model predictions are higher than the observed values. However, the discrepancy does not typically occur until higher values of CMOD have been reached. For example, if it is assumed that the highest CTOD fracture toughness value of pipeline weld metal that might be used in a fitness-for-service assessment is 0.25 mm (0.010 in), then for typical surface-flaw geometries, this toughness value (i.e., CTOD value) would be equivalent to a CMOD of approximately 0.28 mm (0.011 in). The model predictions of CMOD agree favorably with the experimental results until values of CMOD higher than this are reached. Thus the flat-plate yielded-ligament model is, in general, sufficiently accurate over the range of interest. An exception was test 6 (Fig. 24) in which the model predictions were conservative (by a maximum of approximately 40%) at lower pressures. The reason for this discrepancy has not been explained.

The conservatism of the flat-plate yielded-ligament model at higher pressure values appears to be attributable to incorrect modeling of the plastic deformation in the pipe. The model predictions are vertically asymptotic at a value of pressure corresponding to the tensile net-section yield stress, σ_{NSY}, given by Eq. 38. The model asymptote is typically to the left of the data asymptote. The modified version of the model (Eq. 54) called the pipe yielded-ligament model, assumes a more realistic plastic collapse

mechanism and seems to agree more favorably with the experimental results at higher pressure levels. Exceptions are tests 7, 9, 13, and 15 in which the predictions of the flat-plate yielded-ligament model agree more closely. This observed behavior is curious because it is reasonable to expect the data to adhere more closely to the modified model. Two possible explanations are inelastic buckling and tearing. Buckling behavior was observed in several of the tests. Inelastic ovalization during buckling would significantly lower the plastic collapse pressure. Some ductile tearing was also reported in some of the tests. The model predictions based on the original crack length would, therefore, be too low.

In the two tests shown in Fig. 27, the crack length was relatively long (300 mm, 11.8 in). A straightforward application of the flat-plate yielded-ligament model to the calculation of CMOD in this case gives poor results. It is seen that the data become nonlinear much sooner than the model predicts. This was attributed to the importance of yielding through the ligament depth in this case, because the center of a long surface crack receives very little support from the material at the sides of the crack. Use of the flat-plate yielded-ligament model to compute the elastic component of CMOD and accounting for through-depth yielding via the plastic-zone size correction presented in Section 2.3.2 resulted in extremely conservative curves. Upon examining the line-spring calculation more closely, it was found that the largest contribution to CMOD was from the rotation of the crack faces. The increased stiffness of a curved shell against rotation in comparison with the stiffness of a flat plate must, therefore, be accounted for. This was done in the manner described in Section 2.2.4, resulting in the pipe yielded-ligament model with through-thickness plasticity correction. Predictions of this model are shown in Fig. 27; they agree well with the experimental values of CMOD.

2.4.2 Summary

On the basis of experimental results from full-scale tests of pipes in bending, the flat-plate yielded-ligament model permits fitness-for-service predictions of crack-driving force that are conservative by at least 20% compared with the experimental data.

At driving force values above this range of practical interest, the model predictions become more conservative. This has been explained by introducing a modification to the model that more properly accounts for the plastic deformation in a pipe, the resulting model was called the pipe yielded-ligament model. Calculations of COD by the model in its original form are relatively inaccurate for long surface cracks. However, a modification to the model has been proposed that greatly increases its applicability to the long crack case. This final model was named the pipe yielded-ligament model with through-thickness plasticity correction. Because the model is relatively simple to apply, yet predicts crack driving forces that compare well with experimental checks, being accurate or conservative by less than 10% over the range of practical interest, it is felt to be a useful tool in determining the driving force for surface cracks under elastic-plastic deformation. This is an important ingredient in setting allowable flaw-size standards in pipeline girth welds and other structures.

2.5 Allowable Flaw-Size Curves

An allowable flaw-size curve is a plot of flaw depth as a function of flaw length, as shown schematically in Fig. 1. Each point on the curve represents a critical flaw size (length and depth) calculated using an appropriate fracture mechanics model and specified values for applied stress, residual stress, fracture toughness, tensile properties and pipe dimensions. The specified values are conservatively chosen to preclude the possibility of

achieving critical conditions in service. In this section, the fracture mechanics model developed in this program for the calculation of allowable flaw size curves, the pipe yielded-ligament model with through thickness plasticity correction, is described. Guidelines for the selection of stress levels, pipe and girth-weld material properties, and pipe dimensions for use in the analysis are presented. Finally, a representative allowable flaw-size curve is given, and the influence of selected parameter variations on the position of the curve is shown.

2.5.1 Fracture Mechanics Model

The analytical model used to calculate allowable flaw-size curves is the pipe yielded-ligament model wih through thickness plasticity correction. The fracture criterion is the CTOD:

$$\delta_c = CTOD_E + CTOD_{LY} + CTOD_{RS} \qquad (65)$$

where δ_c = fracture toughness in terms of CTOD

$CTOD_E$ = elastic component of CTOD

$CTOD_{LY}$ = ligament-yielding component of CTOD

$CTOD_{RS}$ = residual stress component of CTOD

The idea is that fracture occurs when the driving force for fracture, the CTOD terms in Eq. 65, exceeds the resistance of the material to fracture, δ_c. Values for the fracture toughness, applied stress, tensile properties, and pipe geometry are specified on the basis of pipeline operating conditions (e.g., pressure, temperature, imposed displacements) and pipe and weld requirements (e.g., diameter, thickness, strength, toughness). The remaining variables in Eq. 65 are the flaw depth, a, and the flaw length, ℓ. Using the specified values, Eq. 65 is solved numerically for a as a function of ℓ using a Newton-Raphson iteration procedure. The computer program used for these calculations is given in Appendix A.

The elastic component of CTOD is calculated using the simplified line-spring model discussed in 2.2.3. The equations used in the calculations are:

$$CTOD_E = K^2(1 - \nu^2)/E\bar{\sigma} \tag{44}$$

$$K = t^{\frac{1}{2}}(\sigma_o g_t + m g_b) \tag{66}$$

where g_t and g_b are given by:

$$g_t(\xi) = (\pi\xi)^{\frac{1}{2}}(1.12 + 6.52\xi^2 - 12.39\xi^4 + 89.05\xi^6 - 188.61\xi^8 + 207.39\xi^{10} - 32.05\xi^{12}) \tag{67}$$

$$g_b(\xi) = (\pi\xi)^{\frac{1}{2}}(1.12 - 1.89\xi + 18.01\xi^2 - 87.39\xi^3 + 241.39\xi^4 - 319.94\xi^5 + 168.01\xi^6) \tag{68}$$

$\xi = (a+r_y)/t$ and σ_o and m are computed using Eqs. 27 through 33. For cracks longer than 96 mm (3.8 in), curvature must be accounted for in the compliance calculations. The curvature correction enters the line-spring model by replacing Eq. 26 with Eq.47b and making the associated changes in Eqs. 28 through 33. The revised equations are 69 through 74, in which the subscript c in the symbols α_c and β_c stands for curvature.

$$a_{12}\sigma_o + m\left\{a_{22} + \frac{(2R)^{\frac{1}{2}}[12(1-\nu^2)]^{3/4}}{72(1-\nu^2)t^{\frac{1}{2}}}\right\} = 0 \tag{69}$$

$$\sigma_o = \alpha_c\sigma \tag{70}$$

$$m = -\beta_c\sigma \tag{71}$$

$$\alpha_c = \left\{\ell/[t(1-\nu^2)]\right\}\left\{a_{22} + \frac{(2R)^{\frac{1}{2}}[12(1-\nu^2)]^{3/4}}{72(1-\nu^2)t^{\frac{1}{2}}}\right\} \cdot S^{-1} \tag{72}$$

$$\beta_c = \left\{\ell/[t(1-\nu^2)]\right\}a_{12} \cdot S^{-1} = \beta \tag{73}$$

$$S = \left\{a_{11} + \ell/[t(1-\nu^2)]\right\}\left\{a_{22} + \frac{(2R)^{\frac{1}{2}}[12(1-\nu^2)]^{3/4}}{72(1-\nu^2)t^{\frac{1}{2}}}\right\} - a_{12}^2 \tag{74}$$

In evaluating Eq. 66, the plastic-zone correction, r_y, is added to the crack depth. The r_y is calculated as in Eq. 17, but using depth and thickness in place of length and width, and inserting the appropriate stress ratio:

$$\sin(\pi a/2t)/\sin\left[\pi(a+2r_y)\right]/2t = \cos(\pi\sigma_o/2\bar{\sigma}) \ . \qquad (75)$$

The plastic zone size calculation is nonlinear and self-consistent; both Eq. 70 and Eq. 75 must be satisfied. The plastic zone enters Eq. 70 through the parameters a_{ij}, which are actually functions of the effective crack length, $a+r_y$. These parameters are given as functions of a/t in Fig. 5, above, in the context of an elastic treatment of the ligament. As discussed in Section 2.4.1, yielding through the ligament must be considered in the calculations to obtain agreement with experiment. This is accomplished by replacing a/t on the x-axis of Fig. 5 with $(a+r_y)/t$. Thus, the ligament behind the crack is treated as partially yielded, and having some plastic zone radius, r_y, before the applied stress reaches a certain value given by Eq. 34; above this stress, the ligament is fully yielded and CTOD increases according to Eq. 76. Before the ligament is fully yielded, no plasticity corrections to ℓ are made.

The ligament yielding component of CTOD is given by:

$$CTOD_{LY} = [2(\ell + 2r_y)/E]\,[\sigma - (1 - a/t)\bar{\sigma}] \qquad (76)$$

where r_y is the strip-yield plastic zone solution given in Eq. 17.

The residual stress component of CTOD is estimated by assuming that the residual stresses result from weld shrinkage, and thus, are self-equilibrating. In this case, one can assume that yield-point stresses act over a distance comparable to the weld size or pipe thickness. If so, a displacement of $\sigma_y t/E$ will relieve the residual stress. An approximation of the contribution of such a residual stress to the driving force for fracture is simply to assume that the estimated displacement is all converted to CTOD:

$$CTOD_{RS} = \sigma_y t/E \qquad (77)$$

Evaluating Eq. 77 using the ANGTS pipeline properties listed above, the result is a $CTOD_{RS}$ of 0.038 mm (0.0015 in).

Calculations of allowable flaw-size curves using the equations listed above are most conveniently done by computer. Assistance in the details of the calculation and the computer program used to compute the allowable flaw-size curves for this study are given in Appendix A.

2.5.2 Parameters

The relative position of the allowable flaw-size curve depends on the parameters used to evaluate Eq. 65. For the ANGTS pipeline, the pipe grade, API 5LX-70, and the pipe geometry, 1220-mm (48.0-in) diameter and 15.9-mm (0.625-in) wall thickness, have been specified, but a reliable data base on the tensile properties and the fracture toughness of the pipe and weld are not available.

It is planned to operate the pipeline at -4°C (25°F), but the maximum allowable stress (or strain) normal to the girth welds is not known by the authors. It has been assumed that the pipeline will be in nearly continuous operation at a nearly constant pressure and thus, crack growth in service due to fatigue cycling has been neglected.

For the purposes of this investigation, the maximum credible stress level is assumed to be 90% of the specified minimum yield strength of the pipe, 434 MPa (63.0×10^3 psi). The following tensile properties are assumed for both the pipe and the girth welds:

$$\sigma_y = 482 \text{ MPa } (69.9 \times 10^3 \text{ psi})$$
$$\bar{\sigma} = 517 \text{ MPa } (75.0 \times 10^3 \text{ psi})$$
$$\sigma_u = 551 \text{ MPa } (79.9 \times 10^3 \text{ psi})$$
$$E = 208 \text{ GPa } (30.2 \times 10^6 \text{ psi})$$
$$\nu = 0.29$$

The minimum fracture toughness at the service temperature is assumed to be 0.13 mm (0.005 in). It should be emphasized that this value exceeds the minimum results obtained in this investigation, but it is considered to be an achievable minimum for qualified welding consumables and procedures.

2.5.3 Results and Discussion

Allowable flaw-size curves have been developed using the fracture mechanics analysis model described in Section 2.5.1. For the parameters listed in Section 2.5.2, the resulting curve, Fig. 28, is considered to be the current best-estimate of the allowable flaw-size curve for the ANGTS pipeline.

The position of the curve is strongly affected by the parameters selected. A sensitivity study has been conducted to assess the influence of variations in fracture toughness, tensile properties, and stress levels on the allowable flaw sizes. The results are presented in the form of a reference curve

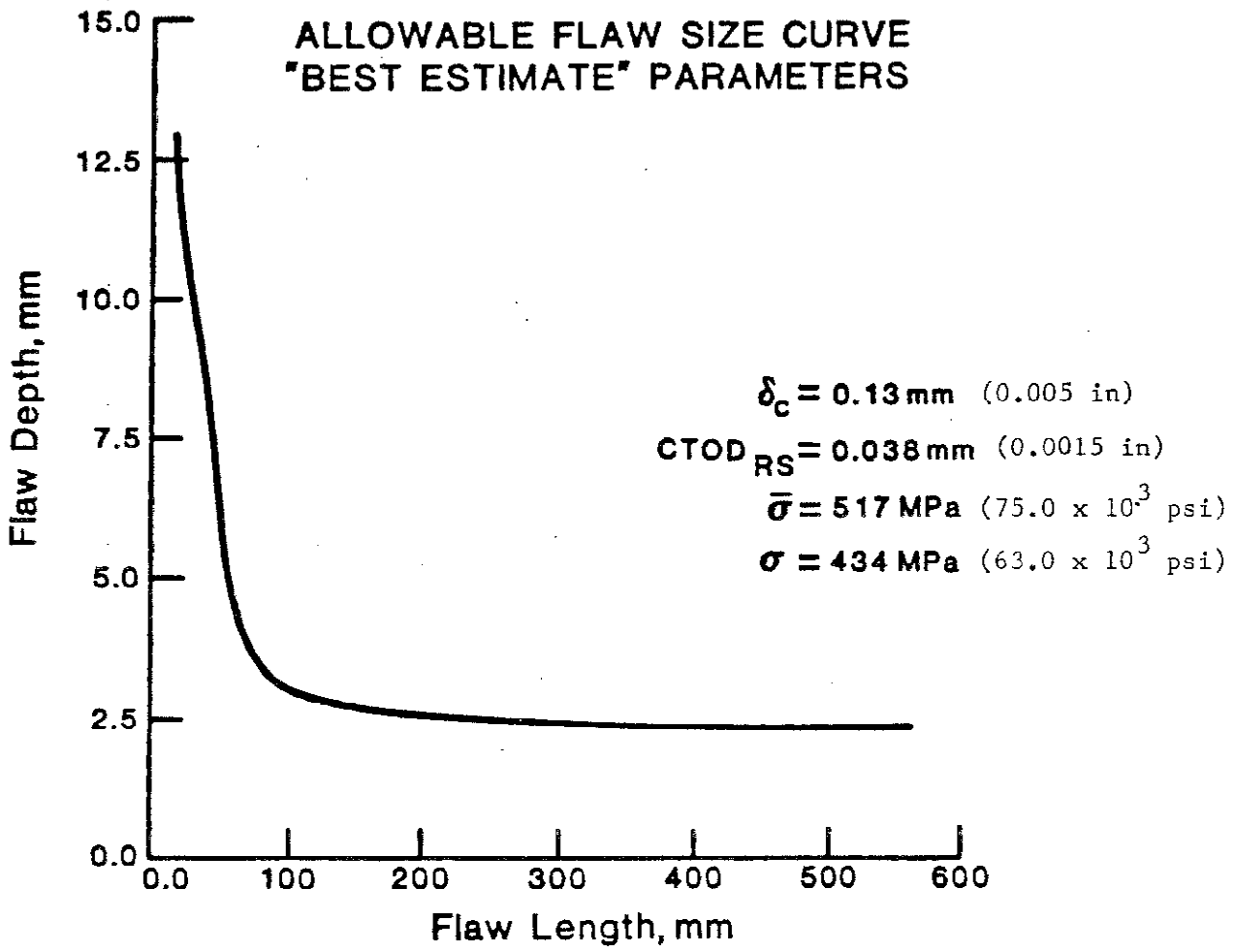

Fig. 28 - Best estimated allowable flaw-size curve.
To obtain flaw depth and length in inches,
multiply by 0.0394.

developed using the parameters listed in Section 2.5.2 and two additional curves developed using values of the variable under study below and above the reference value (Figs. 29-31).

The curves showing sensitivity to toughness variations are shown in Fig. 29. Note that by increasing the fracture toughness from 0.13 mm (0.005 in) to 0.25 mm (0.010 in), the allowable flaw depths are more than doubled for flaws up to 125-mm (4.92-in) long. For longer flaws, the increase in allowable depth decreases to about 30% for flaws that are 500-mm (19.7-in) long.

The curves showing sensitivity to variations in applied stress are shown in Fig. 30. Note that a 10% increase in stress results in a substantial decrease in allowable flaw size. For cracks longer than 125 mm (4.92 in), the allowable depth decreases by more than 50% when the stress is increased from 90% of the specified minimum yield strength (SMYS) to 100% of SMYS, that is, from 434 to 482 MPa (63.0 to 69.9 x 10^3 psi). The reason for this large sensitivity to applied stress is apparent from consideration of Eq. 76. Note that the $CTOD_{LY}$ is proportional to $\sigma - (1 - a/t)\bar{\sigma}$, and thus it is the relative difference between σ and $\bar{\sigma}$ that influences flaw size. The same effect is seen in the curves depicting the influence of flow stress (shown in Fig. 31).

The allowable flaw-size curves developed herein are compared with allowable flaw sizes permitted under Appendix A 16th edition, of API 1104.[2] Comparisons were made at the two toughness levels considered by API, that is, CTOD values of 0.13 mm (0.005 in) and 0.25 mm (0.010 in). The remaining parameters were those listed in Section 2.5.2. The results are presented in Figs. 32 and 33. At the 0.13-mm (0.005-in) toughness level (Fig. 32), the allowable flaw-size curves developed herein are more restrictive than the API allowables at essentially all crack lengths. The differences are largest for crack lengths

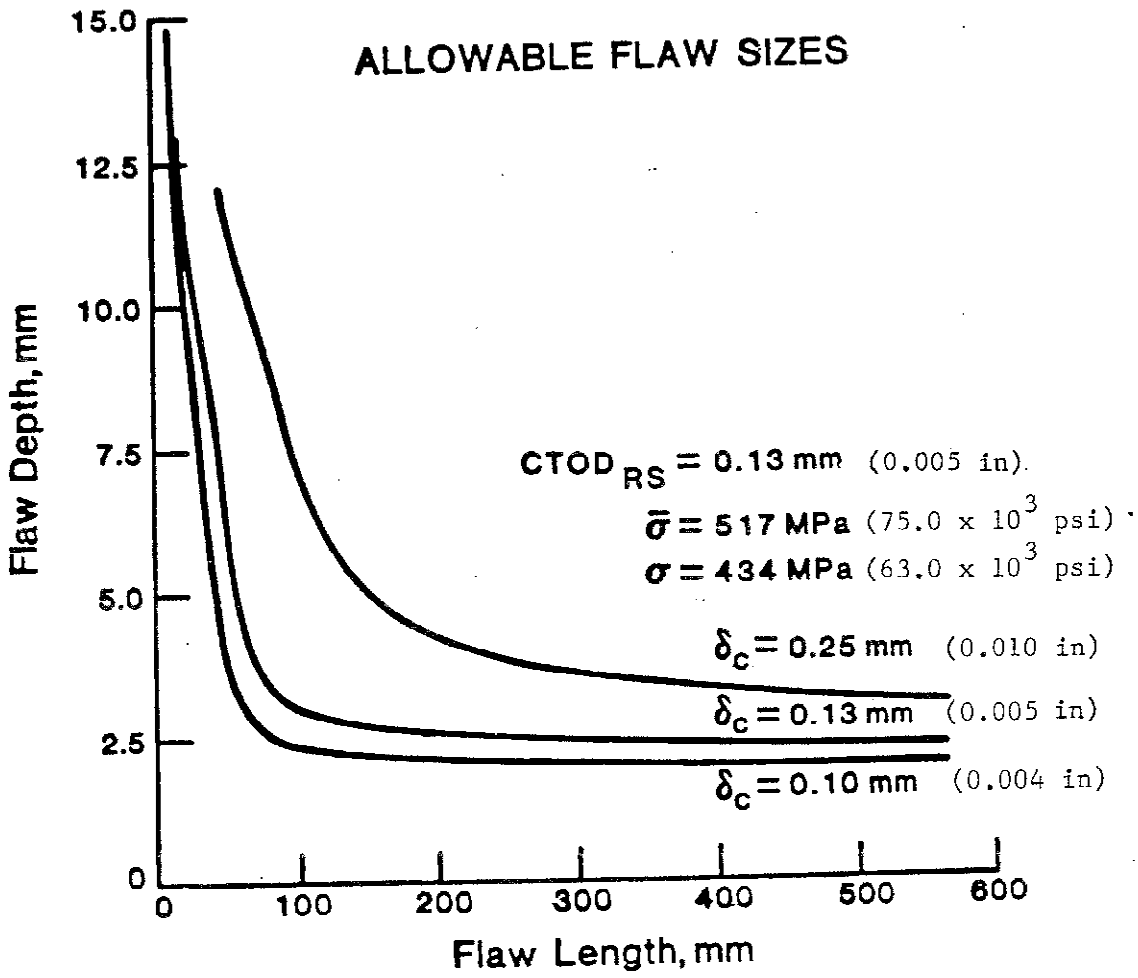

Fig. 29 - Effect of critical COD on the allowable flaw-size curve. To obtain flaw length and depth in inches, multiply by 0.0394.

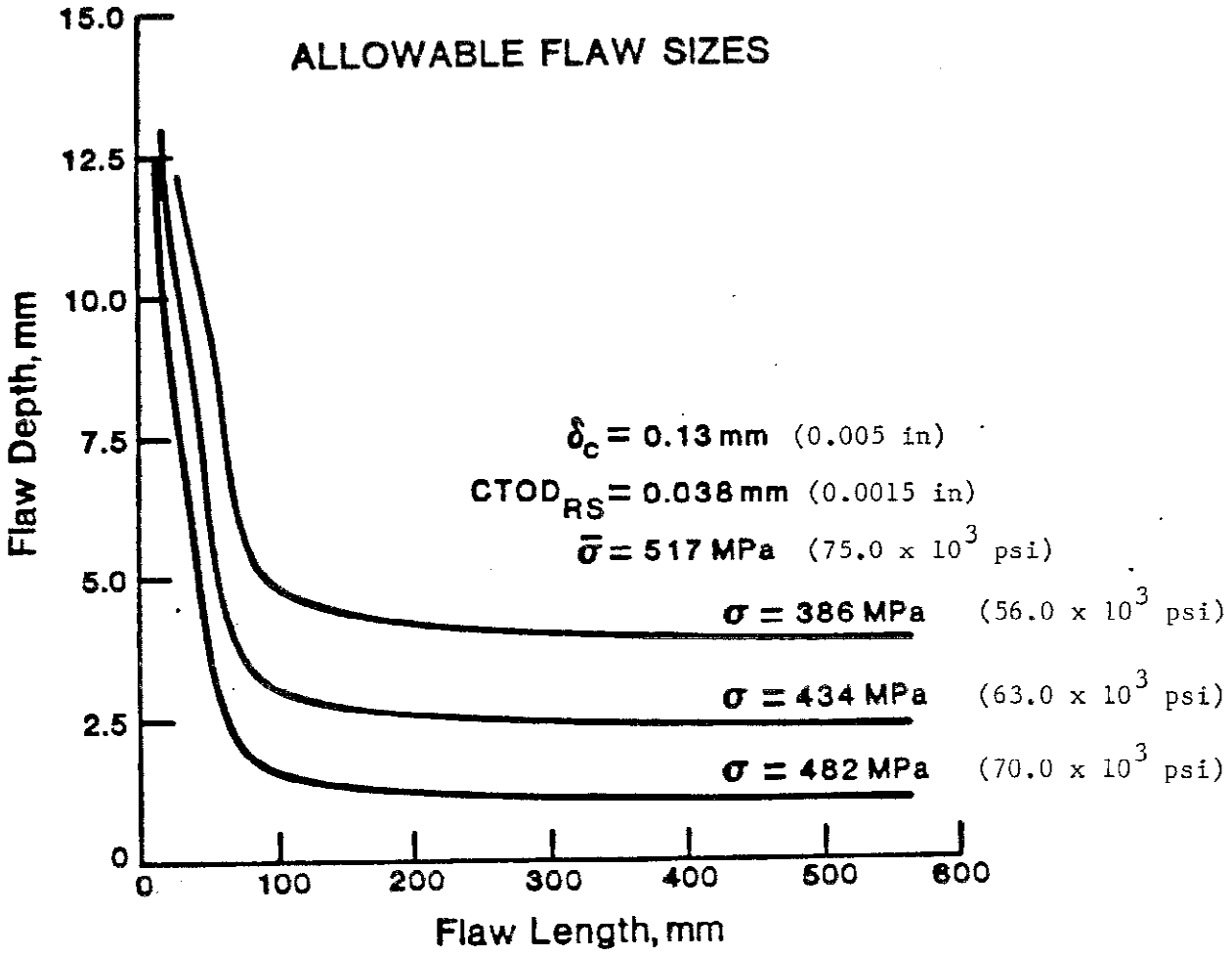

Fig. 30 - Effect of applied stress levels on the allowable flaw-size curve. To obtain flaw length and depth in inches, multiply by 0.0394.

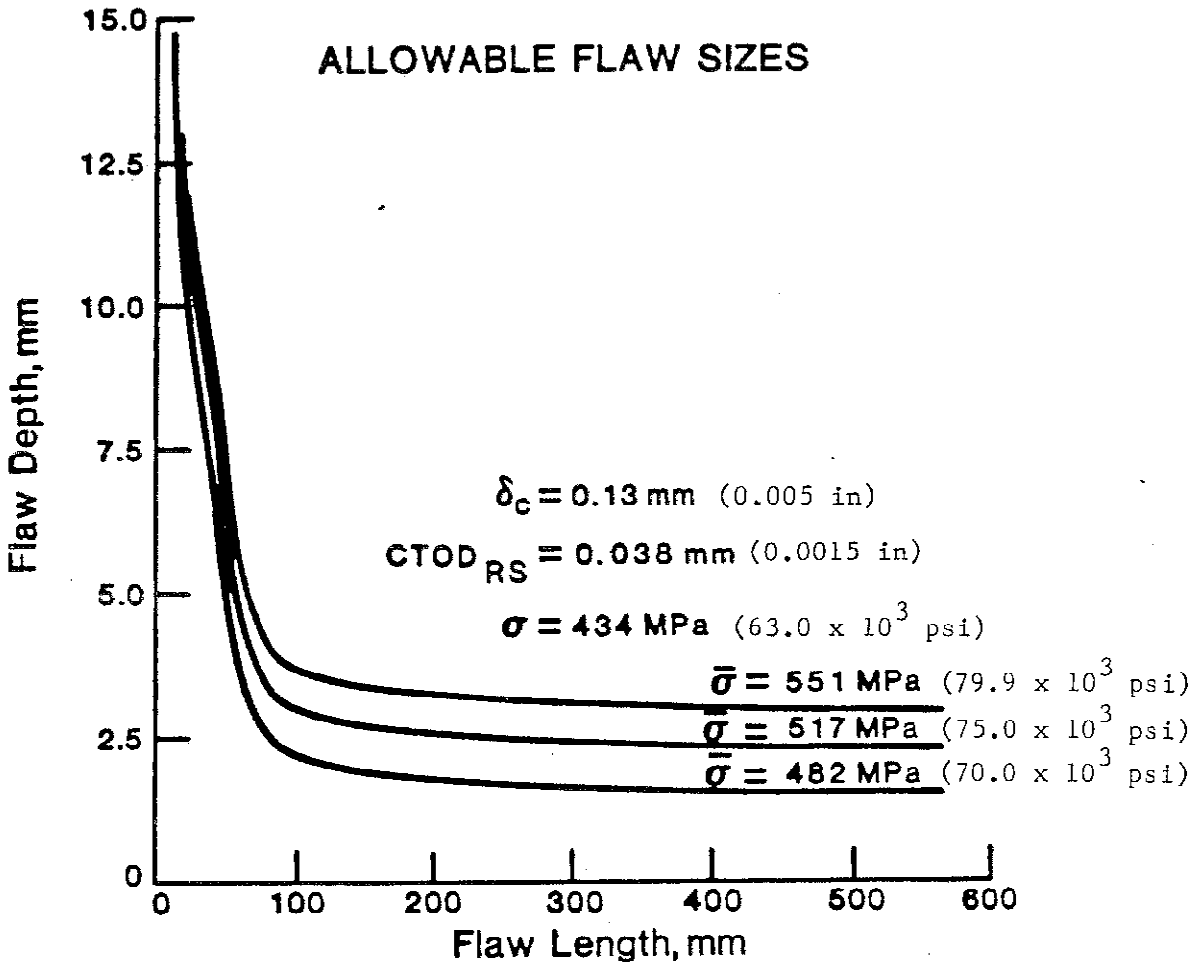

Fig. 31 - Effect of flow stress on the allowable flaw-size curve. To obtain flaw length and depth in inches, multiply by 0.0394.

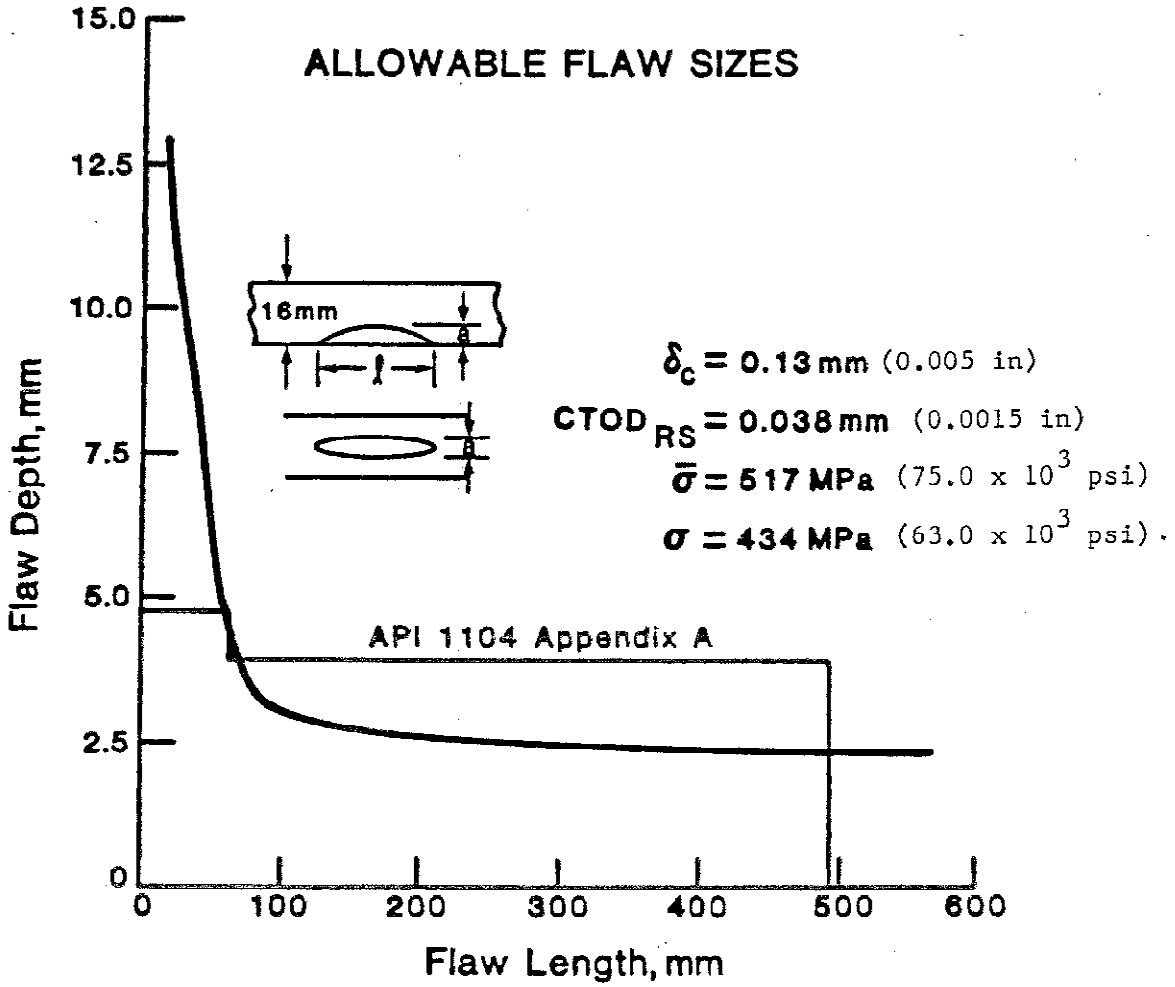

Fig. 32 - Comparison of allowable flaw-sizes with various criteria. To obtain flaw length and depth in inches, multiply by 0.0394.

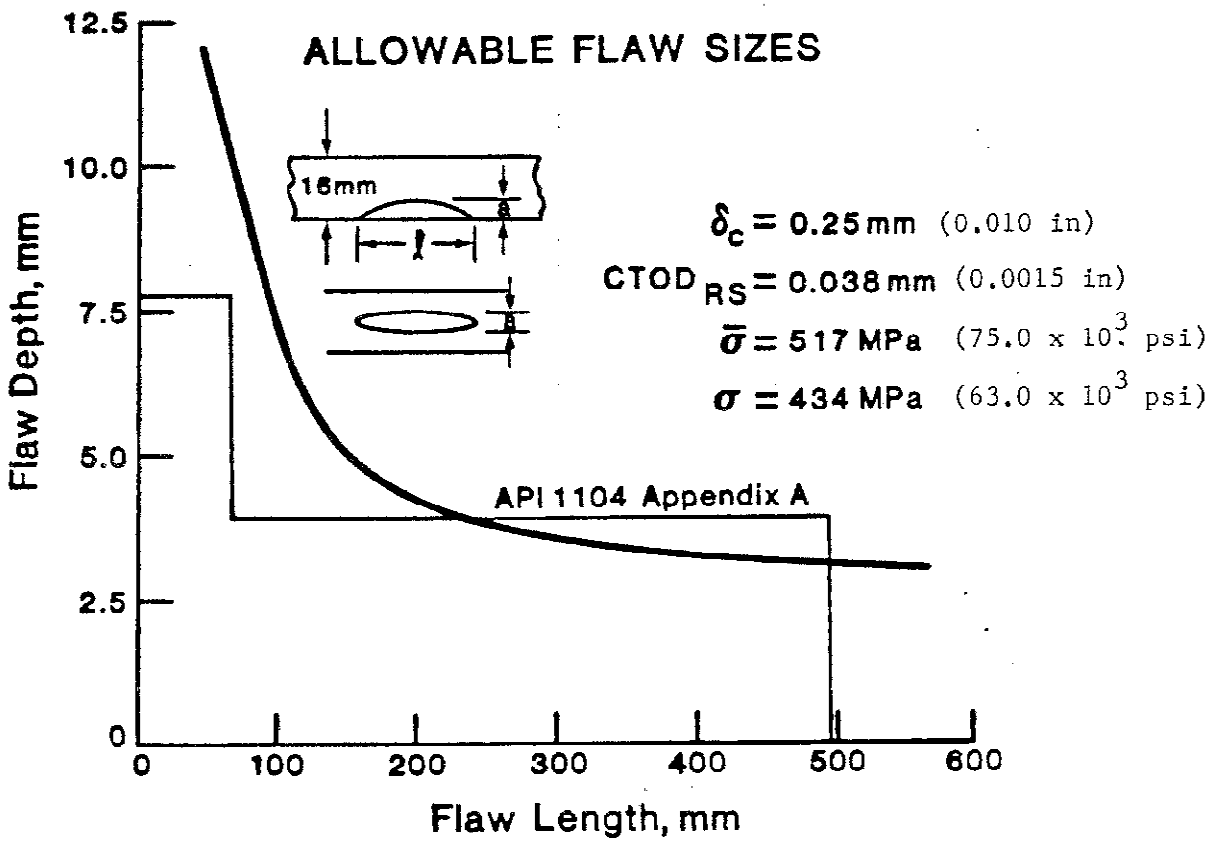

Fig. 33 - Comparison of allowable flaw sizes with various criteria. To obtain flaw length and depth in inches, multiply by 0.0394.

greater than 100 mm (3.94 in). For a flaw that is 250-mm (9.84-in) long, the allowable flaw depths are 2.5 mm (0.098 in) by the present method and 4.0 mm (0.157 in) by the API method. At the higher toughness level (Fig. 33), the allowable flaw sizes developed using the API procedures are more restrictive for crack lengths up to 230 mm (9.06 in) and less restrictive for longer cracks.

The differences in allowable flaw sizes between the present approach and those of Appendix A of API 1104, 16th edition,[2] result from differences in the treatment of ligament yielding, which is not explicitly addressed therein. The assessment basis in Appendix A of API 1104, 16th edition is similar to PD6493 (1980), from the British Standards Institution.[8] Section 8.2.3 of PD6493 (1980) accounts for ligament yielding using a flaw recategorization procedure. Flaws deep enough to produce ligament yielding are treated as through-thickness flaws, whose characteristic size is the flaw length, not its depth. This procedure disallows some flaws, resulting in a more restrictive allowable flaw sizes. The treatment of ligament yielding in our study is more extensive and more specific than that of PD6493 (1980).

2.6 SUMMARY

A fracture mechanics analysis model, the pipe yielded-ligament model with through-thickness plasticity correction, has been developed that relates allowable flaw sizes to applied stress level and weld toughness. For analysis purposes, the weld flaws have been treated as surface cracks. The fracture criterion used is the crack-tip-opening displacement (CTOD); that is, fracture occurs when the CTOD due to imposed strains (the applied CTOD) exceeds the fracture toughness (critical CTOD) of the girth welds.

The validity of the model was confirmed for the case of surface cracks in tensile panels at stress levels below the net-section yield strength. The comparison of analysis and experiment was complicated by the fact that CTOD cannot be readily measured. Thus, it was necessary to make the comparison in terms of crack-mouth-opening displacement (CMOD). CMOD was measured with a clip-on displacement gage and is calculated using the flat-plate yielded-ligament model with through thickness plasticity correction. The model further evaluated by analyzing the results of a series of tests on 900-mm (35-in) pipe conducted by the Welding Institute of Canada. Comparison of analysis, using the pipe yielded-ligament model with through-thickness plasticity correction, and experiment indicated that the line-spring model has acceptable accuracy for CTOD values up to 0.2 mm (0.008 in), the range of interest in developing allowable flaw-size curves.

This pipe yielded-ligament model with through-thickness plasticity correcton has been used to calculate allowable flaw-size curves for operating conditions and girth-weld properties representative of the proposed ANGTS pipeline. The applicability of the model is limited to pipelines with maximum stresses in the longitudinal direction below the specified minimum yield strength of the pipe. It is further limited to pipelines where the yield strengths of the weld and base metal are similar. The required degree of similarity in yield strengths has not been established, but the desirability of higher yield strength in the weld metal has been clearly demonstrated. The use of allowable flaw-size curves can be considered for either general pipeline use or for site-specific engineering assessment. Allowable flaw-size curves generated using typical pipeline operating conditions and weldment properties are more conservative for long flaw lengths than those derived using the procedures of Appendix A of the 16th edition of API 1104.[2]

3. SHARP-FLAW DIMENSIONING

C. M. Fortunko and R. E. Schramm

3.1 Introduction

In the evaluation of pipeline girth-weld quality on the basis of rational fitness-for-service criteria, ultrasonic inspection appears to be a better method than radiography, which has usually been used. Although radiography is well suited for assessing compliance with workmanship quality criteria, the relative insensitivity of radiography to the presence of sharp flaws makes it much less effective as a fitness-for-service inspection tool than ultrasonic inspection.[14] Furthermore, even though experience has shown that some information about the through-wall depth of blunt flaws can be inferred from densitometric analyses of radiographic data, recent work has shown that the reliability of sizing by such methods is very low for sharp flaws less than 0.25-mm (0.0098-in) thick, even when the most sophisticated microdensitometry techniques are employed.[37] Densitometry techniques can provide information only on the through-wall radiographically projected dimension of a canted sharp flaw; they provide no information on overall through-wall flaw height. Therefore, such techniques cannot be reliably used to detect and measure cracks, incomplete fusion, and inadequate penetration.

Sharp flaws are intrinsically better reflectors of ultrasonic energy than are blunt flaws. Consequently, ultrasonic methods theoretically have a higher probability of detecting significant flaws than do radiographic methods. However, tests run on the deliberately flawed manual and automatic welds prepared for this program showed that a high-frequency manual technique using an advanced state-of-the-art data acquisition system was incapable of performing the required

inspection. The primary problem was inability to separate geometric reflectors, such as those originating from the root of the weld, the weld reinforcement, high-low conditions, and other nondetrimental conditions from the reflectors present in the weld due to flaws that must be evaluated in accordance with API Standard 1104.[14] Some of these problems have been overcome in the development of completely automatic ultrasonic inspection systems, and such systems have been successfully demonstrated on the pipeline projects.[11] However, their use has been restricted to a workmanship assessment of automatic welds in which the primary flaw is lack of sidewall fusion. The best currently available systems have proven inadequate for flaw sizing as is required for a fitness-for-service acceptance criteria. These results confirm conclusions in the literature that high-frequency approaches are fundamentally limited in their usefulness in a fracture mechanics analysis of a welded structure.[38]

Recent theoretical and experimental investigations have shown that sharp flaws and cracks in butt welds can be sensitively detected using a new ultrasonic inspection technique.[37-39] The new technique differs from most conventional ultrasonic nondestructive evaluation (NDE) methods in three important respects:[40-44] First, the weld region is insonified using special ultrasonic probing signals: shear waves that are polarized parallel to the surface of the weldment (SH waves). Second, the probing ultrasonic signals are generated and detected using the recently developed periodic-permanent-magnet (PPM) electromagnetic-acoustic transducers (EMATs).[45,46] In contrast with the fluid-coupled piezoelectric transducers, the EMATs do not require intimate coupling and can operate efficiently over most unprepared surfaces. Third, the ultrasonic frequency of operation of the new inspection system is substantially lower (0.5 MHz) than the frequency range used in conventional ultrasonic inspection of ferritic butt weldments (2-10 MHz).

The lowering of the frequency of operation significantly reduces the sensitivity of the SH-wave EMAT system to minor perturbations in flaw surface detail: surface roughness and departure from planarity and branching.[47,48] If the frequency is sufficiently low, the amplitude of the signal scattered by the flaw can be unambigously related to the principal flaw dimensions.[41,49,50] In addition, sharp flaws are more easily detected than blunt flaws of similar dimensions. Of course, these features are highly desirable from the fitness-for-service point of view, which emphasizes the importance of the principal flaw dimensions and assumes that sharp flaws are inherently more critical than blunt flaws.[4,51-53]

The qualitative differences between ultrasonic scattering at low and high frequencies are illustrated in Fig. 34. (It is assumed that the flaw is planar and relatively long in the direction of the normal to the plane of

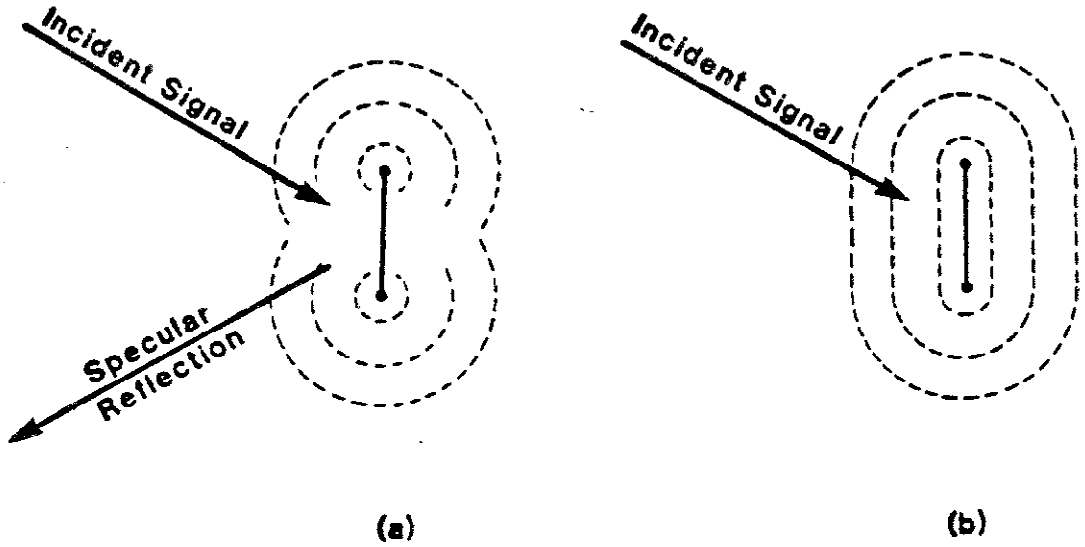

Fig. 34 - Ultrasonic scattering by two-dimensional, planar flaws: (a) high-frequency region; (b) low-frequency region.

reflection). At high frequencies (Fig. 34a), most of the incident ultrasonic energy from the face of the planar flaw is reflected specularly, that is, the angle of reflection with respect to the face normal equals the angle of incidence. Also, a significant portion of the incident signal is diffracted by the tips of the flaw, which act like ultrasonic line sources. If the surface of the flaw exhibits some roughness, some of the incident signal can be scattered incoherently (not shown). Furthermore, depending on the orientation of the flaw and the type of ultrasonic signal used (i.e., shear vs. longitudinal), significant mode conversions can also occur. As a result, the scattered ultrasonic field is very complicated and it is very difficult to infer the flaw dimensions from the ultrasonic data.

At low ultrasonic frequencies (Fig. 34b), the scattered ultrasonic fields are considerably easier to interpret because the specular reflection component becomes negligible and the tip diffractions are merged. Consequently, the scattered ultrasonic fields are much less sensitive to flaw orientation and surface roughness.[48] In addition, at low ultrasonic frequencies, sharp flaws are detected more easily than blunt flaws of similar length and through-wall depth. The principal advantage, however, of operating at low ultrasonic frequencies is that the amplitude of the backscattered signal increases monotonically with the flaw dimensions.

In this report, emphasis is placed on the details of the experimental configurations and procedures. An experimental configuration is described that permits the ultrasonic interrogation of the entire weld zone from the outer surface of the pipe. It has a built-in self-calibration feature that automatically and consistently records the experimental data. This feature is needed to offset variations in the EMAT electromechanical coupling

efficiencies, which may occur in practice as a result of variations in EMAT lift-off distance, material composition, pre-existing residual and applied stresses, and magnetic state.[54]

The physical principles governing the propagation of the special SH-wave probing signals in isotropic plates are discussed in detail. The discussion is confined to the special case of ultrasonically "thin" plates whose wall thickness does not substantially exceed the bulk ultrasonic wavelength (7.4 mm, 0.29 in, at 454 kHz). This restriction is primarily dictated by the choice of a theoretical model used to describe the scattering of low-frequency SH-wave signals by planar flaws of different through-wall depth, position, and orientation with respect to the free surface. However, general scattering theories are found in Refs. 55 through 57.

Considerable attention is focused on experimental evidence that is used to validate the main features of the theory. In addition, experiments are described that establish the inherent sensitivity limitations of the system for different categories of surface and buried flaws. The results are summarized in a set of diagrams that are pertinent to a 454-kHz SH-wave EMAT system operated on plate-like ferritic steel specimens 15.9-mm (0.625-in) thick. An inspection protocol, applicable to automated inspection of newly fabricated pipeline girth welds, is also discussed.

3.2 Inspection, Configuration, and Operation

Recently, several ultrasonic systems have been developed specifically for the purpose of inspecting pipeline girth welds.[42-45] However, the performance of the new systems is limited by uncertainties associated with coupling and the highly complex nature of ultrasonic scattering from flaws when the flaw dimensions of interest are large compared with the ultrasonic wavelength, but not large enough to permit high-resolution imaging. The low-frequency,

SH-wave EMAT system was then specifically designed to overcome most of the main shortcomings of conventional ultrasonic systems that use piezoelectric transducer elements, which typically operate at high ultrasonic frequencies (2-10 MHz).

Figure 35 shows an experimental configuration that has been found to be particularly useful in the detection and limited characterization of elongated flaws in pipeline girth welds. The configuration of Fig. 35 is composed of two identical SH-wave EMATs that are positioned on the outer surface of the pipe and aimed colinearly along the normal to the girth weld. The transmitter EMAT is located closer to the weld than the receiver EMAT. Because SH-wave EMATs are bidirectional, the transmitter EMAT generates two SH-wave signals of equal amplitude, which travel in opposite directions along the normal to the weld. The ultrasonic signal 1, traveling to the left of the transmitter EMAT, insonifies the weld region, while the ultrasonic signal 2, traveling to the right of the transmitter EMAT, passes directly beneath the receiver EMAT. In practice, signal 1 is used to interrogate the weld region, and signal 2 is used to calibrate the overall transduction efficiency of the system.

If a flaw is present in the weld, a portion of the probing signal 1 is backscattered in the direction of the receiver EMAT. The backscattered signal 3 arrives at the receiver EMAT after the reference signal 2 because it travels a longer distance. The two signals, 2 and 3, are shown in the photo of Fig. 36.

The signals in Fig. 36 were observed when an inadequate penetration flaw was insonified in a 1220-m (48.0-in) diameter, 15.9-mm (0.625-in) thick API 5LX-70 SMA-welded pipe section. The center frequency of the ultrasonic signals was 454 kHz, corresponding to an ultrasonic (shear-wave) wavelength of 7.4 mm (0.29 in). In the photo, the first signal (0-30 μs) is caused by

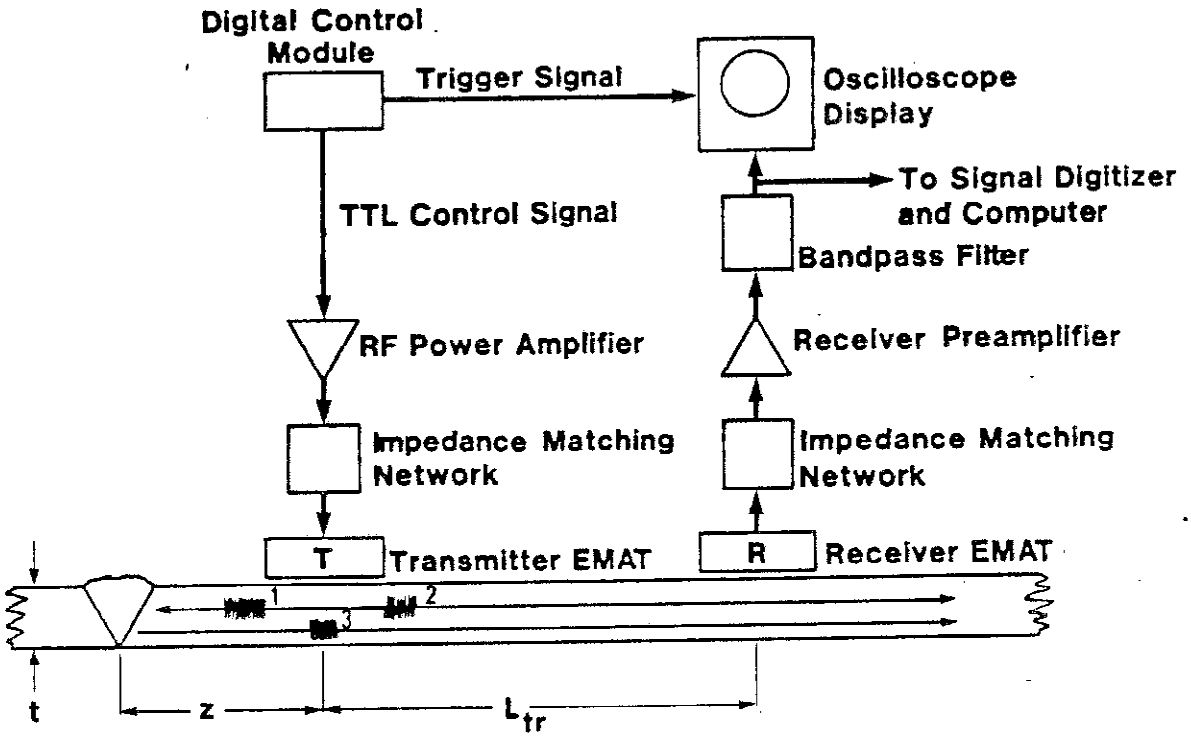

Fig. 35 - Low-frequency, SH-wave EMAT inspection configuration for pipeline girth welds.

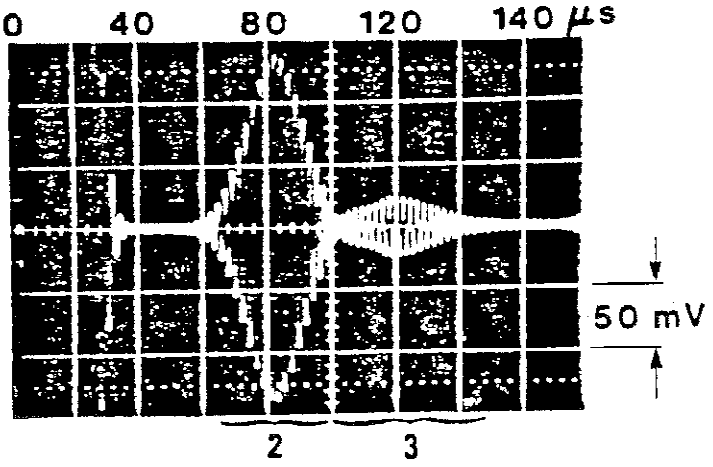

Fig. 36 - Detection of a surface flaw (inadequate penetration) in a 15.9-mm (0.625 in) girth welds using 454-kHz SH waves.

direct electromagnetic interference between the transmitter and receiver EMATs. This signal carries no useful information. The second signal (60-100 μs) is the reference signal 2; the third signal (100-140 μs) is the backscattered signal 3.

It has been determined that the amplitude of the reference signal 2 and the amplitude and shape of the backscattered signal 3 carry useful information about the dimensions, orientation, and position of the flaws within the weld.[39,40] Although it is not possible to reconstruct the shape of the flaw and determine its position and orientation from a single low-frequency ultrasonic measurement (because of poor spatial resolution at low frequencies), it is possible to obtain much useful quantitative information about these parameters from a series of independent measurements along the normal to the girth weld. In particular, by using appropriate signal processing techniques, it is possible to classify the flaws in terms of their position within the weld (i.e., surface vs. interior) and then to estimate their principal dimensions.[39] However, to understand the principles of the ultrasonic data inversion procedures, one first requires a qualitative insight into the physical mechanisms governing the propagation and scattering of low-frequency SH waves in isotropic plates.

3.3 Theory of Horizontally Polarized Plate Wave Propagation

When the frequency of operation is sufficiently low, it is often advantageous to represent the ultrasonic field in an isotropic plate as a modal expansion.[40,55] This representation is also approximately valid when the radius of curvature of the pipes is very large compared with the ultrasonic wavelength and when the observer is located sufficiently far from the transducer. Although clearly limited, the modal representation provides valuable quantitative insights that can be used to optimize the design of low-frequency, SH-wave inspection systems in terms of the important

experimental parameters: plate thickness, frequency of operation, weld-to-EMAT spacing, and the receiver-EMAT-to-transmitter-EMAT spacing.

In an infinite isotropic plate of finite thickness, there are only a finite number of propagating, horizontally polarized plate waves and an infinite number of nonpropagating, horizontally polarized plate waves. Correspondingly, there are a finite number of plate waves polarized in the plane normal to the plate (Lamb waves) that can propagate and an infinite number that are cut off.[58,59] In this report, it is assumed for simplicity that SH-wave signals are not coupled to Lamb waves by elongated weld flaws, whose long dimension is parallel to the SH-wave polarization direction. This assumption is strictly true for two-dimensional geometries and is justified in practice by the inherent insensitivity the of SH-wave EMATs to ultrasonic waves polarized in the plane normal to the plate (Lamb and Rayleigh waves).[60]

In the coordinate system of Fig. 37, the transverse ultrasonic field distributions [particle velocity $v_x^{(n)}$ and stresses $T_{xz}^{(n)}$ and $T_{xy}^{(n)}$] of the n^{th} propagating and nonpropagating SH-wave plate waves are given by:

$$v_x^{(n)}(y) = A_n \cos(n\pi y/t) \tag{78}$$

$$T_{xz}^{(n)}(y) = (-\beta G A_n/\omega) \cos(n\pi y/t) \tag{79}$$

$$T_{xz}^{(n)}(y) = (-n\pi G A_n/tj\omega) \sin n\pi y/t \tag{80}$$

with

$$\beta_n = [(\omega/v_s)^2 - (n\pi/t)^2]^{\frac{1}{2}} \quad \text{for} \quad n = 0, 1, 2, \ldots$$

where: t is the plate thickness, v_s is the bulk shear wave velocity, G is the shear modulus, ω is the angular frequency, $j = \sqrt{-1}$, β_n is the propagation constant, $A_n^2 = j\omega^2/2\beta_y G t \varepsilon_n$, and $\varepsilon_o = 1$ and $\varepsilon_n = \frac{1}{2}$ for $n = 1,2,3,\ldots$

Along the z direction, the fields of the propagating and nonpropagating SH plate waves vary as:

$$v^{(n)}(z,\tau),\ T_{xz}^{(n)},\ \text{and}\ T_{xy}^{(n)}(z,\tau) \sim \exp[-j(\beta_n z + \omega\tau)] \tag{81}$$

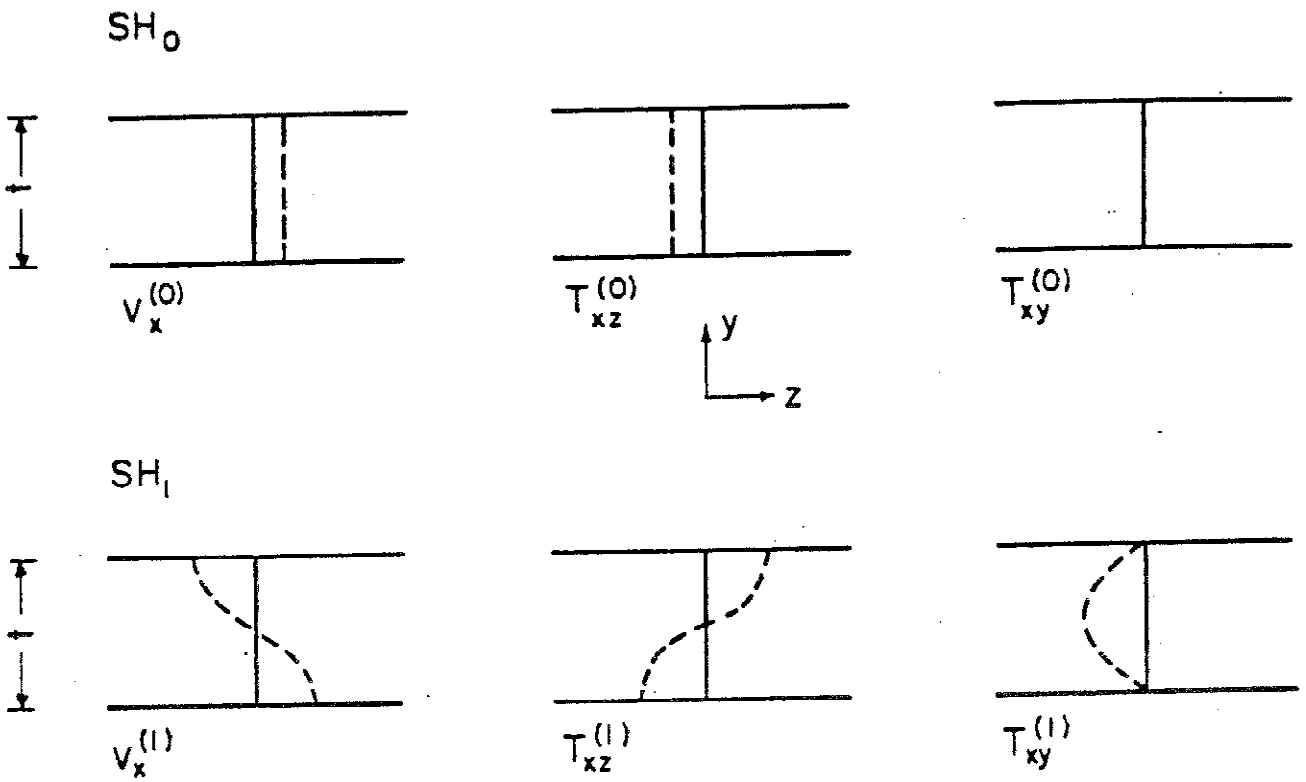

Fig. 37 - Transverse profiles of SH_0 and SH_1 plate waves.

The particle velocity, v_x, and the two stress field components, T_{xz} and T_{xy}, for the two lowest order SH plate waves, the SH_0 and SH_1, are shown in Fig. 37. It is observed that the SH_0 plate wave fields are uniform, but the SH_1 and higher order plate wave fields exhibit sinusoidal variations along the transverse direction, y. The SH_0 plate wave is also unique in that it carries no T_{xz} stress component.

The phase and group velocities, v_p and v_g, of the SH plate waves are given by:

$$v_p^{(n)} = v_s \left[1 - (f_c^{(n)}/f)^2\right]^{-\frac{1}{2}} \tag{82}$$

and

$$v_g v_p = v_s^2 \tag{83}$$

where v_s is the bulk shear-wave velocity, f is the wave frequency and the "cut-off" frequency of an n^{th} SH plate wave is:

$$f_c^{(n)} = nv_s/2t \tag{84}$$

It follows from Eqs. 79 through 84 that each SH plate wave not only exhibits a different variation along the transverse direction, y, but also travels at a different velocity along the direction z. This observation is the basis for the quantitative procedures for flaw characterization and dimensioning from the ultrasonic scattering data obtained using the inspection system and experimental procedures described in the preceding section.

In this report, it is assumed implicitly that both the transmitter and receiver EMATs can only generate and receive the SH_0 and SH_1 plate waves with relative amplitudes of 1 to 1.6.[40] Although the SH_2, SH_3, and SH_4 plate waves can also propagate in a 15.9-mm (0.625-in) thick plate at 454 kHz, they cannot be detected or generated efficiently by the EMATs. Neverthless, their effect must be included in any calculation of the ultrasonic scattering by the flaws.[40]

3.4 Theory of Scattering of Horizontally Polarized Shear Waves by Elongated Flaws

To gain a physical understanding of the scattering of SH plate waves by flaws, it is useful to use the concept of a reflection coefficient, Γ. Here, Γ is defined as the ratio of the amplitudes of the incident and backscattered ultrasonic signals at the EMAT electrical terminals. For the two-dimensional case (no variations in $\vec{v}$ and $\overleftrightarrow{T}$ along x and flaws of infinite length), a very useful relationship for Γ has been derived by Auld.[60]

$$\Gamma = [4(P_1P_2)]^{-\frac{1}{2}} \int_{S_F} (\vec{v}_1 \cdot \overleftrightarrow{T}_2 - \vec{v}_2 \cdot \overleftrightarrow{T}_1) \cdot \hat{n}\, dS \tag{85}$$

where $\hat{n}$ is the inward-directed unit-normal to the incremental surface, dS, and integration is performed over the flaw surface, S_F. Subscript 1 is used to denote the ultrasonic field in the absence of the flaw, and subscript 2 is used to denote the ultrasonic field in the presence of the flaw, assuming that EMATs 1 and 2 in Fig. 34 are used as transmitters. P_1 and P_2 are the electrical power levels delivered to EMATs 1 and 2, respectively, when they are used as transmitters.

Equation 83 can be used to gain valuable insights. Consider the case of a two-dimensional, planar flaw shown in Fig. 38. In this case, Eq. 83 reduces to:

$$\Gamma = j\omega/4(P_1P_2)^{\frac{1}{2}} \int_{\frac{1}{2}S_F} (\Delta u_1 \cdot T_2) \cdot \hat{n}\, dS \tag{86}$$

where Δu is the mode-III displacement jump across the face of the planar flaw and the integration is carried over only one-half of the surface, S_F.

In general, because several SH plate waves can propagate in a practical situation, the reflection coefficient Γ can be rewritten as:

$$\Gamma(z,L_{tr}) = j\omega/4(P_1P_1)^{\frac{1}{2}} \sum_{n=0}^{\infty}\sum_{m=0}^{\infty} \exp(-j\beta_n z)\, a_n \Gamma_{nm} b_m \exp[-j\beta_m(z+L_{tr})] \tag{87}$$

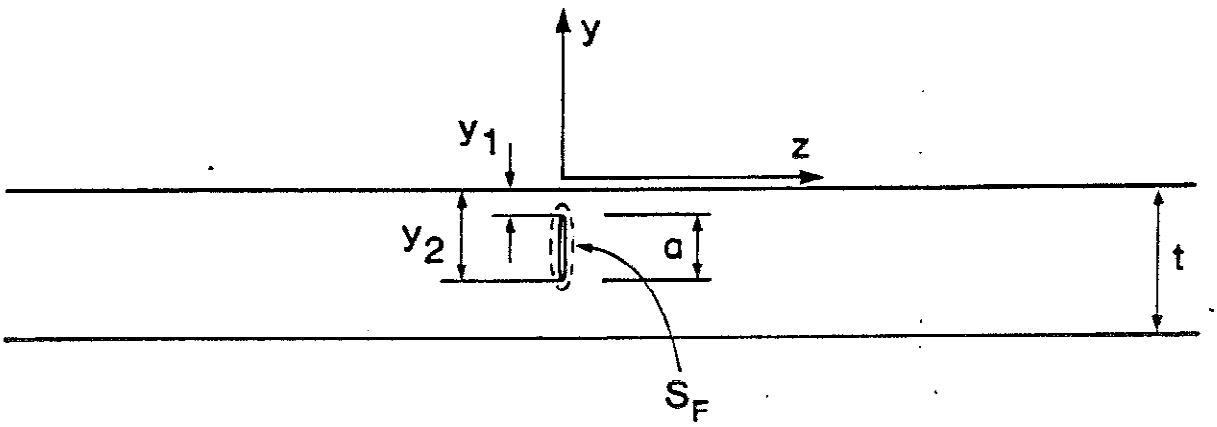

Fig. 38 - Planar flaw geometry.

where z is the distance between flaw and EMAT, L_{tr} is the distance between EMATs, and the quantity Γ_{nm} is defined as:

$$\Gamma_{nm} = \int_{S_F} (\vec{\Delta u}^{(n)} \cdot \vec{\overleftrightarrow{T}}^{(m)}) \cdot \hat{n} \, dS \quad . \tag{88}$$

the quantities a_n and b_m express the relative transduction efficiencies of the different SH plate waves by the EMATs 1 and 2, respectively, and $\overleftrightarrow{T}^{(m)}$ is the stress component T_{xz} associated with the m^{th} plate mode.

In practice, and as described in a preceding section, the ultrasonic scattering data (signal 3 in Fig. 35) is normalized using a reference signal (signal 2 in Fig. 35). This normalized signal, called the reflected signal amplitude ratio, R_s, is given by:

$$R_s(z,L_{tr}) = \frac{-j \sum_{n=0}^{\infty} \sum_{m=0}^{\infty} \exp(-j\beta_n z)\, a_n \Gamma_{nm} b_m \exp[-j\beta_m (z + L_{tr})]}{2\mu t \sum_{\ell=0}^{\infty} a_\ell b_\ell \exp(-j\beta_\ell L_{tr})} \tag{89}$$

If the quantities a_n, b_m, z, and L_{tr} are known and $R_s(z,L_{tr})$ can be measured at a sufficient member of points, the unknown coefficients, Γ_{nm}, can be found from Eq. 89. Equation 89 can be inverted if a_n and b_m vanish for n or $m \geq N = M$. In general, N x N independent measurements are then needed but this number can be reduced by taking into account the symmetry of the matrix Γ_{mn}. Thus, if only the SH_0 and SH_1 plate waves are generated and detected by the EMATs (although more SH plate waves can propagate), only three independent measurements are needed. If signals carried by the SH_0, SH_1, and SH_2 plate waves are detected, then only six independent measurements are required. In practice, more measurements are available, but the size of the Γ_{mn} matrix is determined by the number of SH plate waves that can be generated and detected by the EMATs. The larger the number N, the more information is available for flaw characterization and dimensioning.

Although a detailed treatment of the dependence of the coefficients Γ_{nm} on flaw size, shape, orientation, and position parameters is beyond the scope of this report, it is instructive to consider several cases of practical importance. For a more detailed treatment, the reader should consult Refs. 37, 38, 55-57, 61, and 62.

The magnitudes and phases of the coefficients can be obtained using numerical methods for the vertically oriented surface and interior planar flaws of infinite length.[40] The case of canted, planar flaws is treated in Refs. 40 and 57.

The numerical results for the coefficient Γ_{00} for three different flaw types are shown in Fig. 39 as a function of the flaw through-wall depth, a. To illustrate the dependence of Γ_{00} on the relative position of the flaw within a plate, the numerical calculations were carried out for edge (surface-connected), centered (buried) cracks, and eccentric (buried) cracks. The calculations were carried out for a case of current practical interest (wavelength, λ, = 7.4 mm, 0.29 in; plate thickness, t, = 15.9 mm, 0.625 in).

It is interesting to compare the results for the relatively shallow ($a < \lambda/2$) surface and buried cracks. It is observed that Γ_{00} for the shallow crack case initially exhibits a greater rate of increase than that for a shallow buried crack of the same through-wall depth. However, at $a \sim \lambda/3$ for the surface crack and $a \sim \lambda/2$ for the buried cracks, the rate of increase with a/t is substantially less, and both coefficients tend linearly to 1. Although the rate of increase of Γ_{00} for a shallow buried crack is initially less than that for a shallow surface crack, for $a > \lambda/2$, the results converge asymptotically. As will be seen later, the initial behavior of the coefficients determines the detectability thresholds of surface and buried flaws.

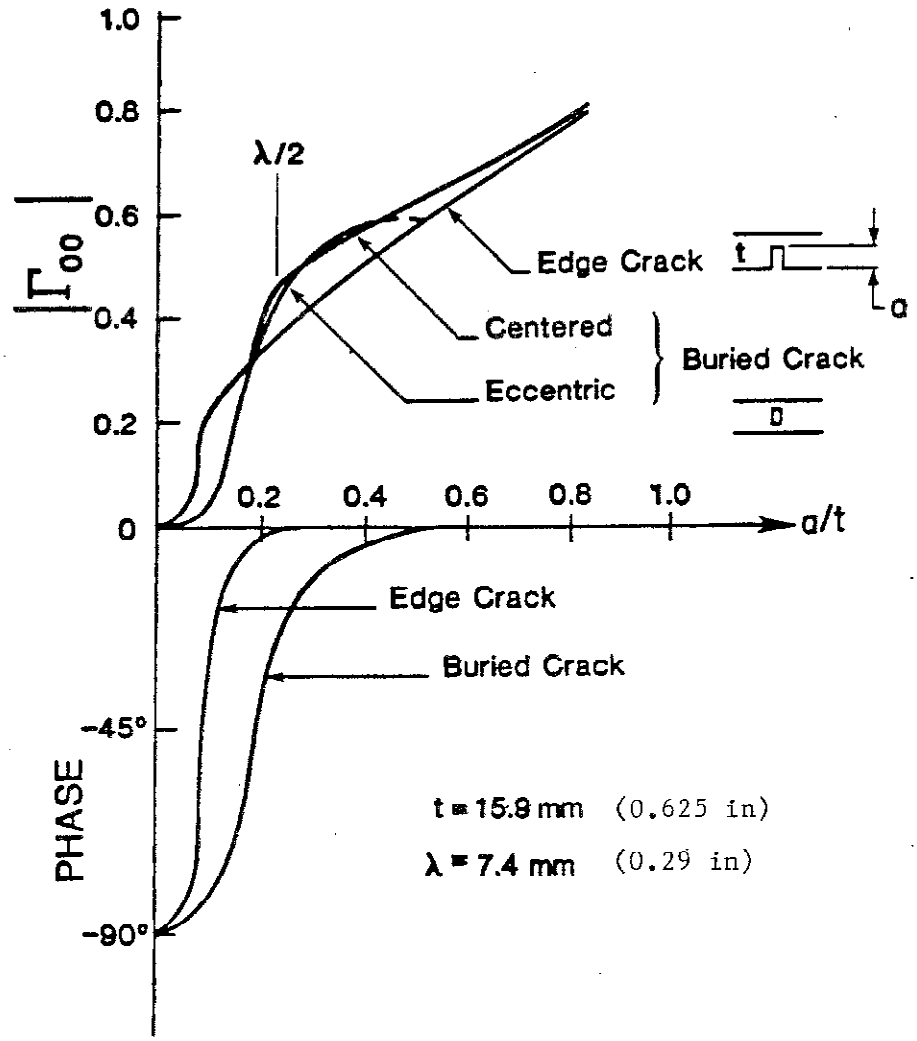

Fig. 39 - Numerical results for the SH-wave plate mode scattering coefficient, Γ_{00}.

It is also interesting to compare the behavior of Γ_{00} with that of $\Gamma_{01} = \Gamma_{10}$ and Γ_{11}. The numerical results for Γ_{01} and Γ_{11} are shown in Figs. 40 and 41. For relatively shallow, vertically oriented, surface cracks ($a << \lambda/4$) the magnitudes of the four scattering coefficients Γ_{00}, Γ_{01}, Γ_{10}, and Γ_{11} are approximately equal. However, as the crack through-thickness dimension, a, is increased, Γ_{00} and Γ_{11} approach unity monotonically, but Γ_{10} and Γ_{01} reach a maximum at $a/t \sim 0.5$ and vanish for $a/t = 1$. In addition, the signs of the coefficients Γ_{01} and Γ_{10} depend on which side of the plate contains the flaw. In contrast, the signs of Γ_{00} and Γ_{11} are always positive. These features can be used to classify flaws with respect to their relative position within the plate.

A comparison of the numerical results for buried, centered, and eccentric flaws shows that the magnitudes of Γ_{01}, Γ_{10}, and Γ_{11} are not significant when $a < \lambda/2$. By symmetry, $\Gamma_{01} = \Gamma_{10} = 0$ for buried, centered cracks. Furthermore, the phases of Γ_{00}, Γ_{10}, Γ_{01}, and Γ_{11} are -90° for very small through-thickness dimensions and approach 0° for deeper cracks. Note that the phases for buried and surface cracks approach 0° more rapidly.

An analysis of the above results indicates that significant results about the flaw characteristics and through-thickness dimensions can be obtained from the knowledge of the scattering coefficients, Γ_{nm}.

3.5 Experimental Verification

Although the main conclusions have been made on the basis of two-dimensional modeling, they have been found to be in very close agreement with experiments conducted on flaws of finite length and calibration standards. Thus, it can be expected that the general results outlined above can be used as a basis for rational inversion procedures for estimating flaw parameters from the available ultrasonic data. Because the magnitude and

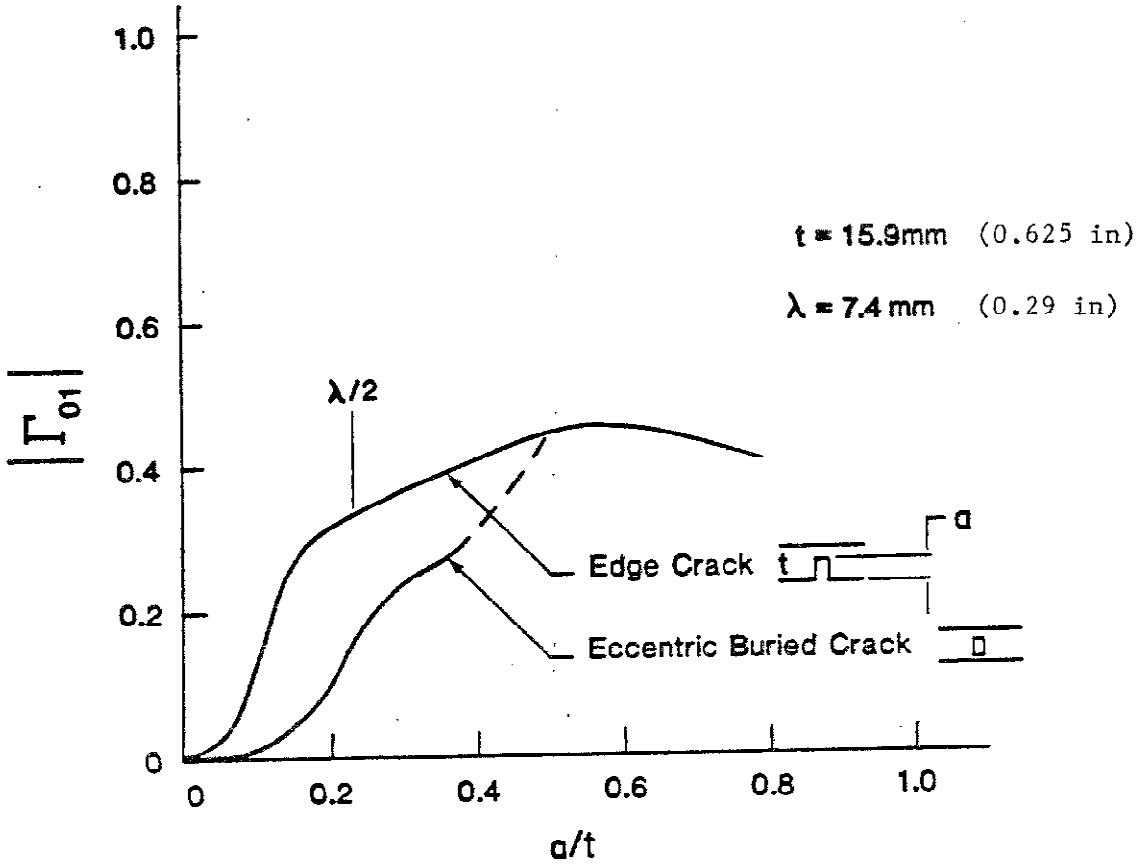

Fig. 40 - Numerical results for the SH-wave plate mode scattering coefficient, Γ_{01}.

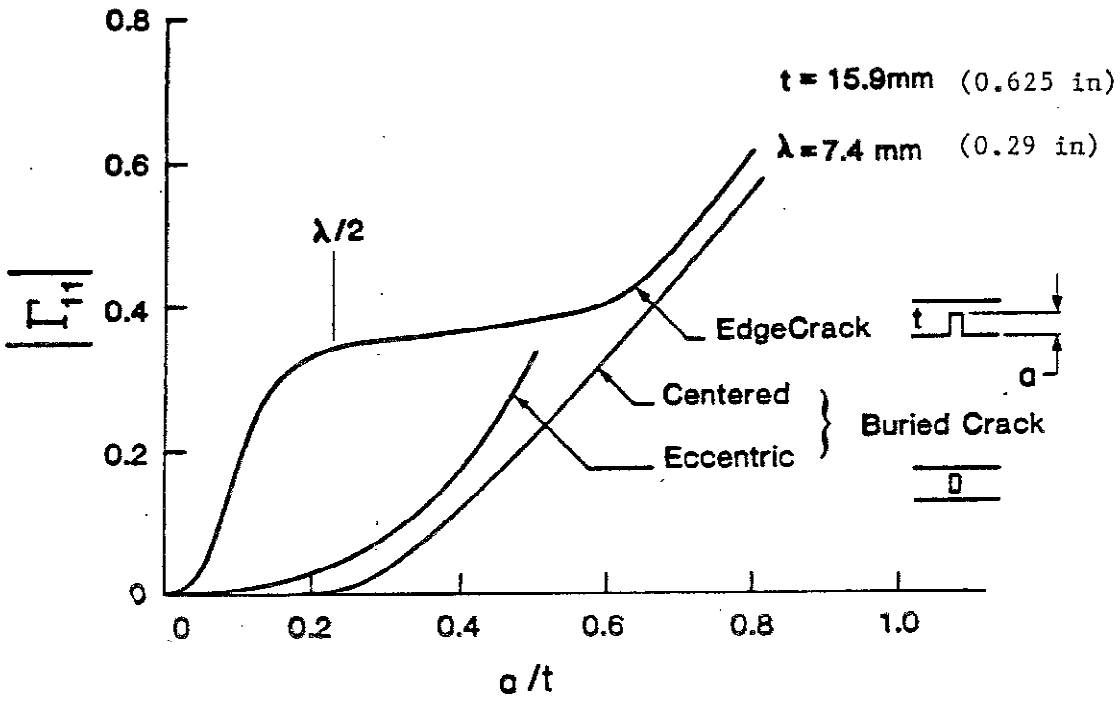

Fig. 41 - Numerical results for the SH-wave plate mode scattering coefficient, Γ_{11}.

phase of the scattered signals depend strongly on the position of the flaw within a plate, classification of flaws with respect to position must be performed first to select the appropriate set of sizing curves.

The theory of Eq. 83 has been directly compared with experimental results. Figure 42 shows a comparison of experimental results for surface notches in flaw-plate calibration specimens with a calculated response, using $a_0 = b_0 = 1$, $a_1 = b_1 = 1.6$, $z = 50$ mm (2.0 in), $L_{tr} = 210$ mm (8.27 in), $f = 454$ kHz, and $t = 15.9$ mm (0.625 in). A slight correction for the effects of two-dimensional diffraction was made. Measurements were taken from the left ("triangles") and right ("squares") of the simulated flaws. It is seen that the experimental data adhere very closely to the calculated curve. Similar results were obtained for other classes of flaws.[63,64]

3.6 Detectability Limitations: Long Flaws

In practice, the detectability of particular flaw types in a girth weld is not determined by ultrasonic-signal-to-electronic-noise considerations. Instead, the detectability limitations are determined primarily by: 1) flaw reflectivity as a function of flaw type, size, position, and orientation and 2) the presence of an ultrasonic background caused by transducer sidelobe radiation and surface irregularities. The ultrasonic background level caused by transducer sidelobe radiation can be reduced by using proper EMAT design techniques. However, the ultrasonic background level caused by topographical irregularities, for example, weld reinforcement, alignment mismatch ("high-low"), and "drop through," cannot be eliminated because, at low ultrasonic frequencies, it is not possible to resolve the flaw signals from the unwanted ultrasonic interferences.

The scattering of SH plate waves by certain surface irregularities (e.g., weld reinforcement and alignment mismatch) can be modeled analytically, but

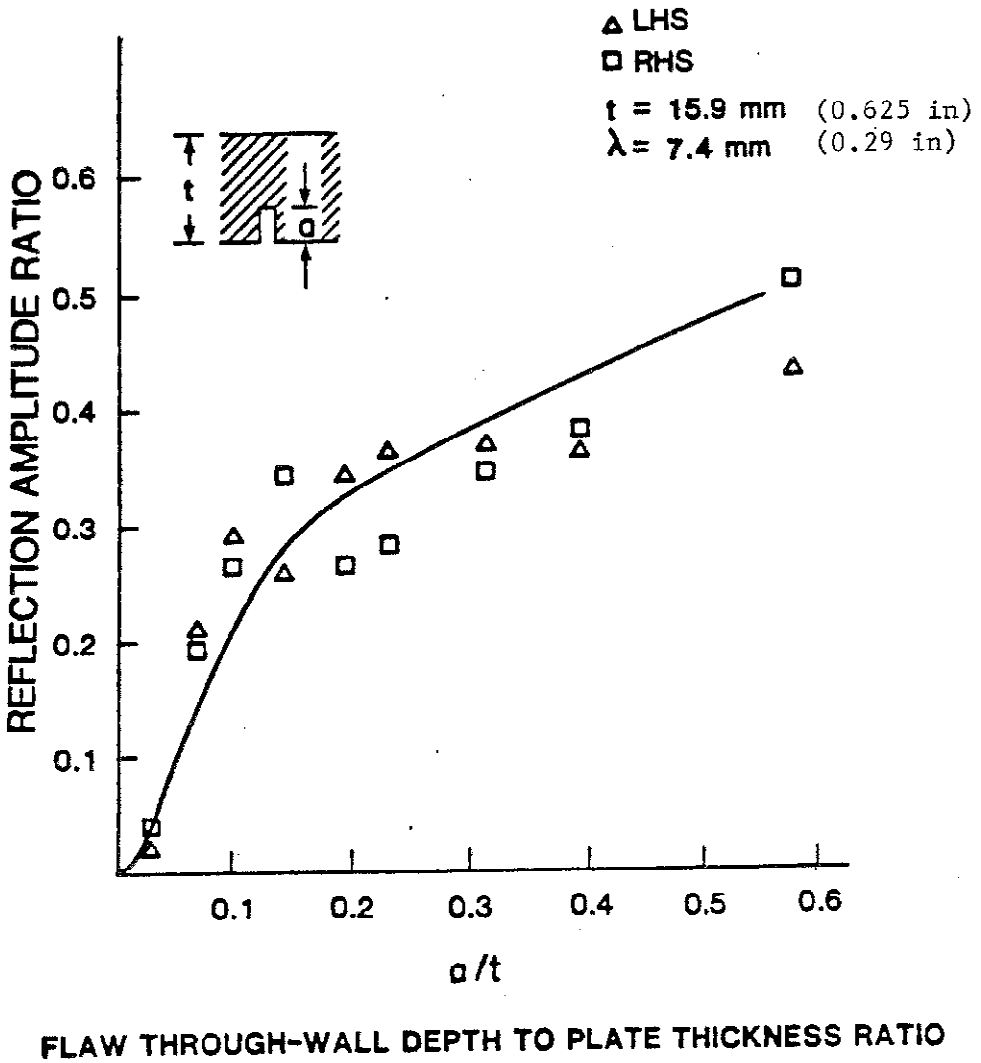

Fig. 42 - Comparison of experimental and theoretical results for vertically oriented surface slots (flat-plate specimens 12-24).

ultimately the results of such calculations must be verified experimentally. Here, a combined analytical-experimental approach is used to determine the principal factors limiting the sensitivity of the SH-wave EMAT system. For simplicity, the analysis is limited to the case of two-dimensional scatterers. Physically, this means that only flaws and surface irregularities longer than the transverse resolution width are considered. (Detectability of sharp flaws shorter than the ultrasonic beam width is discussed in Section 3.7).

To determine the reflectivities of very long, buried and surface flaws, a number of flat-plate calibration specimens were prepared. The specimens were made using 15.9-mm (0.625-in) thick pipeline steel (API-5LX-70) sections that were 1220-mm (48.0-in) long and 120-mm (4.7-in) wide. To permit a systematic study of the effects of flaw position and orientation within a weld, four different categories of artificial flaws were used: 1) thin surface slots, 2) centered, buried slots, 3) off-center, buried vertical slots, and 4) off-center, canted slots. The surface and off-center slots were designed to simulate actual weld flaws (incomplete fusion, inadequate penetration, and cracks) in shielded-metal-arc (SMA) girth welds. The width of the slots was intentionally held below 0.4 mm (0.016 in), which is substantially less than the bulk shear wave wavelength (7.4 mm, 0.29 in) at 454 kHz, the inspection frequency). The artificial flaw dimensions are summarized in Table 5, and the characteristic flaw dimensions, A, B, and C, are defined in Fig. 43.

The buried artificial flaws were made by filling the "V-grooves" in Fig. 43 using a combined tungsten-inert-gas (GTAW), gas-metal-arc (GMA) welding procedure. To simulate the effect of weld reinforcement, alignment mismatch ("high-low") and "drop through," additional flat-plate specimens were prepared. The maximum dimension for the three surface irregularities was 3.2 mm (0.126 in).

Table 5 — Artificial Flaw Dimensions

Specimen No.	A, mm	A, in	B, mm	B, in	C, mm	C, in	Type of Slot
1	6.37	0.251	1.58	0.0622			
2	5.88	0.231	2.15	0.0846			Off-center
3	5.38	0.212	1.95	0.0768			vertical
4	4.88	0.192	2.15	0.0846			slots
5	3.62	0.143	3.12	0.123			(buried)
6	2.38	0.094	4.22	0.166			
7	0	0	5.48	0.216			
8	6.88	0.271	0.76	0.030			Centered
9	6.58	0.259	2.50	0.098			vertical
10	5.5	0.22	3.9	0.15			slots
11	3.62	0.143	7.45	0.293			(buried)
12	0		0.50	0.020			
13	0		0.75	0.030			
14	0		1.03	0.041			
15	0		1.1	0.043			
16	0		1.5	0.059			Vertical
17	0		1.75	0.069			edge
18	0		2.18	0.086			slots
19	0		2.50	0.098			
20	0		3.18	0.125			
21	0		3.78	0.149			
22	0		5.2	0.20			
23	0		6.33	0.249			
24	0		7.47	0.294			
25	Full penetration weld (no defect)						
26	6.07	0.239	0.97	0.083	0.75	0.030	Off-center
27	5.2	0.20	2.55	0.100	2.15	0.085	canted
28	3.33	0.131	5.07	0.200	4.3	0.17	slots

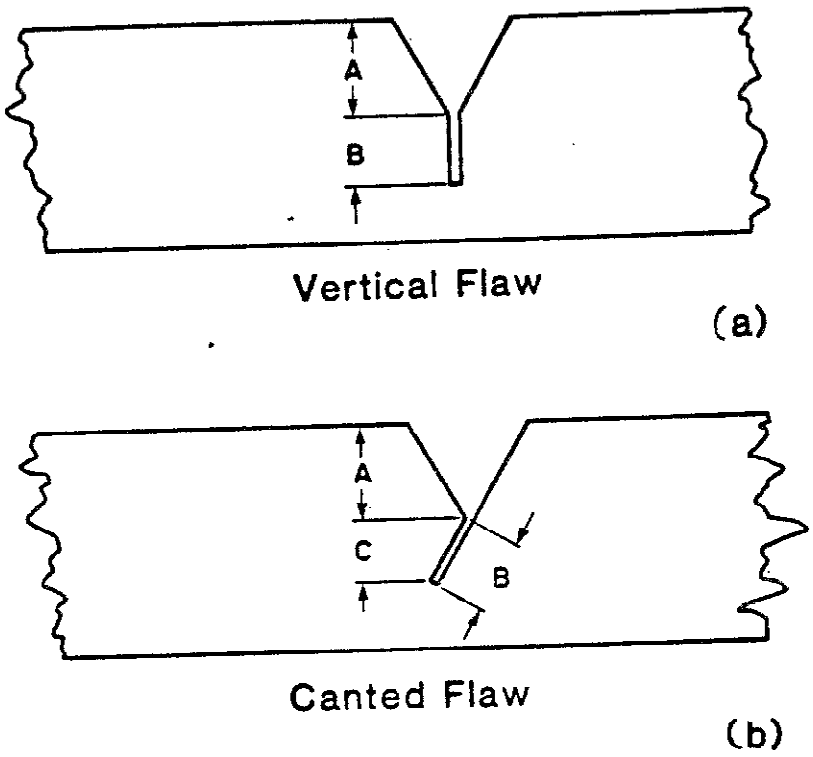

Fig. 43 - Geometry of vertical slot (a) and canted slot (b) calibration specimens. The slot dimensions are summarized in Table 5.

An examination of Eq. 89 shows that the reflection amplitude ratio, R_s, is strongly dependent on the flaw-to-EMAT spacing, z, and on the EMAT-to-EMAT spacing, L_{tr}. A similar result can be obtained for the reflection amplitude ratios of the three topographical irregularities: weld reinforcement, alignment mismatch ("high-low"), and "drop through." For example, in the case of weld reinforcement, the reflection amplitude ratio can be determined from:

$$R_s = \frac{j\beta_0^2 W_w T_w \sum_{n=0}^{\infty} \sum_{m=0}^{\infty} a_n \exp(-j\beta_n z) \Lambda_{nm} b_m \exp[-j\beta_m (z + L_{tr})]}{2t \sum_{\ell=0}^{\infty} a_\ell b_\ell \exp(-j\beta_\ell L_{tr})} \qquad (90)$$

with

$$\Lambda_{nm} = \frac{\sin(\beta_n + \beta_m) W_w/2}{(\beta_n + \beta_m) W_w/2} \left(\beta_n \beta_m \varepsilon_n \varepsilon_m\right)^{\frac{1}{2}} \qquad (91)$$

where W_w and T_w represent the mean width and thickness of the weld reinforcement.

Assuming typical values of W_w = 20 mm (0.79 in), T_w = 1.6 mm (0.063 in), $a_0 = b_0 = 1$, $a_1 = b_1 = 1.6$, and $a_n = b_m = 0$ for $n \geq 2$, it can be shown that the value of R_s does not exceed 0.12 when t = 15.9 mm (0.625 in) and f = 454 kHz.[40] The above estimate has been verified experimentally using actual girth welds and flat-plate calibration specimens.

Figure 44 shows the variation of the amplitude reflection ratio as a function of the distance, z (with L_{tr} = 210 mm, 8.27 in), obtained using a 15.9-mm (0.625-in) thick flat-plate calibration specimen designed to simulate a SMA weld reinforcement. It is apparent that the background signal ratio associated with the simulated weld reinforcement does not exceed 1.2, in excellent agreement with the theory of Eq. 90. This observation is very significant, since the presence of the weld reinforcement is one of the principal factors in determining the ultimate sensitivity of this inspection system.

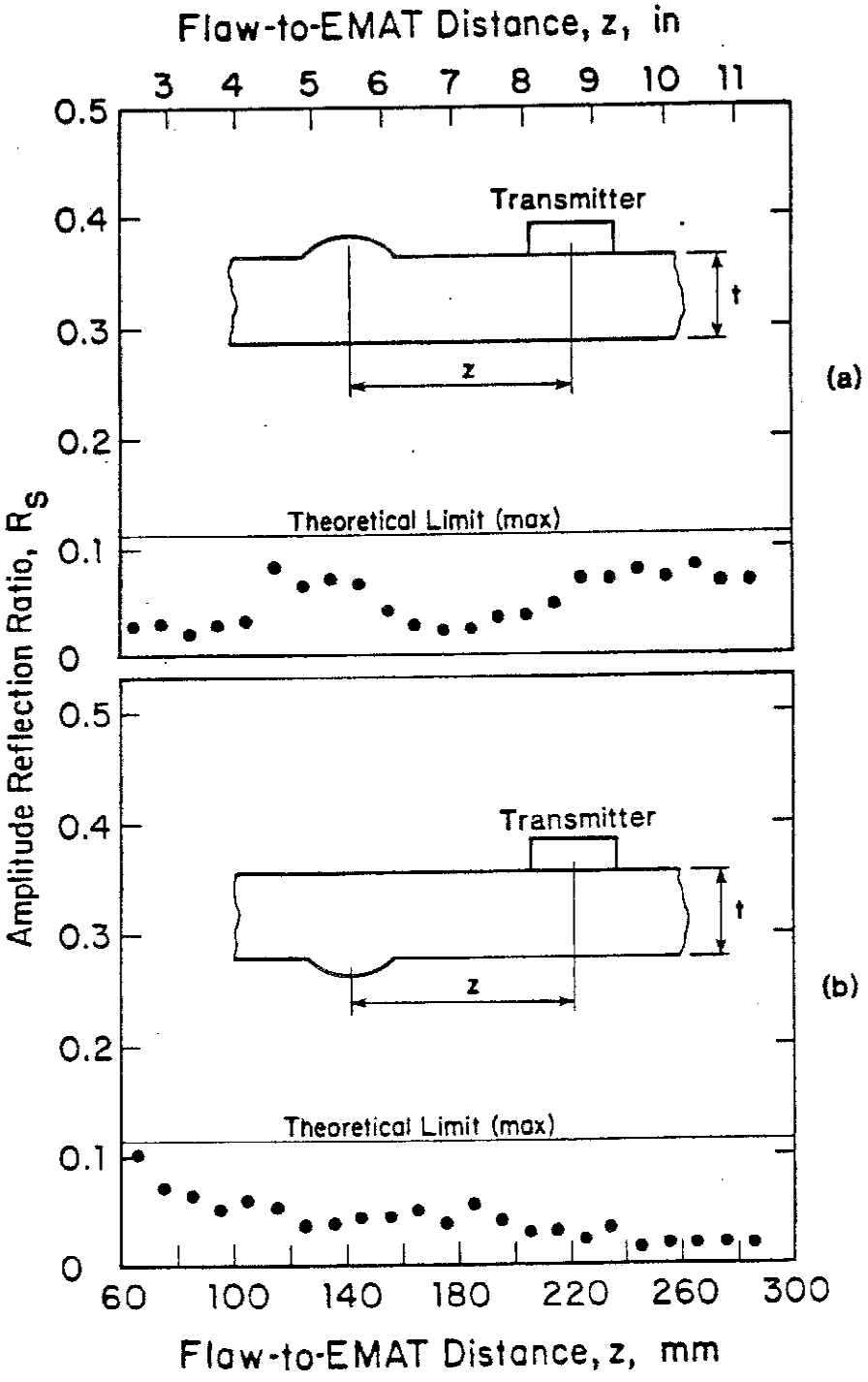

Fig. 44 - Detection of simulated weld reinforcement as a function of the transmitter-EMAT-to-weld-distance, z. L_{tr} = 210 mm (8.27 in).

If vertically polarized plate waves (Lamb waves) were used to probe the weld, the reflected amplitude ratio associated with the weld reinforcement would be significantly larger.[63,65] Physically, this is related to the fact that Lamb waves in a thick plate, which can support several propagating plate modes, are tightly bound to the surfaces and do not exhibit large displacements in the interior of a plate.[59] In contrast, the SH_0 plate wave displacements are uniform and the SH_1, plate wave displacements exhibit only one null at the midplane of the plate (see Fig. 37).

Significant levels of ultrasonic background signals can also be caused by the presence of an alignment mismatch condition ("high-low") and "drop through" (at weld root). Figure 45 shows the measured values of the reflection amplitude ratio, R_s, at 454 kHz as a function of the distance, z, with L_{tr} = 210 mm (8.27 in) and t = 1.59 mm (0.063 in) for a 3-mm (0.12-in) alignment mismatch and a 3.2-mm (0.13-in) bead at the weld root. It is seen in Fig. 45 that the presence of a 2.8-mm (0.11-in) alignment mismatch condition causes a background signal level that is at least twice as large as that for a weld reinforcement or root bead of comparable thickness. For comparison, a plot of the coefficient R_s as a function of z is shown in Fig. 46 for a vertical surface slot 1.5-mm (0.059-in) deep and 100-mm (3.94-in) long.

An analysis using Eq. 89 in conjunction with calculated values of Γ_{00}, Γ_{01}, Γ_{10}, and Γ_{11} shows that buried sharp flaws scatter less efficiently than surface sharp flaws of the same through-wall depth. Physically, this is caused by the fact that shallow surface flaws exhibit a larger mode III displacement jump (in Eq. 86) than buried flaws. This can be verified by using elastostatic expressions for Δu_x in Eq. 88, which are valid when the ultrasonic wavelength is significantly longer than the flaw through-wall dimension a.[41] In addition, shallow flaws lying near the midplane of the plate cannot efficiently scatter the SH plate waves and convert the SH_1 plate waves to SH_0 plate waves, and vice versa. This can also be verified directly

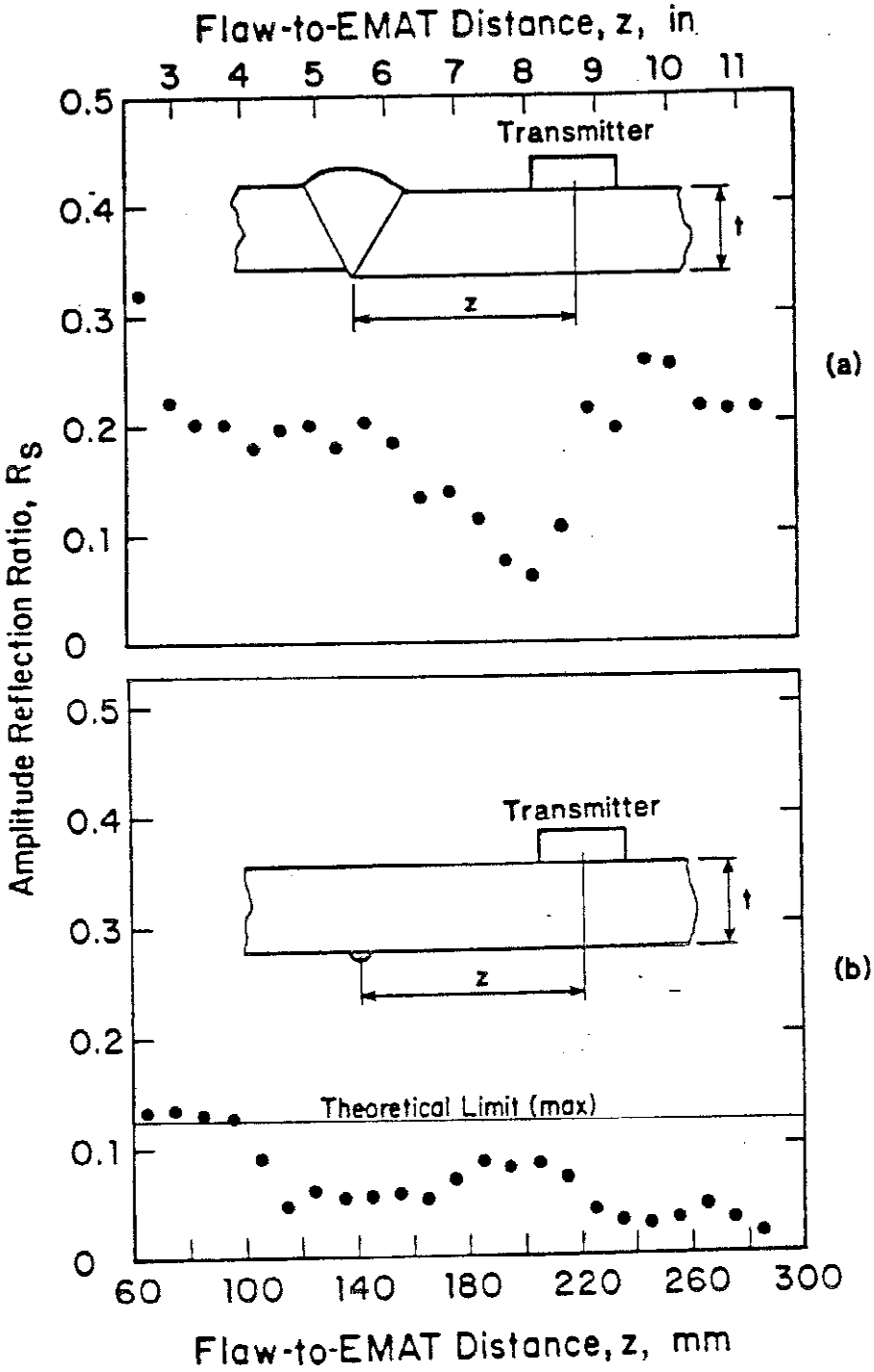

Fig. 45 - Detection of simulated 3-mm (0.1-in) alignment mismatch (a) and "drop through" (b) as a function of the transmitter-EMAT-to-weld-distance, z. L_{tr} = 210 mm (8.27 in).

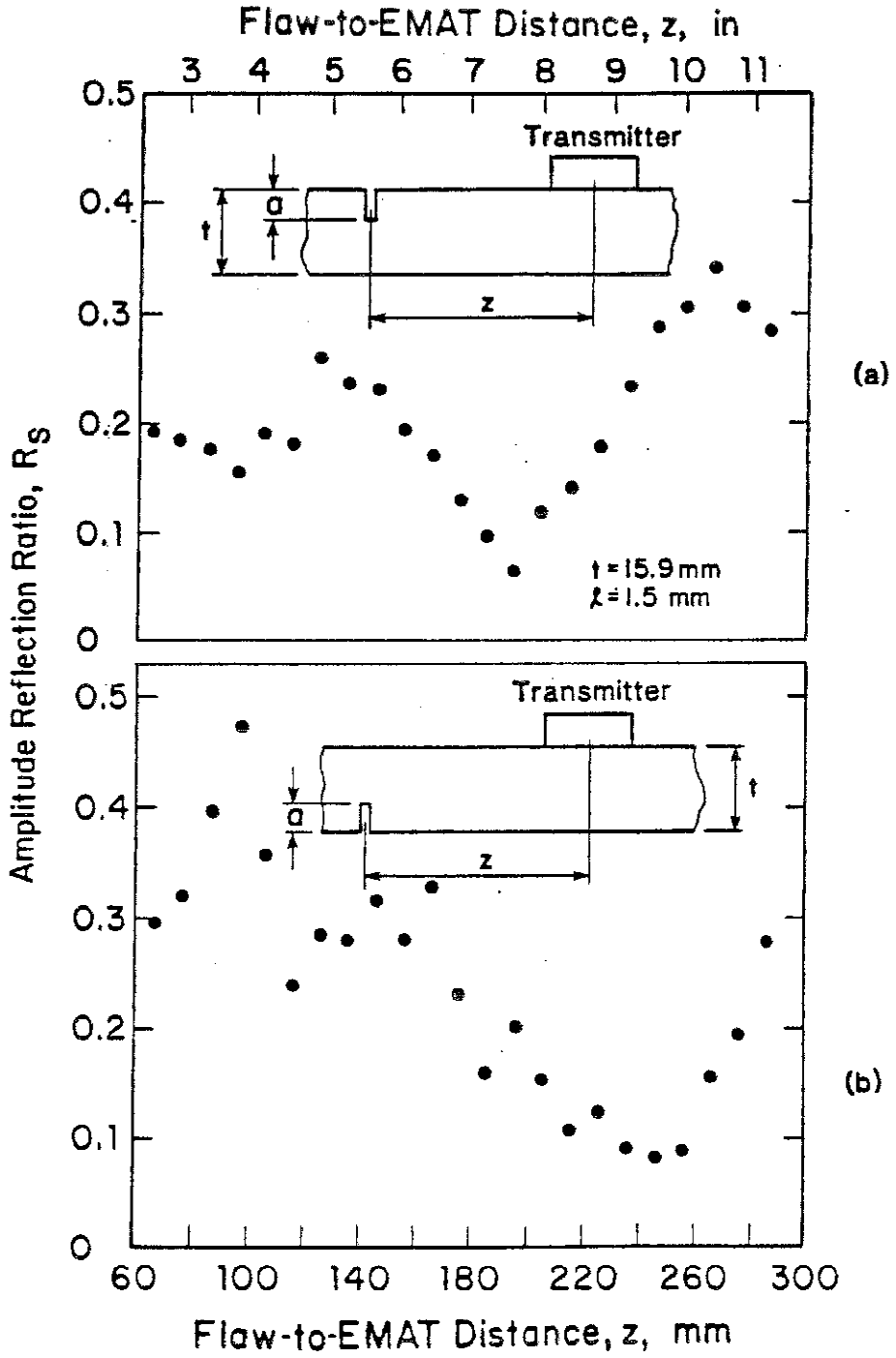

(0.059-in)

Fig. 46 - Detection of a 1.5-mm deep surface slot as a function of the transmitter-EMAT-to-weld distance, z. (a) Slot in top surface of plate. (b) Slot in bottom surface of plate. L_{tr} = 210 mm (8.27 in). Flat-plate specimen 16.

by noting that Γ_{01}, Γ_{10}, and Γ_{11} in Figs. 39 through 41 are negligible for such flaws. As a result, shallow buried flaws are generally more difficult to detect than surface flaws of similar dimensions.

It follows from Eqs. 89 and 90 and from the experimental data shown in Figs. 44 and 45 that the relative amplitudes and phases of the flaw and background ultrasonic signals are characteristically determined by the distances z and L_{tr} and by parameters describing the surface irregularity and the sources of the ultrasonic background. As a consequence, a particular selection of z and L_{tr} can result in significantly higher sensitivity to certain categories of flaws. For example, for certain EMAT-to-weld separation distances, significantly stronger reflections are obtained from flaws located near the root of the weld than from flaws located in other parts of the weld.[40] As a result, in this particular configuration, flaws lying near the root of the weld may be easier to detect than flaws located in other parts of the weld. However, this difficulty can be corrected by devising a detection algorithm that utilizes ultrasonic data from different EMAT positions. In this way, a more uniform interrogation of the entire weld can be ensured. (The additional data are also needed for flaw characterization purposes.)

Equation 89 can be used to study the behavior of the flaw reflection signal as a function of the flaw position within the weld and the EMAT-to-EMAT and EMAT-to-weld separation distances, L_{tr} and z. For simplicity, it can be assumed that the EMATs can only generate and receive signals carried by the SH_0 and SH_1 plate waves. This simplification is justified by the fact that the relative amplitudes (a_0 and a_1) of the two plate waves are 1 and 1.6, respectively.[40] The relative amplitude of the SH_2 plate wave (a_2) is approximately 0.3.[40,64]

To emphasize the influence of flaw position within the weld on the behavior of the flaw amplitude reflection ratio as a function of the separation parameters, z and L_{tr}, it is convenient to fix the value of L_{tr} such that $\beta_0 L_{tr} = \beta_1 L_{tr}$. This corresponds to the actual selection of the EMAT-to-EMAT spacing in the present experimental setup. Furthermore, it is convenient to assume that only three categories of sharp flaws need be considered: 1) surface flaws located near the top surface, 2) interior flaws located near the midplane, and 3) surface flaws located near the bottom surface of the weldment. The bottom surface corresponds to the surface opposite to the surface on which both EMATs are located.

Assuming that the surface flaws, which must be detected, are very shallow, it can be shown that the magnitudes of the scattering coefficients in Eq. 89 (Γ_{00}, Γ_{11}, Γ_{01}, and Γ_{10}) are approximately equal.[40] However, the phases of the four coefficients are determined by which surface contains the flaw. If the flaw is located near the top surface, then the phases of Γ_{00}, Γ_{01}, Γ_{10}, and Γ_{11} are identically equal. However, if the flaw is located on the bottom surface, then the phases of Γ_{01} and Γ_{11} are equal and opposite to the phases of Γ_{01} and Γ_{10}. Finally, if the flaw is located near the midplane of the weldment, then Γ_{01}, Γ_{10}, and Γ_{11} either vanish or are negligibly small, and only Γ_{00} contributes strongly to the reflected signal.

The double summation in Eq. 89 can be evaluated graphically using a vector-diagram (phasor) representation. For simplicity, it is assumed here that the magnitudes of the four scattering coefficients (Γ_{00} Γ_{01}, Γ_{10}, and Γ_{11}) are unity for the three categories of flaws. (This can be readily shown to hold in the elastostatic limit, which is valid when the flaw through-wall depth is a fraction of the ultrasonic wavelength, by using the linear elasticity solutions for Δu_x to evaluate Eq. 88.)[66] Then, the amplitudes of

the vectors (phasors) are determined by the SH plate wave amplitudes, a_n and b_n, and the relative phases are determined by the differences between the SH plate wave propagation constants, β_n, and the EMAT-to-weld distance, z.

Figure 47 shows the evolution of the reflected signal amplitude for the three representative flaw categories as a function of the EMAT-to-weld distance, z. The vector diagrams for the case of surface flaws can be compared directly with the experimental results for surface slots shown in Fig. 46. For convenience, the vector diagrams are evaluated at six characteristic locations: 1) $z = 0$, 2) $z = \pi/2(\beta_0 - \beta_1)$, 3) $z = \pi/(\beta_0 - \beta_1)$, 4) $z = 3\pi/2(\beta_0 - \beta_1)$, 5) $z = 2\pi/(\beta_0 - \beta_1)$, and 6) $z = 5\pi/2(\beta_0 - \beta_1)$. Physically, the above locations correspond to the following flaw-to-EMAT distances in Fig. 46: 0, 60 mm, 120 mm, 180 mm, 240 mm, and 300 mm (0, 2.36, 4.72, 7.09, 9.45, and 11.8 in). The vector diagrams are arranged vertically in the figure, such that the column on the extreme left corresponds to surface slots at the top surface, the center column corresponds to buried slots at the middle, and the column on the right corresponds to surface slots at the bottom surface.

In Fig. 47, the vectors corresponding to the four terms involved in evaluating the summation in Eq. 89 are represented by continuous lines. The resultant, corresponding to the actually observed signal amplitude, is represented by dotted lines.

A comparison of results shown in Fig. 47 with the experimental data in Fig. 46 show good quantitative agreement, except at $z = 120$ mm (4.72 in)for the case of the surface slot in the top surface of the calibration specimen. The discrepancy at $z = 120$ mm (4.72 in) is attributed to the effect of signals carried by the SH_2 plate wave, which has been excluded from the analysis. Similar results have been obtained for other calibration specimens, and the effect was observed for weld flaws.[40]

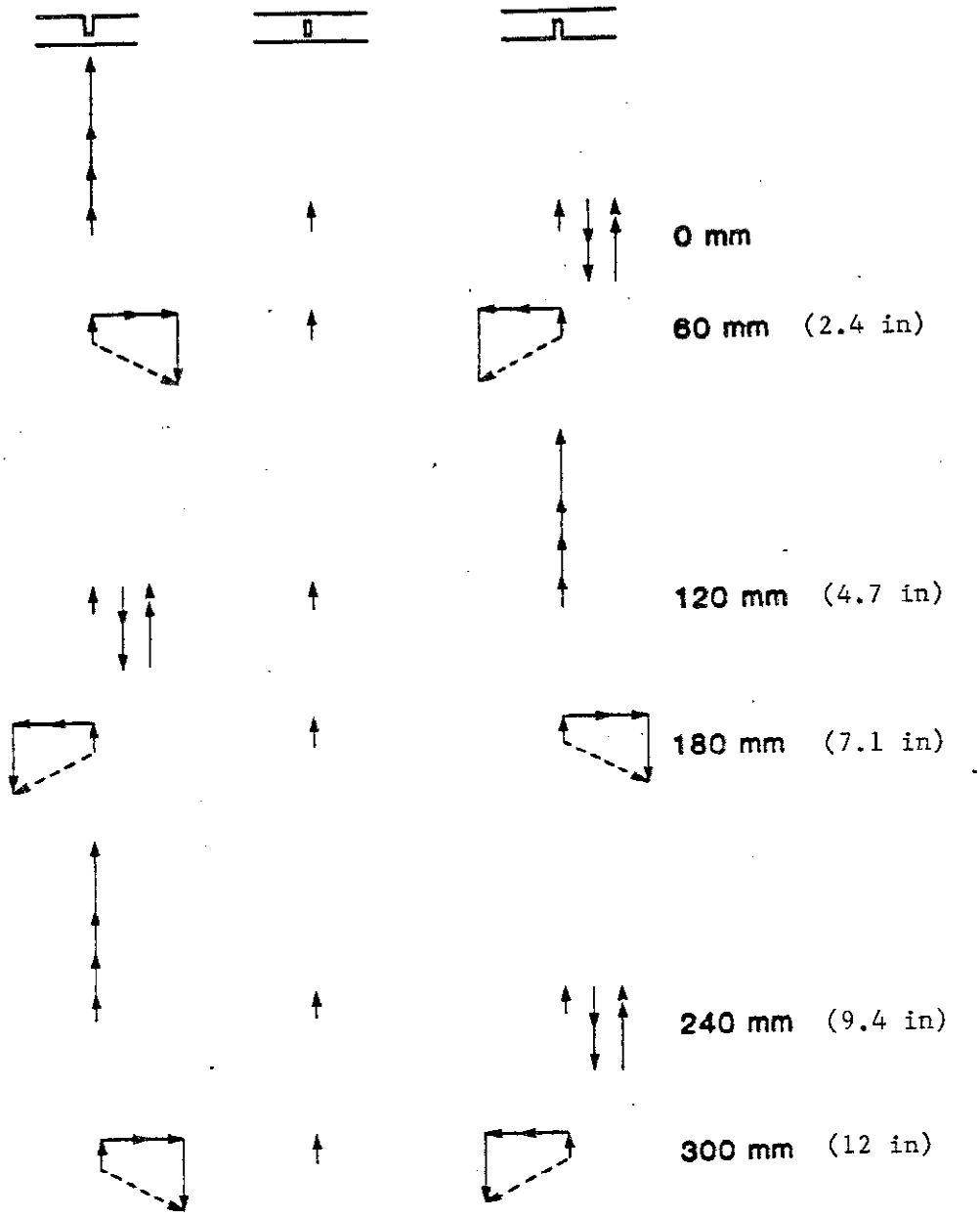

Fig. 47 - Phasor diagram representation of the signals observed for different positions of the calibration slot within a plate at different transmitter-EMAT-to-weld-distances, z. L_{tr} = 210 mm (8.27 in).

Figures 48 through 51 show the results of scattering measurements performed on calibration specimens containing surface and buried slots (see Table 12, Sec. 8) Figures 48 and 49 show the results for vertical slots at two particular EMAT-to-weld separation distances z: 65 mm (2.6 in) and 100 mm (3.94 in). Figure 50 shows the results obtained for vertical slots whose centers coincide with the midplane of the calibration specimen (the cross section of a typical specimen is shown at the top of the figure). The dependence of the reflection amplitude ratio on flaw through-wall depth, a, is shown in the center of Fig. 50. It should be noted that this plot represents an average of results obtained from a wide range (60-160 mm, 2.4-6.3 in) of separation distances, z. The actual behavior of the flaw-amplitude reflection ratio with the distance, z, is shown at the bottom of Fig. 50. Characteristically, the amplitude reflection ratios in both plots (weld-crown up and weld-crown down) fall off monotonically with the distance, z. This effect is caused by the fact that flaws located near the midplane of the weldment are not strongly coupled to the antisymmetric SH plate waves. The monotonic decrease of the reflection amplitude with the distance, z, is caused by two-dimensional diffraction effects.

Figure 51 shows the results obtained for canted slots located above the midplane of the calibration specimens. The cross-sectional view of these calibration specimens is shown at the top of the figure. As in Fig. 50, the average amplitude reflection ratio is plotted as a function of the through-wall flaw depth, a. The evolution of the flaw signal with the distance, z, is shown at the bottom of the figure. In this case, note that the amplitude of the flaw signal does not decrease monotonically with the distance. This effect is caused by the fact that the canted flaws were not located at the midplane of the calibration specimen. As a result, they were weakly coupled to the SH_1 plate waves, causing the interference phenomenon illustrated in Fig. 47.

The experimental flaw responses, shown in Figs. 48 through 51, can be used in conjunction with the experimentally established ultrasonic background levels, shown in Figs. 44 and 45, to determine the inherent flaw sensitivity limits of the low-frequency SH-wave EMAT system. The flaw sensitivity limits can be obtained approximately from the intersection points of the horizontal lines in Figs. 48 through 51, which correspond to the maximum expected background signal level and the measured flaw response curves. A more precise, statistical treatment would require additional experimental measurements and knowledge of the flaw distribution function. Thus, for vertically oriented flaws extending beyond the transverse resolution width of the ultrasonic beam, the minimum detectable flaw depths are 0.75 mm (0.030 in) vertical surface flaws and 2 mm (0.08 in) for vertical buried flaws located the midplane of the weldment. For buried flaws, which are canted at 30° with respect to the surface normal, the corresponding minimum detectable through-wall flaw depth is approximately 3 mm (0.1 in).

3.7 Detectability Limitations: Short Flaws

Because the ultrasonic beam, which insonifies the weld region, has finite width, it is important to understand the relationship between the factors determining the transverse resolution of the SH-wave EMAT system and the inherent detectability limits for flaws of finite length. When the flaws are very long, their length, ℓ, can be measured independently of the depth parameter, a, by scanning parallel to the welding direction. However, when the flaw is short, then it is not possible to determine ℓ and a unambiguously. Furthermore, the reflection amplitude ratio, R_s, is reduced (Eq. 89), thereby increasing the minimum detectable flaw depth.

To understand the physical principles that determine the transverse resolution of the low-frequency SH-wave EMAT system, it is necessary to take

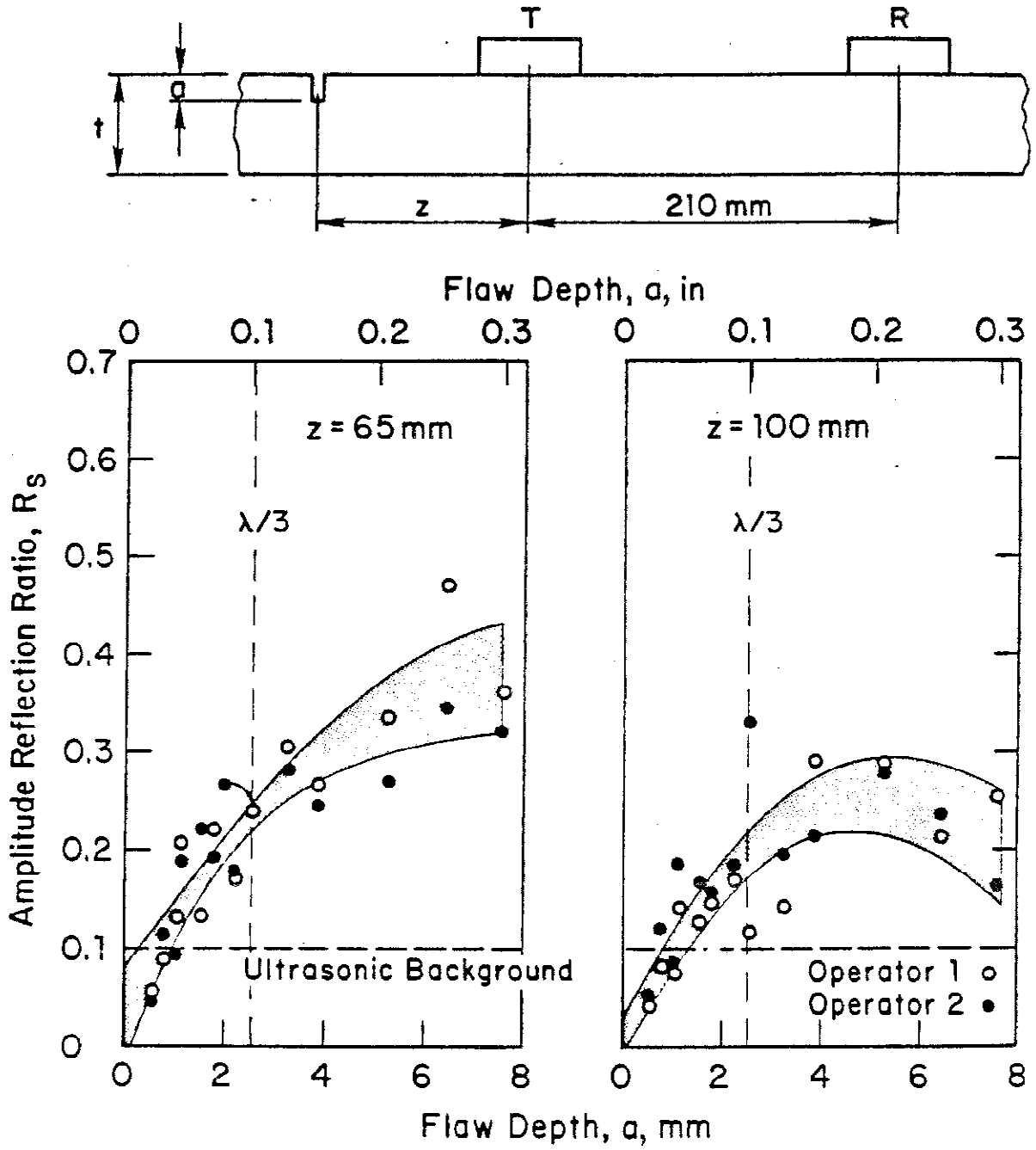

Fig. 48 - Experimental calibration curves for sizing very long surface slots located on the top surface of plate for z = 65 mm (2.6 in), z = 100 mm (3.94 in). Flat-plate specimens 12 through 24.

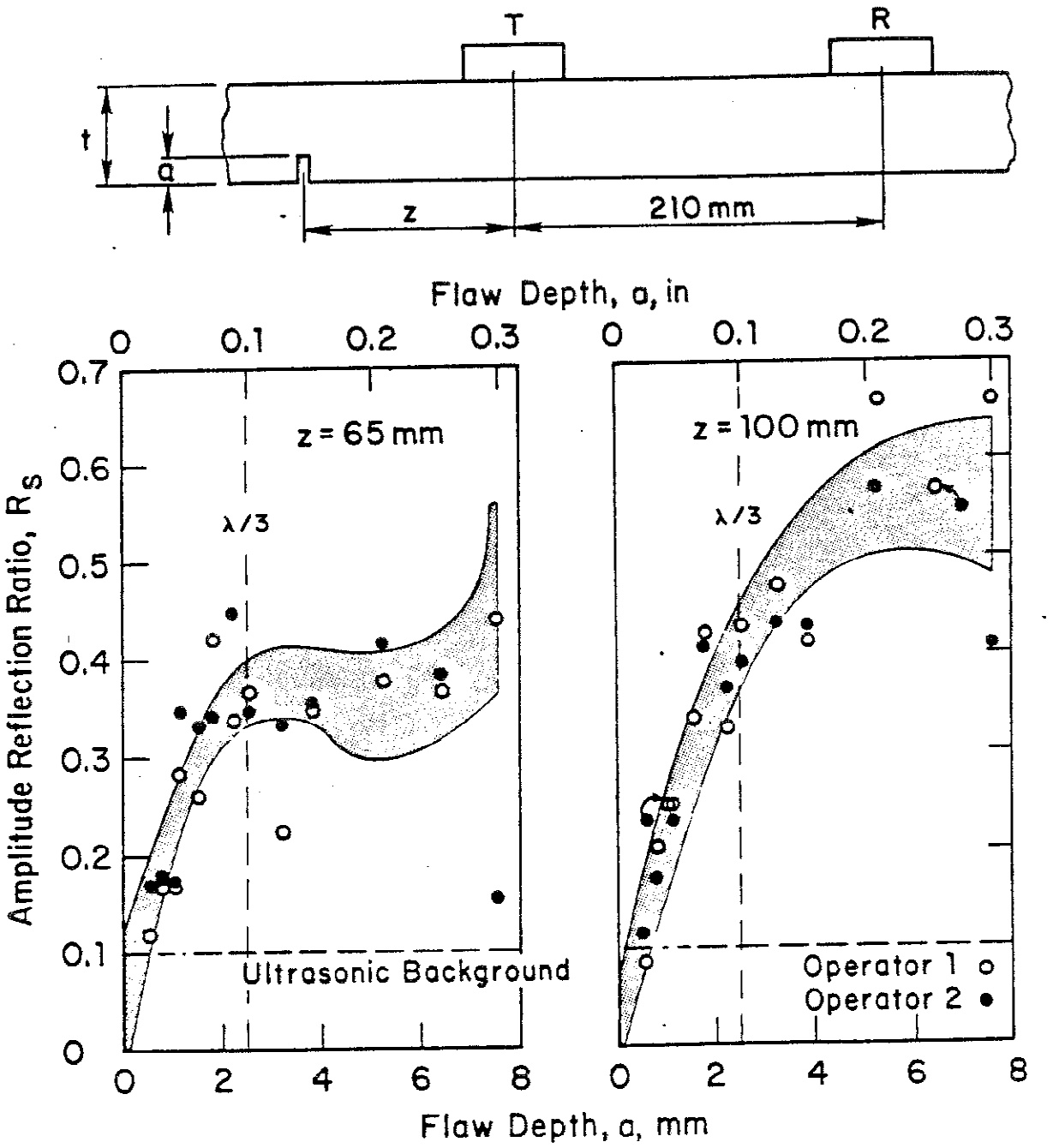

Fig. 49 - Experimental calibration curves for sizing very long surface slots located on the bottom surface of a plate for z = 65 mm (2.6 in), z = 100 mm (3.94 in). Flat-plate specimens 12 through 24.

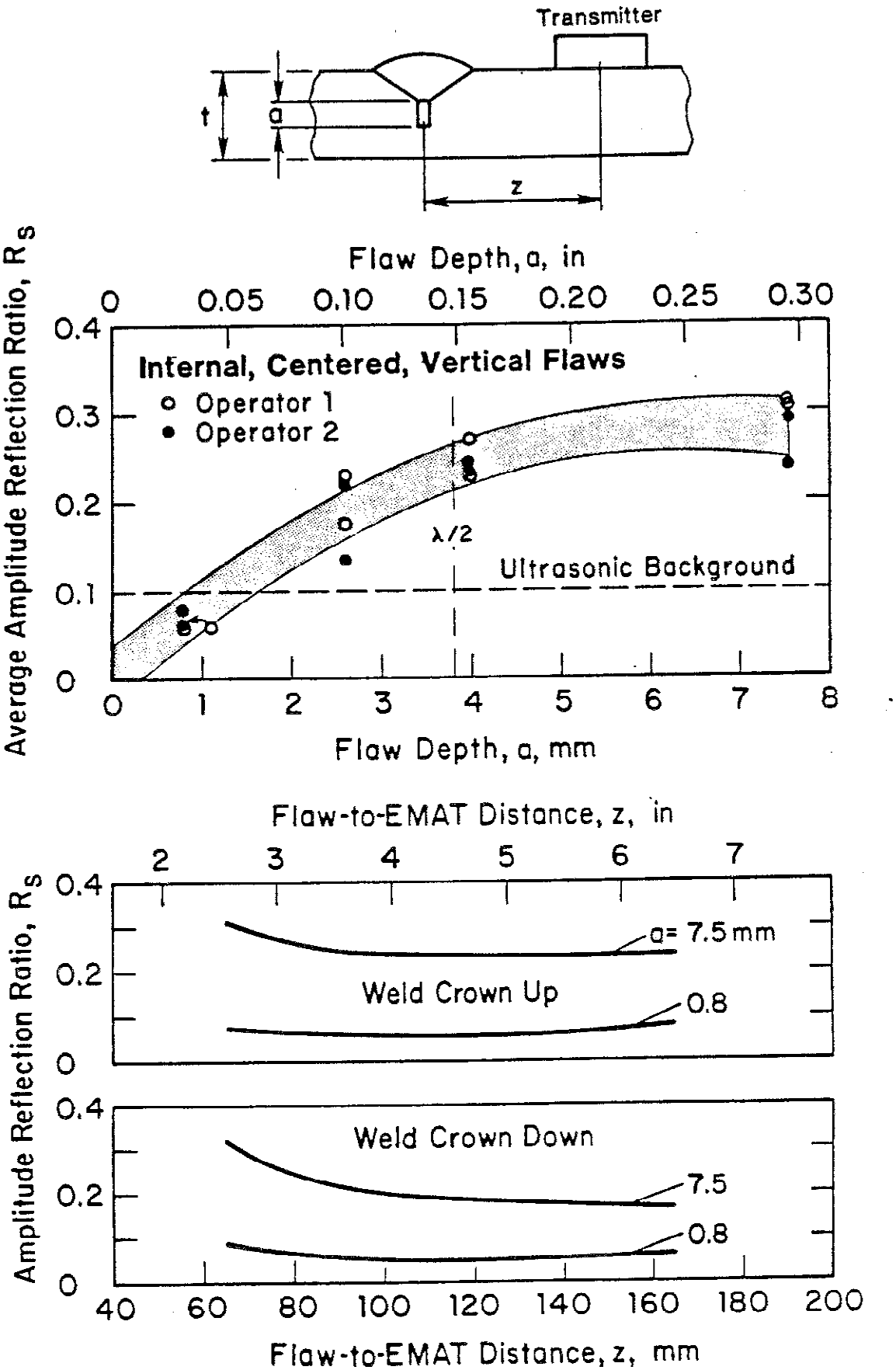

Fig. 50 - Experimental calibration curve for sizing very long, vertical slots buried near the midplane of a plate and typical variations of the signal level as a function of the transmitter-EMAT-to-weld distance, z. L_{tr} = 210 mm (8.27 in). Flate-plate specimens 8 through 11.

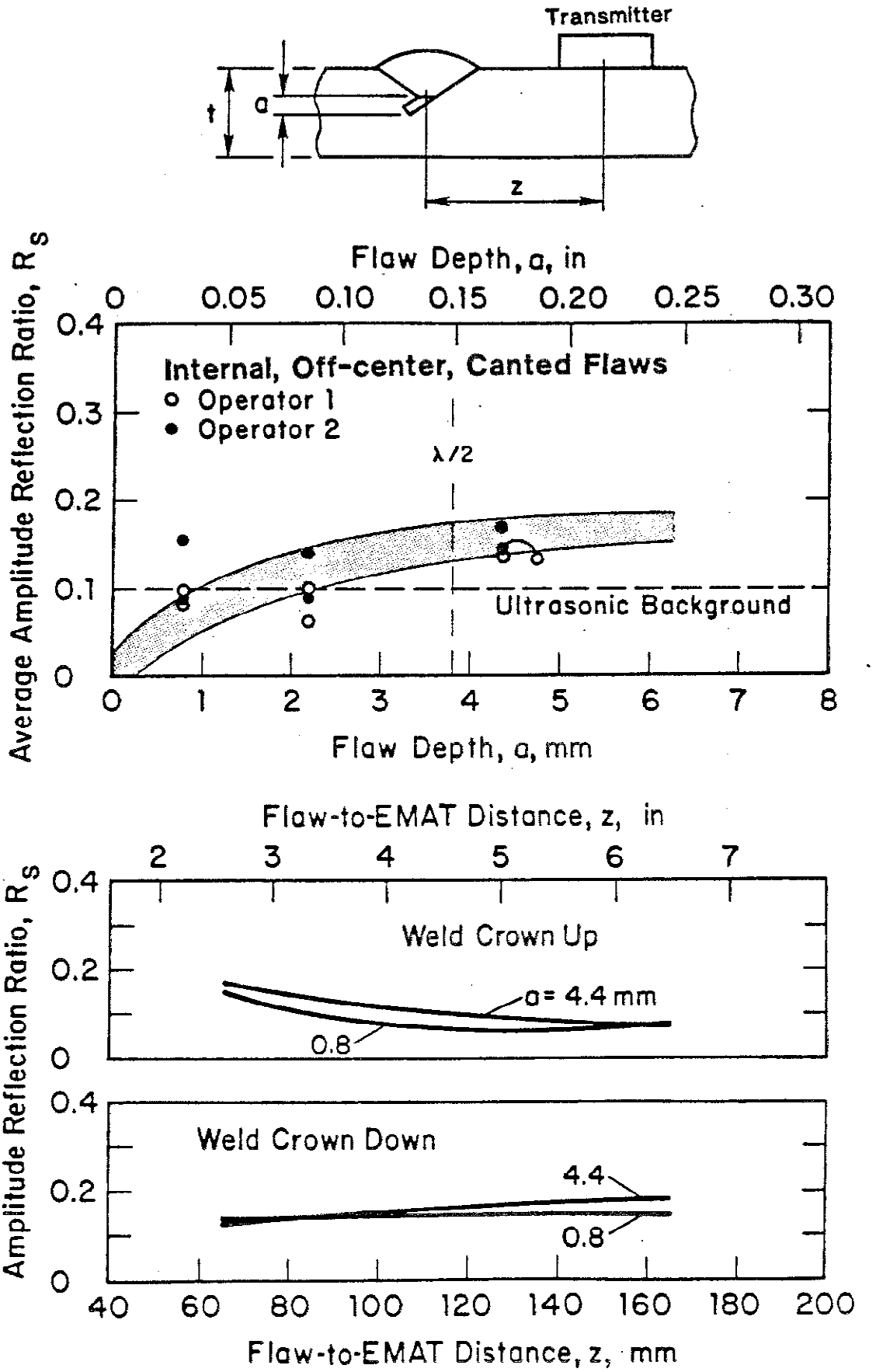

Fig. 51 - Experimental calibration curve for sizing very long canted (30°) slots buried near the midplane of a plate and typical variations of the signal level as a function of the transmitter-EMAT-to-weld distance, z. L_{tr} = 210 mm (8.27 in). Flat-plate specimens 25 through 28.

into account the effects of two-dimensional diffraction. This can be accomplished by generalizing Eqs. 78 and 81 to three dimensions. If the transverse amplitude is Gaussian, as indicated by experimental evidence, then the ultrasonic velocity field distribution near the flaw is given by:

$$v_x(x,y,z,\tau) \approx A_n(1+j)(2)^{-\frac{1}{2}}(\beta_n/2z)^{\frac{1}{2}} \cos(n\pi y/t) \times \exp(-\beta_n w_o^2 x^2/2\lambda z^2) \exp(-j\beta_n x^2/2z) \exp[-j(\beta_n z - \omega\tau)] \quad (92)$$

where w_o is the half-width of the ultrasonic beam near the transmitter EMAT. Corresponding expressions for the field quantities $T_{xz}^{(n)}$ and $T_{xy}^{(n)}$ can be obtained from Eq. 92 by applying Hooke's law. Equation 92 can now be directly substituted in Eq. 88. For elongated flaws, whose surface length, ℓ, exceeds the through-wall depth a by a factor of 4 or more, and assuming $z \ll (z + L_{tr})$, the result is:

$$\Gamma = \frac{j\omega}{4(P_1P_2)} \sum_{n=0}^{\infty}\sum_{m=0}^{\infty} \exp(-j\beta_n z)\, a_n\, \Gamma'_{nm}\, b_m \exp[-j\beta_m(z + L_{tr})] \quad (93)$$

where

$$\Gamma'_{nm} \approx \frac{\Gamma_{nm}}{j\left(\frac{\beta_n}{2z}\right)^{\frac{1}{2}}\left[\frac{\beta_m}{2(z+L_{tr})}\right]^{\frac{1}{2}}} \int_{\frac{-\ell}{2}}^{\frac{\ell}{2}} \exp(-j\beta_n x^2/2z)\, dx \quad (94)$$

The integral in Eq. 94 is recognized as a Fresnel integral whose behavior can be deduced from the Cornu spiral.[67] Specifically, the magnitude of the integral in Eq. 94 increases monotonically for $\ell < (4\pi z/\beta_n)^{\frac{1}{2}} \approx (2\lambda z)^{\frac{1}{2}}$ and then converges in an oscillatory manner to an asymptotic value. In writing Eq. 94, the effect of the exponential profile of the ultrasonic beam, expressed by the last term in Eq. 92, was neglected. This was done on purpose, to emphasize the fact that the transverse resolution of the SH-wave-EMAT system, $(2\lambda z)^{\frac{1}{2}}$,

increases at a significantly lower rate than the ultrasonic beam width, $2\lambda t/\pi\omega_0$. From the above, it can be concluded that flaws that are longer than $(2\lambda z)^{\frac{1}{2}}$, behave essentially as two-dimensional, planar flaws. At 454 kHz and $z = 50$ mm (2.0 in), $(2\lambda z)^{\frac{1}{2}} \approx 27$ (1.1 in).

Because the form of the mode III displacement jump across the face of planar flaw is not generally known, it is not possible to obtain a closed-form expression for Γ'_{mn} as a function of all parameters describing a planar flaw. However, when the flaw length, ℓ, is sufficiently short, it is possible to assume that the phases and amplitudes of the incident ultrasonic fields are constant over the face of the flaw. This assumption is equivalent to the Fraunhofer approximation. It is then possible to calculate the scattering coefficient Γ_{00} approximately; it alone determines the detectability of planar flaws located near the midplane of the plate.

To evaluate Γ_{00} using Eq. 88, a well-known, closed-form elastostatic solution can be used that is valid for elliptical, buried cracks of length ℓ and through-wall depth a:[51]

$$\int_{\frac{1}{2}S_F} \Delta u_1^{(0)}\, dS \approx \frac{8\pi\ell a^2}{3G\Phi(1 - a^2/\ell^2)} \frac{1 - \nu}{2 - \nu} T_1^{(0)} \tag{95}$$

where ν is the Poisson's ratio and $\Phi(1 - a^2/\ell^2)$ is the complete elliptical integral of the second kind.

Equation 95 can be directly substituted into Eq. 88. The result is:

$$\Gamma_{00} \approx -j \frac{8\pi^2}{3} \frac{1 - \nu}{2 - \nu} \left(\frac{\beta_0}{2z}\right)^{\frac{1}{2}} \left[\frac{\beta_0}{2(z + L_{tr})}\right]^{\frac{1}{2}} \frac{\ell a^2}{\lambda t \Phi(1 - a^2/\ell^2)} \tag{96}$$

The corresponding reflection amplitude ratio, R_s, for an elliptical flaw, buried near the midplane of the plate and canted at an angle, θ_n, with respect to the plate surface normal, is given by:

$$R_{ell}(z,L_{tr}) \approx \frac{-(1+j)\,\frac{8\pi^2}{3}\,\frac{1-\nu}{2-\nu}\,\frac{\ell a^2\cos^2\Theta_n}{\lambda t(2\lambda z)^{\frac{1}{2}}\,\Phi(1-a^2/\ell^2)}\,a_1^2\exp(-j\beta_o z)\exp[-j\beta_o(z+L_{tr})]}{\sum_{n=0}^{1} a_n b_n[\beta_n L_{tr}/\beta_o(z+L_{tr})]^{\frac{1}{2}}\exp(-j\beta_n L_{tr})} \qquad (97)$$

For the range of experimental parameters stated previously, and $\ell \sim 25$ mm (0.98 in) a = 2.5 mm (0.098 in), the coefficient R_s is 0.21. This value is in excellent agreement with the experimentally observed value (Fig. 50). Thus, Eq. 97 can be used to estimate the detectability of sharp flaws that are shorter than $(2\lambda z)^{\frac{1}{2}}$. To estimate the detectability of shallow surface flaws, the contribution of the scattering coefficients Γ_{01}, Γ_{10}, and Γ_{11} must be included in the estimate of R_s. Since the function $\Phi(1 - a^2/\ell^2) = \pi/2$ at $a = \ell$ and tends monotonically to unity as a/ℓ tends to zero, the reflection amplitude ratio, R_s, for elongated, sharp flaws is directly proportional to ℓ when $4a < \ell < (2\lambda z)^{\frac{1}{2}}$.[68] Equation 97 does not include a dependence on the beam width, $2w_0$. This follows from the fact that the flaw is insonified by the far-field of the transmitter EMAT. This assumption holds when $(2z/\beta_0 w_0^2)^2 >> 1$, which is clearly satisfied when z > 50 mm (2.0 in), λ = 7.4 mm, (0.29 in)and w_0 = 7.5 mm (0.30 in).

3.8 System Performance Limitations and Standards of Acceptability

The model-based results for flaws whose length cannot be resolved can be combined with the empirically derived results for two-dimensional, planar flaws that are longer than $(2\lambda z)^{\frac{1}{2}}$ to construct a phenomenological model defining the limits of detectability for surface and buried flaws. It is convenient to present the detectability limits graphically with flaw depth, a, plotted as the y-axis and the flaw length, ℓ, plotted as the x-axis. The detectability limits can then be directly related to current flaw acceptance standards based on the industry-wide such as those in Section 6 of API-1104

flaw acceptance criteria based on fitness-for-service considerations.[4,69] This is done in Figs. 52 and 53 for vertically oriented surface and buried planar flaws.

In Figs. 52 and 53 the allowable flaw sizes are defined by length vs. through-wall depth curves, except for Section 6 of the API-1104 Standard,[2] which does not address the flaw through-wall depth. The allowable flaw-size curves were based on a yielded-ligament fracture mechanics model using arbitrary, but realistic, parameters to characterize the toughness of the materials and to estimate the stresses acting on the girth welds.[69] These curves are used here only to illustrate the relationships between the capabilities of the SH-wave EMAT inspection system and different flaw acceptance criteria.

In Figs. 52 and 53, the range of flaw sizes that can be detected is bounded by the heavy solid lines. The range of flaw sizes that cannot be detected is indicated by the shaded areas. It is interesting to note that the maximum flaw length allowable by Section 6 of the API-1104 Standard coincides with the resolution limit of the SH-wave EMAT system, $(2\lambda z)^{\frac{1}{2}}$ when $z = 50$ mm (2.0 in) and the operating frequency is approximately 500 kHz. Shorter flaws are considerably harder to detect. As a consequence, the 454-kHz SH-wave EMAT system may also be appropriately used in conjunction with conventional, workmanship-based acceptance criteria, such as Section 6 of the API-1104 Standard.

It is interesting to observe (Figs. 48 and 49) that the amplitude of ultrasonic signals backscattered from surface flaws increases monotonically in the range $0 < a < \lambda/3$ and reaches a maximum when $a \sim \lambda/3$. On the other hand, in the case of buried flaws (Figs. 50 and 51), the amplitude of the backscattered signals increases monotonically in the range $0 < a < \lambda/2$ and reaches a maximum value at $a \sim \lambda/2$. When the above limits are exceeded, the interaction of the incident ultrasonic fields with the flaw becomes very complicated and the

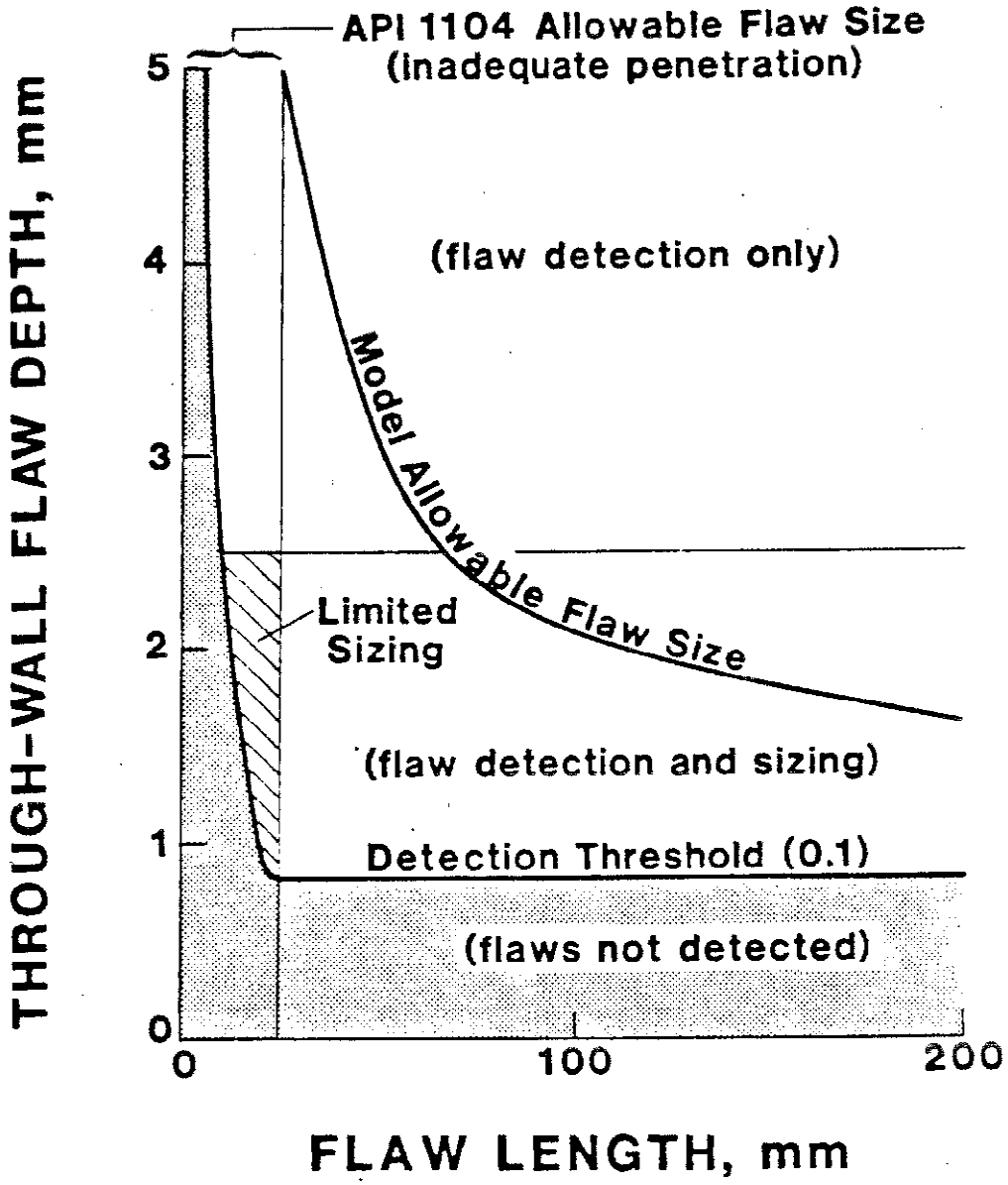

Fig. 52 - Summary of system performance characteristics for vertical surface flaws. To change flaw length and depth to inches, multiply by 0.0394.

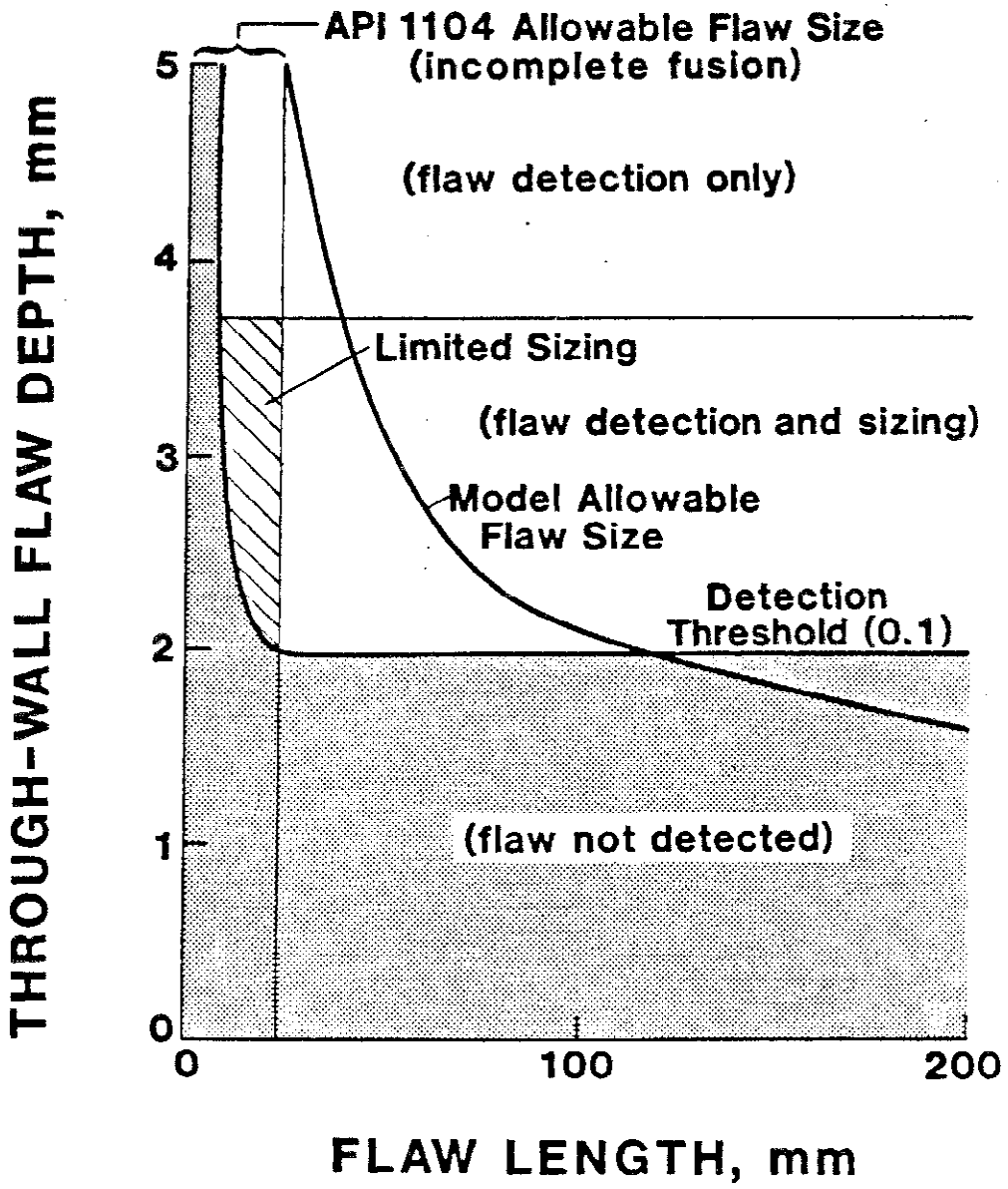

Fig. 53 - Summary of system performance characteristics for buried planar flaws. To obtain flaw length and depth in inches, multiply by 0.0394.

low-frequency (long-wavelength) inversion algorithms for flaw sizing become inoperative. Thus, $a < \lambda/3$ for surface flaws and $a < \lambda/2$ for buried flaws define the maximum flaw depths that can be sized. Deeper flaws can still be detected reliably, but cannot be sized unambiguously. These limits are indicated in Figs. 52 and 53 by horizontal lines parallel to the x-axis. The hatched areas in Figs. 52 and 53 represent a range of detectable flaws when the length $\ell < (2\lambda z)^{\frac{1}{2}}$ and, therefore, cannot be determined independently of the through-wall depth, a. (At 454 kHz the shear wavelength, λ, is approximately 7.4 mm (0.29 in). For comparison, the average through-wall depth of one SMA weld pass is approximately 3 mm (0.1 in).

A consideration of the performance characteristics summarized in Figs. 52 and 53 reveals that the operational wavelength, λ, and the EMAT-to-weld distance, z, must be selected appropriately to assure the detection of flaws that are significant from the point of view of a particular acceptance standard for sharp flaws. The resolution of the system is reduced at longer wavelengths, but the range of flaw dimensions that can be sized is increased. In addition, the detectability limitations are determined principally by the mass-loading effects of the weld reinforcement and the presence of alignment mismatch. Consequently, consideration must be given to limiting the maximum dimensions of the weld reinforcement and alignment mismatch by employing appropriate process and tolerance controls.

3.9 Inspection Protocol

The development of the low-frequency SH-wave EMAT system was guided by a need for a reliable ultrasonic inspection tool that would be capable of detecting significant planar flaws in pipeline girth welds. The detection of significant flaws necessarily involves a decision process based on a set of nondestructive measurements and a set of acceptance criteria. The output of

the detection process is always a binary decision, yes or no, and an associated measure of confidence. The decision is based on models describing the nondestructive measurements, the failure processes and associated safety factors, and the knowledge of the statistical flaw distribution.[70]

Acceptance criteria for sharp flaws are normally specified in terms of the principal length and through-wall depth dimensions. In addition, certain failure models treat surface flaws more severely than buried flaws. As a consequence, the inspection system must be able to classify the flaws in terms of their relative position within the weld and to estimate their principal dimensions. This can be done simultaneously using ultrasonic measurements from different locations along scan lines that are perpendicular and parallel to the pipe circumference. Two possible experimental configurations can be used to accomplish this task; they are illustrated in Fig. 54.

Figure 54a shows the preferred inspection configuration. The configuration of Fig. 54a uses two arrays of EMATs that are translated mechanically along the direction parallel to the girth weld. Each array is composed of a number of independent sets of EMATs that are positioned at different distances from the weld. A simplified inspection configuration is shown in Fig. 54b. The simplified configuration uses only one set of EMATs, as illustrated in Fig. 54, that is scanned along the girth weld in a "zig-zag" manner. In this case, the measurements are repeated on the opposite side of the weld. It is evident that both inspection configurations can perform the scattering measurements that are needed.

A flow chart, exemplifying a possible inspection protocol, is shown in Fig. 55. Because most girth welds are free of significant sharp flaws, the inspection protocol involves a preliminary "detection" threshold, which permits bypassing the decision process involving acceptance criteria. The

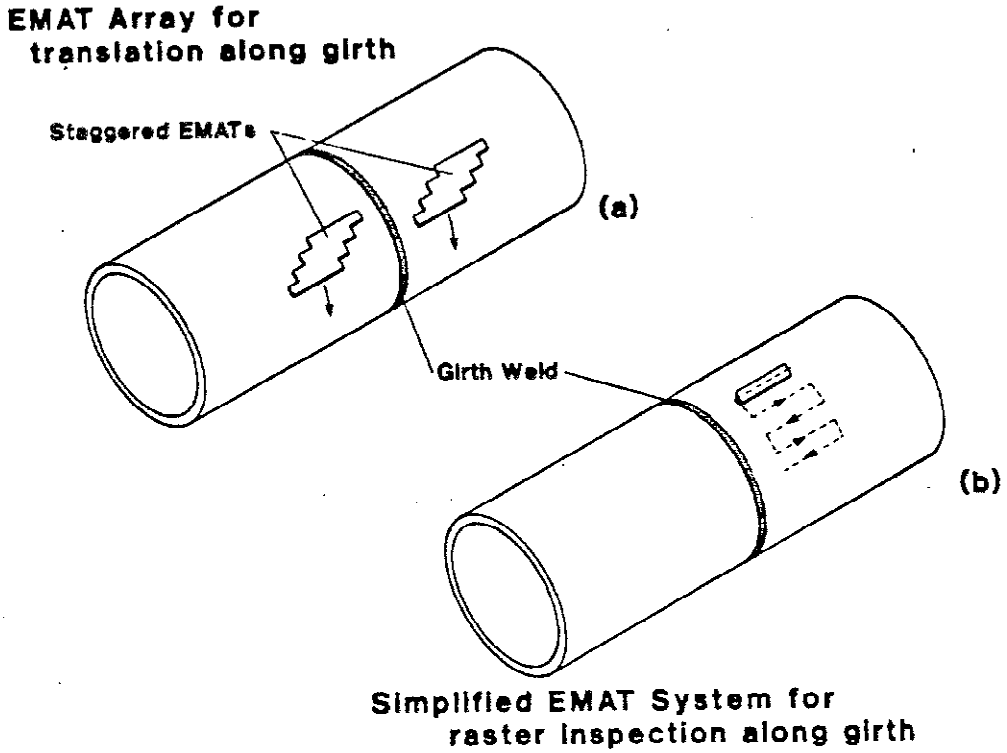

Fig. 54 - Two possible implementations of a practical SH-wave EMAT inspection system.

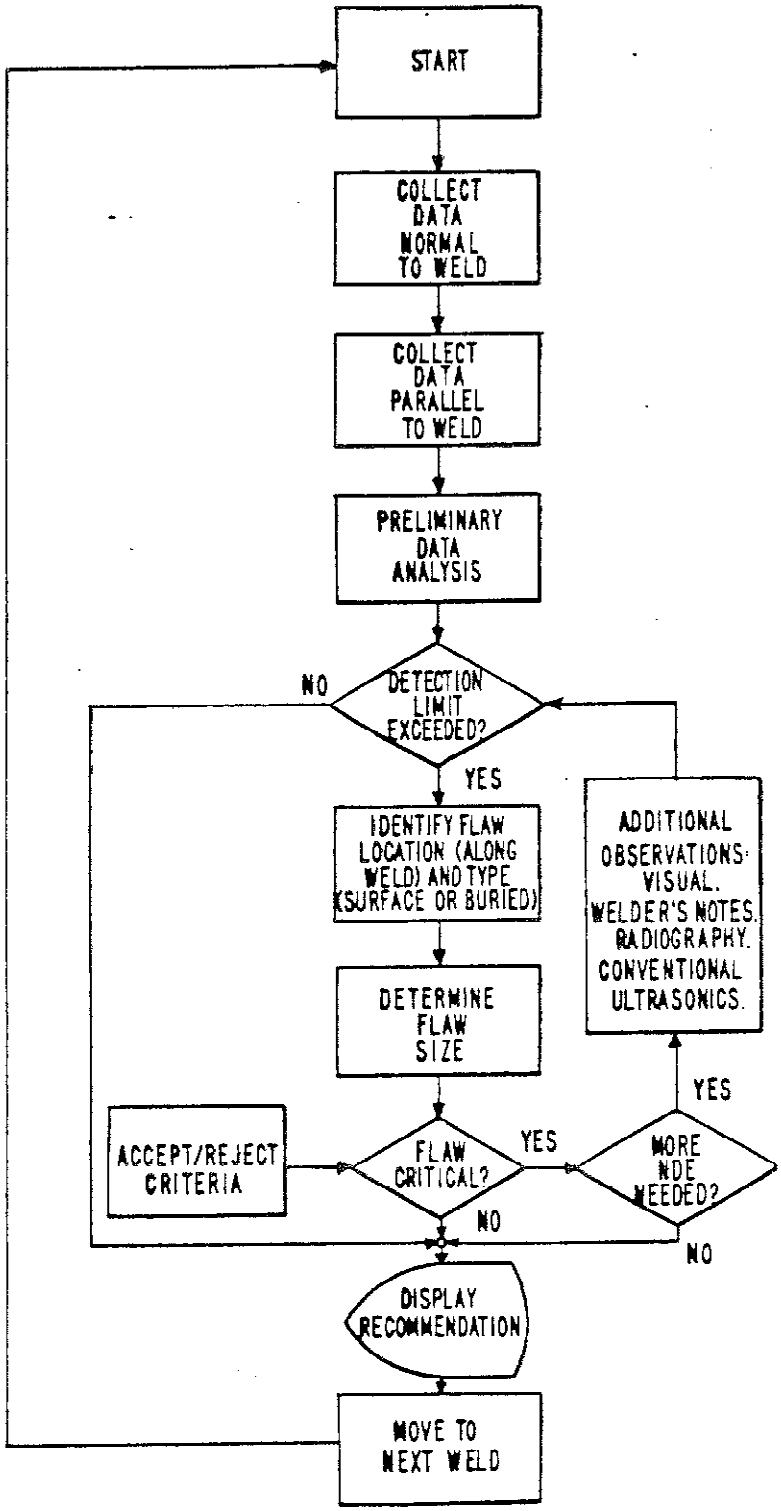

Fig. 55 - An inspection protocol for fully automated inspection of pipeline girth welds.

protocol assumes that ultrasonic measurements are made (as illustrated in Fig. 55) and processed to compute the reflection amplitude ratio, R_s, for each measurement location. If a signal level is observed that exceeds the preliminary detection threshold, then the flaw is classified and measured using the theory developed in this report. The decision concerning the significance of the flaw can then be made. If the measure of confidence is low, then additional available information may be included in the decision process. The additional information may include visual observations, process control information (welder's notes), radiographic data, and conventional ultrasonic data. For this purpose, a subsidiary "loop" is included in the inspection protocol. At the end, the results of the decision process are appropriately displayed and recorded. Permanent recording of the pre-processed low-frequency ultrasonic data is also envisioned.

Since the decision processes must include consideration of factors that cannot be adequately modeled or simulated in a laboratory environment, successful implementation of the proposed inspection protocol will involve considerable field experience. In addition, independent data describing the statistical distribution of flaws will be required from destructive assays.

3.10 Summary

Significant progress has been made in developing a low-frequency ultrasonic system optimized for inspection of girth welds in large-diameter pipelines. This system offers the following advantages: 1) rapid inspection rates, 2) elimination of transducer coupling agents, 3) insensitivity to weld reinforcements, 4) minimum dependence on operator skill and judgement, 5) full automatability, 6) tunability of the system to signal the presence of rejectable flaws based on any established fracture mechanics accept/reject criterion, and 7) permanent data recording. Other ultrasonic inspection

systems provide comparable overall performance. In contrast to existing systems, the present system is designed to provide the specific information on flaw content and sizing required by the accept/reject criteria of a fitness-for-service analysis of flaw significance.

Phenomenological models of the ultrasonic measurement process have been devised to extract the dimension and position information from the ultrasonic data from planar flaws. In addition, the inherent performance limitations of the system have been established theoretically and empirically in a controlled laboratory environment. The results indicate that the new system offers considerable advantages over conventional ultrasonic and radiographic methods. In particular, it uses noncontacting electromagnetic-acoustic transducers whose efficiencies can be calibrated for each measurement. In addition, it operates at low ultrasonic frequencies, which reduce the complexity of data interpretation. At its present state of development, the SH-wave EMAT inspection system has the following deficiencies: 1) performance has not been demonstrated with real flaws under field conditions, 2) field proven hardware remains to be developed, 3) personnel trained in the system are not readily available, 4) equipment calibration standards remain to be developed, and 5) sensitivity of the system to detecting tight cracks closed by compression stresses has not been determined.

4. SIGNIFICANCE OF BLUNT FLAWS

M. B. Kasen

4.1 Introduction

It has thus far been assumed that both sharp and blunt (nonplanar) flaws would be treated as significant and subject to an accept/reject criteria based on analytical fracture mechanics principles. But a number of studies have concluded that flaws such as porosity, slag, and arc burns have a very low probability of initiating cracks in tough weld metal and may be considered innocuous in a fitness-for-service analysis.[71-77] It was therefore of interest to determine if this proposition could be defended in pipeline girth welds.

4.2 Experimental Procedures

A series of girth welds containing large contents of porosity, slag, and arc burns were fabricated in 1016-mm (40-in) API 5LX-65 pipe and in 1220 mm (48-in) API 5LX-70 pipe of 15.9-mm (0.625-in) wall thickness. The objective was to obtain welds having flaw contents equal to or in excess of the worst case obtainable under field welding conditions. Welds meeting API 1104 workmanship quality were also produced. Automatic and manual (SMA) processes were represented, with fixturing, consumables, and personnel reflecting field procedures as much as possible. Welding parameters and joint designs, as reported by the fabricator, appear in Table 6. Typical welding electrode compositions are given in Table 7. Chemical composition of the base and weld metals are given in Table 1 (Section 2). Tensile properties of the weld metal and typical fracture toughness data on the welds are summarized in Table 8. Detailed metallurgical and mechanical characterization is presented in Appendix B. Flaw contents obtained are illustrated in Fig. 56.

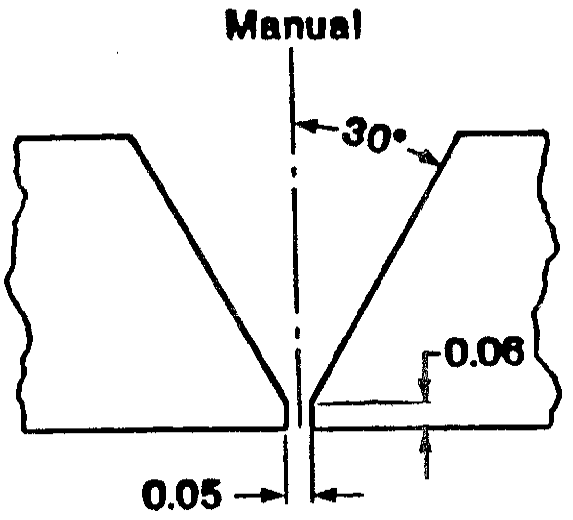

Table 6 – Welding Parameters*

Pass	Ave. Travel Speed, mm/min	in/min	Electrode Diameter, mm	in	Arc Voltage	Current, A
1	292	11.5	4.0	5/32	24/26	150/160
2	269	10.6	4.0	5/32	26/30	150/160
3	269	10.6	4.0	5/32	26/30	150/160
4	200	8.0	4.8	3/16	26/30	150/170
5	180	7.0	4.8	3/16	26/30	150/170
6	200	8.0 (strip)	4.8	3/16	26/30	150/170
7	200	8.0 (strip)	4.8	3/16	26/30	150/170
8	200	8.0 (strip)	4.8	3/16	26/30	150/170
9	200	8.0 (strip)	4.8	3/16	26/30	150/170
10	150	6.0 (cap)	4.8	3/16	26/30	150/160

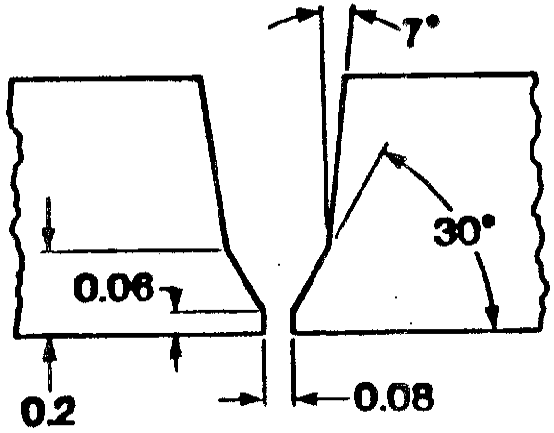

Automatic

Pass	Travel Speed, mm/min	in/min	Wire Feed, m/min	in/min	Arc Voltage
1	430	17	13.3	525	23
2	380	15	11.4	450	22.5
3	3300	13	11.4	450	22.5
4	330	13	11.4	450	22.5
5	280	11	8.64	340	21.5
6	230	9	8.26	325	20.5

Wire diameter: 0.89 mm (0.035 in)
Shielding gas: 50% Ar, 50% CO_2
* As provided by fabricator

Table 7 - Typical Welding Electrode Compositions

Element	Process	
	Shielded Metal Arc*	Automatic†
Mn	0.47-0.51	1.35
Si	0.07-0.10	0.70
Cr	0.12-0.13	----
Ni	1.03-1.70	1.15
Mo	0.01	----
V	0.02-0.03	----
C	---	0.10
S	---	0.015
P	---	0.015

Values reported by the fabricator in percent by weight
*AWS E8010G
†AWS E70S-6

Table 8 — Typical Weld-Metal Properties

Weld Type	Hardness	Yield Strength at 0.2% Offset, 25°C (77°F), MPa	Yield Strength at 0.2% Offset, 25°C (77°F), psi x 10^3	Toughness, COD, at -18°C (-0.4°F) mm	Toughness, COD, at -18°C (-0.4°F) in	Toughness, COD, at 0°C (32°F) mm	Toughness, COD, at 0°C (32°F) in	Critical COD, Slow, Stable Crack Growth mm	Critical COD, Slow, Stable Crack Growth in
Automatic	HRC 30	725.0	105.2	0.082	0.0032	0.094	0.0037	0.074	0.0029 at 0°C (32°F)
Manual	HRB 91	465.0	67.4	0.124	0.0049	0.0187	0.00074	0.079	0.0031 at -18°C (-0.4°F)

(a)

Automatic Weld Porosity, 15% Radiographic Obscuration

(b)

Manual Weld Slag

(c)

Simulated Manual Weld Porosity, 13% Radiographic Obscuration

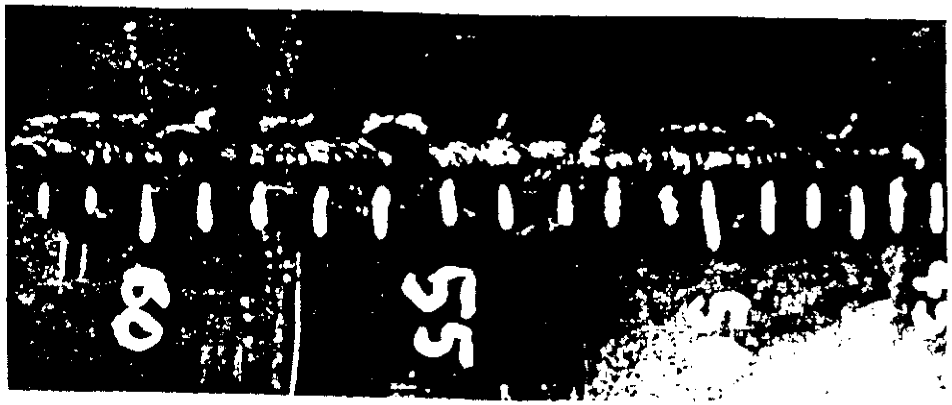

(d)

Arc Burns

Fig. 56 - Typical levels of weld flaws used in the experiments.
Top view: fracture; bottom view: radiograph.

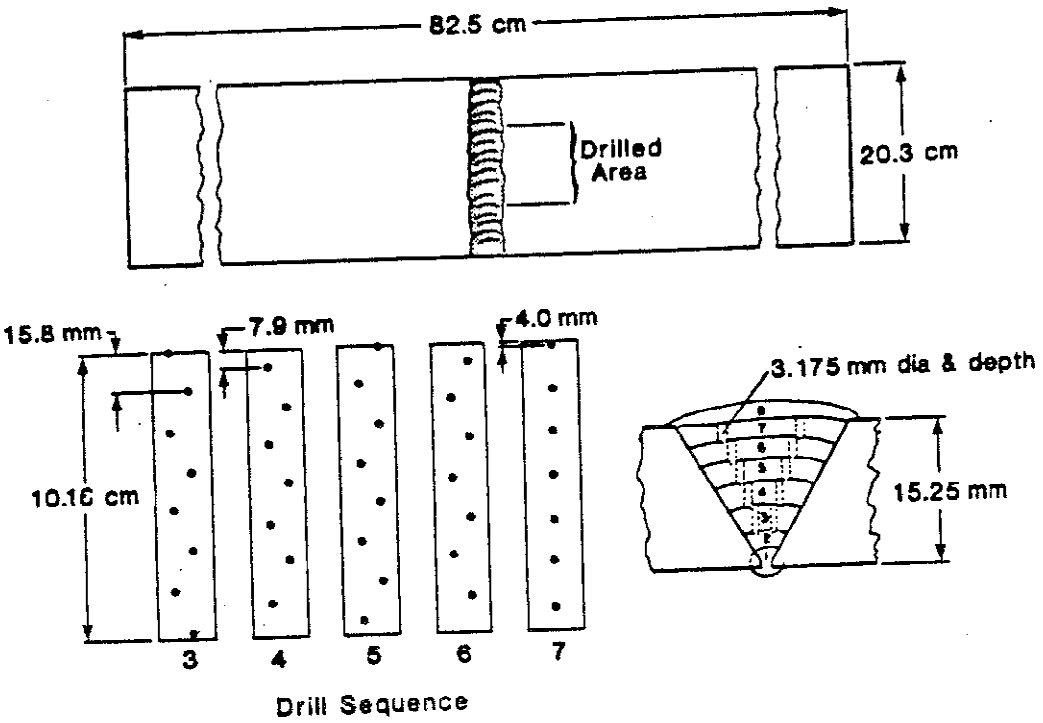

Fig. 57 - Drill pattern used to simulate buried porosity in manual (SMA) welds in API 5LX-70 pipe. To obtain the dimensions in inches, multiply the millimeters by 0.0394.

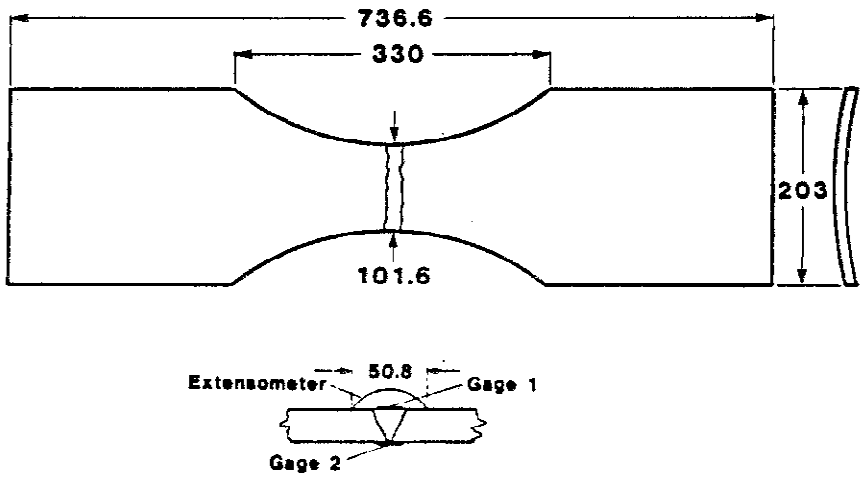

Fig. 58 - Specimen and instrumentation used for low-cycle fatigue studies of the significance of blunt weld flaws in crack initiation. Dimensions are in millimeters; to obtain inches, multiply by 0.0394.

low-cycle fatigue, producing hysteresis loops as illustrated in Fig. 59. A temperature of -2 ±1°C (28 ±2°F) was maintained to simulate the lowest anticipated service temperature of the ANGTS line. This was accomplished by controlled metering of liquid-nitrogen vapor into a chamber surrounding the specimen. The cyclic rate was held to 0.2 Hz or less to minimize internal heating. The imposed strain was either slightly over weld-metal yield (±0.0022) or approximately twice weld-metal yield (±0.0045). The total strain range was, therefore, either 0.0044 or 0.0090. This technique was selected because, although pipelines are not normally subjected to such severe cyclic loading, any flaw found innocuous under the imposed conditions can conservatively be considered innocuous in essentially statically loaded structures.[78] A similar approach has been used to demonstrate the inherently innocuous nature of blunt flaws in pressure vessel weldments.[76,77]

As cyclic testing proceeded, development of cracks in the weld region reduced the effective cross-sectional area, causing a drop in the load required to maintain the selected strain range. Monitoring of the load therefore provided an indication of the number of cyclic reversals required to initiate cracking in each weldment. A 10% load drop, corresponding to development of about a 10% cracked area in the specimen cross section, was used as the criterion for crack initiation. This criterion was selected because, once initiated, crack-growth rates were relatively rapid under the severe test conditions, regardless of flaw content. Cyclic straining was continued until a load drop corresponding to a 40% cracked area was obtained to permit the influence of flaw type and content on crack propagation to be studied. Testing was stopped at 3000 cycles if this criterion had not been reached. Specimens were then broken in tension. The desired strain range was initially established by strain gages located at the weld, as illustrated in

A level of porosity obscuring 12 to 15% of the projected area of the weld radiographs was desired, since this level represents more than twice the obscuration level that would be practically allowable based on the probability of excess porosity interfering with radiographic detection of sharp flaws (see Section 6). This level was easily obtained during automatic welding by disturbing the shielding gas during deposition of two internal weld passes. Several attempts were made to produce this level of obscuration during manual welding by improper welding technique, excessive drying of the E8010G electrodes, or by fracturing the flux coating of the electrodes. Although a large amount of porosity was produced in a given pass, the final welds were found to contain far less than the desired level of obscuration. This flaw was therefore simulated by drilling a pattern of 3.175-mm (0.125-in) diameter holes in five successive interior weld passes and overwelding. The procedure is illustrated in Fig. 57, and the result is illustrated in Fig. 56c.

Slag was produced by improper cleaning of an interior weld pass. As illustrated in Fig. 56b, this typically resulted in formation of "wagon tracks" due to slag entrapment from the E8010G electrodes at the sides of the weld bead. Lying adjacent to the fusion line, this type of slag residue has the highest probability of contributing to brittle fracture because of the stress concentration caused by the weld reinforcement. Arc burns were introduced at random on the heat-affected zones of sound welds after the welding had been completed. This simulated the worst case, because there was no annealing of the brittle martensite phase that forms under the burns due to rapid cooling.

Large, transverse weld specimens, having dimensions and instrumentation as illustrated in Fig. 58, were prepared from selected regions of the welded pipes. These specimens were subjected to fully reversed, strain-controlled,

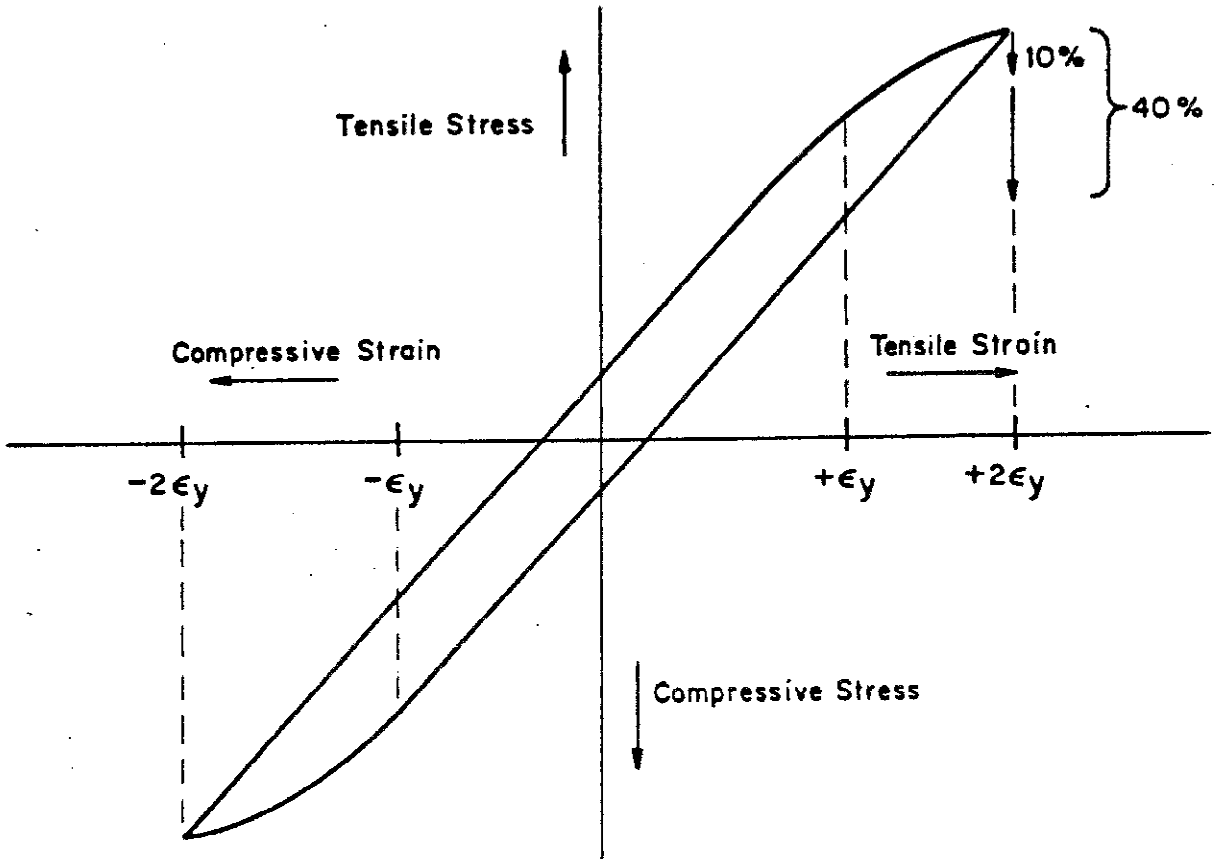

Fig. 59 - Schematic of hysteresis loops formed during low-cycle, strain-controlled fatigue test program. Crack initiation was defined as corresponding to a 10% load drop to maintain the desired strain range. Specimens were broken in tension after a 40% load drop. Tests were run at strain levels just over yield ($\pm\varepsilon_y$ = $\pm$0.0022) and at twice yield ($\pm 2\varepsilon_y$ = $\pm$0.009).

Fig. 58, while control of the 4.45-MN (1 x 10^6 lbf) servohydraulic test machine was provided by an extensometer spanning the weld region. Figure 60 illustrates the actual appearance of hysteresis loops produced by the extensometer and load cell during a test of a sound manual weld.

Specimen asymmetry due to pipe curvature produced a bending moment during compression, tending to cause failure by column buckling rather than in tension-compression. This was countered by development of the specimen-support system illustrated in Fig. 61 and by ensuring that the specimen halves were in good alignment prior to a test. The latter was achieved by slightly bending the specimens to remove the distortion caused by release of residual welding stresses when the specimens were removed from the pipe.

All the specimens were radiographed prior to testing. Several specimens were stereoradiographed after achieving the 40% load drop but before final fracture to determine if useful information could be obtained on the crack path relative to buried flaws. However, the cracked region could not be defined with a resolution justifying continuation of this procedure.

Weldments were tested with the weld reinforcement both intact and removed by flush grinding. Results with the reinforcement intact were of most interest in interpreting flaw significance, since this condition exists in the field. Removing the reinforcement forced failure through the flawed region and provided useful information on flaw interaction during crack initiation and propagation.

4.3 Low-cycle Fatigue Results

Results of tests conducted with the weld reinforcement intact are summarized in Table 9. Similar data for specimens tested with the reinforcement removed appear in Table 10. Results of tests on unwelded parent

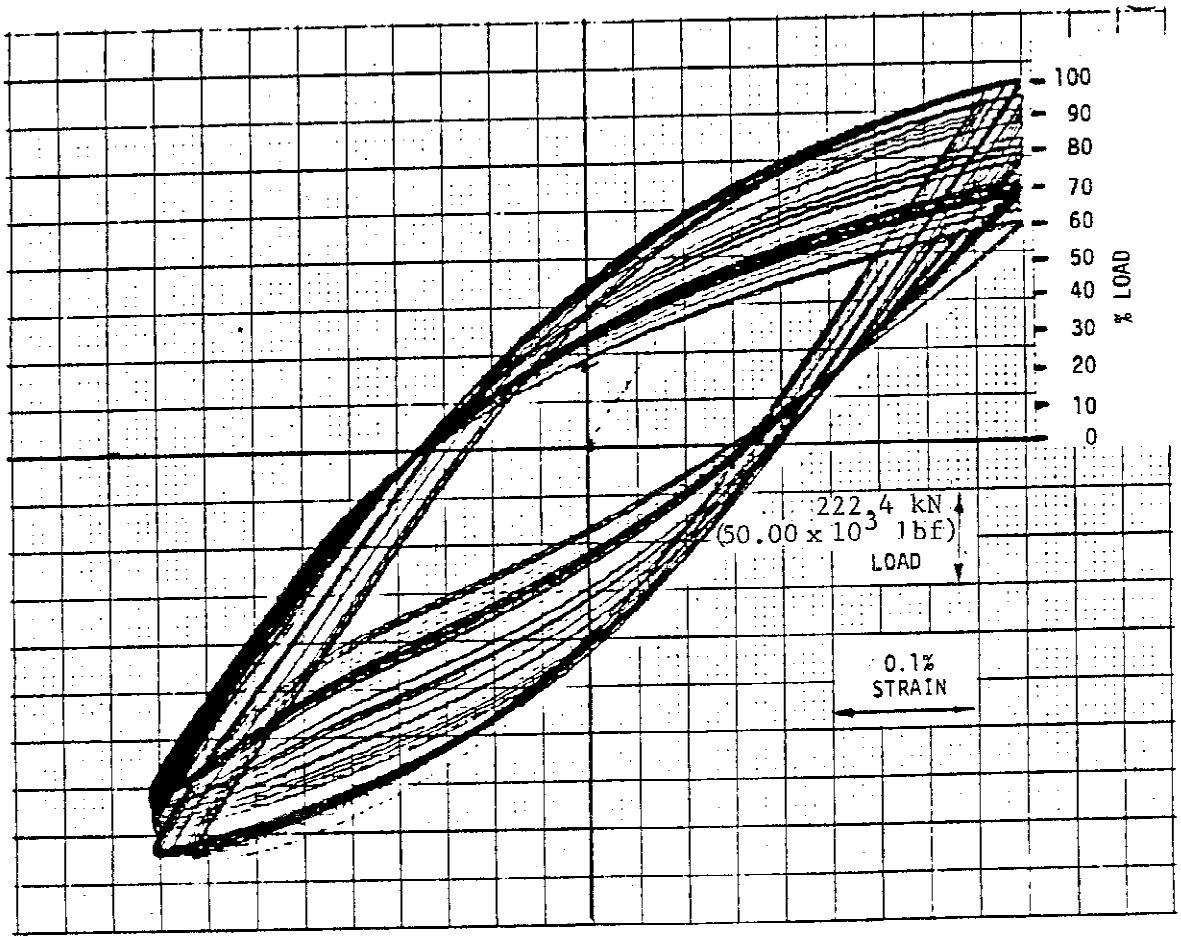

Fig. 60 - Hysteresis loop plot from extensometer on a sound manual weld tested at 0.0090 total strain with weld reinforcement removed. Specimen No. 95103.

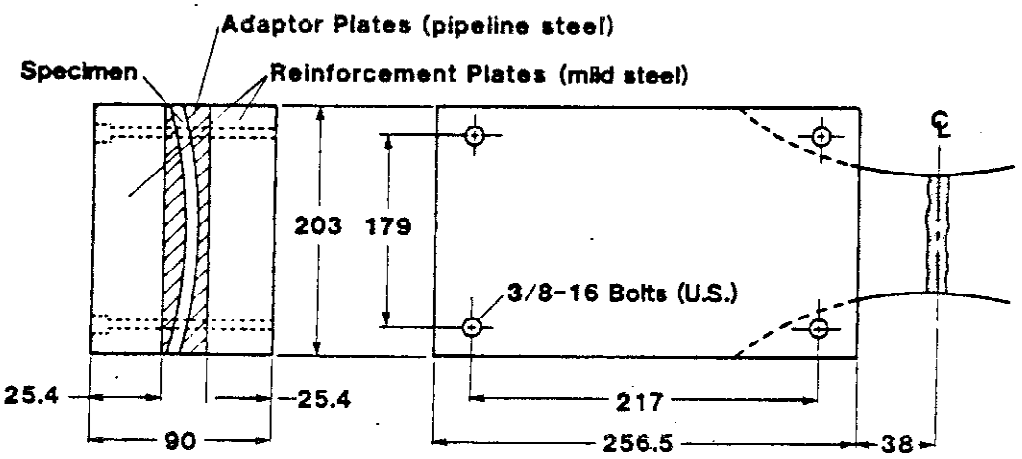

Fig. 61 - Specimen support system required to prevent failure in column buckling during low-cycle fatigue testing. Dimensions are in millimeters; to obtain inches, multiply by 0.0394.

Table 9 - Results of Low-Cycle Fatigue Program Conducted with Welds Having Reinforcement Intact and with Parent Pipe Materials

Flaw Type	Specimen No.	Strain, ±%	Cycles to Load Drop 10%	Cycles to Load Drop 40%
Sound (Automatic)	1-3543	0.45	114	477
	1-5159	0.45	159	516
	1-12103	0.31	585	1005
	1-4351	0.22	*	---
	X2-121129	0.22	885	(1)
Porosity (Automatic)	4-0210	0.45	87	500
	4-2028	0.22	3012	4852
	X2-6674	0.22	397	*
	X2-2028	0.22	863	*
Sound (Manual)	3-6775	0.45	106	128
	X7-8492	0.45	75	272
	3-8391	0.22	1118	1276
	X7-6876	0.22	1358	1933
Slag (Manual)	5-8290	0.45	110	247
	5-0816	0.45	30	49
	X7-5260	0.45	88	185
	5-9098	0.22	1015	1389
	5-98106	0.22	760	1236
Porosity† (Manual)	XP-2	0.44	70	81
	XP-4	0.45	99	127
	XP-6	0.22	812	821
	XP-8	0.22	1095	1117
Arc Burn (Manual)	3-2028	0.45	231	242
	3-2836	0.45	194	295
	3-3644	0.22	1159	1500
Arc Burn (Parent X-65 Pipe)	PA-1	0.45	853	2830
	PA-2	0.22	(1)	---
Parent X-65 Pipe	P-2	0.45	1740	1913
	P-1	0.22	3124	---

*Not achieved after 3000 cycles. Test discontinued.
†Artificially introduced. See text.

Table 10 - Results of Low-Cycle Fatigue Program Conducted with Welds Having Reinforcement Removed

Flaw Type	Specimen No.	Strain, ±%	Cycles to Load Drop 10%	Cycles to Load Drop 40%
Sound (automatic)	1-111119	0.34	120	2130
	1-1119	0.22	*	---
	1-0311	0.22	†	---
Porosity (automatic)	4-4452	0.45	155	165
	4-1220	0.45	30	49
	4-5563	0.45	117	276
	4-2836	0.22	1026	1525
	4-3644	0.22	397	1505
Sound (manual)	3-7583	0.45	81	136
	3-95103	0.45	118	215
	3-0008	0.22	1766	2073
	5-4351	0.22	2621	‡
Slag (manual)	5-115123	0.45	26	44
	5-7179	0.45	104	198
	5-0008	0.45	250	363
	5-6371	0.22	352	442
	5-5563	0.22	132	169
Arc Burn (manual)	3-1018	0.45	169	189

*Not achieved after 2426 cycles. Test discontinued due to malfunction.
†Not achieved after 1754 cycles. Test discontinued due to malfunction.
‡Not achieved after 3000 cycles. Test discontinued.

pipe material and of parent material containing arc burns are included in Table 9. Figure 62 presents the data of Table 9 in graphical form, illustrating the number of cyclic reversals required to initiate cracking (10% load drop) as a function of strain range. Figures 62 a through c illustrate the results with individual flaw types; all results are combined in Fig. 62d. Data of Table 10 do not appear in graphical form; however, the lower bound performance of this group tested with reinforcement removed is indicated by the dashed line on Fig. 62d.

These data show that some welds containing porosity or slag initiated cracking at lower cycles than did sound welds; others withstood higher cyclic loading. A minimum of 30 reversals at twice yield or about 450 reversals at just over yield were required to initiate cracking, regardless of the content of porosity, slag, or arc strikes. Comparison of the performance of welded specimens with that of unwelded plate illustrates that the strain discontinuity at the fusion line caused by the contour of the weld reinforcement was the dominating factor in lowering fatigue life in the welds. Weld failure occurred predominantly at this location, regardless of flaw content. The failure path was occasionally observed to pass through some of the porosity and slag. Neither crack initiation nor propagation was affected by the presence of arc burns in welded specimens. Arc burns initiated cracking only when they were introduced at the minimum cross section of unwelded plate. Here, cracking was observed to begin at the strike after 853 cycles at twice yield (Table 9). No effect was detected at the lower strain level in arc-struck parent plate.

It has frequently been observed that the number of cycles defining low-cycle fatigue life, N_c, can be expressed as a function of total strain range,

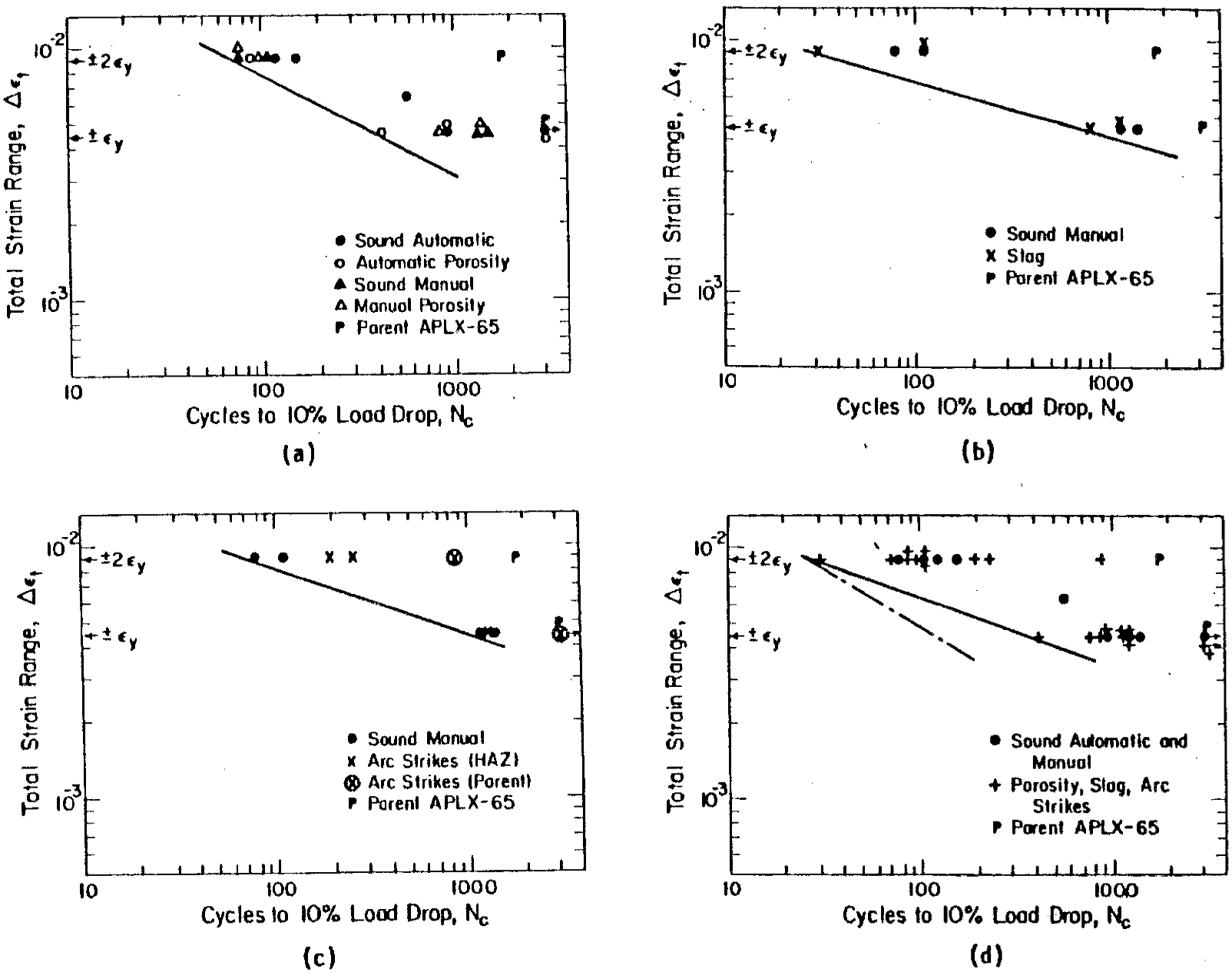

Fig. 62 - Cyclic reversals required to initiate cracking (10% load drop) as a function of strain range for parent metal, sound welds, and welds containing blunt flaws. Results are combined in (d). Solid line is lower bound for initiation in tests with the reinforcement intact. Dashed line in (d) indicates lower bound for tests welded with reinforcement removed.

$\Delta\varepsilon_t$, by a relationship of the form

$$\Delta\varepsilon_t N_c^m = \text{constant} \tag{98}$$

implying a straight line relationship between log $\Delta\varepsilon_t$ and log N_c, having a slope of -m. Gurney[78] has noted that results reported by a number of investigators for steel weldments of different configurations fall within a relatively narrow scatter band on such a plot, producing a slope of approximately -1/3. Figure 63 illustrates that a very similar result is obtained when the average number of cycles to crack initiation is plotted as a function of total strain range for manual welds tested with the reinforcement intact in the present program. Welds containing porosity and slag produced a relationship of the form $\Delta\varepsilon_t N_c^{0.3} = 0.04$. However, the averaged data from the sound welds (including those containing arc burns) appeared to form a different population following the relationship $\Delta\varepsilon_t N_c^{0.4} = 0.07$. This resulted in a divergence between the sound and flawed weld data at the higher ($\pm 2\varepsilon_y$) strain range, suggesting that the high porosity and slag content of the welds had somewhat reduced the cyclic life to crack initiation under this test condition. No effect of the flaw content is observed at the lower ($\pm\varepsilon_y$) strain range.

Figure 64, illustrating the average number of cycles to crack initiation as a function of total strain range for manual welds tested with the reinforcement removed, shows that forcing the failure to occur through the flawed weld interior rather than at the fusion line resulted in fewer cyclic reversals to initiate cracking than in tests with the reinforcement intact. In this test mode, it is seen that slag is a more significant flaw than porosity in reducing cyclic life to crack initiation. But, even under this severe test condition, 26 cyclic reversals were required to initiate cracking at twice yield, whereas 132 cycles were required at just over yield. This suggests

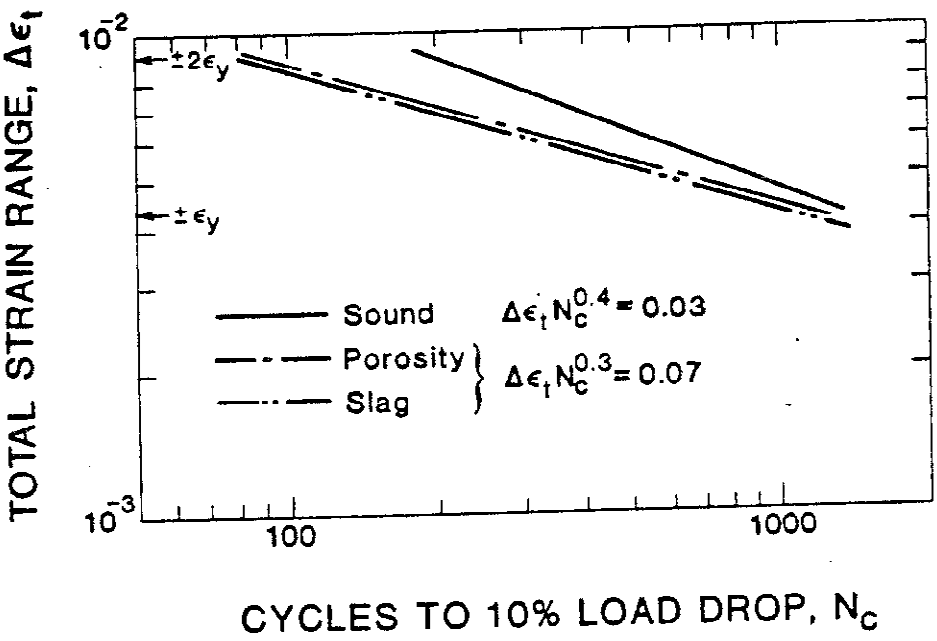

Fig. 63 - Averages of lifetime to crack initiation following Eq. 98 for specimens with weld reinforcement intact.

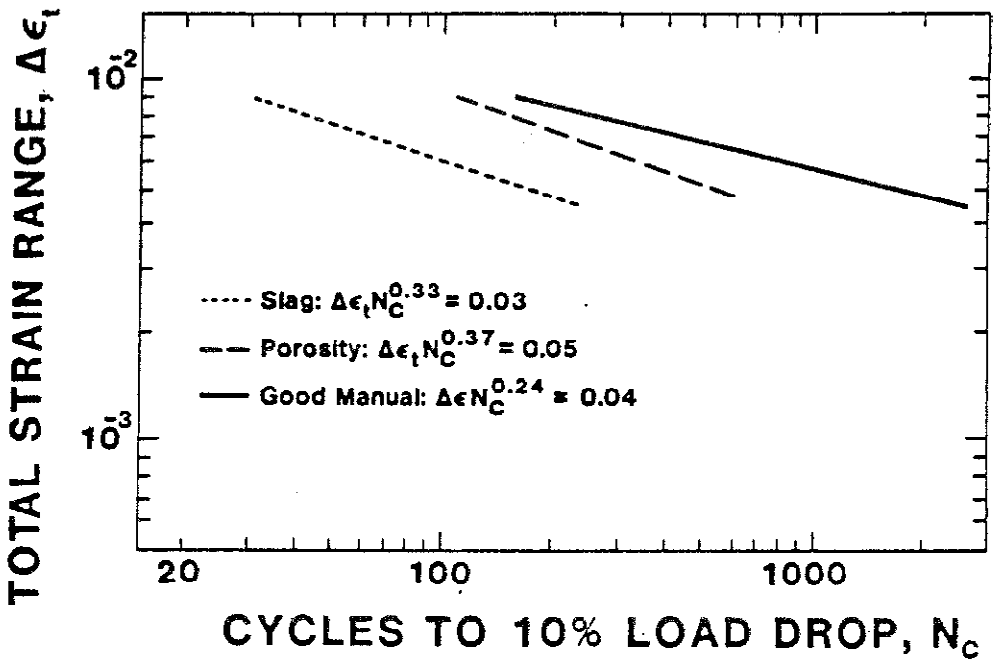

Fig. 64 - Averages of lifetime to crack initiation following Eq. 98 for specimens with weld reinforcements removed.

that, even if the reinforcement were removed, porosity, slag or arc burns would pose little danger to the integrity of pipelines fabricated with welds having the toughness studied in this work.

4.4 Fractographic Analysis

Fractographic examination showed little flaw interaction at the lower strain level ($\pm\varepsilon_y$). As shown in Fig. 65, the cracks in automatic welds containing a large amount of porosity were observed to propagate as single crack fronts with negligible initiation from individual pores. The higher strain ($\pm 2\varepsilon_y$) did cause cracks to form from individual pores in both the manual and automatic welds, with the cracks coalescing to form the fracture surface.

The presence of halos around slag stringers and micropores was noted on the fractured surfaces of all manual welds. This phenomena, illustrated in Fig. 66, is described in the literature as "fisheyes"[79,80] and is attributable to hydrogen embrittlement of the region adjacent to pores and surfaces to which hydrogen has segregated during the welding operation. Their appearance here suggests that hydrogen segregated in this manner is very stable, because the specimens were tested one and one half years after welding. The mechanism of fisheye formation is not well understood; however, lack of fatigue indications on the fisheye surface is indicative of a pop-in type of crack, perhaps reflecting a stress-induced diffusion of hydrogen from its segregated site into the surrounding weld metal during loading. It is generally assumed that fisheyes only form in weld metal stressed beyond yield;[79] however, this has not been firmly established. Whatever their cause, fractographic analysis indicated that the fisheyes contributed relatively little to fatigue crack initiation unless they penetrated the specimen surface. For example, the main

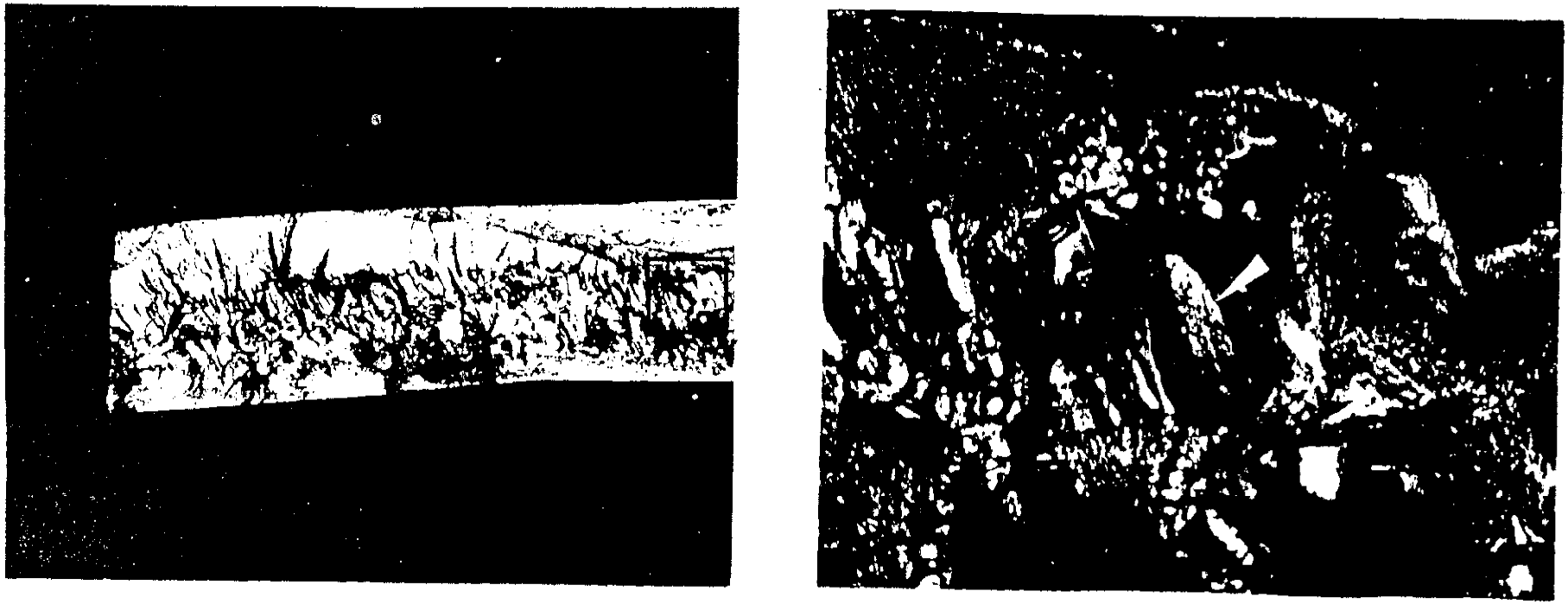

(a) (b)

Fig. 65 - Crack propagation in automatic weld containing porosity and tested at ±0.22% strain. In (b) is an enlargement of the region defined by the box in (a) showing the crack front (arrow) propagating from left to right without evidence of fatigue crack initiation from individual pores ahead of the front. Specimen 4-3644 after 1505 fatigue cycles.

(a)

(b)

(c)

Fig. 66 - Fisheye cracks originating at slag inclusions (a) and at micropores (b) in manual (SMA) welds. Arrow in (c) defines the boundary between the brittle fracture within a fisheye formed at a slag inclusion and the ductile fracture outside the fisheye. In (b) note that the small fisheye penetrating the specimen surface at A served as an initiation point for fatigue crack development, whereas the much larger buried fisheye at B did not do so.

fatigue crack in the specimen illustrated in Fig. 66b initiated and propagated in a region remote from the large internal fisheye.

In addition to the fatigue work described above, two specimens each representing sound automatic welds and welds containing automatic and manual porosity at levels shown in Fig. 56 were pulled to failure in tension at -2 ±1°C (28 ±2°F). Results, given in Table 11, showed no effect of the flaw content on the static tensile strength. All welds failed through the heat-affected zone of the API 5LX-70 pipe.

4.5 Discussion

These results show that the probability of crack initiation from porosity, slag, and arc burns during low-cycle fatigue was very low in the manual and automatic pipeline girth welds tested in this program. Although some reduction in life to crack initiation was noted when welds containing large quantities of porosity and slag were tested at the highest strain range ($\pm 2\varepsilon_y$), the geometrical discontinuity formed by the weld reinforcement was found to dominate the fatigue failure mode in all tests conducted with the reinforcement intact.

This is consistent with the findings of others on the relative effect of the geometrical discontinuity created by the reinforcement as compared with that of buried blunt flaws.[73,77,78,81] In the absence of brittle fracture initiation, the primary structural effect of such flaws is to reduce the effective weld cross section. However, porosity content causing a 12 to 15% radiographic obscuration will reduce the cross-sectional area by only about 1% in welds of the thickness studied in the present work,[78] whereas the weld reinforcement itself typically contributes 5 to 8% to the thickness of the weld region. Therefore, a negligible effect could be predicted for circumstances where the weld-metal yield strength matches or exceeds that of

Table 11 - Ultimate Stress for Welds Pulled to Failure in Tension at -3°C (27°F)

Condition	Ultimate Stress, MPa	Ultimate Stress, psi x 10^3	Radiographic Obscuration
Sound Automatic	651	94.4	None
	648	94.0	
Automatic Porosity	665	96.5	~15%
	651	94.4	
Manual Porosity	675	97.9	~12%
	681	98.8	

the parent pipe material. Table 9 shows that this was the case in the present study.

Even with the reinforcement removed to force failure through the highly flawed weld metal, the welds showed a high tolerance to fatigue crack initiation from the blunt flaws. Because strain levels were well above yield, these data indicate that the probability of crack initiation from such flaws would be negligible if such welds were subjected to the essentially static loading conditions of operating pipelines.

Therefore, the results of this study suggest that porosity, slag, and arc burns are innocuous as fracture initiation sites in girth welds fabricated with materials of the toughness equal to or exceeding that listed in Table 8. The validity of this conclusion has not been experimentally demonstrated for welds of lower toughness. However, as noted by Harrison,[72,73] the rounded, blunt shapes of such flaws and their inherently small critical through-wall dimensions (see Section 5) make them size-for-size less harmful than cracks of equal dimensions. He observes that if the critical flaw size is so small as to indicate serious risk of fracture initiation from porosity and slag, it is doubtful that the selected material has a toughness appropriate for the application. Harrison concludes that porosity and slag required no special consideration in regard to brittle fracture. This concept has been accepted by Commission X of the International Institute of Welding (IIW) following the recommendations of an IIW Working Group on Significance of Defects.[73,74] This Group, representing Japan, England, and Belgium, based its conclusions on: 1) the examination of approximately one hundred cases of fatigue by brittle fracture in ferritic steel weldments, during which no instance of fracture initiation at porosity or slag was observed, 2) results of tests at many laboratories demonstrating that such flaws have little or no effect on static

failure load, and significantly less effect on fatigue life than the surface profile and, 3) consideration of theoretical elastic and fracture mechanics analysis. The group concluded: "Provided materials of adequate notch ductility or fracture toughness for the particular service application have been used to tolerate the smallest planar defects which can reliably and practically detected, porosity, slag inclusions, and surface irregularities, in amounts up to which they can be clearly identified as the only defects present, will have no significance on failure by brittle fracture".[73]

The present work appears to substantiate these general conclusions with one exception: The detection of fisheye crack formation from the surface of entrapped slag in welds made with the E8010G high-hydrogen electrodes suggests that it might be prudent to reserve judgement on the potential significance of slag until the conditions for formation of fisheyes are better defined. Although such cracks were developed during low-cycle fatigue in the present work, they are found on tensile, bend test and similar fracture surfaces produced at low strain rates.[79] The possibility of their formation as the result of pipe-laying stresses or other imposed static loads cannot, therefore, be ruled out at the present time. Should this occur, fisheyes may constitute a signficant flaw in weld metal of lower toughness than that studied in this program.

The probability of arc burns contributing to fracture is related to the probability of crack initiation in the hard martensitic region produced by a burn and to the probability that such a crack is of critical size for fracture propagation in the parent material. As a first approximation, the carbon equivalent (CE) of the parent material might be taken as a measure of the former probability, because this parameter is controlled in the selection of pipeline material to limit the martensite content and hardenability in the

heat-affected zone of the weldment. A typical formula for pipeline construction might be

$$CE = C + Mn/6 + (Cr + Mo + V)/5 + Ni + Cu/15 \qquad (99)$$

yielding a CE value of 0.414 for the API 5LX-65 material used for the arc-burn studies. A typical maximum allowable CE value for 16-mm (0.63-in) thick pipe would be 0.40; consequently, it is concluded that the arc-burn significance tests were conducted under a conservative criterion from a hardenability point of view. Despite these conditions, no cracking was observed in any of the arc burns, either before or after testing.

Even assuming cracking was present, the literature suggests that propagation would be unlikely owing to the high toughness of current pipe materials. Fearnehough and Jones[82] have noted that a number of tests conducted in the United States and England have demonstrated that defect failure in modern pipeline materials is primarily controlled by plastic collapse phenomena and that the critical defect size is, therefore, associated with tensile properties. Results of the study to develop appropriate accept/reject curves for current pipeline materials (see Section 2) support this view in concluding that a model based on ligament yielding is most appropriate. These considerations suggest that the controlling parameter for partial wall defects is flow stress on the remaining pipe wall. Lumb and Fearnehough[83] have analyzed a large number of accidental pipeline failures and data from experimental burst tests by this criteria, noting that in no case was failure was found to initiate from flaws having depths less than 20% of the wall thickness for applied stresses equal to the specified minimum yield strength of the flawed material. This corresponds to a tolerable flaw depth of about 3 mm (0.1 in) for pipe of the thickness studied in the present work. The experimentally determined relationship between arc-burn width and depth

(see Fig. 69) shows that by this criterion a 12-mm (0.47-in) wide arc burn would be acceptable, even if it were treated as a crack of equal dimension. Such a large arc burn is unlikely to occur in practice, substantiating the conclusion about the innocuous nature of this type of flaw in pipe materials that fail by plastic collapse.

Figure 67 combines the results of the present low-cycle, strain-controlled fatigue program on pipeline girth welds tested (reinforcement removed) with the results of a similar low-cycle fatigue program conducted by the British Welding Institute (BWI) in their assessment of the significance of porosity and slag on the performance of pressure vessel weldments.[75,76] Specimen sizes, flaw contents, and parent-metal yield strengths were very similar in both programs. The Welding Institute study was conducted at 25°C (77°F) over a total strain range of approximately 0.0009 (below specimen yield strength) to 0.0045 (approximately twice specimen yield strength), with cyclic strain applied between a preset maximum and zero. In contrast, the present study investigated flaw significance under higher total strains of approximately 0.0044 and 0.0090, produced by fully reversed loading at -2°C (28°F) Therefore, the present work extends the Welding Institute data to higher strain levels and to lower fatigue life. The Welding Institute data reflect cyclic life to a 60% load drop, whereas the present data reflects a 40% drop; however, this difference in failure criteria is insignificant in view of the high crack propagation rates at the higher strain levels.

As noted in Fig. 67, coplotting of the data suggests a change of slope in the log $\Delta\varepsilon_t$-vs.-log N_c plot in the vicinity of 10^3 cycles where the total strain range has reached about 0.007. This is consistent with the observation that the fatigue failure mode changed from propagation of a single fatigue crack front through the flawed welds at the lower strain range ($\pm\varepsilon_y$)

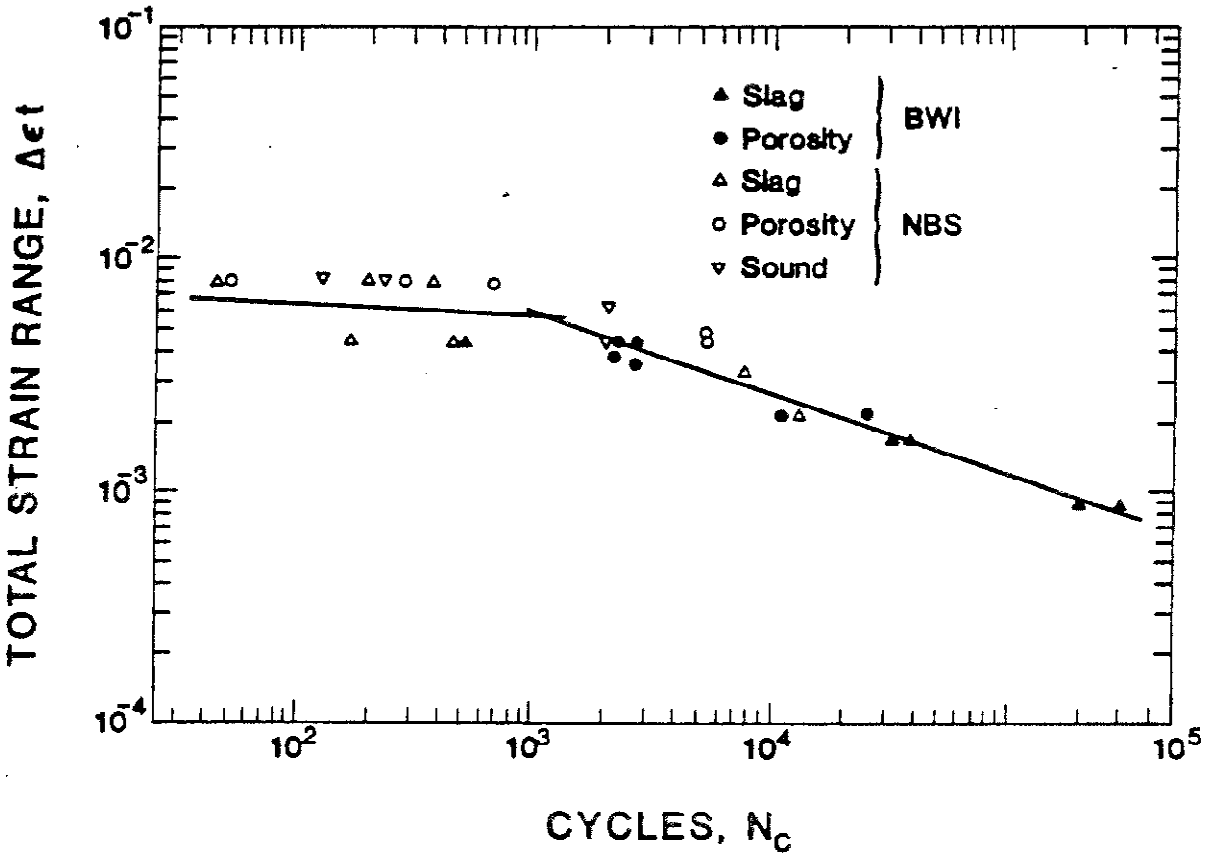

Fig. 67 - Combined results of the NBS low-cycle fatigue study and results published by the BWI in a similar study.[75,76] Change in slope of the number of cyclic reversals to develop cracks in 40 to 60% of the cross-sectional area, N_c, as a function of total strain range is attributed to a change in the failure mode at high strain levels. All data are from welds with the reinforcement removed.

to multiple initiation and coalescence of cracks from individual flaws at the higher strain range ($\pm 2\varepsilon_y$). Newman and Gurney[84] have also noted that multiple initiation of fatigue cracks is usually observed at high stresses, leading to rapid crack coalescence. Thus, the conclusion of Harrison et al.[76] that extrapolating information on flaw significance established under high cycle conditions to endurances of 10^2 cycles on a strain basis may be incorrect for highly flawed welds; a valid extrapolation may be confined to endurances above 10^3 cycles. It also suggests that the constant in Eq. 98 determined from the $\Delta\varepsilon_t$-vs.-N_c curve above 10^3 cycles may not be a valid indication of failure ductility on the first loading cycle for flawed welds.

4.6 Summary

The probability of fracture initiation from buried slag and porosity or from arc burns has been assessed in manually and automatically welded pipeline girth welds. Highly flawed welds and sound welds were subjected to fully reversed, strain-controlled, low-cycle fatigue at strain levels just above weldment yield and at twice yield. The primary criterion for flaw sensitivity was a comparison of the number of cyclic reversals for crack initiation in the flawed welds and in the sound welds. Additional information on the contribution of the flaws to crack initiation was obtained from fractographic analysis of tests conducted with the weld reinforcement removed.

Porosity and slag had no discernable effect on the cyclic life to initiation at the lower strain level. There was evidence of some reduction in cyclic life in the flawed welds, in particular welds containing slag, at the higher strain level. But, even under this most severe test condition, a minimum of 30 cyclic reversals was required to initiate cracking. Arc burns played no part in crack initiation in any of the weldments, regardless of test condition. A comparison between the performance of flawed welds, sound

welds, and unwelded pipe material showed that the geometrical discontinuity formed by the weld reinforcement dominated the crack initiation process, regardless of flaw type or content.

Fractographic examination showed no initiation from individual pores at the lower strain level, but such initiation was observed at the higher strain level. Fisheye cracks surrounding micropores and slag inclusions were observed on the fracture surface of all manual welds tested, indicating localized segregation of hydrogen to such flaws during welding with the high-hydrogen cellulosic electrodes. Such flaws appeared to have a minimal effect on cyclic life to crack initiation, unless they penetrated the surface.

Because the strain levels were above yield and because the flaw levels were equal to or in excess of those anticipated under worst-case field conditions, these data indicate that the probability of crack initiation from such flaws in statically stressed pipelines containing realistic flaw contents is vanishingly remote. Note that the validity of this conclusion has been demonstrated at only one level of weldment toughness and hardenability. Particularly in the case of arc burns, it cannot be assumed that the conclusions reached in this study can safety be extrapolated to weldments of lower toughness.

5. INTRINSIC LIMITATIONS ON DIMENSIONS OF BLUNT FLAWS

M. B. Kasen, G. E. Hicho, and R. C. Placious

5.1 Introduction

Flaws of a three-dimensional, blunt configuration, such as porosity, slag and arc burns, presently account for the majority of remedial welding under workmanship criteria. This partially reflects the sensitivity of radiography to detection of such flaws. Section 4 of this report considered the more general question of the significance of such flaws, assessing their influence on the mechanical stability of weldments under fatigue conditions. We here consider the question of how blunt flaws might be measured, assuming they are considered significant in a fracture mechanics analysis.

Poor sensitivity and diffuse reflection from the flaw periphery limit the detection and measurement of the through-wall depth of porosity and slag by ultrasonic means. Radiography is able to detect such flaws, but gives direct information only on their projected dimensions. Through-wall flaw depth can be estimated by scaling the radiographic density of the flaw to a known density difference--for example, to the density difference caused by a radiographic penetrameter shim of known thickness or to density differences produced by a step wedge exposed and developed under the same conditions as the radiograph of interest. Such an approach was used in applying fracture mechanics principles to assessing the need for remedial welding of flawed girth welds in the Trans-Alaska Oil Pipeline.[4] However, intrinsic and human variables plus uncertainties about conditions under which the field radiographs were made introduced large uncertainties into the measurements. This led to extreme conservatism in assessing blunt flaw significance. Subsequent analysis of the procedures used[85] has shown that some sources of inaccuracy could be ameliorated by improving control over the radiographic inspection

process, and procedures using advanced state-of-the-art electronic techniques could be used to reduce the subjectivity of such measurements.[37] Unfortunately, such improvements would increase the cost of pipeline inspection while providing relatively modest gains in measurement accuracy.

It was therefore of interest to consider more cost-effective ways of assessing blunt-flaw through-wall dimensions. One such approach is based on the rationale that the depth dimension of porosity and slag should be related to the radiographically projected dimensions and that the maximum flaw depth should be intrinsically limited to the depth of the weld pass in which the flaws occur. The Trans-Alaska pipeline work[4] had shown that the depth of arc burns could be correlated with burn widths measured from field radiographs. The present work sought to confirm the validity of the principle for porosity and slag.

5.2 Experimental Procedures

Pipeline segments containing porosity and slag were cut out circumferentially adjacent to the weld reinforcement. The segments were taken from the welds fabricated as detailed in Table 5 and were selected to provide examples of isolated flaws. Samples containing the flaws were then radiographed normal to the weld and in the plane of the pipe so as to reveal both projected flaw length (or width) and flaw depth (through-wall flaw dimension). Slag in the form of "wagon tracks" in the manual welds required sectioning of the welds down the centerline and studying each half independently. The samples of porosity were obtained from automatic welds. Several methods were investigated for measuring the flaws; the method finally selected was an image-enhanced television projection of the flaw images at enlargements up to four diameters. Correlation of flaw dimensions with that of the weld-pass depth was established by measuring pass depth directly from

polished and etched weld cross sections. It was recognized that the true flaw size is somewhat larger than that revealed by the projected dimensions; however, the latter was used because it is the criteria used in all flaw measuring from radiographs, as required for a fracture mechanics analysis. Thirty-nine specimens containing slag and ten containing porosity were studied.

5.3 Results

The experimentally determined relationship between the through-wall depth, D_f, of porosity and slag and the thickness of the weld pass, H, in which the flaws occur is shown in Fig. 68. Similar data illustrating the relationship between the radiographically projected dimensions are illustrated in Fig. 69.

Both techniques confirmed that the through-wall depth of porosity and slag was essentially confined to a dimension equal to or less than that of the depth of the weld pass in which they occur. Flaw depth was also confined to a dimension less than that of the average weld-pass thickness measured between the plate surfaces. The widths of slag stringers, W_f, were always less than slag depth, whereas the length of the pores, L_f, was equal to or larger than their depth. The projected length and depth of pores appeared to be linearly related for very small pores, but this relationship broke down as the pore size approached that of the weld-pass depth. Slag depth could not be predicted from slag width.

Fractures of the porous weld illustrated in Fig. 70 provides additional evidence that porosity in an underlying pass is not likely to be extended into a successive sound pass during multipass welding. Here, the succeeding pass has cut into the porous region of the underlying pass, but the quality of the successive pass was not affected. The difficulty experienced in producing

(a)

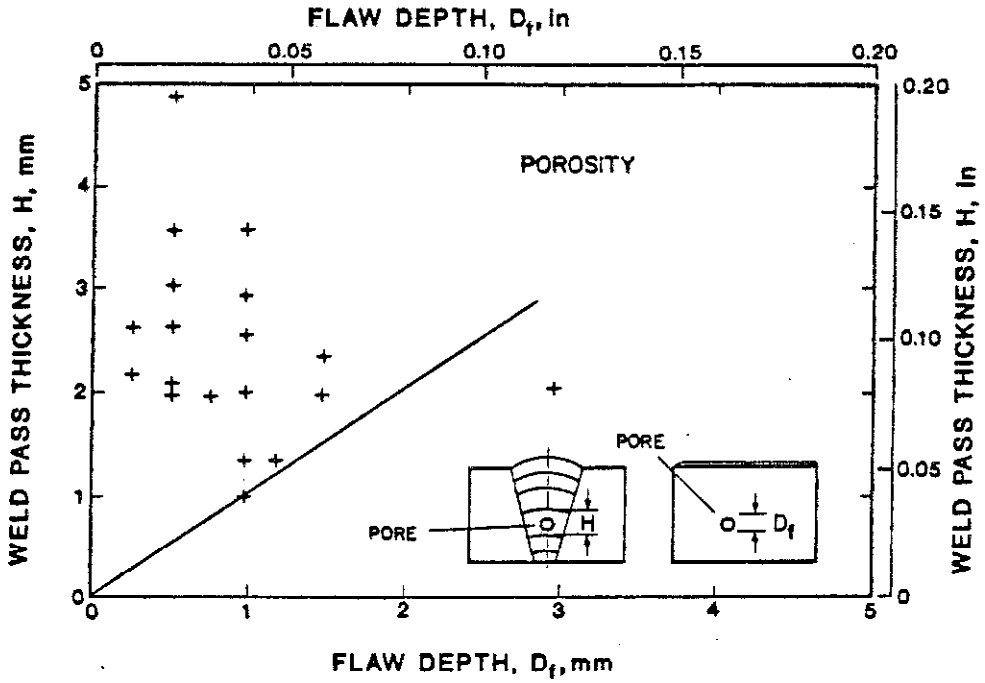

(b)

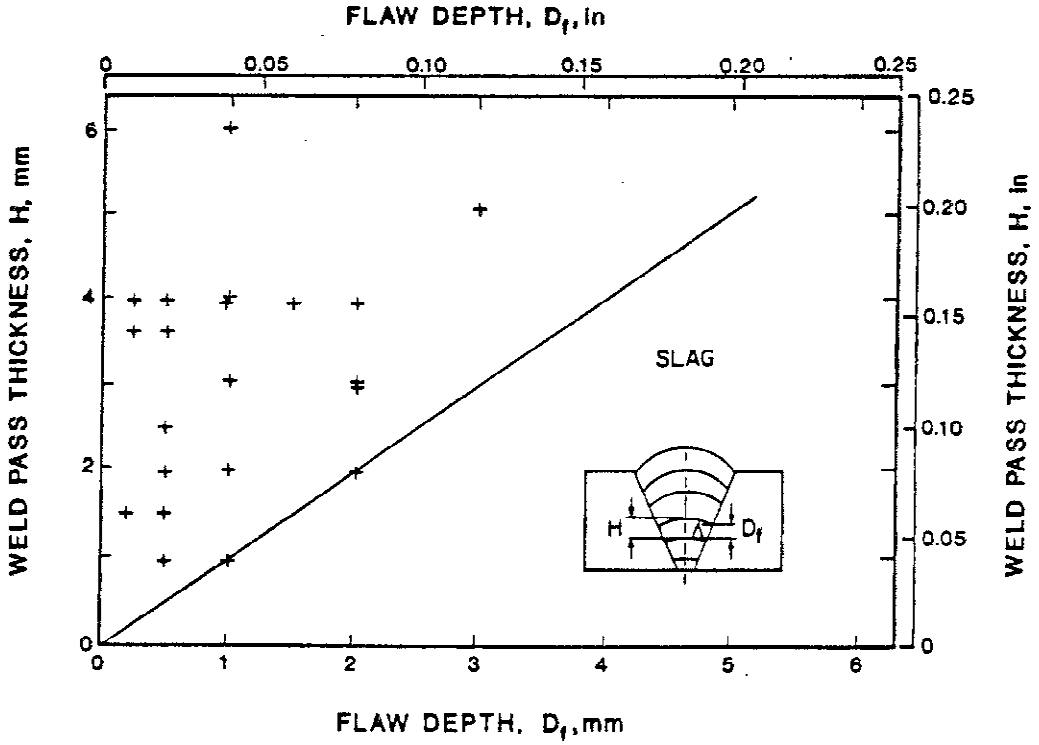

Fig. 68 - Experimentally determined relationship between the through-wall depth of porosity and slag and the thickness of the weld pass in which the flaw occurred.

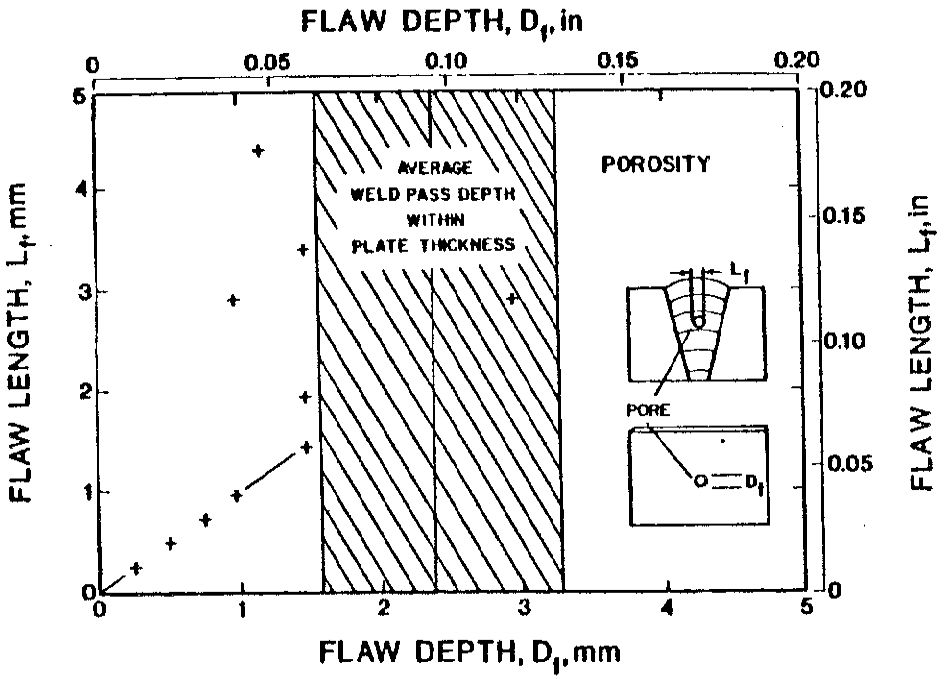

(a)

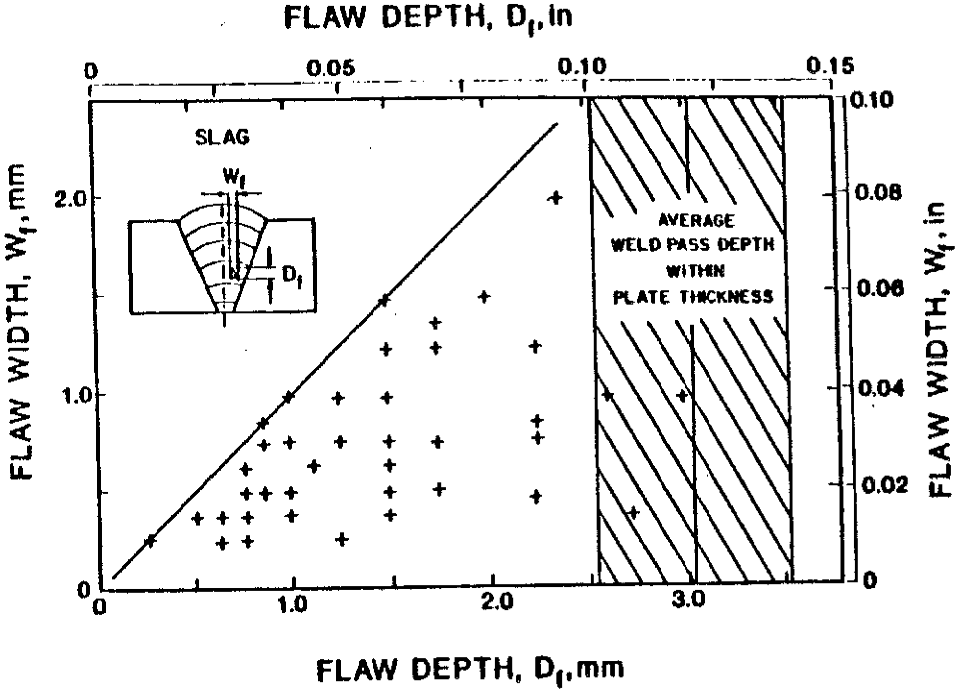

(b)

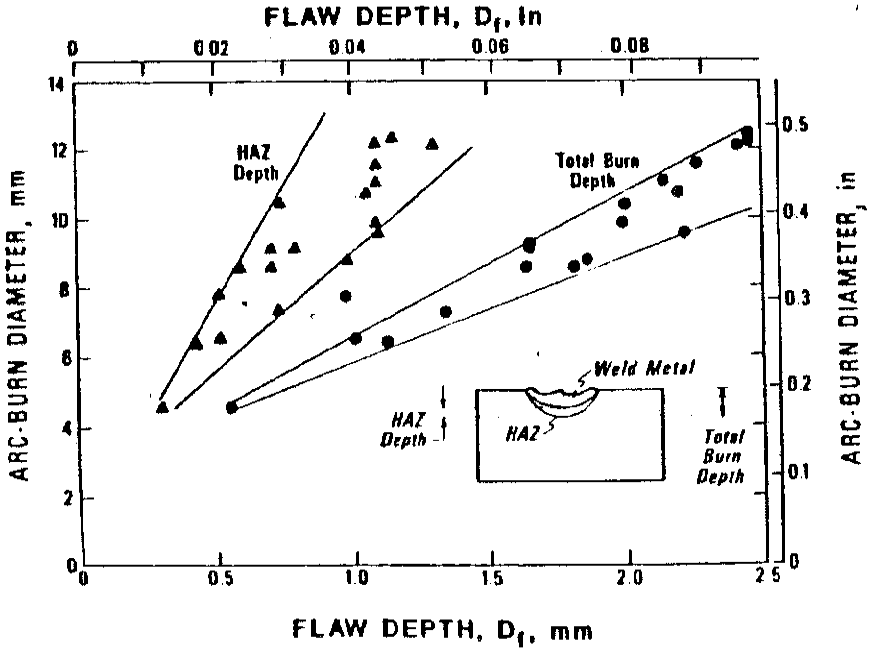

(c)

Fig. 69 - Experimentally determined relationship between the radiographically projected dimensions of blunt flaws and the through-wall depth. Hatched regions in (a) and (b) represent one standard deviation around the mean weld-pass depth. Part (c) is reproduced from Ref. 4.

high levels of buried porosity during manual welding (see Section 4) suggests that this assumption is generally valid.

Results of prior studies on the inherent depth limiations of arc burns are illustrated on Fig. 69c.[4] In practice, the arc-burn depth is taken as the intercept between the burn diameter (or maximum width) on the ordinate of this figure and the lower bound of the scatter band depicting total burn depth. Arc-burn length is measured directly from the radiograph.

5.4 Summary

It has been shown by direct measurement on automatic and manual welds that the maximum through-wall depth of slag and porosity is intrinsically limited to a maximum dimension equal to the depth of the weld pass in which such flaws occur. It was found that the depth of porosity or slag could not be predicted from the projected dimensions of such flaws on a radiograph.

These results confirm that characterizing the average weld-pass thickness associated with a specified welding procedure can provide an upper limit to the through-wall dimensions of porosity and slag, should such information be desired in a fracture mechanics analysis. It is probable that a more precise measurement would rarely be justified in practice, because it is probable that most flaws having depths equal to that of the average typical pipeline girth-weld-pass thickness would likely be acceptable.

These present results complement previous studies demonstrating an inherent limitation to the through-wall depth of arc burns based on burn width.

6. PRACTICAL LIMITATIONS ON BLUNT FLAW CONTENT USING RADIOGRAPHIC INSPECTION

M. B. Kasen

Although the studies described in Section 4 of this report indicate that blunt flaws have a low probability of initiating brittle fracture, their presence may interfere with detection of significant, sharp flaws during the inspection process. This is much less of a concern when ultrasonic techniques are used, because the proximity of blunt and sharp flaws should enhance rather than diminish the flaw signal. But when radiography is used as the inspection method, the high radiographic density produced by blunt flaws can mask the presence of sharp flaws unless limits are placed on the permissable size and distribution of blunt flaws.

Slag does not present a problem in this context because of its localized nature in the weld. However, a primary concern is the possibility that excessive scattered porosity can mask the presence of sharp flaws, such as lack of fusion, incomplete penetration, or cracks, when radiography is used as the primary inspection tool. Studies by the British Welding Institute[72] have suggested that obscuration must be limited to less than 10% of the projected radiographic area to avoid this possibility. The British Standards Institution has, therefore, recommended limiting the permitted obscuration to less than 5% for ferritic steel weldments having a Charpy V-notch energy absorption of not less than 40 J (29 ft-lbf) at the minimum service temperature. For materials of lower toughness, porosity should be assessed as a planar flaw on the basis of flaw interaction.[8] The Working Group on the Significance of Defects under Commission X of the International Institute of Welding has reached a similar conclusion in proposing acceptance levels for

defects that may fail by brittle fracture.[74] This group recommended accepting porosity contents up to 5% of the projected area of the radiograph for welds in ferritic steel having yield strengths up to 482 MPa (70×10^3 psi), provided that the weld metal has a minimum Charpy energy absorption of 41 J (30 ft-lbf) at the minimum service temperature. In other cases of lower toughness, 3% obscuration would be acceptable. These would appear to be reasonable figures, because welds containing less than this level of porosity are easily obtained by good practice, and the probability of 5% obscuration masking sharp flaws in tough weld metal is very low. Since Section 4 has shown that there is a negligible effect on crack initiation due to a 13 to 15% obscuration by porosity, a 3 to 5% level would also appear to be conservative from a performance point of view.

Several procedures have been suggested for correlating the percentage of radiographic obscuration due to porosity in welds with porosity content by volume.[72,86] However, such methods are, for the most part, tedious and time-consuming and provide more detailed information than is required for field interpretation of weld quality. If a 5% maximum obscuration level is chosen, a reasonable means of distinguishing between the appearance of a weld containing porosity at a 3% and at a 5% obscuration level should be sufficient. One possibility is to compare the radiograph with a series of sketches illustrating the appearance of porosity distributions covering the range of interest. Such a series, based on similar sketches currently used in API 1104 and in other weld-quality standards, is shown in Fig. 71. These illustrations suggest that, if an acceptance level of 4% were specified, an interpreter might err one percentage point higher to a 5% level, but would be much less likely to err 2% to a 6% obscuration level. This is because the human eye is much more capable of judging small differences in obscuration at low obscuration levels than at high levels.

The importance of the dot distribution size in the reference standard is illustrated in Fig. 71. Here, it appears that the percentage obscuration increases from top to bottom, whereas in fact each sketch has the same 5% obscuration. This difference in visual perception is caused by a progressively finer dot distribution from top to bottom among the sketches, illustrating that reference sketches containing more simulated large pores than would be likely in the radiographs would give the interpreter a conservative bias.

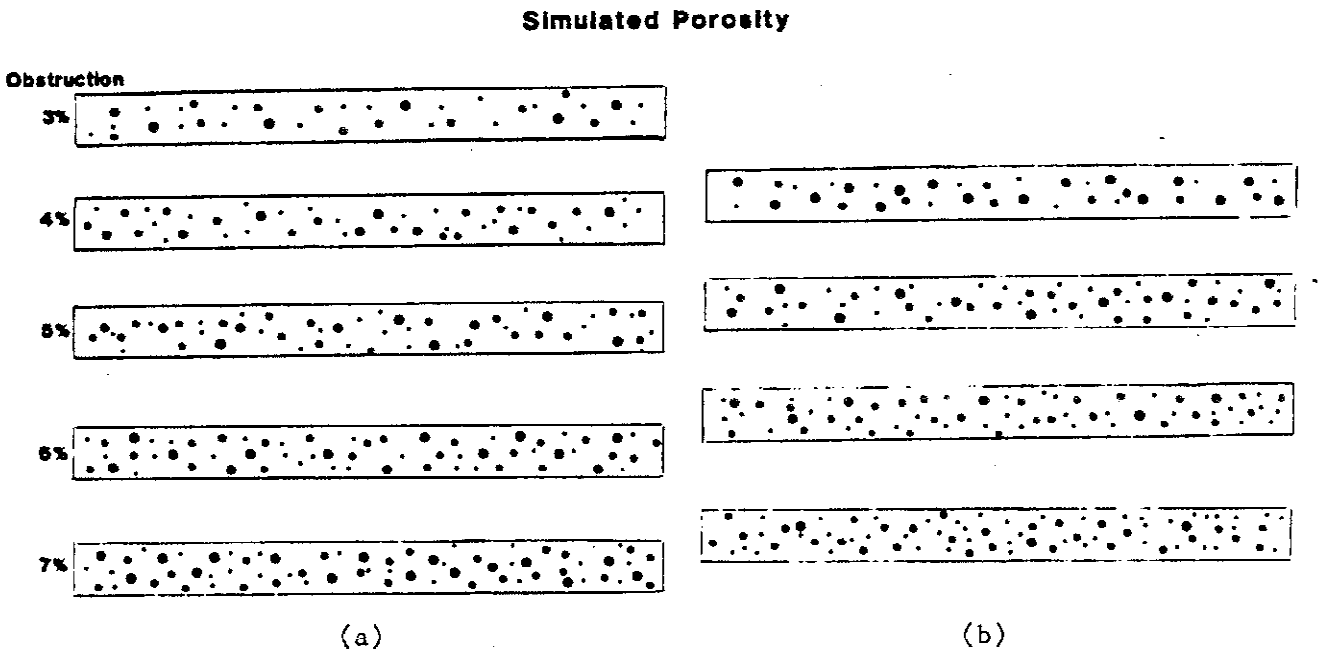

Fig. 71 - Possible development of a radiographic reference standard for establishing limits to permissible obscuration due to scattered porosity. Series (a) illustrates the relative ease of distinguishing percentage differences in obscuration in the 3 to 7% range. Series (b) illustrates that the eye is biased toward a higher degree of obscuration as the size of the scattered porosity decreases. Each of the sketches in (b) contains 5% obscuration.

7. CONCLUSIONS

Studies have been conducted to establish fitness-for-service criteria for large-diameter pipeline girth welds.

1. A fracture mechanics analysis model that relates allowable flaw sizes to applied stress level and fracture toughness has been developed, verified experimentally, and used to calculate allowable flaw-size curves for the proposed ANGTS pipeline. The model is based on a yielded-ligament principle and incorporates a trhough-thickness plasticity correction. Experiments on surface cracks in tensile panels, welded pipe segments, and large-diameter (900 mm, 35-in) pipes confirmed the validity of this model. The applicability of the model is limited to pipelines with maximum stresses in the longitudinal direction below the specified minimum yield strength of the pipe. It is further limited to pipelines where the yield strengths of the weld and base metal are similar. The degree of similarity in yield strengths has not been established, but the desirability of higher yield strength in the weld metal has been clearly demonstrated. The use of allowable flaw-size curves can be considered for either general pipeline use or for site-specific engineering assessment. Allowable flaw-size curves generated using typical pipeline operating conditions and weldment properties are more conservative for long flaw lengths than those derived using the procedures of Appendix A of the 16th edition of API 1104.[2]

2. Radiography has serious deficiencies as an inspection tool in a fitness-for-service analysis. Experience and laboratory studies have shown that it is relatively insensitive to significant sharp flaws in a fracture mechanics evaluation. Through-wall flaw dimensioning from radiographs has also been found to be inaccurate. Ultrasonic methods are sensitive to sharp

flaws and are more adaptable to measuring flaws. However, conventional systems are too slow and complex for routine pipeline inspections. In this study, a new ultrasonic inspection system was developed for this task. The system utilizes electromagnetic transducers (EMATs) to generate long-wavelength shear (SH) waves. Unlike conventional techniques, this approach does not require contact between the ultrasonic transducer and the pipeline. The long-wavelength, low-frequency signal simplifies flaw detection because the signal scales monotonically with increasing through-wall dimension in the range of interest. Specifically, it has been shown that vertically oriented 0.75-mm (0.030-in) deep and 25-mm (0.98-in) long surface flaws and 2-mm (0.08-in) deep and 25-mm (0.98-in) long interior flaws can be reliably detected and measured. Detectability limits for shorter flaws have been determined and related to representative workmanship and alternative acceptance standards. Furthermore, it has been demonstrated that the flaw signal is relatively unaffected by differences in type, orientation, and roughness of the flaws. The use of SH waves enhances sensitivity to sharp flaws oriented perpendicular to the surface, while providing relatively low sensitivity to blunt flaws. This facilitates detectability of the most significant flaws in a fitness-for-service analysis. The system is much less sensitive to the presence of weld reinforcements than are conventional systems. It is adaptable to full or partial automation, and it increases the reliability of flaw detection and sizing because it depends less on operator skill. At its present state of development, the SH-wave EMAT inspection system has the following deficiencies: 1) performance has not been demonstrated with real flaws under field conditions, 2) field proven hardware remains to be developed, 3) personnel trained in the system are not readily available,

4) equipment calibration standards remain to be developed, and 5) sensitivity of the system to detecting tight cracks closed by compression stresses has not been determined.

3. The presence of large quantities of buried porosity and slag, or of arc burns in manual welds has been shown to have a negligible effect on the low-cycle fatigue life of the pipeline girth welds evaluated in this study. A similar result has been shown for porosity in automatic welds. Because the applied strains were well in excess of yield strengths, and the flaw levels were in excess of those anticipated under worst-case field conditions, these results indicate that the probability of crack initiation from such flaws would be negligible if such welds were subjected to the essentially static loading conditions of operating pipelines. These results suggest that such blunt flaws may be considered innocuous as fracture initiation sites in girth welds fabricated with materials of the toughness studied in this program. The validity of this conclusion has not been experimentally demonstrated for welds of lower toughness; however, the conclusion is consistent with that of others who have addressed the problem of blunt flaw significance in weldment failure. It is emphasized that these conclusions pertain only to buried porosity and slag and to arc burns not associated with cracks. Porosity breaking the surface or arc burns containing cracks should be treated as equivalent-sized sharp flaws.

For welds having substantially lower toughness than that evaluated in this program, blunt flaws may be conservatively treated as sharp flaws of equal dimensions. This work has shown that the maximum through-wall dimension of porosity and slag is intrinsically limited by the depth of the weld pass in which they occur or to flaw-width criteria in the case of arc burns. The

upper limit to flaw depth provided by these criteria can therefore be conservatively used in a fracture mechanics analysis, eliminating the need for measuring the through-wall depth of flaws in the field.

Low-cycle fatigue caused fisheye cracks to form adjacent to micropores and slag in all welds made with E8010G cellulosic electrodes, even though testing was performed one and one-half years after welding. This indicated a stable, residual hydrogen content in the weld metal. Available data indicate that such flaws can also occur if static loads approach or exceed weld-metal yield, suggesting the possibility that such flaws could develop during the pipe-laying operation subsequent to the inspection process. Except when they penetrated the surface, such cracks did not appear to affect the fatigue strength significantly, suggesting that they are basically innocuous flaws in weldments of the toughness tested. However, it cannot be assumed that cracking from this source will remain innocuous in weld metal of lower toughness. Conditions under which fisheye cracks develop in high-hydrogen electrode pipeline welds deserve future study.

8. RECOMMENDATIONS

8.1 Implementation of Inspection Methods

The practical implementation of a fitness-for-service inspection system for a pipeline involves many factors outside the scope of this report. Nevertheless, it is instructive to consider the technical factors that might influence the manner in which the inspection system is integrated into an overall quality control program. Three possible options, based solely on perceived technical merit, are listed in Table 12.

8.1.1 Option I

The first option assumes that all of the welds will be inspected by an automated ultrasonic system to provide the basic flaw detection and measuring capability required for the fitness-for-service analysis. It is also envisioned that some fraction of each welder's production be inspected by conventional radiography to provide control over workmanship, serviceability of welding equipment, and quality of consumables. Since welds inspected by radiography would also be inspected by ultrasonic means, radiography would not be used to establish an accept/reject criterion for weld quality. This option is technically preferable because it differentiates between the purpose of each inspection technique and uses each in the area of its greatest strength.

Documentation provided by Section 3 of this report suggests that an ultrasonic system based on low-frequency SH waves generated by electromagnetic

Table 12 - Technical Options for Field Implementation

	Fitness-for-Service Criteria				
	NDE Method		Flaw Assessment		Workmanship
Option	Primary	Backup	Sharp	Blunt	Criterion
I	Automated UT†(EMAT)	None	ℓ vs. a	None	10% RT*
II	Conventional RT	Manual UT (EMAT)	ℓ vs. a	L_f vs. D_f‡	RT
III	Conventional RT	None	ℓ only	L_f vs. D_f	RT

*RT = radiographic inspection
†UT = ultrasonic inspection
‡Assume D_f is limited to average pass thickness

transducers (EMATs) would provide a promising option for flaw detection and measuring with the best adaptability to automation. Such a system will not respond to the presence of blunt flaws unless they are very large or locally concentrated. This is a distinct advantage because, as documented in Section 4 of this report, blunt flaws may be considered intrinsically innocuous, from a fitness-for-service point of view, if minimum toughness levels are maintained. There is no possibility of sharp flaws being obscured by the presence of blunt flaws, because proximity of the two flaw types will enhance the ultrasonic signal.

This option assumes that blunt flaws not detected by the ultrasonic inspection method can be neglected, based on the work described in Section 4. Strictly speaking, this assumption has only been validated for weld metal of the toughness studied in this program; however, the conservatism built into the present investigation, along with the conclusions reached by others who have studied the problem, suggests that the assumption would probably be valid for any reasonable minimum toughness specified for pipeline construction. Additional conservatism arises from the realization that slag, which this work has shown to be the most likely of the blunt flaws to initiate fracture, is relatively easily detected by ultrasonic means due to its solid nature.

8.1.2 Option II

Option II considers the case where Option I is premature for existing technology. Here, radiography is assumed to be the main inspection system, and ultrasonic methods are used selectively to measure the through-wall depths of sharp flaws that are detected by radiography. Flaw length would be measured directly from the radiographs. This option is less technically desirable because of the relatively poor sensitivity of radiography to sharp

flaws, which are the most significant from a fitness-for-service point of view. Again, it would appear that development of a portable, manual variant of the ultrasonic system described in Section 3 of this report would be very useful in this option.

Some restriction must be placed on the allowable content of blunt flaws when radiography is used as the primary inspection tool. Section 6 has discussed the limitations imposed on porosity content due to obscuration concerns. The extent to which large individual pores reduce the weld cross-sectional area and, therefore, reduce the weldment tensile strength must also be considered in some circumstances. This is unlikely to be a problem in girth welds made in thick-wall line pipe where the average weld pass thickness (and therefore the maximum through-wall dimension of a pore) is a small percentage of total wall thickness. But it could become a problem where thinner wall pipe is used or where welds are fabricated with automatic processes producing deep, narrow weld passes. Such concerns can be avoided by limiting the allowable dimensions of individual pores to that of a permissible sharp flaw based on a fracture mechanics accept/reject criteria, assuming pore depth to be equivalent to that of the weld pass.

In addition to limits on the quantity and size of allowable porosity, consideration must also be given to its distribution. A localized cluster of porosity exceeding the obscuration limit could conservatively be treated as a single crack of length equal to the maximum cluster dimension and having a depth equal to that of the average weld pass. Since a linear distribution of porosity is frequently found to be associated with incomplete penetration,[87] it would be prudent to treat closely spaced groups as an equivalent-sized single crack.

In view of the tolerance of tough weld metal to relatively large sharp flaws (see Section 2), it is unlikely that applying a fracture mechanics assessment to the significance of porosity will result in appreciable remedial welding.

Where it is desired to do so, limitations on the allowable length of entrapped slag may also be conservatively established by considering the slag inclusion to be a sharp flaw of the length indicated on the radiograph to have a through-wall dimension equal to that of the average weld pass depth.

As with porosity, this procedure is not expected to contribute substantially to the amount of remedial welding required where weld metal of appropriate toughness is used. Should it be desirable to place a limitation on acceptable slag width, the present work suggests that a rational limitation would be the same as for slag depth. Although Fig. 68b (Section 5) shows that it is not possible to determine slag depth from projected width, it indicates that the maximum width will not exceed that of the weld pass depth.

Excessively wide slag width may, therefore, be taken as an indication of an excessively deep weld pass. Note that applying this approach to the manual girth welds studied in the present work would result in a practical limitation of 3 mm (0.1 in) on slag width and depth--the same as has been proposed as upper limits on these parameters under the brittle fracture criteria in the British Standard Institution Document PD 6493 (1980).[88]

Where it is deemed necessary to analyze the significance of arc burns on a fitness-for-service basis, they may also be treated as equivalent-sized sharp flaws having lengths equal to that of the burns and having through-wall depths scaled from the maximum burn widths by use of Fig. 68c (Section 5). A precedent for this approach was established by the Trans-Alaska Pipeline (TAPS) work.[89]

These suggested limitations on the content of blunt flaws when inspection is conducted by radiography are summarized in Table 13.

8.1.3 Option III

This option assumes that appropriate ultrasonic methods for sizing planar flaws are not available and that all inspection criteria must depend on information obtained by radiographic techniques. This option is least technically desirable, since sharp flaws are not easily detected and sharp-flaw depth cannot be accurately measured using radiography. Unlike blunt flaws, one cannot, in general, assume an inherent limitation on the through-wall dimension of sharp flaws. The only alternative is to limit sharp flaw length by the criteria of existing workmanship standards.

On the other hand, the suggested treatment of blunt flaws presented under Option II and detailed in Table 13 are equally relevant to this option. Since the majority of current remedial welding is done to remove blunt flaws having sizes in excess of that permitted by workmanship codes, this proposed alternative criteria for acceptability of blunt flaws could substantially reduce pipeline construction costs by providing a more rational approach to deciding when remedial welding is justified to remove such flaws.

Table 13 - Suggested Limitations on Allowable Content of Blunt Flaws

POROSITY	
Quantity	
	Less than 5% radiographic obscuration
Size	
	Equivalent single crack*
Distribution	
Clusters:	Over 5% obscuration treat as equivalent single crack*
Linear:	Treat groups separated by less than twice wall thickness as equivalent single crack*
SLAG	
	Treat as equivalent single crack*
ARC BURNS	
	Treat as equivalent single crack*

*Through-wall depth inherently limited to average weld pass depth.

8.2 Implementation of Fitness-for-Service Criteria

A fracture mechanics approach to assessing the significance of weld flaws to pipeline integrity can be applied in several ways, depending on the objective of the user. Its use in determining the technical basis for requiring remedial welding in the event of code violations revealed during a postconstruction audit has already been demonstrated during the TAPS program. However, the full potential of the approach requires applying the principles before and during pipeline construction to reduce the need for remedial welding consistent with pipeline structural integrity and safety and, hence, to reduce construction cost.

The latter philosophy can be implemented in two basic ways: One is to establish accept/reject criteria for weld flaws before the construction begins. This would require defining the maximum applied and residual stresses and strains for designated portions of a line where such judgments can be effectively made and combining that information with a characterization of the minimum fracture toughness of the weld metal, as deposited by the consumables and processes selected for the line. Allowable flaw-size curves based on such data could then be routinely applied during construction. Procedures assuring maintenance of minimum weld-metal fracture toughness during construction would probably be required. Consideration might be given to generating a series of allowable flaw-size curves reflecting differences in weld-metal toughness, which would permit welds of lower than expected toughness to be accepted, provided that the increased restrictions on flaw size associated with the lower toughness were not exceeded. Advantages of this generalized approach are overall economy and simplicity of field implementation. The criteria established by this approach may be overly conservative for some portions of the line; however, this can be minimized by proper selection of line segments.

Alternatively, a specific-site approach may be selected, either in conjunction with the generalized approach or independently applied. This involves an engineering critical assessment of welds at highly stressed locations, locations where the welds are subjected to unusually low temperatures or where other environmental factors must be taken into consideration. Since toughness, stress, and allowable flaw size are related by the fracture mechanics model, allowable flaw-size curves can be constructed to address any desired set of conditions. It would be necessary to generate appropriate accept/reject criteria reflecting the specific prevailing conditions. Such an approach would probably result in requests for variances from accepted code requirements. Therefore, at the start, it might prove useful to generate a family of allowable flaw-size curves covering the variables anticipated during construction. Availability of such a family might significantly facilitate implementing either the generalized or specific-site approach.

When qualifying weld metal to a fracture toughness criteria, it should be recognized that weld metal deposited with high-hydrogen, cellulosic electrodes will initially have a low toughness due to the high-hydrogen content in the weld deposit. Toughness will increase with aging time after welding, because the hydrogen content is lowered by diffusion.[90] Therefore, qualifying conditions should include a delay time subsequent to welding, selected to represent the toughness at the time of maximum weldment stress in the line. Since residual hydrogen content is affected by a number of factors, it may be necessary to characterize the change in toughness with aging time for a particular welding procedure.

8.3 Future Research

8.3.1 Fracture Mechanics

Procedures for the use of elastic-plastic fracture mechanics for the derivation of allowable flaw-size curves are in the early stages of development. Further work is recommended to increase confidence in the analytical results. Future research needs in the areas of analytical model development, model verification, and implementation are summarized below.

Analytical Model Development The present analytical model presented is a relationship among stress, flaw size, and toughness. For applicability to situations where the strains exceed yield, a relationship among strain, flaw size, and toughness is needed. Further developments should be incorporated into the strain-based model: First, the behavior of small flaws in a large section (such as large-diameter pipe) needs to be modeled to account for gross-section yielding. Second, the differing stress-strain relationships of the weld and the base plate should be incorporated into the model. Third, the influence of residual stresses on fracture at high strain levels should be assessed.

Model Verification The model verification studies in the present program were limited to the analysis of results of large-diameter-pipe tests conducted as part of an independent program. Direct observations of the spread of plasticity are needed for proper modeling of the plastic-zone circumferentially cracked pipe in bending. Further tests are needed to verify the curvature correction proposed herein. And finally, verification of the

fundamental assumption of the fracture mechanics approach would greatly contribute to confidence in the analysis, that is, verification that large-diameter pipe does fracture at a critical value of CTOD measured in a fracture toughness test.

Implementation. Given an allowable flaw-size curve, an implementation strategy is needed to ensure that the assumptions used in the derivation are adhered to during pipeline construction. Improvements in the CTOD testing method are needed, particularly for evaluating weld-metal toughness. A statistical sampling procedure is needed to ensure that the yield strength and toughness of the pipeline girth welds exceed the values used to establish the allowable flaw-size curves.

8.3.2 Inspection

Recent studies have shown that it is feasible to increase substantially the detection sensitivities of the SH-wave EMAT system with respect to planar flaws that are canted with respect to the through-thickness direction. Examples of such flaws include cracks in the heat-affected zone (HAZ) and incomplete fusion. To improve the detectability of such flaws, the present SH-wave EMAT system would have to be augmented by an additional SH-wave EMAT that would be sensitive to the SH_2, SH_3, and SH_4 plate waves. It can be shown theoretically that these three plate waves are scattered much more strongly by canted planar flaws than the dominant SH_0 and SH_1 modes.[91] The technology for constructing such transducers is now available.[92]

Another topic that requires further quantitative investigation is the effect of residual and applied residual stresses on the functioning of the SH-wave EMATs. It is believed that under certain circumstances, the efficiencies and pure-mode characteristics of the periodic-permanent-magnet

EMATs may be significantly degraded. As a consequence, the EMAT performance characteristics should be verified experimentally using a pipe section welded by approved procedures and subjected to realistic membrane and residual stresses. Current understanding of how SH-wave EMATs function on a surface under stress is very limited.

It is believed that additional work is needed in the area of signal analysis. For example, accurate estimation of the SH-plate wave scattering coefficients could be obtained by nonlinear least-squares fitting of the measured signal amplitudes as function of the distances separating the EMATs from the weld along scan lines that are perpendicular to the pipe girth. Then, the confidence levels in the ultrasonic measurements would be improved. Also, better estimates of flaw shape, cant angle, position within the weld, and other relevant characteristics would be obtained. The least-squares fitting approach is particularly appropriate since an accurate, predictive model for the flaw scattering amplitudes is now available.

Finally, it is believed that construction of a fieldable prototype of the 454-kHz SH-wave EMAT system is necessary. The fieldable system would be needed to establish the influence of specific environmental conditions and welding practices on the inherent limitations of SH-wave EMATs and suggest possible improvements. The prototype system would be evaluated as a limited section of pipeline that has been fully characterized using other available nondestructive testing (NDT) procedures, including ultrasonics, radiography, and penetrant and visual examination.

8.3.3 Metallurgy

Metallurgical parameters affecting the toughness of weldments in pipeline steels deserves further study. The sensitivity of weld-metal toughness to variations in chemical composition of the filler material, to variations in welding procedure, and to the interaction of such parameters should be better defined to increase confidence in the assumption of an existing minimum toughness level in the fitness-for-service analysis. American Welding Society (AWS) classifications of electrodes used in pipeline construction presently give electrode producers wide latitude in selecting a chemistry that will produce weld metal meeting the minimum mechanical properties of the specification. This is because, up to now, weld strength has been the dominating consideration. For example, the AWS specification for type E8010G electrodes commonly used in manual welding of API 5LX-65 and API 5LX-70 pipelines establishes minimums for Mn, Si, Cr, Ni, Mo, and V, but requires that only one of these elements meet the minimums in order to comply with the specification. It is expected that this compositional latitude will, in itself, cause a substantial variation in weld-metal toughness; however, the extent to which this is true is presently unknown. An equal uncertainty exists with regard to the variation in toughness produced by a given electrode composition at different heat input levels. These uncertainties now require that each manufacturer's proprietary electrode be evaluated for toughness under a specific welding procedure. This is a tedious and expensive process. Resolving these uncertainties will permit establishment of parameters necessary for prequalifying electrode types on the basis of toughness, thus reducing cost while maintaining weldment reliability.

The present study indicates a negligible probability of fracture initiation from arc burns in contemporary pipeline materials. However, a relationship between arc-burn significance and toughness, hardenability, and other metallurgical parameters has not been established. It would be desirable to do so to provide increased confidence in the findings of the present study. For example, it would be valuable to determine if any circumstances exist under which excessive deterioration of heat-affected-zone toughness could significantly exacerbate the significance of arc burns.

The conditions under which fisheye cracks can form in weld metal deposited by the shielded-metal-arc process should be determined. It is of particular importance to determine the probability of their formation as a result of pipe-laying stresses because, should this occur, significant flaws could be introduced into the welds after the inspection process. The literature suggests that this is a distinct possibility, because such flaws have been most often observed during bend testing where the weld metal has been strained beyond yield. The study should correlate the probability of fisheye formation with the hydrogen content of the electrodes and should establish the required postweld heating conditions required to eliminate their formation, should they prove to be a problem in pipeline construction.

9. ACKNOWLEDGMENTS

This study was supported by the Materials Transportation Bureau (MIB) of the U.S. Department of Transportation. Mr. Lloyd Ulrich, Alaska Natural Gas Pipeline Project, (MTB) Office, Alaska Natural Gas Pipeline Projects, was contract manager. Support for the nondestructive inspection studies was partially supplied by the Welding Research Council, Dr. Glenn Oyler, Research Director.

We particularly appreciated the cooperation of the Northwest Alaskan Pipeline Company, Salt Lake City, Utah. The continued support of Mr. Edward B. Clark of that company was deeply appreciated.

Many people made essential contributions to the present study. We gratefully acknowedge the cooperation of Nova, an Alberta Corporation, in providing data from their large-scale test program. The girth welds investigated in this study were fabricated by the H. C. Price Company, Dewey, Oklahoma, under the direction of Mr. Richard Gwin and Mr. Steve Madden. Artificially flawed manual welds were prepared by the Lincoln Electric Company, Cleveland, Ohio, under the direction of Mr. Jerry E. Hinkel. Low-cycle fatigue studies were performed at the Denver facility of the Martin Marietta Corporation by Mr. John Shepic and Mr. Richard Gibb. Radiographic support was provided by the Rocky Flats Division, Rockwell International Corporation, under the direction of Mr. Jack Summers. Calibration specimens required for the ultrasonic study were prepared by Dr. Jerry E. Jones, Colorado School of Mines, Golden, Colorado.

Many NBS people contributed significantly to this study. We particularly acknowledge the contributions of J. David McColskey, Don Harne, Doug Chrisholm, Mel Jadah, Mike Lauriente, Bill Carpenter, and Dr. Richie Mikesell to the success of the experimental program. We are grateful to Ms. JoAnne Wilken for preparation and typing.

10. APPENDIXES

Appendix A - Details of Calculation of Allowable Flaw-Size Curves

D. T. Read

The method used here to calculate allowable flaw-size curves was to calculate many critical flaw sizes (critical length-depth pairs) and then draw a curve through these points. Each point on such a curve is a solution to Eq. 65 of Section 2.5.1 of this report; that is, at each point, the total CTOD is equal to the material fracture toughness.

Because of the complexity of the relationships between CTOD and applied stress and flaw size, closed-form solutions are not found. Instead, an iterative approach is used. For each flaw length value, CTOD is calculated for a series of flaw depths. Using a Newton-Raphson iteration procedure, the computer program guides the selection of new depth values until the calculated CTOD matches the material fracture toughness. When the correct depth is found (to within 1 part in 10^6), the length-depth pair is added to the list of such pairs to be used for the allowable flaw-size curve, and a new value of flaw length is selected. Typically 60 to 100 length-depth pairs are sufficient to define the curve.

The computer program we used is listed below. Each curve requires approximately 40 s of processor time on a modern large-scale scientific computer.

Following the program listing, an example calculation of CTOD for one crack length is shown. This example begins with a listing of input parameters. Then a specific value of flaw length is chosen, and the calculation steps, including check for full-ligament yielding, iterative plastic-zone calculation, calculation of CTOD, and comparison to material fracture toughness, are listed. Table A-1 gives quantities that are needed for the calculation.

A visual aid to this solution process, Fig. A-1 shows the behavior of Eqs. 70 and 75. The calculated r_y value occurs where the two curves intersect.

Computer Program

```
      PROGRAM YIELIG(INPUT,OUTPUT=/1000,TAPE88=/1000,TAPE1,TAPE2)
      REAL NU
C  NOTATION:
C       H IS CRACK DEPTH
C       C IS CRACK HALF LENGTH
C       T IS PLATE THICKNESS
C       R IS PIPE RADIUS
C       W IS PLATE FULL WIDTH
C       C1 IS 2*C/W
C       A1 IS H/T
C       DELTA2 IS (EFFECTIVE CRITICAL CTOD) * E / W / YIELDST
C       E IS YOUNG'S MODULUS
C        NU IS POISSON'S RATIO  (***** REAL NUMBER ******)
C       STRESS IS APPLIED STRESS
C       YIELDST IS YIELD STRENGTH
C       S IS STRESS/YIELDST
C       A() IS ARRAY OF CRACK DEPTH VALUES
C       FL() IS ARRAY OF CRACK LENGTH VALUES
      COMMON PI, DELTA2, C1, S
      COMMON /GEOM/ H, C, T, R
      COMMON /MATPR/ YIELDST, E, NU
      DIMENSION FL(100), A(100), LMESS(8)
      PI = 3.141592654
      PRINT 1
1     FORMAT(* PROGRAM TO CALCLATE AND PLOT A VS L CURVES USING THE YIEL
     1DED LIGAMENT MODEL.*,//)
      PRINT 2
2     FORMAT(* CRITICAL COD, YIELD STRENGTH, AND APPLIED STRESS ARE NOW
     1READ IN.*)
4     READ (1,*) CODCR, YIELDST, STRESS
      IF(EOF(1).NE.0) GOTO 9999
      CODRES = 0.0015
      YSKSI = YIELDST / 1000.
      SKSI = STRESS / 1000.
C
C  SET UP AND MARK THE PLOT
C  PLOTTING SUBROUTINES FROM THE *DISSPLA* (REG. TRADE MARK)
C  PACKAGE ARE USED IN THIS PROGRAM.
C
      CALL ID(*DAVE READ, X3853)A VS L$*,100)
      CALL COMPRS
      CALL NOBRDR
      CALL AREA2D(2., 2.)
      CALL HWSPEC(88,*FILE*)
      CALL ENDPL(0)
      CALL RESET (*NOBRDR*)
C
      CALL TITLE(*ALLOWABLE FLAW SIZES$*,100,
     1  *DEFECT LENGTH, IN$*,100,
     2  *DEFECT DEPTH, IN$*,100,
     3  6.0, 6.0)
C
```

```
      CALL GRAF (0.0, 5.0, 25.0, 0.0, 0.1, 0.6)
C
      ENCODE(80, 410, LMESS) CODCR
410   FORMAT(#CRITICAL CTOD = #,F7.3,# IN.$#)
      CALL MESSAG(LMESS,100,1.6, 5.5)
C
      ENCODE(80,415,LMESS) CODRES
415   FORMAT(#RES. STRS. CTOD RED. = #,F8.4,# IN.$#)
      CALL MESSAG(LMESS,100,1.6, 5.0)
C
      ENCODE(80,420,LMESS) YSKSI
420   FORMAT(#FLOW STRENGTH = #,F5.1,# KSI.$#)


      CALL MESSAG(LMESS,100,1.6, 4.5)
C
      ENCODE(80,430,LMESS) SKSI
430   FORMAT(#APPLIED STRESS = #,F5.1,# KSI.$#)
      CALL MESSAG(LMESS,100,1.6, 4.0)
C
C
C
      PRINT 10, CODCR, YIELDST, STRESS
10    FORMAT(* CRITICAL COD = *, F12.6,* IN*,/,
     1  * YIELD STRENGTH = *,F12.0,* PSI*,/,
     2  * APPLIED STRESS = *, F12.0,* PSI.*)
C   HERE WE SPECIFY A STEEL PIPELINE, 48 INCHES IN DIAMETER
      E = 30.2E6
      NU = 0.29
      R = 24.
      W = 2. * PI * R
      T = .625
C  EFFECTIVE CRITICAL COD IS CRITICAL COD LESS RESIDUAL STRESS EFFECT.
      CODCR = CODCR - CODRES
      DELTA2 = E * CODCR/W/YIELDST
      NPTS = 100
      RELLMAX = 0.15
      S = STRESS / YIELDST
      DO 1000 IPT = 1,NPTS
      C1 = RELLMAX * FLOAT(NPTS - IPT) / FLOAT(NPTS)
      C = W * C1 / 2.
C  THREE CANDIDATE VALUES OF FIRST TRIAL VALUE OF A1 ARE CALCULATED
      A1SIMP = 1. - S + DELTA2/2./C1
      A1LY = 1. - S
      A1NSY = (1. - S) / C1
      A1NSY = AMIN1(A1NSY,1.0)
      A1TR = AMIN1 (A1SIMP, 0.99999*A1NSY)
      DEVTARG = 1.0E-06
      STEPSZ = 1.00
      DEVPREV = 1.0E100
      DO 300 IIT = 1, 15
      DEVVAL = DEV (A1TR)
      DEVSIZ = ABS(DEVVAL)
      IF(DEVSIZ .GT. DEVPREV) GO TO 280
```

```
      DEVREL = ABS(DEVVAL/DELTA2)
      IF(DEVREL. LT. DEVTARG) GOTO 312
      A1TRN = A1TR - STEPSZ * DEVVAL/DDEVDA(A1TR)
      IF(A1TRN.GT.A1NSY.OR.A1TRN.LT.(A1LY/2.)) GOTO 280
      A1TR = A1TRN
      DEVPREV = DEVSIZ
      IF(STEPSZ .LT. 1.0) STEPSZ=AMIN1(1.3*STEPSZ,0.5*(STEPSZ+1.0))
      GOTO 299
280   STEPSZ = STEPSZ/2.
      DEVPREV = 1.0E100
      A1TR = 0.75 * A1LY
299   CONTINUE
300   CONTINUE
      AFAIL = A1TR*T
      FLFAIL = W * C1
      PRINT 306, FLFAIL, AFAIL
306   FORMAT(' FLAW DEPTH ITERATION FAILED TO CONVERGE AT',/,
     ^  ' LENGTH = ',F7.2,'  DEPTH = ',F5.2)
312   A1 = A1TR
      FL(IPT) = W * C1
      A(IPT) = T * A1
      IF(A1.GT.0.75) GOTO 1020
1000  CONTINUE
1020  ILAST = IPT


      DO 1040 I = 1, ILAST
      PRINT 1025, FL(I), A(I)
1025  FORMAT(2E14.5)
1040  CONTINUE
C
C
      CALL CURVE(FL,A,ILAST,0)
      CALL FRAME
      CALL ENDPL(-1)
C
C
      GOTO 4
9999  CALL DONEPL
      CALL EXIT
      END



      FUNCTION DEV(A1)
      REAL NU
      COMMON PI, DELTA2, C1, S
      COMMON /GEOM/ H, C, T, R
      COMMON /MATPR/ YIELDST, E, NU
      H = T * A1
      W = 2. * PI * R
```

```
C  FOR THIS VERSION, ALWAYS USE SIMPLIFIED LINE SPRING
C  USE OF CURVEATURE IN SLS DEPENDS ON CRACK LENGTH
      IF(H  .GT.  0.0) GO TO 100
      CALL NEWMAN(H, C, T, W, F, Q)
      SLY = 1.-A1
C  COD-J FACTOR M SET TO 1 IN DENOMINATOR OF
C    TERM ON RIGHT OF NEXT STATEMENT.
      DELELAS = SLY*SLY*F*F*PI*H/Q/W
      IF (S .GT. SLY) GOTO 200
C  COD-J FACTOR M SET TO 1 IN DENOMINATOR OF
C   2 ND TERM ON RIGHT OF NEXT STATEMENT.
      DEV = DELTA2 - S*S*F*F*PI*H/Q/W
      RETURN
100   CONTINUE
      STRESS = S * YIELDST
      CALL LSJ(YIELDST, E, NU, H, C, T, R, STRESS, 0.0,  CTOD,CMOD,
     ^  STAPLY,STCLOS)
      DELELAS = CTOD*E/W/YIELDST
      IF (STAPLY .GT. 0.0) SLY = STAPLY/YIELDST
      IF (STAPLY .GT. 0.0) GO TO 200
      DEV = DELTA2 - DELELAS
       GO TO 300
200   CONTINUE
      CP1 = (2./PI) * ASIN( SIN(PI*C1/2.) / COS(PI*(1.-(1.-S)/A1)/2.) )
      RY1 = 0.5 * (CP1-C1)
      DEV = DELTA2 - DELELAS - 2.*(C1+RY1)*(S-SLY)
300    CONTINUE
       WRITE(2,310) S, STRESS, STAPLY, SLY
310    FORMAT(' S = ', E14.5, ' STRESS = ', E14.5, ' STAPLY = ',
     ^  E14.5, '  SLY = ', E14.5)
       WRITE(2,315) H, C
315    FORMAT(' H = ', E14.5,' C = ', E14.5)
       WRITE(2,320) DELTA2, DELELAS, DEV
320    FORMAT(' DELTA2 = ', E14.5, 'DELELAS = ', E14.5, ' DEV = ',E14.5)
      END




      FUNCTION DDEVDA(A)
      Y = DEV(A)
      AM = A * 0.99 - 1.0E-03
      IF(AM.LT.0.0) AM=0.0
      YM = DEV(AM)
      DDEVDA = (Y - YM) / (A - AM)
      END
```

```
      SUBROUTINE NEWMAN(H, C, T, W, F, Q)
      COMMON PI, DELTA2, C1, S
      REAL M1, M2, M3
      CSAV = C
C  FORMULAS SET UP FOR C > H
      IF (H .GT. C) C=H
      ARG = (PI/2.) * (2. * C / W) * SQRT(H/T)
      FW=1./SQRT(COS(ARG))
C  ANGULAR FACTOR = FPHI = 1 AT ROOT
      FPHI = 1.
C  G FACTOR = 1 AT ROOT
      G = 1.
      M1=1.13-0.09*(H/C)
      M2=-0.54+0.89/(0.2+H/C)
      M3=0.5-1./(0.65+H/C)+14.*(1.-H/C)**24
      F=(M1+M2*(H/T)**2+M3*(H/T)**4)*FPHI*G*FW
      Q=1.+1.464*(H/C)**1.65
      C = CSAV
      RETURN
      END


      SUBROUTINE LSJ(SFLOW,E,NU,H,C,T,R,ST,SB,  CTOD,CMOD,STAPLY,STCLOS)
      REAL NJ, NU7, NU8, KF
       DATA (PI=3.14159265)
C  SIMPLIFIED LINE SPRING MODEL FOR CALCULATION OF APPLIED CTOD FOR
C  SURFACE FLAW AS A FUNCTION OF STRESS FOR ELASTIC CASE WITH ROOT PLASTIC
C  ZONE CORRECTION.
C  NOMENCLATURE
C HPHYS = PHYSICAL CRACK DEPTH
C H = EFFECTIVE CRACK DEPTH
C T = PLATE THICKNESS
C CPHYS = PHYSICAL CRACK HALF-LENGTH
C C = EFFECTIVE CRACK HALF-LENGTH
C W = PLATE FULL WIDTH
C ST = APPLIED TENSILE STRESS
C SB = APPLIED BENDING STRESS
C SFLOW = FLOW STRENGTH
C E = YOUNG'S MODULUS
C NU = POISSON'S RATIO
C LLY = FLAG FOR LIGAMENT YIELDING
C ASSUME PROPORTIONAL LOADING.  LET BONT = M/S
      BONT = SB/ST
C *****  HERE THE CALCULATION BEGINS  *****
      HPHYS = H
      HSAV = H
      CPHYS = C
C LLY IS FLAG INDICATING LIGAMENT YIELDING. LLY<0 MEANS NO LY.
```

```
      LLY=-100
C PROCEDURE TO SEE IF LIGAMENT IS FULLY YIELDED OR NOT
C MAXIMUM EFFECTIVE VALUE OF H IS H + (T-H)/2
C AT THIS H VALUE, MAXIMUM CLOSURE STRESS HAS BEEN REACHED
C MAXIMUM CLOSURE STRESS, AT FULL LIGAMENT YIELD, IS SCMAX
C  MAXIMUM CLOSURE STRESS OCCURS WHEN SFLOW IS APPLIED ON
C  THE WHOLE LIGAMENT
      SCMAX=SFLOW*(T-H)/T
C  MAXIMUM ALLOWED EFFECTIVE H EXTENDS HALFWAY ACROSS THE LIGAMENT
      H=H+(T-H)/2.
C STAPLY IS APPLIED STRESS AT FIRST OCCURENCE OF FULL LIGAMENT YIELD
      CALL CALC1(H,C,T,R,NU, O2,O3,O4,D,NU7,NU8)
      STAPLY=SCMAX*D/(NU7*(O4+NU8)-NU8*O3*BONT)
      IF( ST  .GT.  STAPLY ) GO TO 52
C LIGAMENT IS NOT FULLY YIELDED
C SET STAPLY = -1000. TO INDICATE THAT THE LIGAMENT HAS NOT FULLY
C YIELDED
      STAPLY = -1000.
C CALCULATION OF ROOT PLASTIC ZONE STARTS HERE
C SAVE STARTING VALUE OF H, NO PLASTIC ZONE, AS HSAV
C  H STARTS AT H IS HSAV,  AND INCREASES
C UNTIL THE CORRECT PLASTIC ZONE SIZE
C IS REACHED BY AN ITERATIVE CALCULATION
C  NOMENCLATURE:     HSAV IS VALUE OF H BEFORE ENTERING ITERATION
C                    HSTART IS VALUE OF H AT START OF ITERATION
C                    HCI IS VALUE OF H AT START OF CURRENT ITERATION
C                    DELTAH IS SMALL INCREMENT OF H
C BEGIN ITERATION
      H = HSAV
      HSTART=H
      DO 50 I1=1,30
      HCI=H
      DELTAH=.01*H
      IF (DELTAH .LT. 0.0001) DELTAH = 0.0001
      H=H+DELTAH
      CALL CALC1(H,C,T,R,NU, O2,O3,O4,D,NU7,NU8)
      CALL CLOSUR(O2,O3,O4,D,NU7,NU8,ST,SB,   STCLOS,SBCLOS)
C  STCLOS, SBCLOS ARE TENSILE AND BENDING CLOSURE STRESSES FOR H-DELTAH
C  SAVE THESE VALUES OF TENSILE AND BENDING CLOSURE STRESSES
      STCSAV=STCLOS
      SBCSAV=SBCLOS
C ALTERNATE PROCEDURE IS TO CALCULATE CLOSURE STRESS FROM THE
C PLASTIC ZONE SIZE.  THE IDEA IS TO FORCE CONSISTENCY.
C CLOSURE STRESS FROM PLASTIC ZONE SIZE IS SCLOSPZ
      CALL SCPZ(H,HSTART,T,SFLOW,  SCLOSPZ)
C SCLOSPZ IS ALTERNATE CLOSURE STRESS FOR H+DELTAH
      SCPZSAV=SCLOSPZ
      H=H-DELTAH
      CALL CALC1(H,C,T,R,NU,  O2,O3,O4,D,NU7,NU8)
      CALL CLOSUR(O2,O3,O4,D,NU7,NU8,ST,SB,  STCLOS,SBCLOS)
      CALL SCPZ(H,HSTART,T,SFLOW,  SCLOSPZ)
```

```
C DSTCDH, DSBCDH ARE DERIVATIVES OF CLOSURE STRESS, MOMENT WRT H
        DSTCDH=(STCSAV-STCLOS)/DELTAH
        DSBCDH=(SBCSAV-SBCLOS)/DELTAH
        DSCPZDH=(SCPZSAV-SCLOSPZ)/DELTAH
C   MAKE THE INDICATED CORRECTION TO H
        H=H+(STCLOS-SCLOSPZ)/(DSCPZDH-DSTCDH)
        IF(HCI.  LT.  0.000001) GO TO 50
        IF( ABS((H-HCI)/HCI)  .LT.  0.001 ) GO TO 55
50      CONTINUE
C ITERATION COMPLETE.  H IS EFFECTIVE CRACK LENGTH
        PRINT 51, H, C
51      FORMAT(* ITERATION ON PLASTIC ZONE SIZE FAILED TO CONVERGE.*,/,
     ^  * H = *,F7.4,*  C = *, F7.4)


        GO TO 55
52      CONTINUE
C LIGAMENT IS FULLY YIELDED. H=HPHYS+(T-H)/2
C HERE WE CALCULATE THE CMOD AND CTOD UP TO LIGAMENT YIELDING
C THESE WILL BE ADDED TO THE CONTRIBUTION CALCULATED BY THE YIELDED
C LIGAMENT MODEL LATER
         LLY=100
        SBAPLY=BONT*STAPLY
       CALL CLOSUR(D2,D3,D4,D,NU7,NU8,STAPLY,SBAPLY,  STCLLY,SBCLLY)
       STCLOS = STCLLY
       SBCLOS = SBCLLY
       ST = STAPLY
       SB = SBAPLY
C   CTOD ACCRUING AFTER LIGAMENT YIELDS WILL BE CALCULATED ELSEWHERE
55      CONTINUE
C WE NOW HAVE A PLASTIC-ZONE-CORRECTED CLOSURE STRESS STCLOS
C A PLASTIC-ZONE-CORRECTED CLOSURE MOMENT SBCLOS
C NOW CALCULATE DELTA AND THETA, TO GET COD S
        DELTA=4.*C*(ST-STCLOS)/E
C   USE CURVED PLATE EXPRESSION FOR LONG CRACKS, FLAT PLATE
C   EXPRESSION FOR SHORT CRACKS
         IF (2.*C .GT. 0.025*2.0*PI*R) GO TO 70
        THETA = (SB-SBCLOS) * 8.*(1.+NU)*C/(3.+NU)/E/T
       GO TO 80
70      THETA = SQRT(R/T) * (2./3.) * ((3.*(1.-NU*NU))**0.75)
     ^    * (SB-SBCLOS)/E
80      CONTINUE
C   HERE WE CALCULATE APPLIED K FACTOR, TO GET CTOD
       CALL KCALC(STCLOS, SBCLOS, H, T,  KF)
        CTOD = KF*KF*(1.-NU*NU)/E/SFLOW
        CMOD=DELTA+THETA*T
       H = HPHYS
       END
```

```
      SUBROUTINE SCPZ(H,HSTART,T,SFLOW,  SCLOSPZ)
C THIS SUBROUTINE CALCULATES ALTERNATE CLOSURE STRESS SCLOSPZ
C FROM PLASTIC ZONE SIZE
      PI = 3.1415927
       HPLAS=HSTART+2.*(H-HSTART)
       IF(HPLAS  .LT.  1.0E-10) GO TO 10
       Q=SIN(PI*HSTART/2./T)/SIN(PI*HPLAS/2./T)
       IF(Q  .GT.  0.9999) GO TO 10
       SCLOSPZ=(2.*SFLOW/PI)*ACOS(Q)
      RETURN
10     SCLOSPZ = 0.0
       END



       SUBROUTINE CALC1(H,C,T,R,NU,  D2,D3,D4,D,NU7,NU8)
       REAL NU, NU7, NU8
       DIMENSION X(13), Y(19), Z(13)
        DATA (PI = 3.14159265)
      DATA
     &(  X(1)=1.9761),
     &(  X(2)=11.487),
     &(  X(3)=7.7086),
     &(   X(4)=15.0143 ),
     &(   X(5)=280.121 ),
     &(   X(6)=-1099.72),
     &(   X(7)=3418.98 ),


     &(   X(8)=-7686.92),
     &(   X(9)=12794.1 ),
     &(   X(10)=-13185.),
     &(   X(11)=7868.27),
     &(  X(12)=-1740.25 ),
     &(   X(13)=124.136)
      DATA
     &(  Y(1)=1.9735),
     &(   Y(2)=-2.2166 ),
     &(   Y(3)=21.6051 ),
     &(   Y(4)=-69.3133),
     &(   Y(5)=196.3 ),
     &(   Y(6)=-406.261),
     &(   Y(7)=644.935 ),
     &(   Y(8)=-408.957),
     &(   Y(9)=-159.693),
     &(   Y(10)=-988.988),
     &(   Y(11)=4266.55),
     &(   Y(12)=-2997.14 ),
     &(   Y(13)=-6050.78 ),
     &(   Y(14)=8855.36),
     &(   Y(15)=3515.43),
     &(   Y(16)=-11744.1 ),
     &(   Y(17)=4727.98),
     &(   Y(18)=1695.61),
     &(  Y(19)=-845.896 )
```

```
      DATA
     ^(  Z(1)=1.971 ),
     ^(   Z(2)=-4.4277 ),
     ^(   Z(3)=34.4952 ),
     ^(   Z(4)=-165.732),
     ^(   Z(5)=626.393 ),
     ^(   Z(6)=-2144.46),
     ^(   Z(7)=7043.42 ),
     ^(   Z(8)=-19003.2),
     ^(   Z(9)=37853.3 ),
     ^(   Z(10)=-52595.5),
     ^(   Z(11)=48079.3),
     ^(   Z(12)=-25980.2 ),
     ^(   Z(13)=6334.24)
       X1=H/T
       D2=0.
       D3=0.
       D4=0.
      IF( X1  .LT.  1.0E-5)  X1=1.0E-5
       DO 10 K=1,13
       I = K - 1
       D2=D2+X(K)*(X1**(2.*I))
       D3=D3+Y(K)*(X1**I)
       D4=D4+Z(K)*(X1**I)
10     CONTINUE
      DO 20 K=14,19
       I=K-1
       D3=D3+Y(K)*(X1**I)
20     CONTINUE
       D2=X1*X1*D2
       D3=X1*X1*D3
       D4=X1*X1*D4
C  IN THE NOTATION OF KING'S PAPER ON THE SIMPLIFIED LINE SPRING MODEL,
C D2=A11  D3=A12   D4=A22
C NU=NU, NU7=(C/T)*(2/(1-NU*NU))
      NU7=(C/T)*2./(1.-NU*NU)
C  THE QJANTITY N8 DEPENDS ON THE CRACK LENGTH.  FOR CRACKS LESS
C  THAN 2.5 % OF THE CIRCUMFERENCE, WE USE THE FLAT PLATE EXPRESSION.


C  FOR LONGER CRACKS, THE EXPRESSION FOR CURVEATURE IS USED
       IF(2.*C  .GT.  .025*2.*PI*R) GO TO 30
       NU8 = (C/T)*2./3./(1.-NU)/(3.+NU)
        GO TO 40
30      NU8 =  SQRT(R/T) * (1./6.) / (( 3.*(1.-NU*NU) ) **.25)
40     D=(D2+NU7)*(D4+NU8)-D3*D3
      END
```

```
      SUBROUTINE CLOSUR(D2,D3,D4,D,NU7,NU8,ST,SB,  STCLOS,SBCLOS)
      REAL NU7, NU8
C CLOSURE STRESS, SIGMA SUB C, IS STCLOS
C CLOSURE MOMENT, M SUB C, IS SBCLOS
       STCLOS=(NU7*(D4+NU8)*ST-NU8*D3*SB)/D
       SBCLOS=(-NU7*D3*ST+NU8*(D2+NU7)*SB)/D
      END



      SUBROUTINE KCALC(STCLOS,SBCLOS,H,T, KF)
      REAL KF
      DIMENSION U(7), V(7)
      DATA (PI = 3.141592654)
      DATA (U(1) = 1.12),
     ^  (U(2) = 6.52),
     ^  (U(3) = -12.39),
     ^  (U(4) = 89.05),
     ^  (U(5) = -188.61),
     ^  (U(6) = 207.39),
     ^  (U(7) = -32.05)
      DATA (V(1) = 1.12),
     ^  (V(2) = -1.89),
     ^  (V(3) = 18.01),
     ^  (V(4) = -87.39),
     ^  (V(5) = 241.9),
     ^  (V(6) = -319.94),
     ^  (V(7) = 168.01)
       X1 = H/T
       G1 = 0.0
       G2 = 0.0
       DO 10 K=1,7
      I = K - 1
      G1 = G1 + U(K)*(X1**(2*I))
      G2 = G2 + V(K)*(X1**I)
10    CONTINUE
      KF = (STCLOS*G1 + SBCLOS*G2)*SQRT(PI*X1)*SQRT(T)
      RETURN
      END
```

Example Allowable Flaw-size Calculation

An example of a hand calculation of critical flaw depth for a given flaw length follows. Computer results, instead of guesses, were used to reach the final step in both the plastic-zone and critical-depth iterations. The allowable flaw-size calculations are complex; computer costs are insignificant compared with manpower costs.

I. Input parameters

δ_c = 0.125 mm

$CTOD_{RS}$ = 0.038 mm

$\bar{\sigma}$ = 517 MPa

σ = 434 MPa

E = 2.08 x 10^5 MPa

ν = 0.29

R = 610 mm

t = 15.9 mm

II. Short flaw, use Eqs. 28 through 33

Long flaw, use Eqs. 69 through 74

Dividing line is $2c = 0.025 \times 2\pi \times R$ = 96 mm

III. Critical condition: $\delta_c = CTOD_E + CTOD_{LY} + CTOD_{RS}$

Therefore we demand $CTOD_E + CTOD_{LY}$ = 0.087 mm

IV. Procedure: for every ℓ, find a so that

$CTOD_E + CTOD_{LY}$ = 0.087

A. Choose ℓ = 201.1 mm for this example. From II, above, we see that we have the long-flaw case.

B. Choose a trial a value, 2.75 mm.

(The first trial a value is arbitrary, but the better the choice, the fewer iterations needed.)

C. Calculate $CTOD_{EL} + CTOD_{LY}$ for this a value.

1. Check for full ligament yielding.

a. Using Eq. 14,

$$\sigma_c = (1 - a/t)\ \bar{\sigma} = 427.6 \text{ MPa}$$

b. At full ligament yielding, $a + 2r_y = t$; $r_y = 6.575$ mm;

$$a_{eff} = a + r_y = 9.32 \text{ mm}$$

$$a_{eff}/t = 0.586$$

To apply Eq. 70 we need α_c from Eq. 72, which requires S from Eq. 74.

In Eqs. 72 and 74 we need a_{11}, a_{12}, and a_{22}:

From Table A-1, $a_{11} = 3.136$; $a_{12} = 1.746$; $a_{22} = 0.993$

Applying Eq. 72 we find

$$S = \left\{3.136 + \frac{201.1}{15.9\ (1-0.29^2)}\right\}\left\{0.0993 + \frac{(2.610)^{\frac{1}{2}}\ [12(1 - 0.29^2]^{3/4}}{72\ (1 - 0.29^2)\ 15.9^{\frac{1}{2}}}\right\} - (1.746)^2$$

$$= (3.136 + 13.809)\ (0.993 + 0.8018) - 3.0485$$

$$= 27.364$$

Applying Eq. 72 and using values from the previous step where needed, we get

$$\alpha_c = 13.809\ \{0.993 + 0.8018\}/27.364 = 0.9057$$

Applying Eq. 70, we find

$$\sigma_c = 0.9057 \text{ X } 434 = 393.1 \text{ MPa}$$

c. We note that $\sigma_0 < \sigma_c$, therefore the ligament is not fully yielded.

Therefore, we know

$CTOD_{LY} = 0$

$r_y < 6.575$ mm

2. Find the value of r_y for which Eqs. 70 and 75 are satisfied.

a. Guess initial value of r_y:

let $r_y = 4.164$ mm

b. Apply Eq. 70

$r_y = 4.164$

$(a/t)_{effective} = 0.4355$

From Table A-1, $a_{11} = 0.8989$; $a_{12} = 0.5917$; $a_{22} = 0.3955$.

Equation 74 gives:

$S = (0.8989 + 13.809)(0.3955 + 0.8018) - 0.3501$

$= 17.260$

Equation 72 gives: $\alpha_c = 13.809\ (0.3955 + 0.8018)/\ 17.260$

$= 0.9579$

Equation 70 gives: $\sigma_0 = 0.9579 \times 434 = 415.7$ MPa

c. Apply Eq. 75

$$\frac{\sin(0.2717)}{\sin(1.0944)} = \frac{0.2683}{0.8887} = 0.3019$$

arc cos $(0.3019) = 1.2641$

$\sigma_0 = 416.1$ MPa

d. σ_o from Eq. 70 agrees with σ_0 from Eq. 75 to better than 1 part in 1000. This is sufficient for a hand calculation.

Therefore, $r_y = 4.164$ for the trial a value, and a = 2.75 mm.

3. Apply Eq. 66

We need g_t and g_b

From Table A-1, we have $g_t = 2.7187$ and g_b 1.5561

We already have $\sigma_0 = 415.9$, averaging results of IV.C.2.b. and IV.C.2.c.

To get m, we apply Eq. 73 and then Eq. 70. Using values calculated above, we have

$$\beta_c = 13.809 \times 0.5917/17.260 = 0.4734$$

From Eq. 70, $m = -0.4734 \times 434 = -205.4$ MPa

In applying Eq. 66, we convert t to meters to retain consistent units:

$$K = (0.0159)^{\frac{1}{2}} [415.9 \times 2.7187 - 205.4 \times 1.5561]$$
$$= 102.3 \text{ MPa} \cdot \text{m}^{\frac{1}{2}}$$

4. Apply Eq. 11

$$CTOD_E = 8.913 \times 10^{-5} \text{m}$$
$$= 8.913 \times 10^{-2} \text{mm}$$
$$= 0.08913 \text{ mm}$$

5. Our calculated CTOD is within 2.4% of the critical value. This is sufficiently accurate for a hand calculation.

V. Therefore, for ℓ = 201.1 mm, we have found a = 2.75 mm, and we have one point on the allowable flaw-size curve.

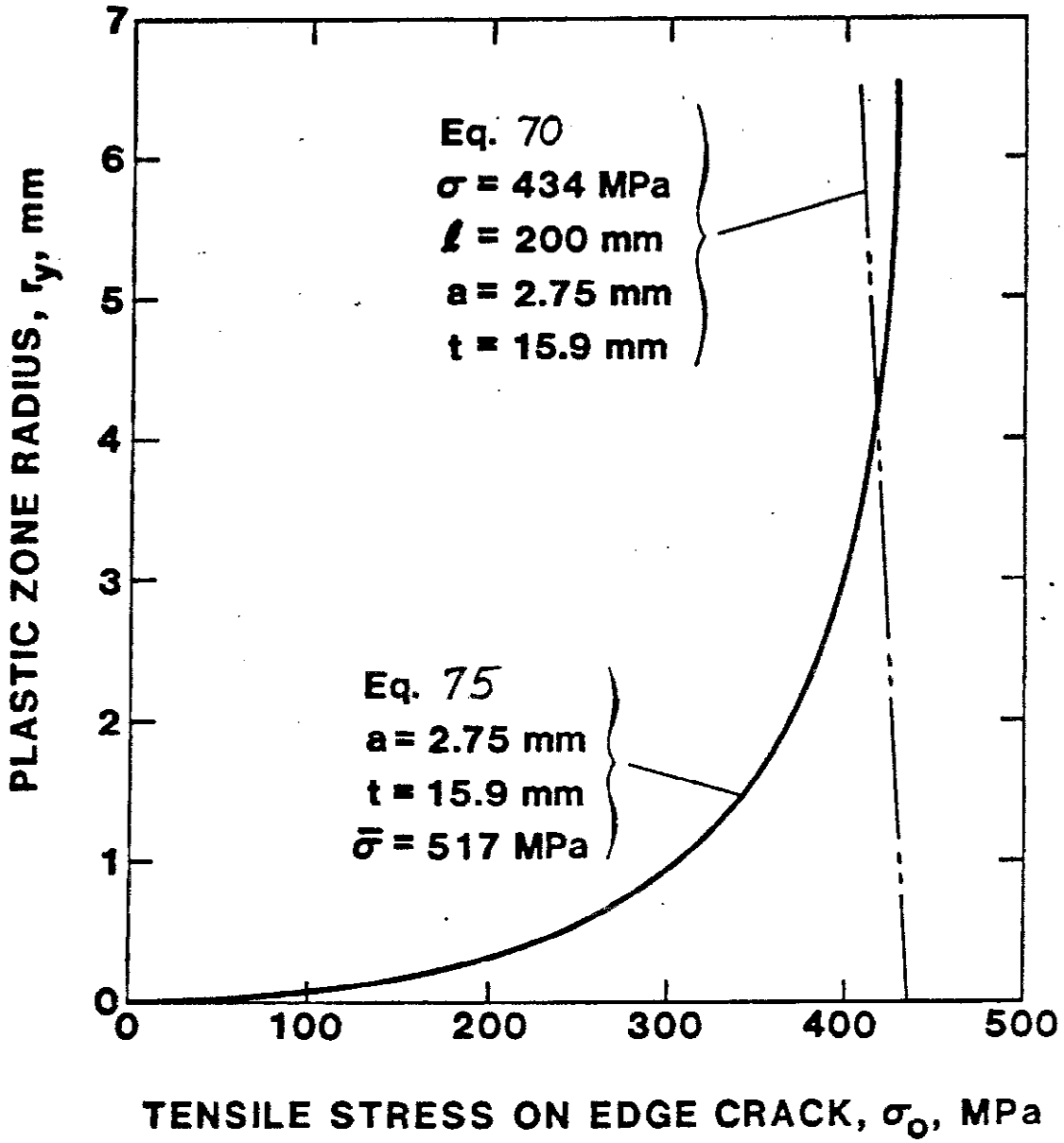

Fig. A-1 — Plot of plastic zone radius, r_y, vs. tensile stress on equivalent edge crack, σ_0, for two different equations. The intersection of the two curves is the plastic-zone radius for the specified input parameters. To obtain inches, multiply millimeters by 0.0394; to obtain psi x 10^3, divide MPa by 6.894.

Table A1. Parameters used in calculation of allowable flaw size curves.

EFFECTIVE a/T	A11	A12	A22	G7	G8	EFFECTIVE a/T
.0100	.0002	.0002	.0002	.1986	.1955	.0100
.0200	.0008	.0008	.0008	.2814	.2729	.0200
.0300	.0018	.0017	.0017	.3456	.3307	.0300
.0400	.0032	.0031	.0029	.4007	.3787	.0400
.0500	.0050	.0048	.0045	.4503	.4205	.0500
.0600	.0073	.0069	.0065	.4966	.4582	.0600
.0700	.0100	.0093	.0087	.5401	.4930	.0700
.0800	.0131	.0122	.0113	.5822	.5255	.0800
.0900	.0168	.0155	.0143	.6232	.5563	.0900
.1000	.0209	.0191	.0175	.6637	.5856	.1000
.1100	.0256	.0233	.0211	.7038	.6139	.1100
.1200	.0309	.0278	.0251	.7439	.6412	.1200
.1300	.0367	.0328	.0294	.7842	.6676	.1300
.1400	.0432	.0383	.0340	.8248	.6934	.1400
.1500	.0504	.0443	.0389	.8659	.7186	.1500
.1600	.0583	.0508	.0444	.9076	.7434	.1600
.1700	.0669	.0578	.0501	.9501	.7677	.1700
.1800	.0764	.0654	.0562	.9934	.7917	.1800
.1900	.0867	.0736	.0626	1.0377	.8155	.1900
.2000	.0980	.0824	.0695	1.0830	.8392	.2000
.2100	.1102	.0918	.0767	1.1293	.8628	.2100
.2200	.1236	.1019	.0844	1.1769	.8864	.2200
.2300	.1380	.1127	.0925	1.2258	.9101	.2300
.2400	.1537	.1243	.1010	1.2760	.9340	.2400
.2500	.1707	.1366	.1100	1.3277	.9581	.2500
.2600	.1891	.1498	.1194	1.3810	.9827	.2600
.2700	.2090	.1639	.1294	1.4359	1.0077	.2700
.2800	.2304	.1788	.1398	1.4926	1.0332	.2800
.2900	.2536	.1948	.1508	1.5511	1.0593	.2900
.3000	.2787	.2118	.1623	1.6117	1.0861	.3000
.3100	.3058	.2299	.1744	1.6745	1.1137	.3100
.3200	.3349	.2492	.1872	1.7395	1.1422	.3200
.3300	.3664	.2698	.2006	1.8070	1.1716	.3300
.3400	.4004	.2917	.2148	1.8771	1.2020	.3400
.3500	.4371	.3150	.2296	1.9500	1.2335	.3500
.3600	.4767	.3400	.2453	2.0259	1.2662	.3600
.3700	.5194	.3665	.2618	2.1049	1.3000	.3700
.3800	.5655	.3949	.2793	2.1874	1.3351	.3800
.3900	.6154	.4251	.2977	2.2735	1.3716	.3900
.4000	.6692	.4575	.3171	2.3635	1.4094	.4000
.4100	.7274	.4920	.3376	2.4576	1.4487	.4100
.4200	.7903	.5289	.3593	2.5561	1.4895	.4200
.4300	.8584	.5684	.3822	2.6592	1.5319	.4300
.4400	.9321	.6107	.4064	2.7674	1.5759	.4400
.4500	1.0120	.6560	.4321	2.8809	1.6216	.4500
.4600	1.0986	.7045	.4593	3.0000	1.6692	.4600
.4700	1.1925	.7566	.4882	3.1251	1.7186	.4700
.4800	1.2944	.8124	.5187	3.2566	1.7700	.4800
.4900	1.4051	.8723	.5512	3.3950	1.8236	.4900
.5000	1.5255	.9367	.5857	3.5406	1.8794	.5000
.5100	1.6565	1.0060	.6223	3.6940	1.9376	.5100
.5200	1.7991	1.0805	.6613	3.8557	1.9985	.5200
.5300	1.9546	1.1608	.7027	4.0263	2.0621	.5300
.5400	2.1242	1.2473	.7469	4.2064	2.1289	.5400
.5500	2.3094	1.3407	.7940	4.3969	2.1990	.5500
.5600	2.5119	1.4416	.8443	4.5985	2.2729	.5600
.5700	2.7335	1.5508	.8981	4.8121	2.3508	.5700
.5800	2.9763	1.6690	.9556	5.0388	2.4332	.5800
.5900	3.2427	1.7972	1.0174	5.2798	2.5207	.5900
.6000	3.5354	1.9365	1.0837	5.5366	2.6137	.6000
.6100	3.8575	2.0882	1.1551	5.8101	2.7130	.6100
.6200	4.2125	2.2535	1.2321	6.1026	2.8191	.6200
.6300	4.6046	2.4341	1.3154	6.4160	2.9330	.6300
.6400	5.0384	2.6319	1.4056	6.7526	3.0555	.6400
.6500	5.5194	2.8491	1.5037	7.1147	3.1877	.6500
.6600	6.0541	3.0882	1.6105	7.5055	3.3305	.6600
.6700	6.6498	3.3520	1.7274	7.9283	3.4853	.6700
.6800	7.3156	3.6442	1.8556	8.3868	3.6533	.6800
.6900	8.0617	3.9686	1.9957	8.8854	3.8362	.6900
.7000	8.9009	4.3302	2.1525	9.4289	4.0356	.7000
.7100	9.8467	4.7345	2.3253	10.0230	4.2528	.7100
.7200	10.9178	5.1883	2.5175	10.6740	4.4904	.7200
.7300	12.1349	5.6995	2.7322	11.3889	4.7503	.7300
.7400	13.5233	6.2777	2.9725	12.1758	5.0348	.7400
.7500	15.1134	6.9341	3.2437	13.0437	5.3464	.7500
.7600	16.9421	7.6822	3.5496	14.0027	5.6880	.7600
.7700	19.0542	8.5384	3.8965	15.0642	6.0623	.7700
.7800	21.5039	9.5220	4.2912	16.2410	6.4728	.7800
.7900	24.3575	10.6563	4.7418	17.5472	6.9227	.7900
.8000	27.6959	11.9695	5.2580	18.9988	7.4159	.8000
.8100	31.6176	13.4953	5.8513	20.6134	7.9564	.8100
.8200	36.2439	15.2744	6.5350	22.4106	8.5483	.8200

APPENDIX B - Metallographic Analysis and Mechanical Characterization of API 5LX-70 Weldments

J. G. Early

METALLOGRAPHIC ANALYSIS

Metallographic examinations were carried out on sections representative of the automatic gas-metal-arc (GMA) girth weld and the manual shielded-metal-arc (SMA) girth weld on API 5LX-70, 15.9-mm (0.625-in) thick pipeline steel. Weld procedures are described in Section 4.2.

The automatic weld shown in Fig. B-1 contains seven passes, including the root pass, hot pass, fill passes, and the reinforcement pass. The base-plate microstructure, shown in Fig. B-2, is heavily banded and consists of alternate layers of polygonal ferrite and nonpolygonal ferrite (acicular ferrite or low-carbon bainite). The banded microstructure originating from chemical segregation in the ingot is a result of the plate-rolling operations prior to pipe fabrication. The plate midthickness region (Fig. B-2b) exhibits thicker nonpolygonal ferrite layers than regions near the plate surfaces. The manual SMA weld, shown in Fig. B-3, contains eight passes.

MECHANICAL CHARACTERISTICS

Hardness

Profile sections from each weldment containing weld metal, HAZ, and base metal were prepared for hardness surveys. Profile schematics of the two types of girth welds identifying the weld-pass boundaries are shown in Fig. B-4. Vickers hardness measurements and Rockwell A Scale hardness measurements were taken throughout the base metal, HAZ, and selected individual weld passes. The average hardness numbers were converted, where necessary, to the Rockwell

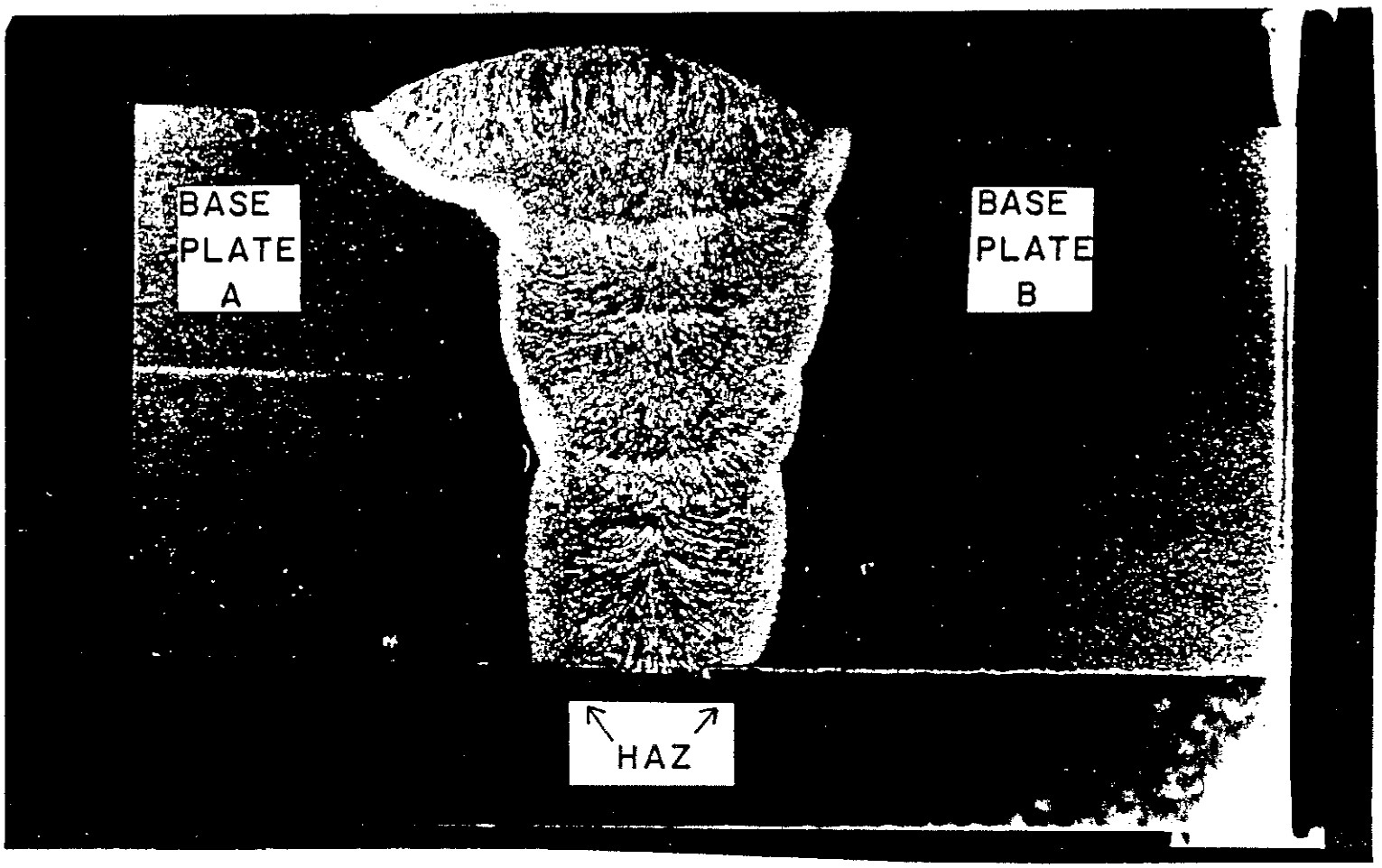

Fig. B-1 – Profile section of automatic GMA girth weld in plate W1-1. Cross section shows base metal, HAZ, and weld metal. Plate rolling direction is ←——→. Etch: 5% nital. Magnification: 5X.

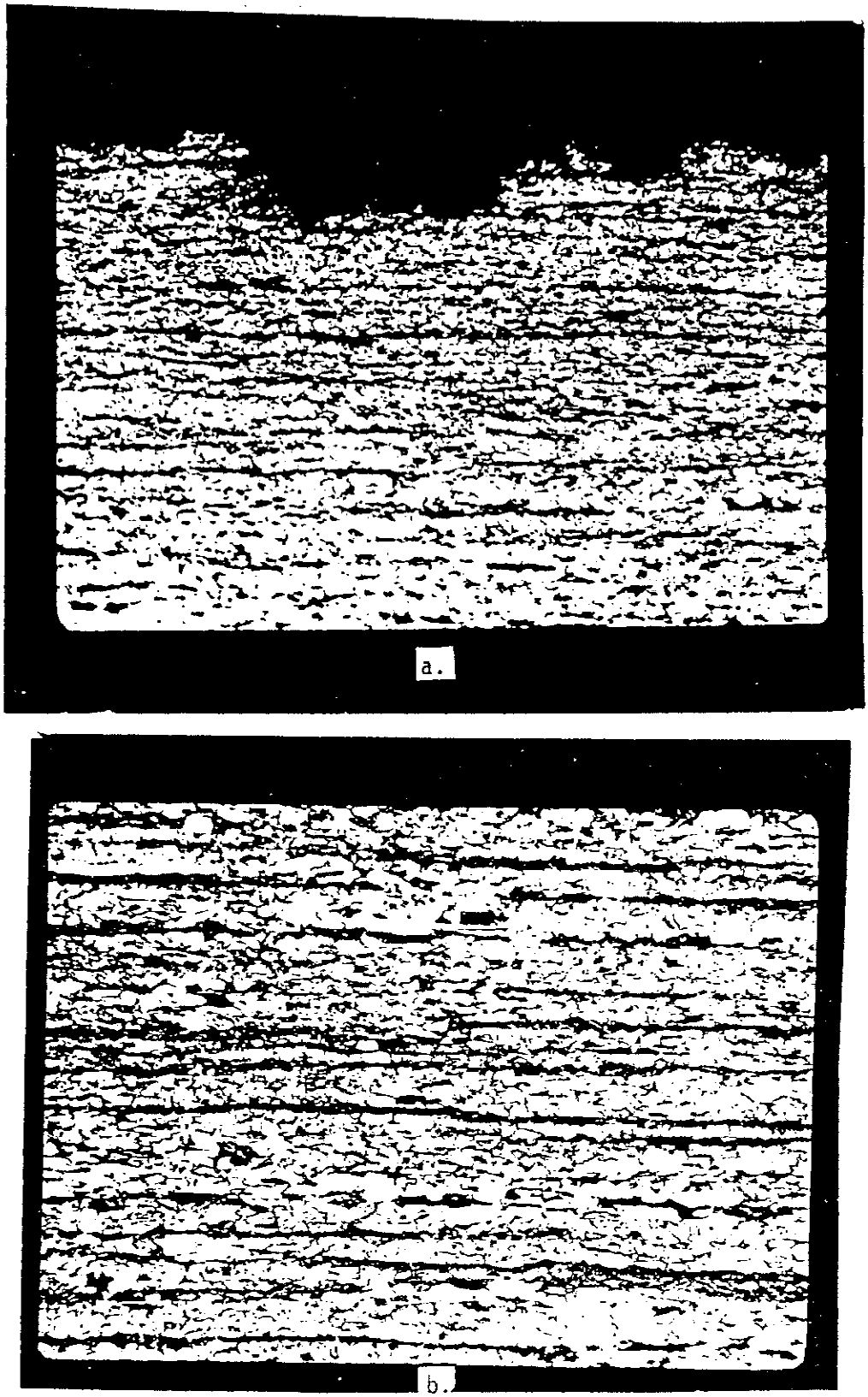

Fig. B-2 — Photomicrograph of base plate A from plate W1-1. Light etching phase is polygonal ferrite; dark etching is nonpolygonal ferrite. Plate rolling direction is ⟷. (a) Near outside plate surface. (b) Near plate midthickness. Etch: 5% nital. Magnification: 200X.

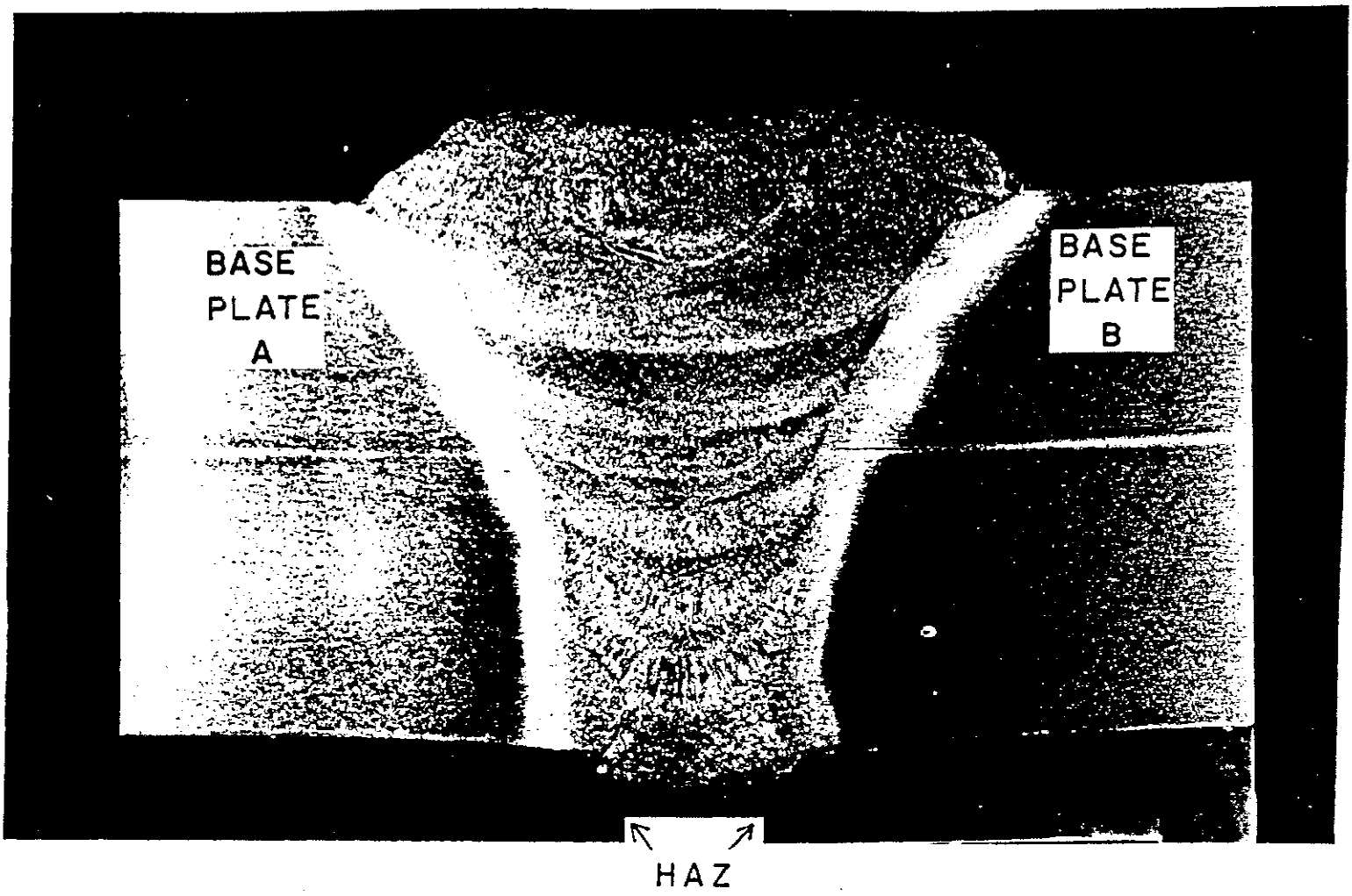

Fig. B-3 — Profile section of manual SMA girth weld in plate W4-2. Cross section shows base metal, HAZ, and weld metal. Plate rolling direction is ←——→. Etch: 5% nital. Magnification: 5X.

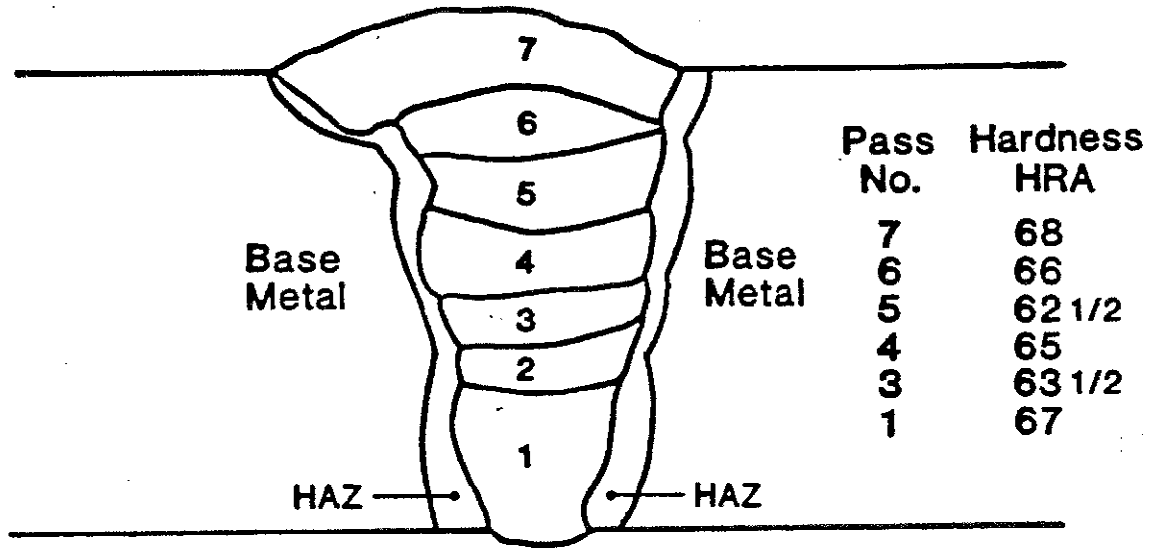

Automatic GMA Weld, Plate W1-1

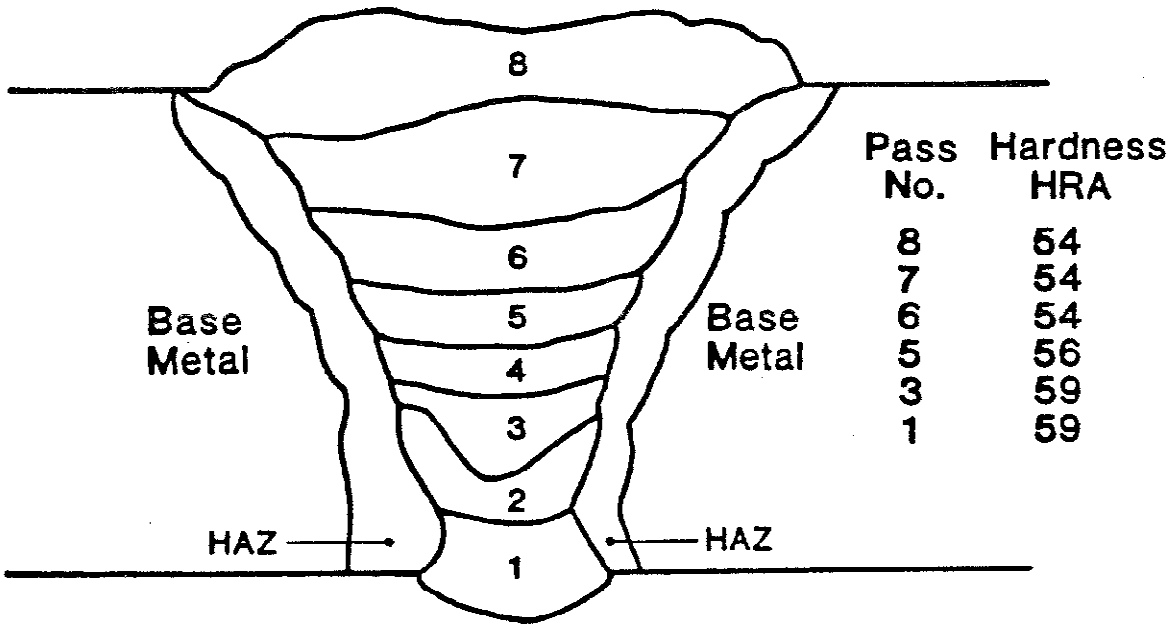

Manual SMA Weld, Plate W4-2

Fig. B-4 - Profile schematics of automatic and manual girth welds.

A Scale, HRA, for comparison. The hardness values for individual weld passes are indicated in Fig. B-4, and the summary of all hardness results are given in Table B-1.

The average hardness of the HAZ in the automatic weld is intermediate, lying between the lower base-metal hardness and the higher weld-metal hardness. For the manual weld, the average HAZ hardness is somewhat higher than the base-metal or weld-metal hardness. Furthermore, the average HAZ and weld-metal hardness values for the automatic weld are higher than the average values for the manual weld. These observations are consistent with the observation that the automatic weld is generally narrower than the manual weld, indicating either lower average heat input, higher average welding rates, or a combination of both, resulting in less tempering of the automatic weld HAZ and a higher cooling rate for the automatic weld metal.

Tensile Strength

The tensile properties of the weld metal from both weld types were determined at -101°C (-150°F) and +24°C (+75°F). The strength at intermediate temperatures was determined by interpolation between the two temperatures. Standard ASTM subsize round tensile specimens, 0.635-cm (0.250-in) diameter with a 2.54-cm (1.00-in) gage length, were prepared such that the reduced gage length section contained only weld metal with the specimen axis parallel to the weld axis. The gage-length section of specimens from the automatic weld generally sampled weld passes 4 and 5, whereas specimens from the manual weld generally sampled weld passes 5 and 6, (Fig. B-4).

The tensile tests at -101°C (-150°F) were carried out inside an environmental chamber in which the atmospheric temperature was controlled by balancing cooling from liquid nitrogen and heating from electric resistance heaters. The specimen temperature was measured with a thermocouple attached to the gage-length section, and the test temperature was controlled to ±3°C (±5°F)

Table B-1 - Hardness Data Summary

Weld Type	Average HRA Values				
	Base Metal		HAZ*		Weld Metal
	A Side	B Side	A Side	B Side	
Automatic	57 (HRB 93)	57 (HRB 94)	62 (HRC 23)	62 (HRC 23)	65½ (HRC 30)
Manual	57 (HRB 93)	56½ (HRB 92)	60 (HRC 20)	60 (HRC 20)	56 (HRB 91)

*Converted from Vickers hardness numbers.

during the tests. The test machine crosshead speed was 0.13 mm/min (0.005 in/min) to yield and 0.76 mm/min (0.030 in/min) after yield. The tensile properties for each girth-weld type and of the API 5LX-70 base material are summarized in Table B-2.

The manual-weld specimens were taken from two welds; the automatic-weld test specimens were taken from a single weld. The results of the tensile tests for the manual-weld specimens from both plates at the two test temperatures indicate good weld uniformity, and thus the measured tensile properties can be used as representative of each weld type. The average ultimate tensile strength and yield strength of the automatic weld increased 15% and 11%, respectively, as the test temperature was lowered from +24°C (+75°F) to -101°C (-150°F). For the manual weld, the average strength properties increased about 21% for the same change in test temperature. The tensile ductility parameters, percent elongation, and percent reduction in area were not found to be strongly temperature dependent.

Fracture Toughness

It was anticipated that these weldments would have sufficient plasticity so that slow, stable crack extension would occur within the temperature range of interest. Crack-tip-opening displacement (CTOD) tests were carried out over the temperature range of +24 (+75°F) to -101°C (-150°F). The temperature dependence of the fracture toughness was determined for the weld metal and HAZ regions of both weld types. An estimate of the lowest temperature at which reproducible, slow, stable crack growth would occur was made from the temperature dependence data and a multiple specimen resistance curve approach[93,94] and was used to determine the critical CTOD at the initiation of stable crack growth.

Table B-2 — Tensile Properties of the Test Materials at Room Temperature

Material	Yield Strength 0.2% Offset, MPa	Yield Strength 0.2% Offset, psi x 10^3	Tensile Ultimate Strength, MPa	Tensile Ultimate Strength, psi x 10^3	Elongation in 25 mm (1 in), %	Reduction of Area, %	Notes
Base metal	491*	71.2	549	79.6	26	69	Average of three tests
Manual weld AWS E8010G	465	67.4	555	80.5	28	66	
Automatic weld AWS E70S-6	725	105	810	117	21	66	

* The upper yield strength of the base metal was 532 MPa (77.2 psi x 10^3).

All fracture tests were carried out in three-point bending on specimens of the preferred geometry, as described in British Standards BS5762 (1979).[93] In the weld-metal specimens, the machined notches were oriented parallel to the weld axis and centered totally within the weld. For the HAZ specimens, the machined notches were oriented parallel to the weld axis and centered so that the final crack location after precracking would place the central portion of the fatigue crack front in the HAZ.

The introduction of fatigue precracks into weld-metal and HAZ specimens presents a special problem because of the requirements on the straightness of the fatigue crack front.[95] Typically, the transverse residual stress pattern associated with multipass welds in plates and pipe (e.g., from surface to surface through the plate thickness or pipe-wall thickness) changes from tensile stresses near each surface to a balancing compressive stress in the interior. Fatigue crack growth in this stress environment often results in two areas of growth near the surfaces in the residual tensile stress region and little or no growth in the residual compressive stress region, as shown in Fig. B-5. There is some evidence that measured fracture toughness properties from specimens exhibiting this bimodal fatigue crack shape are higher than those from specimens with a straighter crack shape, particulary in the elastic-plastic toughness region.[96]

To reduce the effect of nonuniform fatigue cracks, the ligament region ahead of the notch in all CTOD specimens was compressed about 1% following the procedure of Dawes.[97,98] The actual load necessary to cause a 1% plastic strain in the through-thickness direction was within 5% of the calculated load. Several studies with weld-metal specimens have shown little effect of the compression treatment on the measured crack-opening displacement.[96,97]

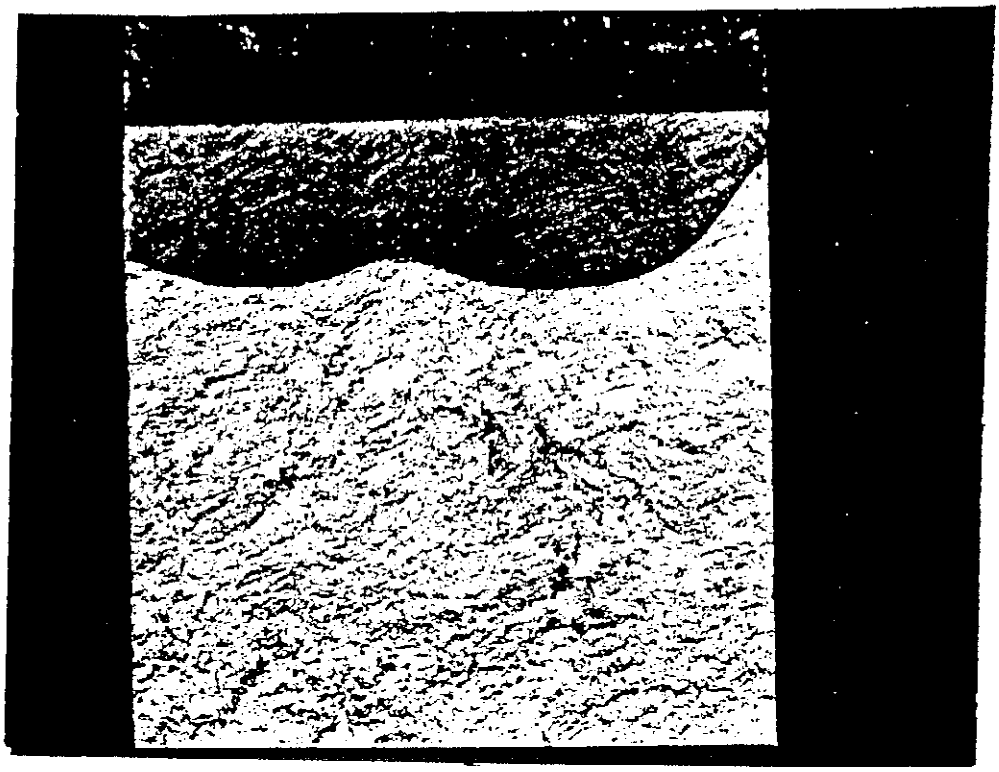

a.

b.

Fig. B-5 — Fractographs of COD specimens illustrating the effect of compression pretreatment on fatigue crack growth. (a) Without compression pretreatment; type E8010 weld metal; test temperature = +24°C (+75°F). (b) With compression pretreatment; type E8010 weld metal; test temperature = -45°C (-50°F). Magnification: 7X.

After the compression pretreatment, fatigue precracks were grown at 24°C (75°F) by sinusoidal loading of each specimen at a frequency of 20 Hz with maximum and minimum loads of 6.7 kN (1.5 lbf) and 0.1 kN (0.02 lbf). The final ratio of crack length to specimen width was about 0.50. The average number of cycles required was 25,500 for the automatic-weld specimens with a range of 22,300 cycles to 29,000 cycles. For the HAZ specimens, the average number of cycles was 24,660 with a range of 21,000 cycles to 27,000 cycles. For the manual weld and HAZ specimens, the averages were 21,130 cycles and 20,940 cycles, with ranges of 20,000 cycles to 22,500 cycles and 19,000 cycles to 22,000 cycles, respectively. The shapes of the resulting fatigue cracks were generally straight except near the surfaces, with little evidence of the bimodal behavior, as can be seen in Fig. B-5b.

The crack-opening-displacement procedure was based on British Standard BS5762 (1979).[93] Each specimen was loaded in displacement control at a rate of 0.25 mm/min (0.010 in/min). The instantaneous load and displacement, as measured by a clip gage attached to the specimen surface, were continuously recorded. The temperature was monitored by a thermocouple attached to one of the screw-in knife edges on the specimen. At the conclusion of each test, the specimen was rapidly unloaded and heat-tinted to mark the extent of crack growth. Each specimen was then cooled in liquid nitrogen and broken, and the amount of crack extension was determined.

The CTOD value for each test was calculated using the relations:

$$CTOD = \frac{K^2(1 - \nu^2)}{2\sigma_y E} + \frac{0.4(W - a)V_p}{0.4W + 0.6(a + h_c)} \qquad \text{(B-1)}$$

and

$$K = YP/(tW^{\frac{1}{2}})$$

where: Y = stress intensity coefficient at a/W
P = load
t = specimen thickness
W = specimen width
V_p = plastic component of clip-gage opening displacement
h_c = distance of clip gage from specimen surface

The interpretation of the calculated value of CTOD depends on observations of the load-displacement behavior and the type and extent of crack growth at the test temperature. The results of the analysis of the temperature dependence of the fracture toughness are summarized in Tables B-3 and B-4 and Fig. B-6. The weld-metal data for both welding processes show a regular progression in crack growth behavior from low test temperatures to high test temperatures: for example, unstable or brittle fracture or pop-in without evidence of slow, stable crack growth at the lowest temperatures; through unstable brittle fracture or pop-in after some slow, stable crack growth at intermediate temperatures; to slow, stable crack growth through the maximum applied load at the highest temperatures. The higher-strength automatic weld did not exhibit slow, stable crack growth until the test temperature was increased to -18°C (-0.4°F). The lower-strength manual weld exhibited slow; stable crack growth at -46°C (-51°C).

The HAZ data for both welding processes showed a similar regularity in the crack growth behavior at the lowest and highest test temperatures: no stable crack growth at the lowest temperature and only slow, stable crack growth through maximum applied load at the highest temperatures. However, considerable variability in crack growth behavior was observed at the intermediate temperatures, with less correlation between the presence or absence of slow, stable crack growth and temperatures.

The greater variability in the HAZ results is probably associated with the geometrical relationship between the weld and specimen notch orientation. The welds are single-V type so that when the fatigue crack is grown only the central portion of the crack (about 25% of the crack front) lies in the HAZ. The remainder of the fatigue crack lies in the weld metal on one side and the plate base metal on the other side. Thus, the resulting or controlling

Table B-3 - Temperature Dependence of Fracture Toughness for the Automatic Weld

Specimen Number	Type*	Temperature, °C	Temperature, °F	a/W	CTOD Criterion†
W133	W	-73	-98	0.5042	δ_c = 0.028
W135	W	-46	-51	0.5287	δ_c = 0.076
W128	W	-18	-0.4	0.5388	δ_u = 0.094
W1214	W	-18	-0.4	0.5215	δ_u = 0.089
W129	W	-18	-0.4	0.5189	δ_u = 0.079
W139	W	0	32	0.4971	δ_{max} = 0.084
W138	W	21	70	0.5101	δ_{max} = 0.122
W134	W	21	70	0.5093	δ_{max} = 0.104
W1216	HAZ	-101	-150	0.5018	δ_c = 0.018
W123	HAZ	-101	-150	0.4959	δ_c = 0.041
W121	HAZ	-73	-99	0.4854	δ_c = 0.061
W1218	HAZ	-18	-0.4	0.5064	δ_{max} = 0.437
W1212	HAZ	0	32	0.5133	δ_{max} = 0.262
W1213	HAZ	0	32	0.5053	δ_{max} = 0.508
W1210	HAZ	24	75	0.5080	δ_{max} = 0.442

* WM = weld metal; HAZ = heat-affected zone

† where: δ_c = CTOD at unstable fracture or onset of arrested brittle crack growth without evidence of slow crack growth.

δ_u = CTOD at unstable fracture on onset of arrested brittle crack growth with evidence of slow crack growth.

δ_{max} = CTOD at maximum applied force.

Table B-4 - Temperature Dependence of Fracture Toughness for the Manual Weld

Specimen Number	Type	Temperature, °C	Temperature, °F	a/W	CTOD Criterion *
W434	WM	-101	-150	0.5044	δ_c = 0.010
W436	WM	-101	-150	0.5050	δ_c = 0.053
W431	WM	-73	-99	0.5143	δ_c = 0.036
W432	WM	-46	-51	0.5086	δ_u = 0.097
W439	WM	-18	-0.4	0.5200	δ_u = 0.084
W4117	WM	-18	-0.4	0.5033	δ_{max} = 0.229
W438	WM	0	32	0.5173	δ_{max} = 0.226
W433	WM	+21	70	0.5054	δ_{max} = 0.236
W412	HAZ	-101	-150	0.5026	δ_c = 0.053
W4110	HAZ	-101	-150	0.5132	δ_c = 0.018
W415	HAZ	-73	-99	0.5971	δ_c = 0.114
W4114	HAZ	-18	-0.4	0.5074	δ_{max} = 0.127
W4113	HAZ	-18	-0.4	0.5142	δ_c = 0.076
W417	HAZ	-18	-0.4	0.5292	δ_u = 0.155
W418	HAZ	0	32	0.5117	δ_u = 0.188
W4111	HAZ	0	32	0.5121	δ_{max} = 0.432
W419	HAZ	24	75	0.5159	δ_{max} = 0.249
W411	HAZ	21	70	0.5057	δ_{max} = 0.226

* where: δ_c = CTOD at unstable fracture or onset of arrested brittle crack growth <u>without</u> evidence of slow crack growth.

δ_u = CTOD at unstable fracture on onset of arrested brittle crack growth <u>with</u> evidence of slow crack growth.

δ_{max} = CTOD at maximum applied force.

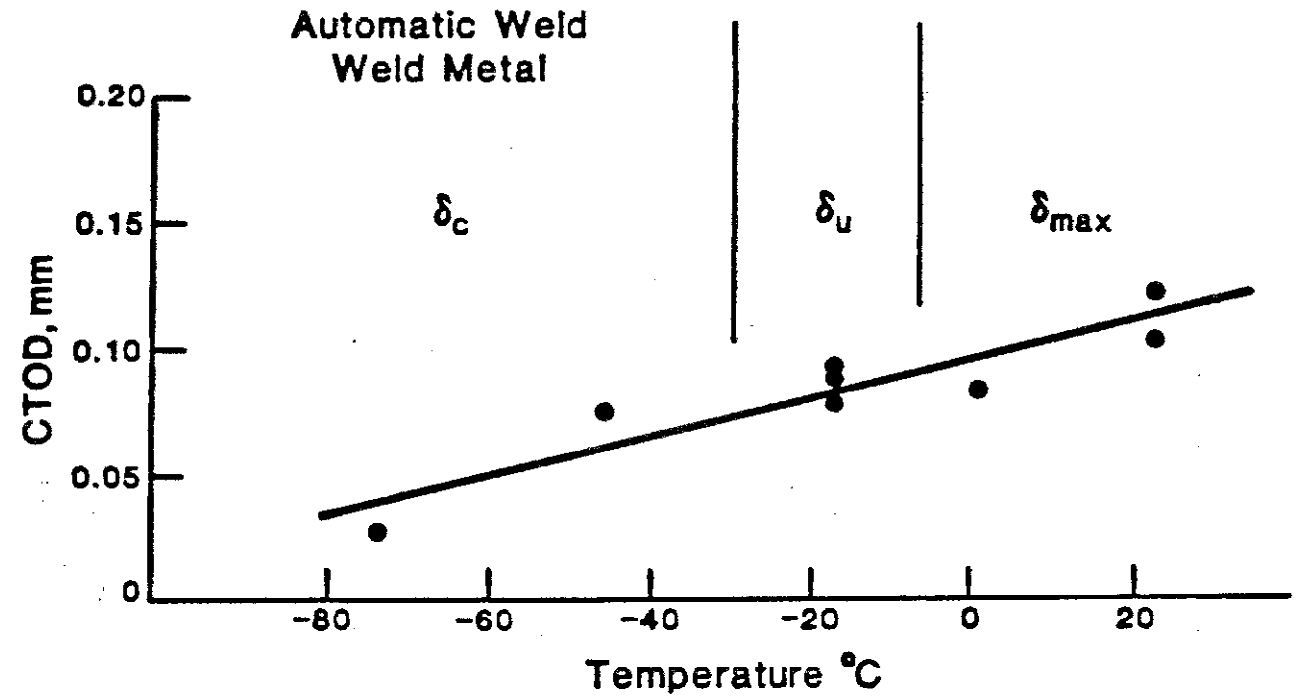

(a)

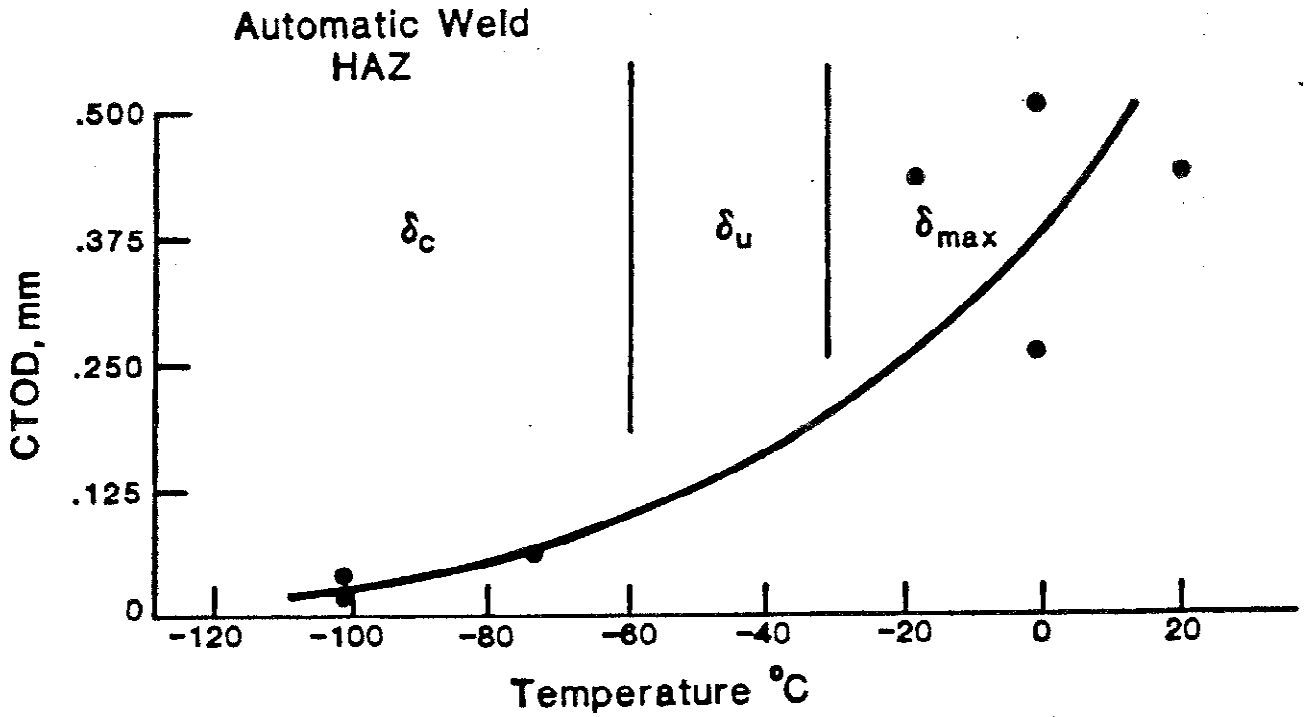

(b)

Fig. B-6. — Temperature dependence of crack-opening displacement for (a) automatic GMA girth weld and (b) HAZ from the automatic girth weld.

fracture toughness is variable because it depends on the detailed shape of the fatigue crack, the resulting stress intensity due to the applied load, and the expected difference in toughness in each of the three regions.

Using the temperature dependence of the CTOD toughness parameter as shown in Table B-3 and B-4, an estimate was made of the lowest temperature at which consistent and reproducible slow, stable crack growth would occur. At this temperature, arrested brittle crack growth or pop-in would not be expected. These temperatures were estimated to be 0°C (32°F) for the automatic weld and -18°C (-0.4°F) for the manual weld, and the temperatures for each HAZ were estimated to be -18°C (-0.4°F) and 0°C (+32°F), respectively.

A multiple-specimen resistance curve approach was used to determine the critical CTOD, δ_i, at the initiation of stable crack growth. The crack-opening-displacement procedure was based on Appendix A of British Standard BS5762 (1979).[93] Each fatigue precracked specimen was loaded in displacement control at a rate 0.25 mm/min (0.010 in/min) to various values of clip-gage displacement to obtain various amounts of crack, δ, for each increment of slow, stable crack growth. Then each specimen was rapidly unloaded and heat-tinted to mark the extent of stable crack growth. Each specimen was cooled in liquid nitrogen, fractured, and the amount of crack extension measured. The results of these tests are summarized in Tables B-5 and B-6 and Figs. B-7 and B-8. The δ_i representative of the initiation of stable crack growth was taken as the value of crack-tip-opening displacement at zero crack extensions, $\Delta a = 0$. The values of δ_i for the automatic and manual girth welds are 0.074 mm (0.0029 in) at 0°C (32°F) and 0.079 mm (0.0031 in) at -18°C (-0.4°), respectively, and the HAZ values of δ_i are 0.14 mm (0.0055 in) at -18°C (-0.4°F) and 0.17 mm (0.0067 in) at 0°C (+32°F), respectively.

Table B-5 — Critical CTOD for Initiation of Slow, Stable Crack Growth for the Automatic Weld

Specimen Number	Type	Temperature, °C	°F	P, kN	lbf x 10^3	a/W,	Δa, mm	in	CTOD, mm	in
W122	WM	0	-32	17.1	3.84	0.5018	0.431	0.0170	0.076	0.0030
W126	WM	0	32	18.1	4.07	0.5006	0.356	0.0140	0.097	0.0038
W124	WM	0	32	17.4	3.91	0.5060	0.660	0.0260	0.099	0.0039
W1217	WM	0	32	17.5	3.93	0.5041	0.533	0.0210	0.107	0.0042
W1215	HAZ	-18	-0.4	17.9	4.02	0.5081	0.152	0.0060	0.109	0.0043
W1310	HAZ	-18	-0.4	18.9	4.25	0.5059	0.086	0.0034	0.163	0.0064
W1311	HAZ	-18	-0.4	18.3	4.11	0.5113	0.401	0.0158	0.190	0.0075
W1312	HAZ	-18	-0.4	19.4	4.36	0.5054	0.142	0.0056	0.196	0.0077

Table B-6 — Critical CTOD for Initiation of Slow, Stable Crack Growth for the Manual Weld

Specimen Number	Type*	Temperature, °C	°F	P, kN	lbf x 10^3	a/W	Δa, mm	in	CTOD, mm	in
W4119	WM	-18	-0.4	13.92	3.129	0.5092	0.066	0.0026	0.094	0.0037
W4118	WM	-18	-0.4	14.41	3.240	0.5042	0.122	0.0048	0.119	0.0047
W4116	WM	-18	-0.4	14.54	3.269	0.5137	0.277	0.0109	0.142	0.0056
W413	WM	-18	-0.4	14.52	3.264	0.5079	0.246	0.0097	0.167	0.0066
W414	HAZ	-18	-0.4	14.12	3.174	0.5140	0.361	0.0142	0.185	0.0073
W4120	HAZ	0	32	14.14	3.179	0.5117	0.129	0.0051	0.150	0.0059
W4112	HAZ	0	32	14.79	3.325	0.5169	1.85	0.0728	0.178	0.0070
W4115	HAZ	0	32	15.50	3.485	0.5131	0.081	0.0032	0.231	0.0091
W4121	HAZ	0	32	16.06	3.610	0.5087	0.193	0.0076	0.300	0.0118

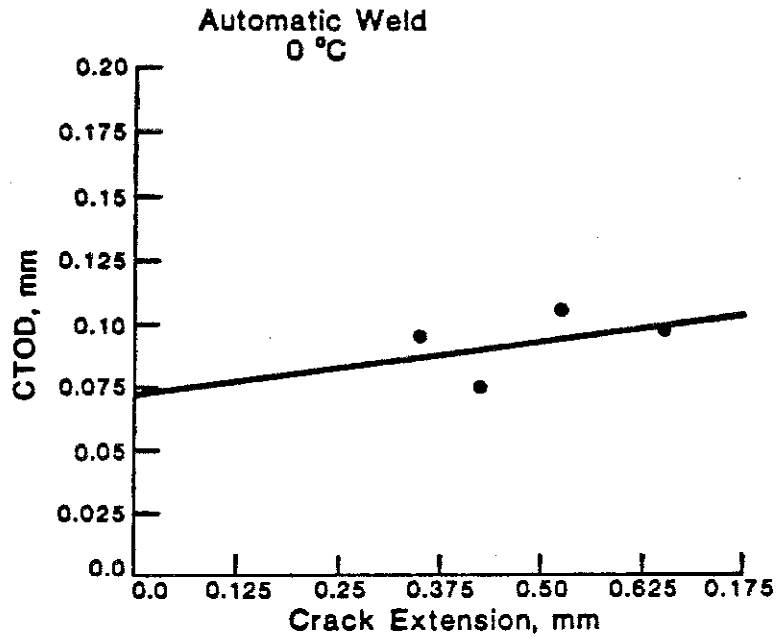

(a)

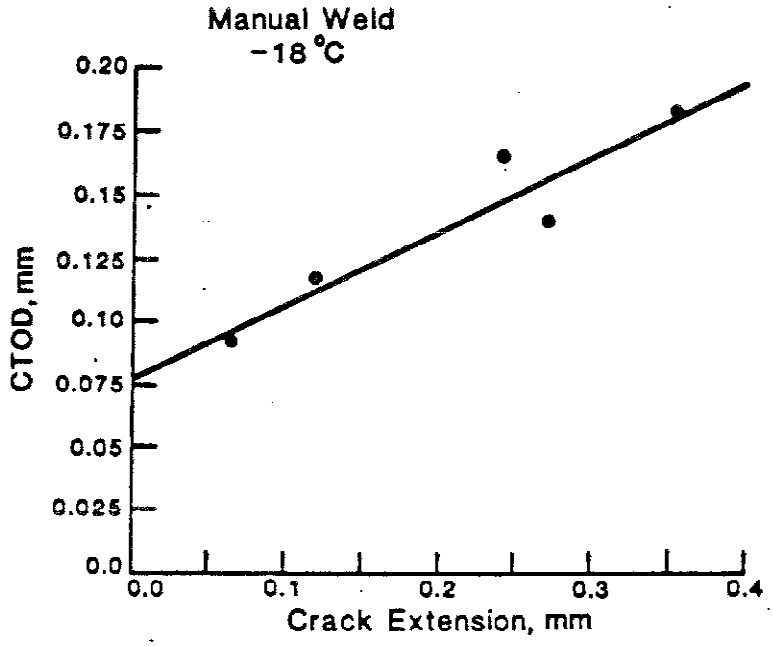

(b)

Fig. B-7 — Crack-opening displacement for the initiation of slow, stable crack growth (a) for the automatic girth weld at 0°C (32°F) and (b) for the manual SMA girth weld at -18°C (-0.4°F). To obtain inches, multiply the millimeters by 0.0394.

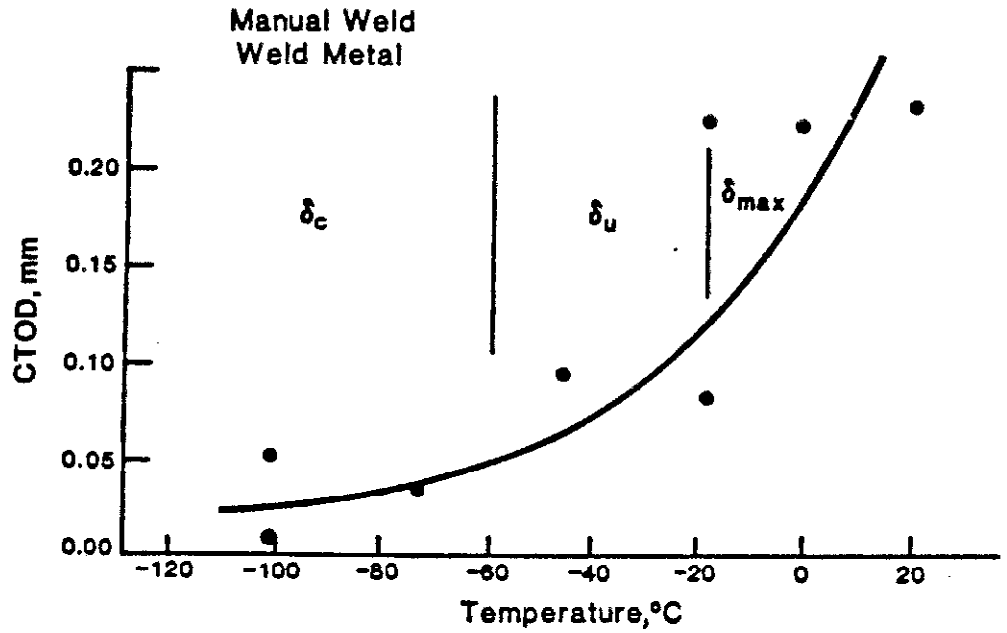

(a)

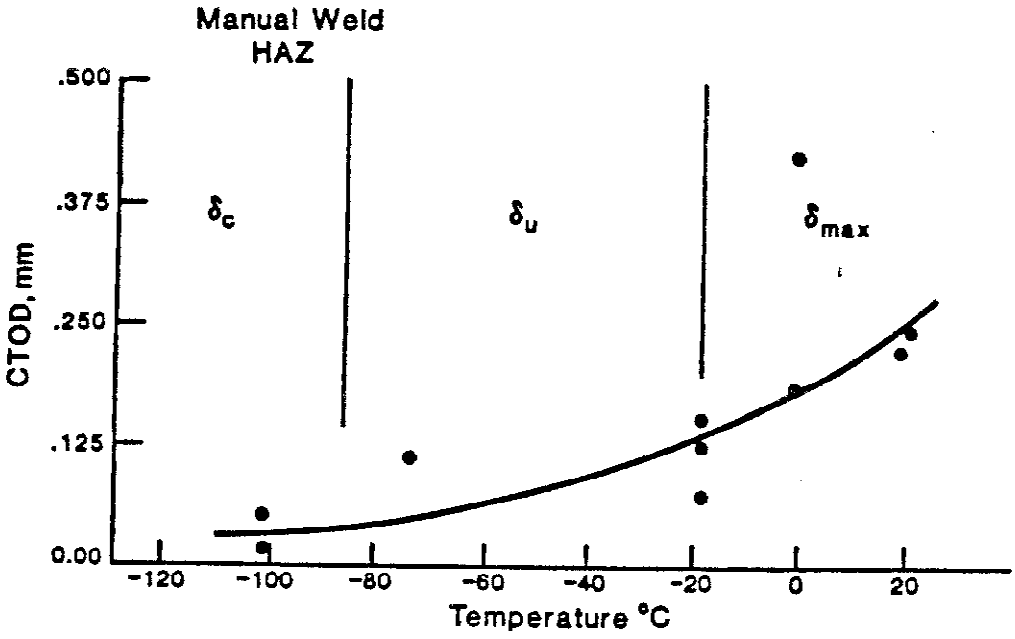

(b)

Fig. B-8 — Temperature dependence of crack-opening displacement for (a) the weld metal and (b) the HAZ in the manual SMA girth weld.

The measured δ_{max} of 0.083 mm (0.0033 in) at 0°C (+32°F) for the automatic weld is consistent with the calculated δ_i of 0.074 mm (0.0029 in) because of the lack of a strong temperature dependence of the CTOD (Fig. B-6a) and the very shallow slope of the CTOD-vs.-stable crack extension curve (Fig. B-7a). The δ_{max} of 0.023 mm (0.00091 in) at -18°C (-0.4°F) for the manual weld is consistent with the calculated δ_1 of 0.079 mm (0.0031 in) because of the stronger temperature dependence of the CTOD (Fig. B-6b) and the steeper slope of the CTOD-vs.-crack extension curve (Fig. B-7b). Although considerably greater scatter was observed in the HAZ data, the same general relationship was observed when comparing the calculated δ_i to δ_{max}.

11. REFERENCES

1. "Minimum Federal Safety Standards for Liquid Pipeline," Code of Federal Regulations, Title 49 Transportation, Part 195, Office of the Federal Register, National Archives and Records Service, General Services Administration (revised 1 Oct. 1975). Available like a journal in libraries.

2. "Standard for Welding Pipelines and Related Facilities," 15th & 16th Edition, API Standard 1104, American Petroleum Institute, New York (July 1983).

3. "Consideration of Fracture Mechanics Analysis and Defect Dimension Measurement Assessment for the Trans-Alaska Oil Pipeline Girth Welds," NBSIR 76-1154, National Bureau of Standards, Gaithersburg, Maryland (Oct. 1976).

4. R. P. Reed, H. I. McHenry, and M. B. Kasen, "A Fracture Mechanics Evaluation of Flaws in Pipeline Girth Welds," Weld. Res. Counc. Bull. 245, (Jan. 1979).

5. A. A. Butchman, "Trans-Alaska Crude Oil Pipeline" (petition for waiver of girth weld defects), Fed. Regist. 42 119, 31512 (1977).

6. J. W. Barnum, "Trans-Alaska Crude Oil Pipeline" (decision on petition for waiver of girth weld regulations), Fed. Regist. 41 233 52933-52949 (1976).

7. "Draft British Standard Rules for Derivation of Acceptance Limits for Defects in Fusion Welded Joints," Document 75/77081 DC, British Standards Institution, London (Feb. 1976).

8. "Guidance on Some Methods for the Derivation of Acceptance Levels for Defects in Fusion Welded Joints," PD 6493 (1980), British Standards Institution, London (1980).

9. "Specifications for Field Welding of Carbon Steel Pipelines," BS 4515 (1969), British Standards Institution, London (1969).

10. M. M. P. Carne and J. D. Harrison, "Proposals for a Fracture Mechanics Based Criterion for the Acceptance of Defects in Pipeline Girth Welds," presented at the American Welding Society International Conference, Pipeline Welding and Inspections, Houston, Texas (Sept. 21-22, 1982).

11. A. G. Glover, and R. I. Coote, "Alternative Inspection Methods and Defect Acceptance Standards for Large Diameter Gas Pipelines," presented at the American Welding Society International Conference, Pipeline Welding and Inspection, Houston, Texas (Sept. 21-22, 1982).

12. "Method of Assessment for Defects in Fusion-Welded Joints with Respect to Brittle Fracture," Japan Welding Engineering Society Standard WES 2805-1980, The Japan Welding Engineering Society, Tokyo (1980).

13. E. L. Von Rosenberg and C. P. Royer, "Pipeline Welding Standards," presented at the American Welding Society International Conference, Pipeline Welding and Inspection, Houston, Texas (Sept. 21-22, 1982).

14. R. P. Reed, M. B. Kasen, H. I. McHenry, C. M. Fortunko, and D. T. Read, "Fitness-for-Service Criteria for Pipeline Girth-Weld Quality," Final Report to the U.S. Department of Transportation, National Bureau of Standards, Boulder, Colorado (1 Nov. 1983). Available from NTIS, Springfield, Virginia.

15. "A Critical Evaluation of Numerical Solutions to the 'Benchmark' Surface-flaw Problem," Exp. Mech., 20, No. 8, 253-264 (1980).

16. J. C. Newman, Jr. and I. S. Raju, "Analyses of Surface Cracks in Finite Plates under Tension or Bending Loads," NASA Technical Paper 1518 (1979). Available from NTIS, Springfield, Virginia.

17. J. G. Merkle, "A Review of Some of the Existing Stress Intensity Factor Solutions for Part-through Surface Cracks," ORNL-TM-3983, U.S. Atomic Energy Commission (Jan. 1973).

18. J. C. Newman, Jr., "Predicting Failure of Specimens with Either Surface Cracks or Corner Cracks at Holes," NASA TN D-8244 (1976). Available from NTIS, Springfield, Virginia.

19. G. R. Irwin, "Plastic Zone near a Crack and Fracture Toughness," Proceedings Seventh Sagamore Ordance Materials Research Conference, Vol. IV., Syracuse University Press, Syracuse, New York, 63-78 (1960).

20. D. S. Dugdale, "Yielding of Steel Sheets Containing Slits," Mech. Phys. Solids, 8, 100-108 (1960).

21. G. R. Irwin, "Characterization of Part-through Cracks in Tension," The Surface Crack: Physical Problems and Computational Solutions, ed. J. L. Swedlow, ASME, New York, 1-10 (1972).

22. R. B. King, "Elastic-Plastic Analysis of Surface Flaws Using a Simplified Line-Spring Model," Eng. Fract. Mech., in press.

23. A. S. Kobayashi, "Crack Opening Displacement in a Surface Flawed Plate Subjected to Tension or Plate Bending," Proceedings of the Second International Conference on Mechanical Behavior of Materials, American Society for Metals, Metals Park, Ohio, 1073-1077 (1976).

24. A. S. Kobayashi, "Crack Opening Displacement in a Surface Flawed Plate Subjected to Tension or Plate Bending," Document No. D-180-19446-1, The Boeing Aerospace Company, Seattle (1976).

25. J. R. Rice and N. Levy, "The Part-through Surface Crack in an Elastic Plate," J. Appl. Mech., 39, 185-194 (1972).

26. J. R. Rice, "The Line-Spring Model for Surface Flaws," The Surface Crack: Physical Problem and Computational Solutions, ed. J. L. Swedlow, ASME, New York, 171-185 (1972).

27. D. M. Parks, "The Inelastic Line. Estimates of Elastic-Plastic Fracture Mechanics Parameters for Surface Cracked Plates and Shells," ASME 80-C2/PVP-109, ASME, New York (1980).

28. R. R. Lockett and D. M. Parks, "The Line Spring Model for J Analysis of Surface-Cracked Plates and Shells," presented at the Second International Symposium on Elastic-Plastic Fracture Mechanics, Philadelphia (1981).

29. M. Shiratori and T. Miyoshi, "Evaluation of the J Integral for Surface Cracks," presented at the Second International Symposium on Elastic-Plastic Fracture Mechanics, Philadelphia (1981).

30. D. M. Parks, "Inelastic Analysis of Surface Flaws Using the Line Spring Model," Proceedings of the Fifth International Conference on Fracture, Pergamon, Oxford, 2589-2598 (1981).

31. R. B. King, Y. W. Cheng, D. T. Read, and H. I. McHenry, "J-Integral Analysis of Surface Flaws in Pipeline Steel Plates," ASTM STP 803, Vol. I, American Society for Testing and Materials, Philadelphia, 1444-1459 (1983).

32. Y. W. Cheng, H. I. McHenry, and D. T. Read, "Crack Opening Displacement of Surface Cracks in Pipeline Steel Plates," presented at the ASTM 14th Symposium on Fracture Mechanics, Los Angeles (1981).

33. P. T. Heald, G. M. Spink, and P. J. Worthinton, "Post Yield Fracture Mechanics," Mater. Sci. Eng., 10, 129-136 (1972).

34. R. deWit and J. H. Smith, "Development of Some Analytical Fracture Mechanics Models for Surface Defects in Plates of Ductile Metals," Continuum Modeling of Discrete Systems, University of Waterloo Press, Ontario, Canada (1980).

35. H. Tada, P. C. Paris, and G. R. Irwin, The Stress Analysis of Cracks Handbook, Del Research Corporation, Hellertown, Pennsylvania (1973).

36. R. Coote, Nova Corporation, Calgary, Canada, private communication.

37. S. A. Wenk, "Radiographic Video Technique for Sizing Defects in Pipe Welds," Mater. Eval., 39, No. 8, 748-751 (1981).

38. P. A. Doyle and C. M. Scala, "Crack Depth Measurement by Ultrasonics," Ultrasonics, 16, No. 3, 164-170 (1978).

39. C. M. Fortunko and R. E. Schramm, "Ultrasonic Nondestructive Evaluation of Butt Welds Using Electromagnetic-Acoustic Transducers," Weld. J., 61, No. 2, 39-46 (1982).

40. C. M. Fortunko, R. B. King, and M. Tan, "Nondestructive Evaluation of Planar Defects in Plates Using Low-Frequency Shear Horizontal Waves," J. Appl. Phys., 53, No. 5, 3450-3458 (1982).

41. C. M. Fortunko, "Ultrasonic Detection and Sizing of Two-Dimensional Defects at Long Wavelengths," Appl. Phys. Lett., 38, No. 12, 980-982 (1981).

42. N. Nielsen, "P-Scan System for Ultrasonic Weld Inspection," Br. J. NDT, 23, No. 3, 63-69 (1981).

43. A. deSterke, "Automated Ultrasonic Inspection of Circumferential Welds in Pipelines," Met. Constr., 12, No. 3, 42-46 (1981).

44. W. C. Minton, "Ultrasonic Inspection of Pipeline Welds," in Proceedings 1980 Pipeline Welding and Inspection Conference, ed. D. Weir, American Welding Society, Miami, 65-76 (1980).

45. R. F. Lumb, "Nondestructive Testing of Pipeline Girth Welds in the 1980's," Br. J. NDT, 24, No. 7, 197-207 (1982).

46. C. M. Fortunko, C. F. Vasile, and R. B. Thompson, "Electromagnetic Transducers for Weld Inspection," presented at 37th National Fall Conference of The American Society for Nondestructive Testing, Detroit, Michigan (Oct. 3-6, 1977).

47. C. F. Vasile and R. B. Thompson, "Excitation of Horizontally Polarized Elastic Waves by Electromagnetic Transducers with Periodic Magnets," J. Appl. Phys., 50, No. 4, 2583-2588 (1979).

48. M. deBilly, F. Cohen-Tenondji, G. Quentin, K. Lewis, and L. Adler, "Ultrasonic Evaluation of Geometrical and Surface Parameters of Rough Defects in Solids," J. Nondestruct. Eval., 4, 244-261 (1980).

49. B. A. Auld and S. Ayter, "Perturbation Method for Analyzing the Effect of Ultrasonic Echo Returns on Rough Surfaces in Material Cracks and Voids,". 1980 IEEE Ultrasonics Symposium Proceedings., ed. B. R. McAvoy, IEEE, New York 852-856 (1980).

50. J. M. Richardson and R. K. Elseley, "Extraction of Low-Frequency Properties from Scattering Measurements," 1979 IEEE Ultrasonics Symposium Proceedings, ed. B. R. McAvoy, IEEE, New York, 336-341 (1979).

51. B. Budiansky and J. R. Rice, "On the Estimation of a Crack Fracture Parameter by Long Wavelength Scattering," J. Appl. Mech., 45, No. 6, 453-454 (1978).

52. C. D. Lundin, "The Significance of Weld Discontinuities - A Review of Current Literature," Welding Research Council Bulletin 222, Welding Research Council, New York (1976).

53. M. B. Kasen and R. P. Mikesell, "Interim Report on the Significance of Blunt Flaws in Pipeline Girth Welds," Proceedings of International Conference on Pipeline and Energy Plant Piping, ed. N. F. Eaton, Pergamon, Toronto, 329-336 (1980).

54. R. B. Thompson, "The Relationship between Radiating Body Forces and Equivalent Surface Stresses: Analysis and Application to EMAT Design," J. Nondestruct. Eval., 1, 79-86 (1980).

55. S. K. Datta, C. M. Fortunko, and R. B. King, "Sizing of Surface Cracks in a Plate Using SH Waves," 1981 IEEE Ultrasonics Symposium Proceedings, ed. B. R. McAvoy, IEEE, New York, 863-867 (1981).

56. S. K. Datta and A. H. Shah, "Scattering of SH Waves by Embedded Cavities," Wave Motion, in press.

57. S. K. Datta, A. H. Shah, and C. M. Fortunko, "Diffraction of Medium and Long Wavelength Horizontally Polarized Waves by Edge Cracks," J. Appl. Phys., 53, No. 4, 2895-2903 (1982).

58. J. Krautkramer and H. Krautkramer, Ultrasonic Testing of Materials, Second Edition, Springer-Verlag, Berlin, 338-343 (1977).

59. W. J. Pardee and R. B. Thompson, "Half-Space Radiation by EMATs," J. Nondestruct. Eval., 1, 150-181 (1980).

60. B. A. Auld, "General Electromechanical Reciprocity Relations Applied to the Calculation of Elastic Wave Scattering Coefficients," Wave Motion, 1, 3-10 (1979).

61. N. N. Egorov and A. V. Kharitonov, "Diffraction of Shear Normal Modes by a Surface Crack in an Elastic Plate," Sov. Phys. Acoust., 25, No. 1, 34-37 (1979).

62. R. B. King and C. M. Fortunko, "Extended Variational Solution for Scattering from Flaws in Plates," J. Appl. Phys. 53, No. 5, 3459-3460 (1982).

63. R. B. Thompson, "A Model for Electromagnetic Generation of Rayleigh and Lamb Waves," IEEE Trans. Sonics Ultrason. 20, No. 4, 340-346 (1973).

64. C. M. Fortunko and R. E. Schramm, "An Analysis of Electromagnetic-Acoustic Transducer Arrays for Nondestructive Evaluation of Thick Metal Sections and Weldments," in Proceedings 1982 Review of Progress in Quantitative NDE, eds. D. O. Thompson and C. E. Chimenti, Plenum, New York (1983), in press.

65. R. B. Thompson, S. A. Alers, and M. A. Tennison, "Application of Direct Electromagnetic Lamb Wave Generation to Gas Pipeline Inspection," Proceedings 1972 Ultrasonics Symposium, ed. A. deKlerk, IEEE, New York, 91-94 (1972).

66. H. Tada, P. C. Paris, and G. R. Irwin, The Stress Analysis of Cracks Handbook, Del Research, Hellertown, Pennsylvania, 5.1-8.1 (1973).

67. M. Born and E. Wolf, Principles of Optics, Pergamon, Oxford, 430-433 (1975).

68. J. C. Newman, Jr., "A Review and Assessment of the Stress-Intensity Factors for Surface Cracks," in Part-through Crack Fatigue Life Prediction, ed. J. B. Chang, ASTM STP 687, American Society for Testing and Materials, Philadelphia, 16-42 (1979).

69. R. B. King, and Y. W. Cheng, Fracture and Deformation Division, National Bureau of Standards, Boulder, Colorado, private communication.

70. J. M. Richardson and A. G. Evans, "Accept-Reject Decisions for Structural Ceramics: Application to Failure from Voids," J. Nondestruct. Eval., 1, No. 1, 37-52 (1980).

71. J. D. Harrison, "Low Cycle Fatigue Tests on Welded Joints in High Strength Steels," Proceedings, Conference on Welded Structures, Welding Institute, Cambridge (1971).

72. J. D. Harrison, "The Basis for a Proposed Acceptance Standard for Weld Defects, Part 1: Porosity," Met. Const. Br. Weld. J., 4, 99-107 (1972a).

73. J. D. Harrison, "The Basis for a Proposed Acceptance Standard for Weld Defects, Part 2: Slag Inclusions" Met. Const. Br. Weld. J., 4, 262-268 (1972b)

74. F. M. Burdekin, University of Manchester, personal communication.

75. C. R. Boulton, "Acceptance Levels of Weld Defects for Fatigue Service," Weld. J., 56, 13-22 (1977).

76. J. D. Harrison, G. L. Archer, and C. F. Boulton, "Significance of Defects in Pressure Vessels under Fatigue Loading," Tolerance of Flaws in Pressurized Components, The Institution of Mechanical Engineers, London, 255-270 (1978).

77. Y. Ishii and K. Iida, "An Analysis of Intermediate Cycle Fatigue Strength of Defective Welded Joints," Trans. Jap. Weld. Soc., 3, 1-8 (1972).

78. T. R. Gurney, Fatigue of Welded Structures, 2nd Edition., Cambridge University Press, Cambridge, England (1979).

79. N. Bailey, "Fisheyes, Hydrogen Embrittlement, and Removal," Weld. Inst. Res. Bull., 15, 369-372 (Dec. 1974).

80. A. Matting and M. Neitzel, "The Influence of Weld Defects on the Fatigue Behavior of Welded Constructions," Br. Weld. J., 14, No. 1, 3-12 (1967).

81. G. L. Archer, "Research on the Significance of Defects in Weld Regions of Pressure Vessels," Proceedings Conference on Pressure Vessel Standards, The Impact of Change, The Welding Institute, London, 100-106 (1972).

82. G. D. Fearnehough and D. G. Jones, "An Approach to Defect Tolerance in Pipelines,"paper ERS E. 199, Proceedings Conference on Defect Tolerance of Pressure Vessels, paper ERS E.199, Institution of Mechanical Engineers, Great Britain (1978).

83. R. F. Lumb and G. D. Fearnehough, "Toward Better Standards for Field Welding of Gas Pipelines," Weld. J. Res. Suppl., No. 54, 63-s-71-s (1975).

84. R. P. Newman and T. R. Gurney, "Fatigue Tests on ½ in. Thick Transverse Butt Welds Containing Slag Inclusions: 1st Interim Report," Br. Weld. J., 11, No. 7, 341-352 (1964).

85. R. C. Placious, D. A. Garrett, M. B. Kasen, and H. Berger,"Dimensioning Flaws in Pipeline Girth Welds by Radiographic Methods," Mater. Eval., 39, 755-560 (1981).

86. J. Norrish and D. C. Moore, "Porosity in Arc Welds and its Effect on Mechanical Properties," Proceedings Second Conference on the Significance of Defects in Welds, Welding Institute, Cambridge (1968).

87. J. D. Harrison, "The Basis for a Proposed Acceptance Standard for Weld Defects, Part 1: Porosity," Metal. Const. Brit. Weld. J., 4, 97-107 (1972).

88. "Guidance on Some Methods for the Derivation of Acceptance Levels for Defects in Fusion Welded Joints, PD6493, British Standards Institution, London (1980).

89. R. P. Reed, H. I. McHenry, and M. B. Kasen, "A Fracture Mechanics Evaluation of Flaws in Pipeline Girth Welds," Weld. Res. Counc. Bull. 245, Welding Research Council, New York (Jan. 1979).

90. P. Tait and D. M. Haddrill, "Fracture Toughness of Some Mild Steel Manual Metal-Arc Weld Deposits," Weld. Met. Fabr., 370-375 (1970).

91. S. K. Datta, University of Colorado, Boulder, Colorado (private communication.

92. R. B. King and C. M. Fortunko, "Determination of In-Plane Residual Stress in Plates Using Horizontally Polarized Shear Waves," J. App. Phys., 54, 3027-3035, (1983).

93. "Methods for Crack Opening Displacement (COD) Testing," BS5762 British Standards Institution, London (1979).

94. J. D. Harrison, "The State-of-the-Art in Crack Tip Opening Displacement (CTOD) Testing and Analysis," Report No. 7302.10/80/210.2, The Welding Institute, Cambridge, England (1980).

95. G. Kaufman, "Developments in Fracture Mechanics Test Methods Standardization" ASTM STP 632, American Society for Testing and Materials, Philadelphia, 11- (1977).

96. H. G. Pisarski and M. G. Dawes, "Measurement of Crack Opening Displacement in Weldments with Particular Reference to Offshore Structures," Fracture Mechanics, Rome, Italy (June 1980).

97. M. G. Dawes, "Fatigue Precracking Weldment Fracture Mechanics Specimens," Met. Constr. and Brit. Weld. J., 3, No. 2, 61-65 (1971).

98. M. G. Dawes, "Contemporary Measurement of Weld Metal Fracture Toughness," Weld. J. 55, 1052-1057 (1976).

12. BIBLIOGRAPHY OF RELEVANT NBS PUBLICATIONS

12.1 Fracture Mechanics

"Consideration of Fracture Mechanics Analysis and Defect Dimension Measurement Assesssment for the Trans-Alaska Oil Pipeline Girth Welds," Vols. I and II, NBSIR 76-1154, National Bureau of Standards, Boulder, Colorado (1976).

Y. W. Cheng, R. B. King, D. T. Read, and H. I. McHenry, "Post Yield Crack-Opening Displacement of Surface Cracks in Steel Weldments," submitted for publication in Fracture Mechanics, Fifteenth Symposium, American Society for Testing and Materials, Philadelphia.

Y. W. Cheng, H. I. McHenry, and D. T. Read, "Crack-Opening Displacement of Surface Cracks in Pipeline Steel Plates," to be published in Fracture Mechanics, Fourteenth Symposium, STP 793, American Society for Testing and Materials, Philadelphia.

R. deWit and J. H. Smith, "Development of Some Analytical Fracture Mechanics Models for Pipelien Girth Welds," Fracture Mechanics, Twelfth Conference, STP 700, American Society for Testing and Materials, Philadelphia, 513-528 (1980).

R. B. King, Y. W. Cheng, D. T. Read, and H. I. McHenry, "J-Integral Analysis of Surface Cracks in Pipeline Steel Plates," to be published in Elastic-Plastic Fracture Mechanics, Second International Symposium, American Society for Testing and Materials, Philadelphia.

H. I. McHenry, D. T. Read, and J. A. Begley, "Fracture Mechanics Analysis of Pipeline Girth Welds," Elastic-Plastic Fracture, STP 668, American Society for Testing and Materials, Philadelphia, 632-642 (1980).

D. T. Read and H. I. McHenry, "Strain Dependence of the J-Contour Integral in Tensile Panels," Advances in Fracture Research, Pergamon, New York (1980).

R. P. Reed, H. I. McHenry, and M. B. Kasen, "A Fracture Mechanics Evaluation of Flaws in Pipeline Girth Welds," Bulletin 245, Welding Research Council, New York (1979).

12.2 Inspection and Dimensioning of Flaws

S. K. Datta, C. M. Fortunko, and R. B. King, "Sizing of Surface Cracks in a Plate Using SH Waves," Proceedings, 1981 Ultrasonic Symposium, ed. B. R. McAvoy, IEEE, New York, 863-867 (1981).

C. M. Fortunko, "Ultrasonic Detection and Sizing of Two-Dimensional Defects at Long Wavelengths," Appl. Phys. Lett., 38, No. 12, 980-982 (1981).

C. M. Fortunko, R. B. King, and M. Tan, "Nondestructive Evaluation of Planar Defects in Plates Using Low-Frequency Shear Horizontal Waves," J. Appl. Phys., 53, No. 5, 3450-3458 (1982).

C. M. Fortunko and R. E. Schramm, "An Analysis of Electromagnetic-Acoustic Transducer Arrays for Nondestructive Evaluation of Thick Metal Sections and Weldments," Proceedings, 1982 Review of Progress in Quantitative Nondestructive Evaluation, eds. D. O. Thompson and C. E. Chimenti, Plenum Press, New York (1983), in press.

C. M. Fortunko and R. E. Schramm, "Ultrasonic Nondestructive Evaluation of Butt Welds Using Electromagnetic-Acoustic Transducers," Weld. J., 61, No. 2, 39-46 (1982).

M. B. Kasen, G. E. Hicho, and R. C. Placious, "Inherent Through-Wall Depth Limitations on Blunt Flaws in Welds," accepted for publication in Weld J.

R. B. King and C. M. Fortunko, "Extended Variational Solution for Scattering from Flaws in Plates," J. Appl. Phys., 53, No. 5, 3459-3460 (1982).

R. C. Placious, "Radiographic Inspection of Pipeline Welds," Pipeline Welding and Inspection, American Welding Society, Miami, 51-63 (1980).

R. C. Placious, D. A. Garrett, M. B. Kasen, and H. Berger, "Dimensioning Flaws in Pipeline Girth Welds by Radiographic Means," Mater. Eval. 39, 755-760.

12.3 Significance of Blunt Flaws

M. B. Kasen, "Significance of Blunt Flaws in Pipeline Girth Welds," accepted for publication in Weld. J.

M. B. Kasen and R. P. Mikesell, "Interim Report on the Significance of Blunt Flaws in Pipeline Girth Welds," Pipeline and Energy Plant Piping: Design and Technology, Welding Institute of Canada, Pergamon Press, Toronto, 329-336 (1980).

M. B. Kasen and R. P. Mikesell, "Effect of Blunt Flaws Studied in Pipeline Girth Welds," Oil Gas J. (Technol.), 155-159 (March 30, 1981)

12.4 General

M. B. Kasen and C. M. Fortunko, "Fitness-for-Purpose Criteria for Pipeline Girth Welds," presented at Pipeline Welding and Inspection Conference, American Welding Society, Houston, Texas (Sept. 21-22, 1982).

R. P. Reed, "Goal: Better Standards for Pipeline Welds," Weld, Des. Fabr., 68-71 (1981).

C. Smith, "Putting It All Together--Alaskan Pipeline Weld Criteria," Dimensions, , 3-5 (1980).